

# Sheffield Hallam University

*An investigation into the design and performance of an automatic shape control system for a Sendzimir cold rolling mill.*

DUTTON, Kenneth.

Available from the Sheffield Hallam University Research Archive (SHURA) at:

<http://shura.shu.ac.uk/19587/>

## A Sheffield Hallam University thesis

This thesis is protected by copyright which belongs to the author.

The content must not be changed in any way or sold commercially in any format or medium without the formal permission of the author.

When referring to this work, full bibliographic details including the author, title, awarding institution and date of the thesis must be given.

Please visit <http://shura.shu.ac.uk/19587/> and <http://shura.shu.ac.uk/information.html> for further details about copyright and re-use permissions.

SHEFFIELD 01 477

795062301 2

TELEPEN



**Sheffield City Polytechnic Library**

**REFERENCE ONLY**



ProQuest Number: 10694468

All rights reserved

INFORMATION TO ALL USERS

The quality of this reproduction is dependent upon the quality of the copy submitted.

In the unlikely event that the author did not send a complete manuscript and there are missing pages, these will be noted. Also, if material had to be removed, a note will indicate the deletion.



ProQuest 10694468

Published by ProQuest LLC (2017). Copyright of the Dissertation is held by the Author.

All rights reserved.

This work is protected against unauthorized copying under Title 17, United States Code  
Microform Edition © ProQuest LLC.

ProQuest LLC.  
789 East Eisenhower Parkway  
P.O. Box 1346  
Ann Arbor, MI 48106 – 1346

AN INVESTIGATION INTO THE DESIGN AND PERFORMANCE OF AN  
AUTOMATIC SHAPE CONTROL SYSTEM FOR A SENDZIMIR COLD  
ROLLING MILL

Kenneth Dutton, B.Sc., C.Eng., M.I.E.E.

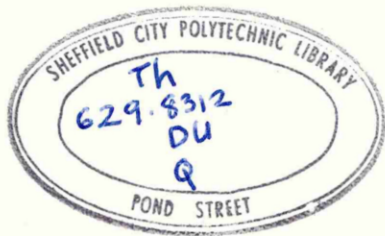
May 1983

A thesis submitted in line with the requirements of the CNAA, as partial fulfilment of the conditions necessary for the award of the Ph.D. (Doctor of Philosophy) Degree.

Department of Electrical & Electronic Engineering,  
Sheffield City Polytechnic,  
Pond St.,  
Sheffield,  
S1 1WB.

Collaborating Establishment:

British Steel Corporation,  
Sheffield Laboratories,  
Moorgate,  
Rotherham,  
S60 3AR.



7950623 01

To Lizzie my wife and Suzie my daughter

(with many thanks for your patience during my prolonged absences from normal family life, and also with the hope that outstanding tasks around the house may now stand a chance of completion.)

## Declaration

Whilst registered for this degree I have not been a registered candidate for any other academic award. None of the material in this thesis has been used in any other submission for an academic award.

All sources of information are acknowledged and duly referenced.

Ken Dutton

## Request for Confidentiality

As the subject of this research is now being installed as a working scheme by the author at a British Steel Works it is requested that this thesis be allowed to remain confidential for the time allowed in the CNAAs rules. The original purpose of the research was to give British Steel a lead in this area, and the information in this thesis should therefore remain undisclosed to competitors for as long as possible.

## ACKNOWLEDGEMENTS

During the course of this work discussions have clearly taken place with many different people, as a result of which much helpful comment has been forthcoming. I heartily thank anyone to whom this applies.

Special thanks are due to my supervisors for their guidance and encouragement, namely to Professor M. J. Grimble of Strathclyde University (formerly of Sheffield City Polytechnic) and Dr. K. A. Jukes of Bristol Polytechnic (formerly also of Sheffield City Polytechnic). Thanks also to Mr. M. A. Foster of British Aluminium (who was formerly my industrial second supervisor whilst he was employed at BSC Sheffield Labs.) and to Dr. G. F. Raggett of Sheffield City Polytechnic.

I am also grateful to all friends and colleagues at BSC Sheffield Laboratories and BSC Stainless, Shepcote Lane, Sheffield, who have been involved with this work, and to Dr. J. F. Barrett of Strathclyde University for his useful ideas and comments.

Many thanks also to Mrs. J. Harper for typing the manuscript.

Finally, my thanks to my superiors in BSC Stainless and the BSC Research Organisation for permission to use this work as the subject of this submission.

## Papers Published

- Dutton K., "Shapemeters and Shape Control Systems: Survey of Literature", BSC internal Research Report SH/IC/8216/-/78/A, 1978, (Drafted 1976).
- Dutton K., "Description of the Operation of Sendzimir Mill Eccentric Actuators", BSC internal Technical Note MC/CA/8216/-/79, 1979.
- Dutton K., "The Development of a Mathematical Model Describing the operation of Sendzimir Mill Eccentric Actuators", BSC internal Technical Note MC/CA/8216/1/79, 1979.
- Dutton K., "Mathematical Definition of Sendzimir Mill Cluster Geometry and Roll Force Distribution", BSC internal Technical Note MC/CA/8216/2/79, 1979.
- Dutton K., "A Mathematical Model for Prediction of Sendzimir Mill Workroll Profile and Strip Shape", BSC internal Technical Note MC/CA/8216/3/81, 1981.
- Dutton K., Barrett J.F. and Grimble M.J., "The Shape Control Problem for a Sendzimir Cold Steel Rolling Mill", Proc. Symposium on Application of Multivariable Systems Theory, Plymouth, 1982.
- Harrison R.S.T., Walton A.B. and Dutton K., "Data Logger of Strip Shape for Number 5 Sendzimir Mill, Shepcote Lane," BSC internal Technical Note TS/MC3/8216/5/82/A, 1982.
- Dutton K., "Overview of the Development of an Automatic Shape Control System for a Sendzimir Cold Steel Rolling Mill", Submitted for presentation at the IEE Colloquium "Industrial Applications of State Estimation and Multivariable Control", London, 18th January 1984.

An Investigation into the Design and Performance of  
an Automatic Shape Control System for a Sendzimir  
Cold Rolling Mill

Ken Dutton

SYNOPSIS

Shape (or flatness) control for rolled steel strip is becoming increasingly important as customer requirements become more stringent. Automatic shape control is now more or less mandatory on all new four-high cold mills, but no comprehensive scheme yet exists on a Sendzimir mill. This is due to the complexity of the control system design on such a mill, where many more degrees of freedom for control exist than is the case with the four-high mills.

The objective of the current work is to develop, from first principles, such a system; including automatic control of the As-U-Roll and first intermediate roll actuators in response to the measured strip shape. This thesis concerns itself primarily with the As-U-Roll control system.

The material presented is extremely wide-ranging. Areas covered include the development of original static and dynamic mathematical models of the mill systems, and testing of the plant by data-logging to tune these models. A basic control system philosophy proposed by other workers is modified and developed to suit the practical system requirements and the data provided by the models. The control strategy is tested by comprehensive multivariable simulation studies. Finally, details are given of the practical problems faced when installing the system on the plant. These include problems of manual control inter-action bumpless transfer and integral desaturation.

At the time of presentation of the thesis, system commissioning is still in progress and production results are therefore not yet available. Nevertheless, the simulation studies predict a successful outcome, although performance is expected to be limited until the first intermediate roll actuators are eventually included in the scheme also.

## CONTENTS

	<u>Page No.</u>
<u>CHAPTER 1. INTRODUCTION</u>	
1.1 Background to the Shape Control Problem	1
1.2 Means of Shape Control in Four-High Stands	9
1.3 Description of the Present Project and Thesis	11
 <u>CHAPTER 2. PHYSICAL DESCRIPTION OF THE SENDZIMIR MILL INSTALLATION</u>	
2.1 Introduction	13
2.2 Mechanical Description of the Sendzimir Stand	14
2.3 Mechanical Description of the Mill's Control Actuators	18
2.3.1 Push-Up System Operation	20
2.3.2 Side Eccentrics Operation	22
2.3.3 Screwdown System Operation for Gauge Control	23
2.3.4 As-U-Roll Operation for Shape Control	24
2.3.5 First Intermediate Rolls for Shape Control	30
2.4 The ASEA Shapemeter System	33
2.4.1 Description of the Stressometer Roll	33
2.4.2 Description of the Signal Processing	34
 <u>CHAPTER 3. STATIC MATHEMATICAL MODEL OF THE MILL</u>	
3.1 Introduction and List of Principal Symbols	38
3.2 Modelling of the Control Actuators	46
3.3 Modelling of Roll Force Distribution in the Cluster	69
3.4 Rolling Load and Roll Flattening Calculations	77
3.5 Philosophy of Roll Stack Deflection Model	85
3.6 Calculation of Loading Pattern on the Upper Central Second Intermediate Roll	88
3.7 Upper Central Second Intermediate Roll Deflection Calculation	101
3.8 Treatment of First Intermediate Rolls	115
3.8.1 Calculation of Loading Acting upon IIRs	115
3.8.2 Calculation of IIR deflection	119
3.9 Treatment of the Upper Workroll	122
3.9.1 Calculation of Loading on Upper WR	122
3.9.2 Evaluation of Workroll Deflection Profile	124
3.9.2.1 Deflection due to a Force on the LH end of the Roll	127

3.9.2.2	Deflection due to a Force on the RH end of the Roll	138
3.9.2.3	Deflection due to a Force over the Strip	139
<hr/>		
3.10	Calculation of Strip Shape	145
3.11	The Computer Model and the Mill Gain Matrix	155
3.12	Discussion of Results	160
<u>CHAPTER 4. DYNAMIC MATHEMATICAL DESCRIPTION OF THE PLANT</u>		
4.1	Introduction	174
4.2	The As-U-Roll Actuators	174
4.3	First Intermediate Roll Lateral Adjustment Actuators	180
4.4	Transfer of Strip Between Mill and Shapemeter	182
4.5	The Shapemeter System	184
<u>CHAPTER 5. PLANT TESTING FOR MODEL VALIDATION</u>		
5.1	Introduction	186
5.2	Test Instrumentation and Set-Up	187
5.3	Static Model Validation	190
5.4	Dynamic Model Validation	196
5.4.1	The As-U-Roll Actuators	196
5.4.2	First Intermediate Roll Actuators	197
5.4.3	Transfer of Shape Between Mill and Shapemeter (Including Shapemeter)	199
5.4.4	Closed-loop controlled As-U-Rolls	203
<u>CHAPTER 6 CONTROL SYSTEM DESIGN</u>		
6.1	Introduction	207
6.2	Parameterization of Shape Measurements	207
6.3	Target Shape for the Control System	216
6.4	Control System Philosophy	222
6.5	Control System Design	224
<u>CHAPTER 7 DYNAMIC SIMULATION STUDIES</u>		
7.1	Introduction	236
7.2	Description of the Simulation	237
7.3	Calculation of Initial States	241
7.4	Post-Initialization Operation of the Simulation	244
7.5	Simulation Results	246
7.6	Hybrid Simulation of As-U-Roll Control	261

	<u>Page No.</u>
<u>CHAPTER 8 SYSTEM IMPLEMENTATION ON THE MILL</u>	
8.1 Introduction	266
8.2 Limiting of Relative Actuator Travel	266
8.3 Integral Desaturation in the Controller & Bumpless Transfer	271
8.4 Computer Hardware	276
8.5 Plant Interfaces	277
8.6 Shapemeter Edge Rotor Compensation	282
8.7 System Interaction with First Intermediate Roll Control	288
 <u>CHAPTER 9 CONCLUDING REMARKS</u>	 292
 <u>REFERENCES</u>	 301
 <u>APPENDICES</u> (see following two pages)	

<u>APPENDICES</u>		Page
<u>APPENDIX 1 HETENYI'S THEORY OF BEAMS ON ELASTIC FOUNDATIONS</u>		<u>No.</u>
A1.1	Differential Equation of the elastic line	A1.1
A1.2	Beams of Infinite Length	A1.4
A1.3	Beams of Finite Length	A1.14
A1.4	Summary of Procedure	A1.20
 <u>APPENDIX 2 CALCULATION OF FOUNDATION MODULUS</u>		 A2.1
 <u>APPENDIX 3 BENDING THEORY FOR A CANTILEVER HAVING AN ELASTICALLY SUPPORTED ROOT</u>		 A3.1
 <u>APPENDIX 4 EFFECTS OF NON-RIGHT-CYLINDRICAL ROLLS ON BEAM THEORY</u>		 A4.1
A4.1	Roll Camber Definition	A4.1
A4.2	Incorporation in the Theory	A4.3
A4.3	Tapered First Intermediate Rolls	A4.5
 <u>APPENDIX 5 EXAMPLES OF MATRICES GENERATED</u>		 A5.1
A5.1	Transpose of Parameterization Matrix (i.e. $\tilde{X}_0^T$ ) for the theoretical case of 8 covered Rotors	A5.1
A5.2	$(\tilde{X}_0 \tilde{X}_0^T)^{-1}$ corresponding to A5.1	A5.1
A5.3	$\tilde{X}_0^T$ Matrix for 21 covered Rotors.	A5.2
A5.4	$(\tilde{X}_0 \tilde{X}_0^T)^{-1}$ corresponding to A5.3	A5.2
A5.5	A "Theoretical" 8x8 $\tilde{G}_p$ Matrix	A5.3
A5.6	Transformed Plant Matrix for "Theoretical" 8x8 system	A5.3
A5.7	Precompensator for "Theoretical" 8x8 system	A5.3
A5.8	Calculated 8x8 $\tilde{G}_p$ Matrix	A5.4
A5.9	Comparable Matrix after Gunawardene (16)	A5.4
A5.10	31x8 $\tilde{G}_p$ Matrix for 1.61m Strip	A5.5
A5.11	25x8 $\tilde{G}_p$ Matrix for 1.3m Strip	A5.6
A5.12	19x8 $\tilde{G}_p$ Matrix for 0.99m Strip	A5.6

APPENDIX 6 DETAILS OF THE AUTHOR'S DYNAMIC  
SIMULATION PACKAGE

	A6.1
A6.1 Fundamental Method of Solution of Differential Equations	A6.1
A6.2 Simulation of an Integrator	A6.4
A6.3 Simulation of a First Order Lag	A6.6
A6.4 Simulation of a Second Order System	A6.7
A6.5 Simulation of a Lead-Lag (Phase Advance) Network	A6.8
A6.6 Simulation of a Transport Lag	A6.10
A6.7 Use of the Simulation Package Routines	A6.11

APPENDIX 7 OUTLINE SPECIFICATION OF SINGLE-BOARD  
MICROCOMPUTERS USED

A7.1

## CHAPTER 1

### INTRODUCTION

#### 1.1 Background to the Shape Control Problem

By the end of the 1960's and beginning of the 1970's, the problem of designing automatic gauge (i.e. thickness) control systems for cold metal rolling mills had largely been solved. (See for example Bryant (1)). The resultant improvements in consistency of strip gauge, coupled with an increasing demand for ever thinner products, inevitably led to an increase in customer rejections of rolled metal strip on the grounds of poor flatness - e.g. material having wavy edges or a buckled middle. The controlling of such defects falls within the field of shape control, and the desire for shape control systems grew rapidly within the metal rolling industry.

The term "shape" is, in truth an unfortunate misnomer, and can lead to some confusion during discussions. Let us define the meaning which will attach to the term "shape" throughout this work. Rolled strip is said to have "good shape" if it is free (or almost free) from internal stresses when removed from the mill. Such strip will lie flat if placed upon a flat surface. Bad shape rolled into a strip (whose shape was previously good) arises basically because of non-conformity between the cross-sectional profile of the incoming strip, and the profile of the roll gap through which it is rolled. Such non-conformity will cause the profile of the rolled strip to change, thus causing differential elongation at

different points across the strip width (neglecting width-wise spread). If this strip were to be slit into narrow lengthwise ribbons, some would then be found to be longer than others. Within the as-rolled strip, these length differentials must be accommodated within the boundaries set by the strip length. This clearly gives rise to internal stresses which will remain in the strip after rolling, and results in a tendency for the strip to buckle. If these stresses are large enough to overcome the section modulus of the strip, visible buckling will occur, and "Manifest bad shape" is the result. If however, the stresses are less than this level, the strip will still appear to be flat, and is said to possess "latent bad shape". (It should be noted that in the literature some workers have confusingly used the term "latent" bad shape to refer solely to shape which is masked by tension during rolling, and which then becomes "manifest" when the tension is removed). Figure 1.1 shows the "latent" and "manifest" effects which may result from a certain internal stress distribution. Manifest bad shape may take a number of forms dependent upon the nature of the internal stress distribution in the strip. Figure 1.2 illustrates some of the more common forms (2).

There have arisen over the years several methods of quantifying strip shape. A literature survey was carried out by the author in 1976 (published as an internal British Steel Corporation document only) which yielded some 73 papers and other documents pertaining to research

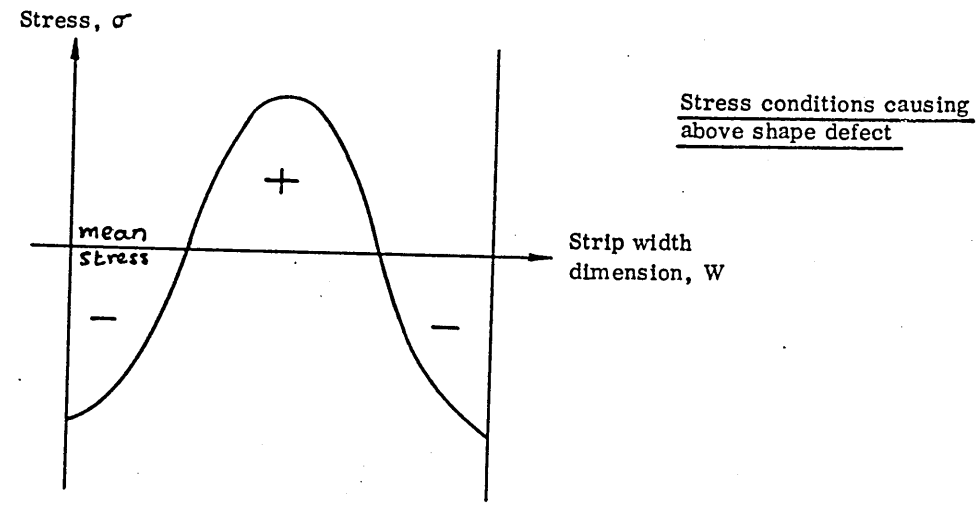
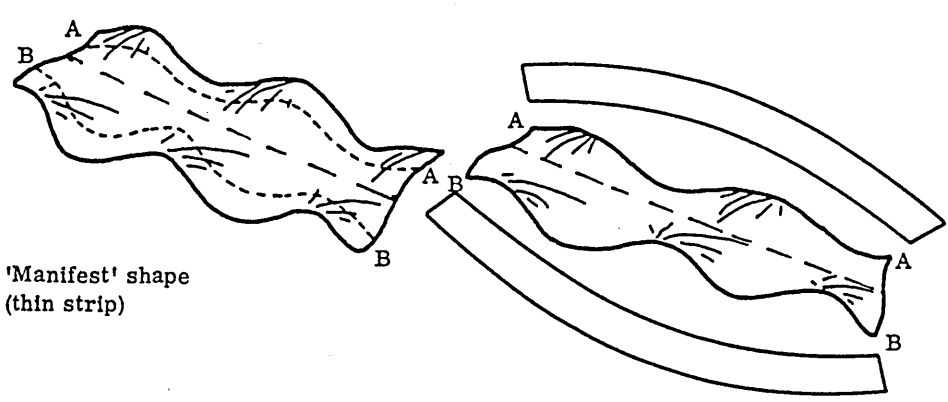
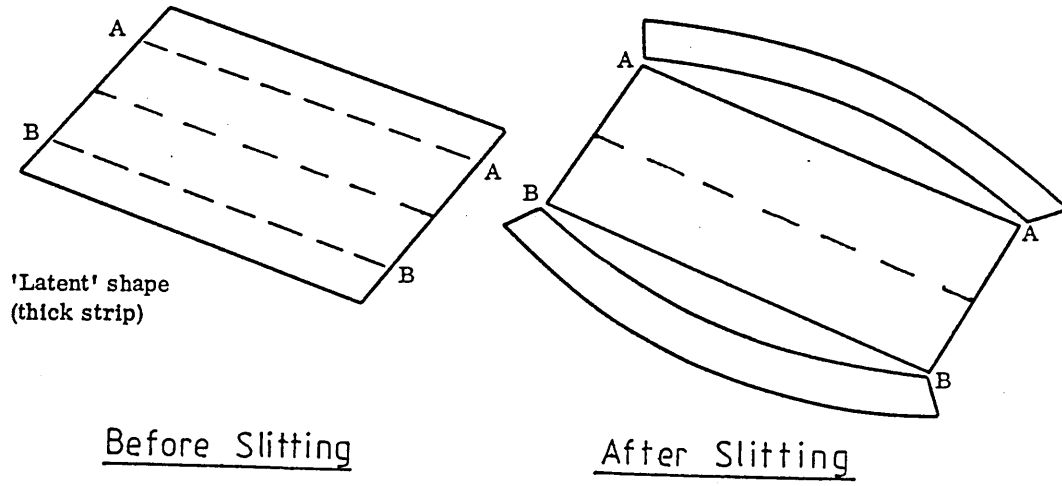


Fig.1.1 EXAMPLE OF BAD SHAPE

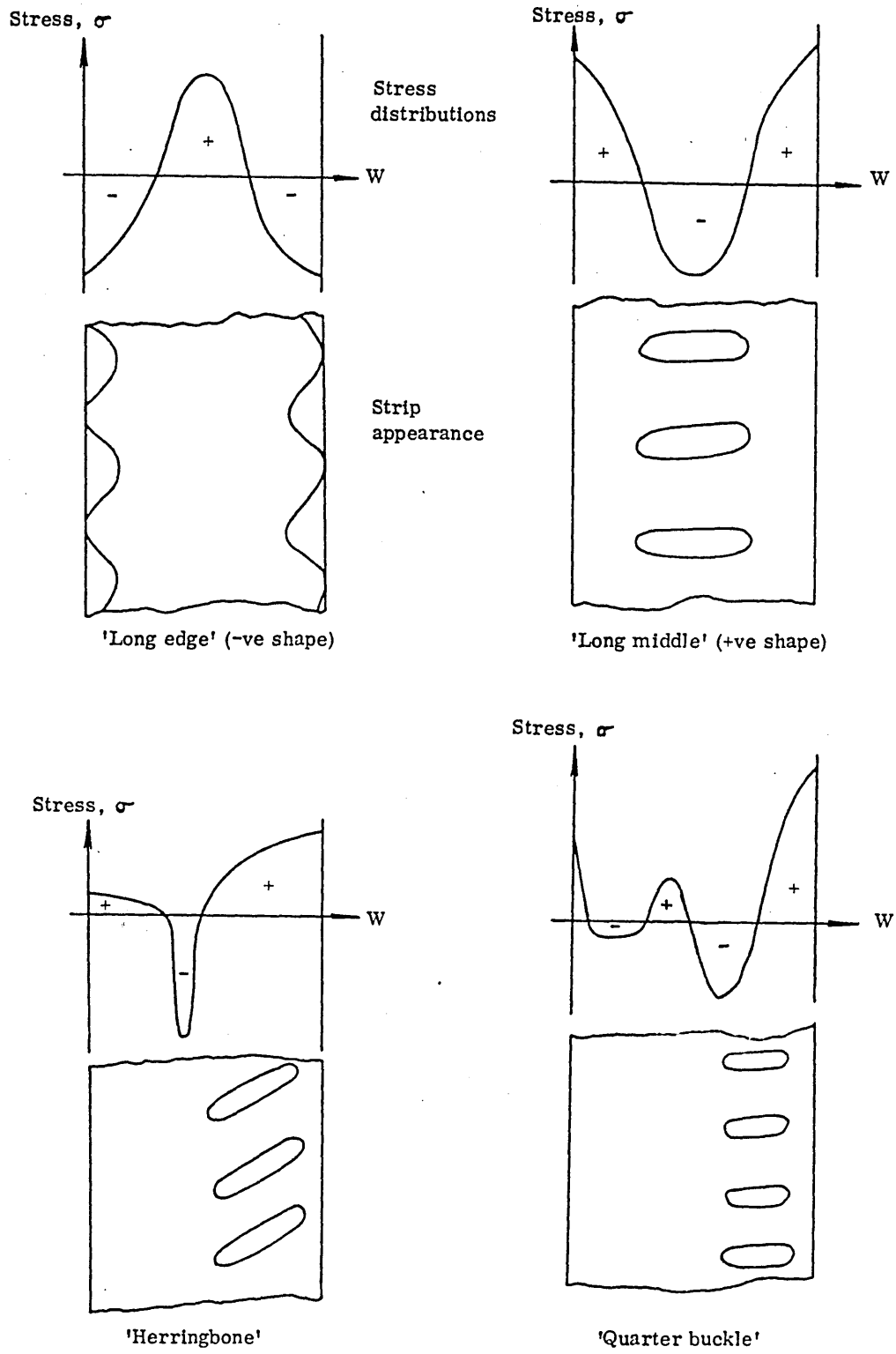


Fig1:2 TYPICAL FORMS OF BAD SHAPE

in this area, and no less than seven methods of assigning a numerical value to "shape" had been proposed at that time. Of these, only two are of direct relevance to the present work, the remainder being of academic interest only or used only by other workers (e.g. in Japan). As mentioned above, if strip having bad shape is slit into lengthwise ribbons, length differentials will result between the ribbons. Pearson (3) in 1964 defined shape as being given by  $\frac{\Delta l}{l.w} \cdot 10^4$  "mons per unit width". Where  $\Delta l$  represents the length difference between longitudinal filaments of mean length  $l$ , and  $w$  is the transverse spacing of the filaments. A second definition based upon the different filament lengths in slit strip defines shape in dimensionless "I-units", one I-unit being equal to  $\frac{\Delta l}{l} \cdot 10^5$  where  $\Delta l$  here refers to the difference between the longest and shortest filaments (4).

Some sensors of strip have been developed over the years which attempt directly to measure  $\frac{\Delta l}{l}$ , but these will measure only manifest shape which is not obscured by rolling tension, and are therefore of limited application (see for example (3)). Many different designs of instruments for shape measurement have been reported in the literature, some using rollers in various arrangements in contact with the strip (e.g. (5-8)), others based upon non contact methods of various types ((9-11) and several others besides). The two most well-established "shapemeters" in commercial use however are of the segmented-roll type, being the ASEA "stressometer" roll (4,5) and the Loewy-Robertson "Vidimon" roll (6) which was originally designed

by British Aluminium. These two devices both measure shape indirectly, by measuring the differential stresses at a number of points across the strip width (which could then be converted to the shape definitions above if desired, using knowledge of Young's Modulus for the strip.) The ASEA device is the one used in the present project, and is described in detail in Chapter 2.

These reliable devices for shape measurements have only become commercially available in the last ten years or so, yet they have already been applied to many rolling mills around the world. In the majority of cases, they are used simply to display to the mill operator what the shape of the strip he is rolling looks like, and he will then adjust the mill controls accordingly so as to achieve a better shape - i.e. the operator forms part of the "closed-loop" control scheme. (Note that on mills without shapemeters, the only ways in which the operator can assess strip shape are to stop the mill and release the rolling tension so that a visual assessment of manifest shape can be made, or to strike the strip - e.g. with a broom handle - and use his experience to assess the results - neither method having the attribute of ultimate accuracy). Some shapemeters however have been incorporated in closed-loop automatic shape control (ASC) schemes. The first well documented scheme was the application of an ASEA stressometer roll to a Canadian aluminium mill (4). The first application (known to the author) of an ASC scheme to a steel mill, involves the

use of the Loewy-Robertson Vidimon roll on a large tandem mill at British Steel Corporation's Shotton works (12). Several other ASC systems are known around the world, but they are all operating on conventional four-high mill stands (i.e. stands having two workrolls, supported by one backup roll each, in a vertical plane - Fig. 1.3). It is a much more difficult matter to apply an ASC system to a Sendzimir type mill (this will be clarified later), and although several Sendzimir mills are known to be equipped with shapemeters, at this time it is believed that only one other mill is actively considering an AFC scheme. It is hoped that the work described in this thesis will therefore lead to one of the first Sendzimir mill ASC systems ever to operate.

It should perhaps be mentioned at this point, that since the thesis includes work on an ongoing industrial development, some aspects of the work (especially the implementation of the scheme) will not be finished before the thesis submission date. Hence, it will not be possible to include, say, operating results in the discussion. Nevertheless, the various modelling aspects of the work have been made as self-contained as possible so that "completion" is possible in several areas.

F - Application of Rolling Load by Screwdown Systems  
A, B - See Text (Sect. 2.1)

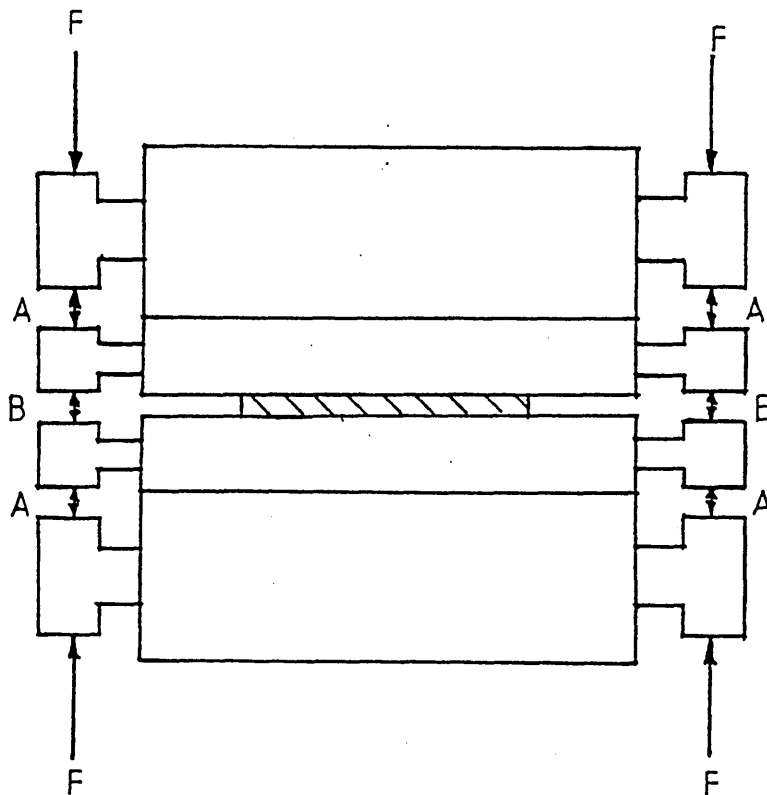


Fig. 1.3 Side View of Roll Stack (4-High Mill)

## 1.2 Means of Shape Control in Four-High Stands

If strip having good shape is rolled by a mill and found to have bad shape after rolling, the reason is that the cross sectional profile of the strip being rolled did not coincide with the profile of the roll gap (see section 1.1). There is a number of reasons why this may be so. Referring to figure 1.3, when a rolling load is applied, since the only support for the rolls is by means of their neck bearings, the rolls will bend giving a "crowned" profile to the strip (i.e. thickest in the centre). Since cold rolled steel strip is normally required to have a small parabolic crowned cross section, this is acceptable in principle. Nevertheless, the amount of crown caused in the roll gap by roll bending must accurately match the crown in the incoming strip, otherwise bad shape will result. Workrolls are usually ground with parabolic crowns, carefully calculated so that under normal rolling conditions the roll gap profile will match the cross section of the incoming strip. Further crown is imparted to the workrolls in the form of "thermal camber" during rolling. This arises because the heat generated during rolling can more readily escape from the ends of the rolls than the centre, and the centre therefore expands more than the edges. Now, if the mill rolls are correctly ground for steady state rolling (including the effects of thermal camber), it can be seen that the roll gap profile will be incorrect whenever the rolls are cold (e.g. at the beginning of a coil). Thus bad shape can

result when the rolls are not at their correct temperature, or if the crown ground onto the rolls is incorrect (which can occur due to roll wear even if it was originally correct), or if the profile of the incoming material is different from that for which the rolls are designed (which can often be the case, especially when material is bought from different suppliers), also the preceding stand in a tandem mill may have upset the shape if not scheduled correctly.

The foregoing description, in itself, suggests the normal methods of adjusting shape in rolling stands. Firstly, to control thermal effects, differential cooling is often employed, whereby cooling sprays arranged at many points across the rolls are selectively switched on or off as required. This means of control is particularly favoured by operators of aluminium rolling mills - see for example (4) - but is also used on steel mills. The major control on most mills where shape control is possible is to bend the workrolls during rolling. In the 4-high type of mill, this is usually achieved by hydraulic jacks situated between the roll chocks as indicated in figure 1.3. "A" represents jacks placed between the backup roll and workroll chocks, whilst "B" represents jacks placed between the workroll chocks. Either method can be used, each having its own advantages. Stone and Gray (13) have shown that in general, backup roll bending (i.e. with jacks operating between the backup roll necks, outboard of the chocks) is the best system, but it is very expensive to engineer and maintain and is not used much in the steel

industry except in heavy plate mills (to the best of the author's knowledge).

The reasons for using a Sendzimir type of mill rather than a four-high mill for certain purposes will be outlined in Chapter 2, but the foregoing description of mechanisms for control of shape in four-high mills has been included here for completeness.

### 1.3 Description of the Present Project and the Thesis

In the mid 1970's two large Sendzimir mills were built at British Steel Corporation's Shepcote Lane works. These mills are described in Chapter 2. Each mill is equipped with ASEA "Stressometer" shapemeter rolls which provide the mill operators with information about the shape of the strip being rolled (the shapemeters are also described in Chapter 2). It was decided at an early stage that these mills would eventually be furnished with closed loop automatic shape control schemes. Likely suppliers of such schemes were contacted, but for various reasons BSC decided to develop the scheme locally; and so the project was born.

A great deal of original work has been necessary to progress this project, as will be made clear in the following chapters. Any collaboration with other workers which has taken place will also be made clear at the appropriate points.

Prior to the control system design, a large amount of mathematical modelling and simulation had been carried out. Chapter 3 describes the development of models per-

taining to the static behaviour of the mill stand and its various control actuators. These models attempt to predict the effects upon strip shape of any combination of mill actuator movements. The resultant information is used in Chapter 4 where a model is developed pertaining to the dynamic behaviour of all parts of the plant relevant to shape control (i.e. the mill actuators, the characteristics of the strip between the mill and the shapemeter, the shapemeter itself and its electronic systems, and the shape controller). Chapter 5 describes plant testing which was carried out to check the accuracy of the various models. The development of the control system itself is covered in Chapter 6, whilst Chapter 7 introduces the dynamic simulation methods used to test the various systems developed. (These were all developed by the author, as no dynamic modelling package was otherwise available to him). Chapter 8 includes as much as can be said at the time of writing concerning the actual installation of the control system on the plant, and concluding remarks end the work in Chapter 9.

CHAPTER 2

PHYSICAL DESCRIPTION OF THE  
SENDZIMIR MILL INSTALLATION

PHYSICAL DESCRIPTION OF THE  
SENDZIMIR MILL INSTALLATION

2.1. Introduction

The major limitations of the 4-high mill stand from the point of view of shape control are twofold. Firstly, any change made to the screwdown mechanism on the stand for purposes of gauge control, will change the degree of roll-bending evident in the workrolls. This will cause a shape change in the strip leaving the mill, which may be significant for certain gauges and materials. Secondly, since roll bending is only applied at the roll necks, only a limited amount of roughly parabolic bending is possible. This severely limits the amount of shape correction possible, and the forms of shape which can be corrected (e.g. on a 4-high mill no correction could be made to the "herringbone" or "quarter buckle" shapes shown in fig. 1.2 by means of roll bending; and if differential cooling is available, even this is of limited use due to the magnitude of corrective action possible and sometimes to the relatively long time constant involved). A further limitation of the 4-high mill becomes apparent if it is desired to take high reductions on hard materials (e.g. stainless steel). Under these circumstances, rolling theory suggests the use of small diameter workrolls, and if used in a 4-high stand these would be prone to an unacceptable degree of bending under the high rolling loads required.

The Sendzimir rolling stand is designed to overcome to a large extent these limitations. It is, however, an

extremely complex mechanical system, and the primary purpose of this chapter is to describe the mechanics of the system so that the later chapters on modelling can be readily reconciled with the plant. The following section describes the general layout of the mill stand, and this is followed by a section devoted entirely to a description of the control actuators, which are not at all easily described in writing! The final section describes the operation of the ASEA "Stressometer" shapemeter system.

## 2.2 Mechanical Description of the Sendzimir Stand

The Sendzimir mill permits the use of small diameter workrolls by providing massive support, in an extremely rigid housing. Various configurations are available, but the mills at BSC, Shepcote Lane, are of the twenty roll type. Figure 2.1 shows an end view of the roll stack (or cluster) of such a mill, using standard notation for the various rolls. Each of the backup roll assemblies (A-H, fig. 2.1) is segmented into seven separate short rolls, with support to the housing being provided by a saddle (which is bolted to the housing) between each pair of segments as indicated in figure 2.2. Each segment is known as a "backing bearing", and is free to rotate on the shaft which passes through the saddles. The complete mill housing is of monoblock construction (i.e. machined from a single piece of steel) and is extremely stiff. The other rolls in the cluster (I-T, fig. 2.1) have no neck bearings, but are free to float (the upper half of the cluster is prevented from collapsing during threading of the mill, by means of tie rods which allow rolls I-K, O and P to move downwards by only a limited amount when

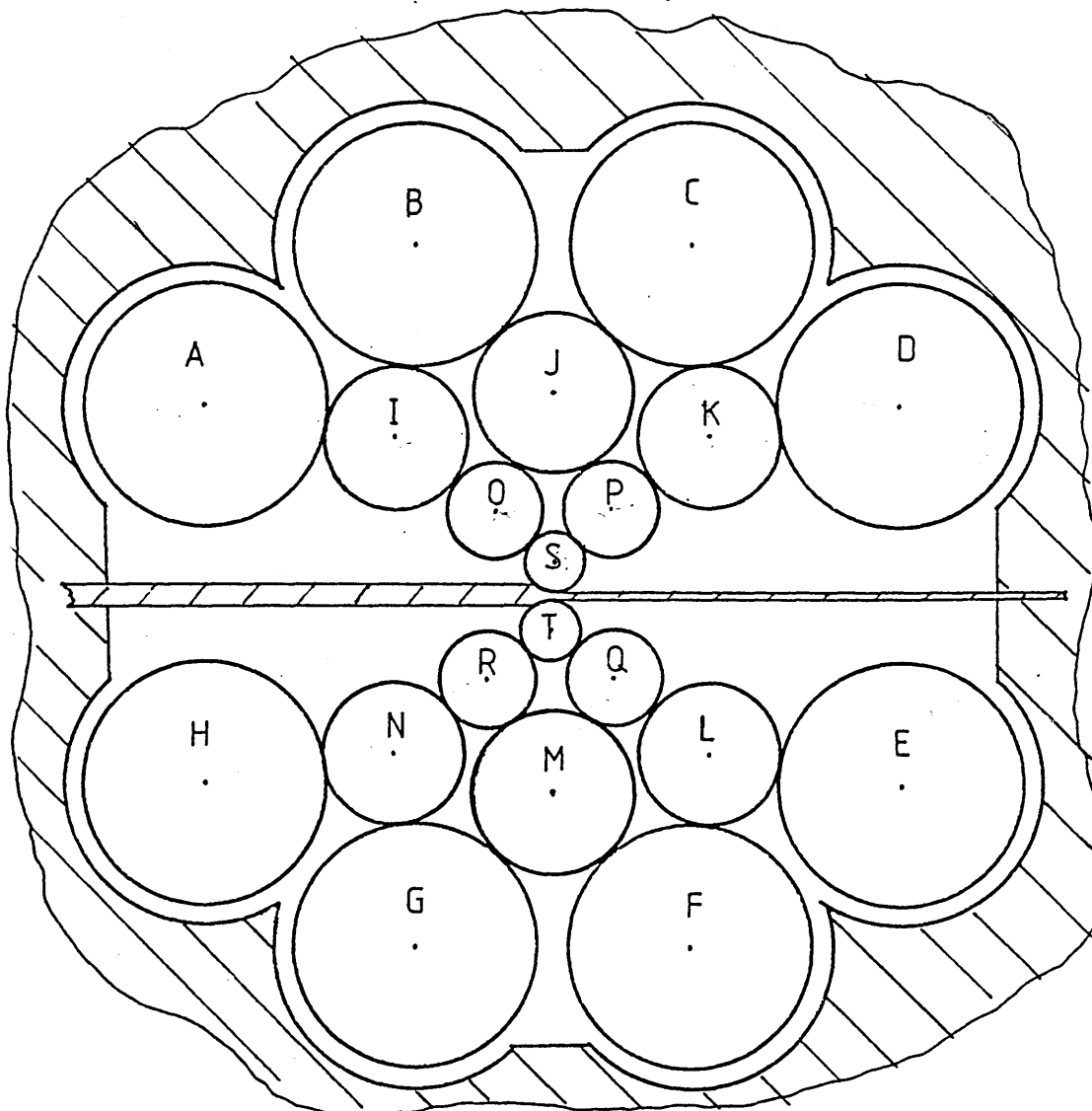


Fig. 2.1 Roll Stack Arrangement (20-Roll Sendzimir Mill)

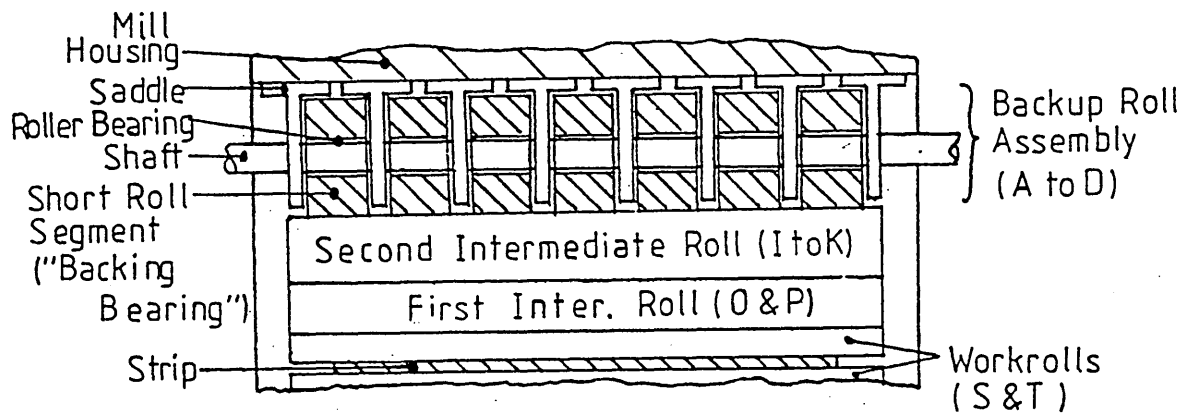


Fig. 2.2 Schematic Section of one Upper Backup Roll Assembly

the upper workroll is removed). The mill drive (from a single motor) is applied to the outer second intermediate rolls (I,K,L and N) and transmits to the workrolls by inter-roll friction. This means of construction provides great support to the thin workrolls, and unwanted roll bending is minimized. The mill type under consideration is designated ZR21B-63, wherein "Z" stands for the Polish "Zimna" meaning "cold", "R" stands for "reversing", "21" is an indication of the mill housing bore sizes, "B" indicates a modification to the mill housing dimensions to allow slightly larger workrolls than standard to be used if required and "63" is the mill width in inches (1600mm). The layout of the plant is indicated in figure 2.3.

To give an idea of scale a typical set of nominal roll diameter may be as follows:

Backing Bearings	(A-H)	0.406 m
Second Intermediate (Drive) Rolls (I,K,L,N)		0.235 m
Second Intermediate (Idler) Rolls	(J,M)	0.230 m
First Intermediate Rolls	(O-R)	0.135 m
Workrolls	(S-T)	0.075 m

The distance from the roll gap to each shapemeter is approximately 2.91m, from the shapemeter to the deflector roll 0.56m and from the deflector roll to the coiler 1.85m. The mill housing weighs some 200T.

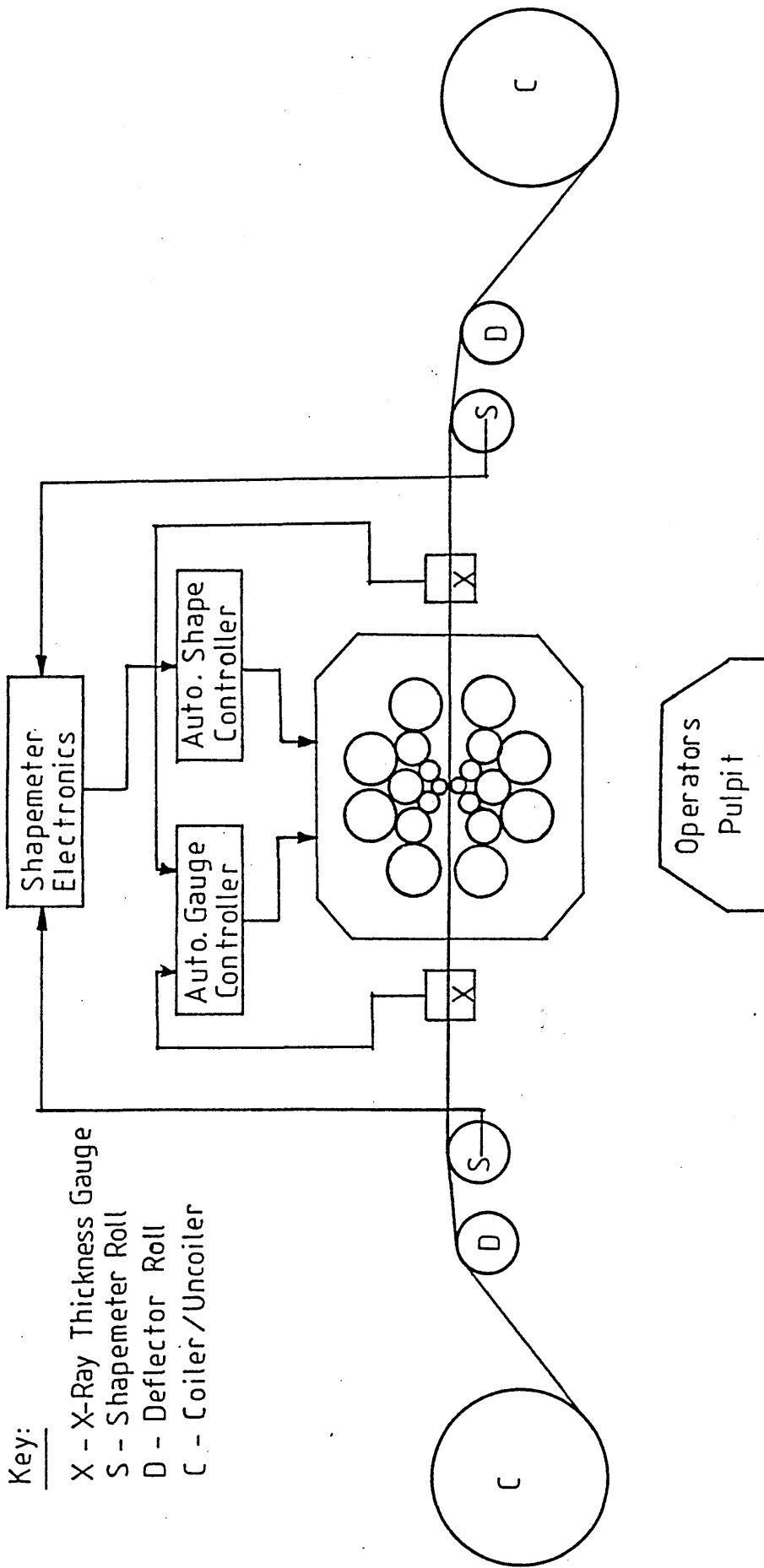
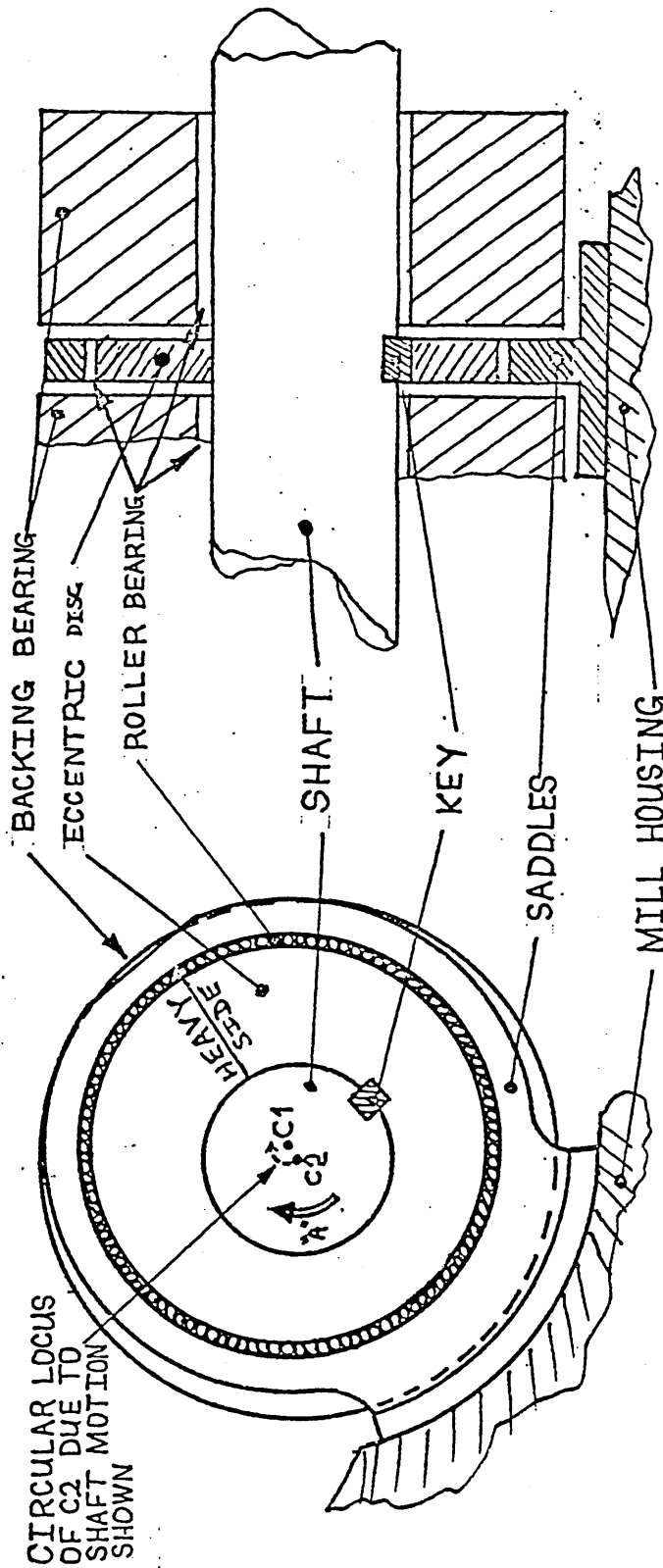


Fig.2.3 Pictorial Representation of the Plant Layout

### 2.3 Mechanical Description of the Mill's Control Actuators

The mill is equipped with various actuators which allow the cluster to be opened up for roll changing and strip threading, the pass line height to be adjusted (i.e. the path taken by the strip during rolling) and also perform functions of gauge and shape control. During the author's reading of the literature, no description of the operation of these actuators (other than the most rudimentary details, which would only be of use to those already in possession of the appropriate facts) could be found. Even Sendzimir's brochures appeared rather vague in this area. Therefore, many hours were spent in studying BSC's sets of plant drawings, and also studying the plant itself, in order to gain sufficient insight into the working of these systems to allow them to be modelled. The information thus gleaned is described in this section, and the author has also passed it on in discussions with other workers, in this field, to help their work to proceed (14-18).

Referring back to fig. 2.2, it will be recalled that each of the outer rolls (A to H) in the Sendzimir mill cluster is segmented into seven backing bearings, mounted on roller bearings, and running on a shaft supported by eight saddles which are bolted to the mill housing. Wherever the shaft passes through a saddle, it is keyed into an eccentric disc which can rotate in the saddle bore on roller bearings (see figure 2.4). Therefore, if the shaft is rotated through some angle (as indicated at



Key:  
 c1 - Centre of Housing Bore, Saddle Bore & Ecc. Disc o.d.  
 c2 - Centre of Ecc. Disc i.d., Shaft & Backing Bearings

Fig.2.4 Saddle Details

"A" in fig. 2.4), since it is keyed to the eccentric disc, both shaft and disc will rotate in the saddle bore together. This causes the centre of the shaft (C2 in fig.2.4 - which is also of course the centre of the backing bearings at each side of the saddle) to move around the fixed centre of the saddle bore (C1 in fig.2.4 - which is also the centre of the mill housing bore). Due to the geometry of eccentric motion, the locus of C2 is a circle about C1, whose radius is equal to the eccentricity in the disc - this will not be proved here. Thus, rotation of the shaft causes the backing bearings at either side of the saddle to move relative to the mill housing. Since the shaft is keyed to an identical eccentric disc in each of the eight saddles, rotation of the shaft causes an identical motion at each saddle, and therefore the entire set of backing bearings on the shaft moves relative to the mill housing and parallel with its original position.

### 2.3.1 Push-up System Operation

The lower backup roll assemblies (F and G in fig.2.1) each have the construction described above. If figure 2.4 is taken to represent a saddle on shaft G, then the corresponding saddle on shaft F is constructed as a mirror image of fig.2.4. The necessary rotational movement is simultaneously imparted to shafts F and G by means of a rack and pinion arrangement as shown in fig. 2.5. There is such an arrangement at each end of the shafts, the racks being constrained to move simultaneously. The mill operator sets the position of the racks by operating an

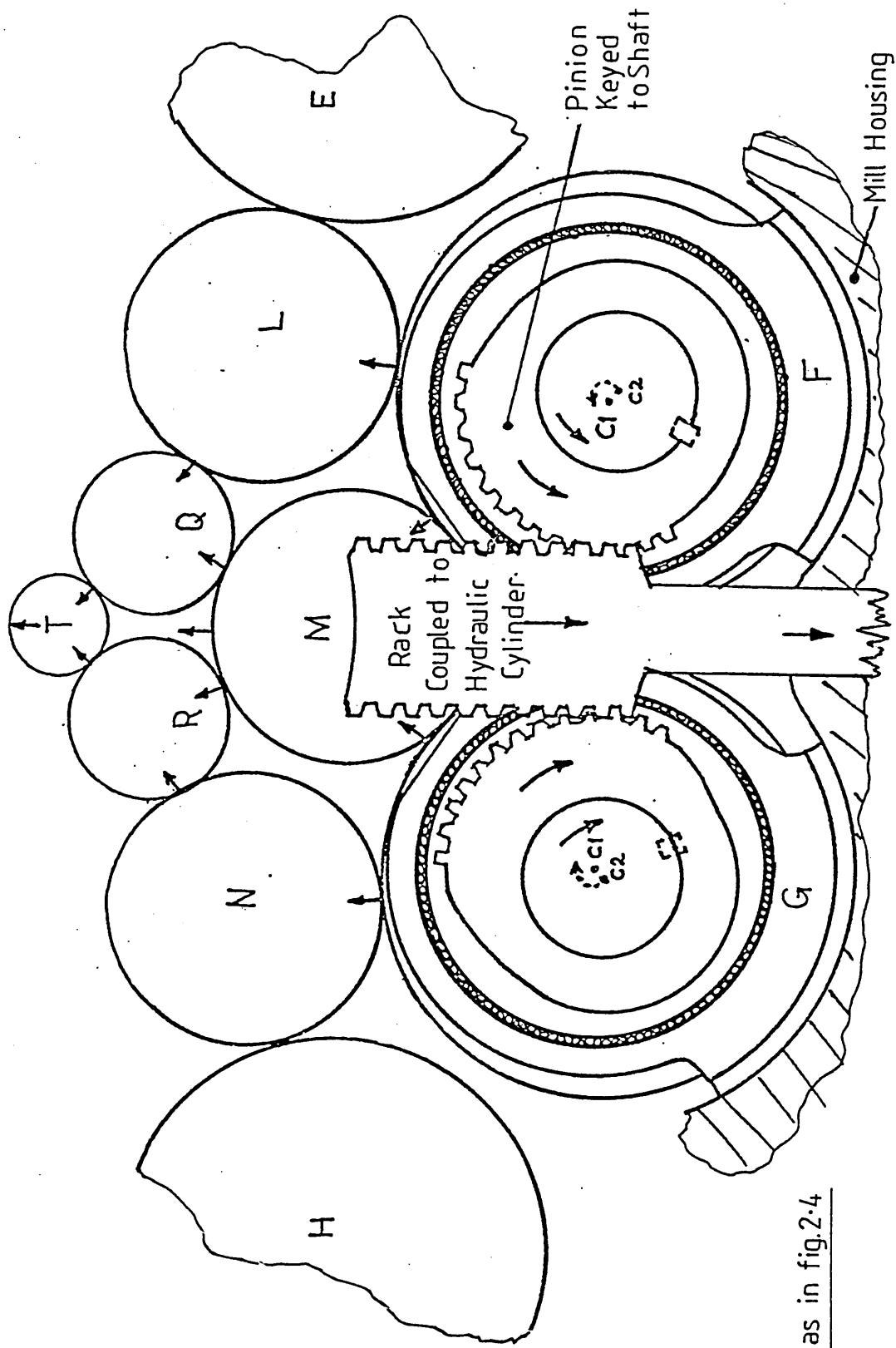


Fig.2.5 Operation of Push-up System

c1,c2 - as in fig.2.4

electrical solenoid valve which controls the hydraulic push-up cylinder connected to the racks. The way in which this affects the magnitude of the roll gap is indicated by the arrows in fig.2.5.

The major function of the push-up system is to allow the mill cluster to be opened up for strip threading and roll changing. Under normal rolling conditions the racks are usually in the fully closed (down) position, and are not used for any control action.

### 2.3.2 Side Eccentrics Operation

The pairs of backup roll assemblies (A,H) and (D,E) at each side of the mill are equipped with similar mechanisms to the push-up system described in the previous sub-ection. The main difference is that the operation is via electric drives and pinions situated only at the back of the mill. The shafts of assemblies A and H are simultaneously contra-rotated as described above, and so are the shafts of assemblies D and E. Note, however, that the two systems (A,H) and (D,E) are adjusted independently.

The function of these eccentrics is to allow the mill pass line to be correctly set (as otherwise the pass line would vary according to the combination of roll diameters - especially workrolls - in use at the time). The side eccentrics are usually set at the beginning of a pass, and then left undisturbed.

### 2.3.3 Screwdown System Operation for Gauge Control

The term "screwdown" is somewhat misleading for a mill equipped with hydraulic cylinders, but it is still employed by convention. It arises from the fact that until recent years, all four-high rolling stands employed electrically or mechanically driven screws to position the rolls and vary the rolling load. Many modern mills (including almost all Sendzimir mills) employ hydraulic "screws" which are in reality "rams".

The two upper backup roll assemblies (B and C in fig. 2.1) are equipped with an identical arrangement to that described for the push-up system in sub-section 2.3.1 above (and fig.2.5 - inverted, and with the roll designations for the upper half of the cluster!). The difference is that whereas the push-up system is used only for roll changing and mill threading, the screwdown system is used for control during rolling. It is used to control strip thickness (gauge) either manually by the operator or automatically as part of the automatic gauge control system shown in figure 2.3. In the latter case, the automatic system uses hydraulic servo valves to position the screwdown cylinders, in response to signals of strip gauge received from the X-ray gauges at each side of the mill.

It is important to note that as described previously, the operation of these eccentrics causes the backup roll assemblies to move parallel with their original positions. Due to the massive support provided by the monoblock mill

housing, this motion remains essentially parallel even when it reaches the workroll. Therefore, compared with the four-high mill (section 1.2), there is very little effect upon strip shape due to making gauge changes. This is a primary advantage of the Sendzimir mill stand.

#### 2.3.4 As-U-Roll Operation for Shape Control

For purposes of shape control, it is necessary deliberately to be able to bend the workrolls during rolling (section 1.2). The system employed in the Sendzimir mill is referred to by Sendzimirs' trade name "As-U-Roll" (since it allows roll bending "as-u-roll"), this also operates on the upper pair of backup roll assemblies, B and C.

Each of the saddles supporting either of the two shafts B and C is fitted with an extra eccentric ring, interposed between the saddle bore and the screwdown eccentric disc as shown in figure 2.6. The eccentricity of this ring is much less than that of the screwdown disc (typically less than 20 percent of screwdown eccentricity) since workroll motion required for shape correction is exceedingly small.

The As-U-Roll eccentric ring at each saddle can be rotated independently of the shaft and screwdown system (and of the As-U-Roll rings at the other saddles) by moving a forked rack which engages with cheek pieces fastened to each side of the ring as shown in figure 2.7 and 2.8. The forked rack straddles the pair of saddles

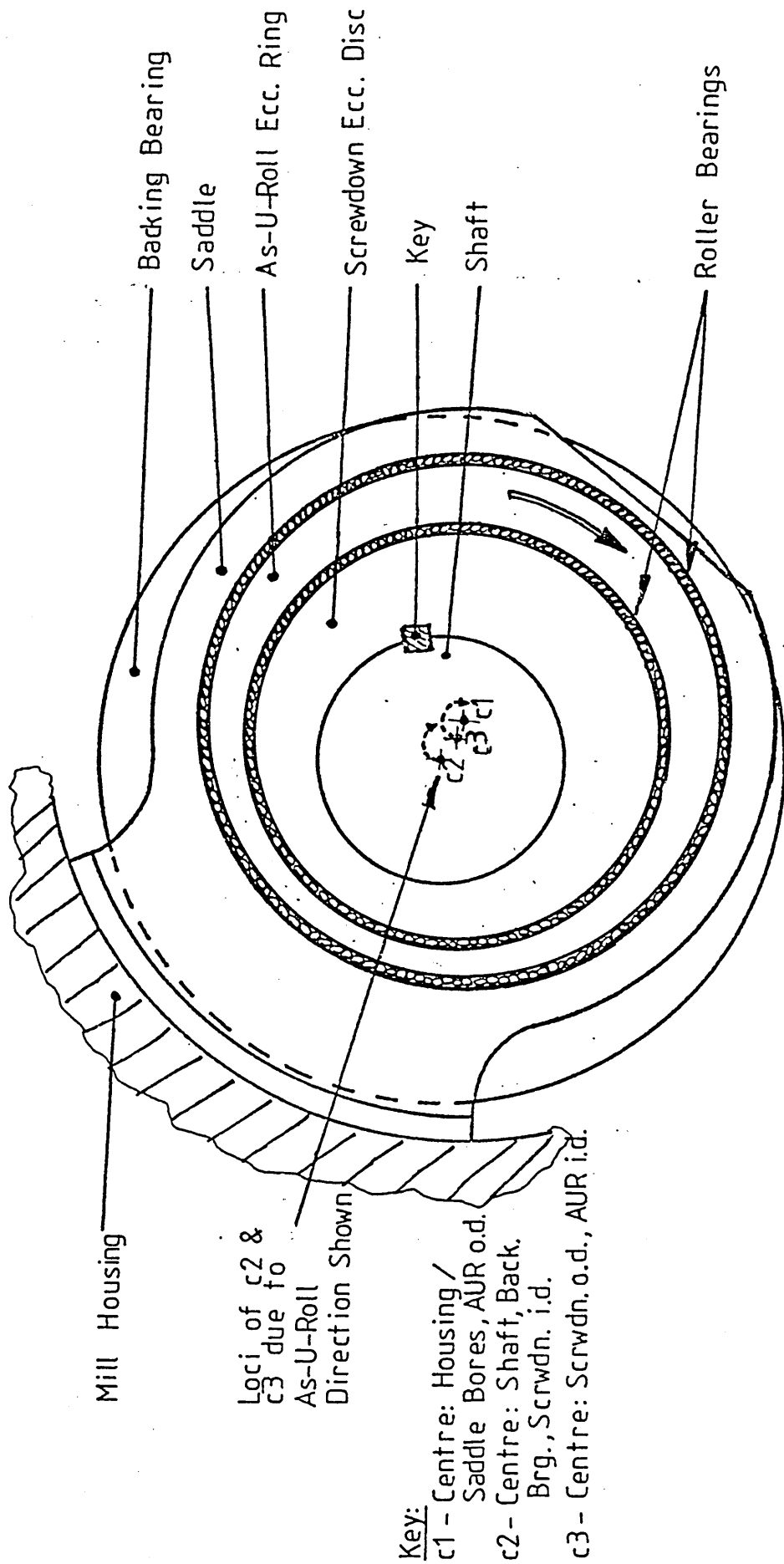


Fig. 2.6 Saddle Details - Shafts B & C Only

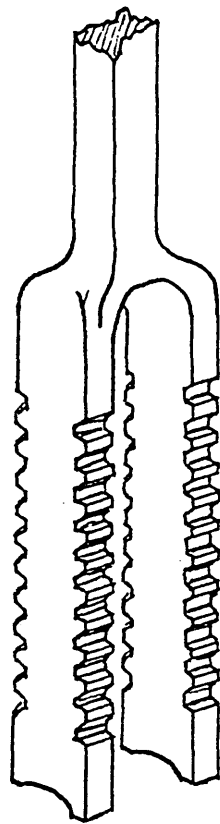
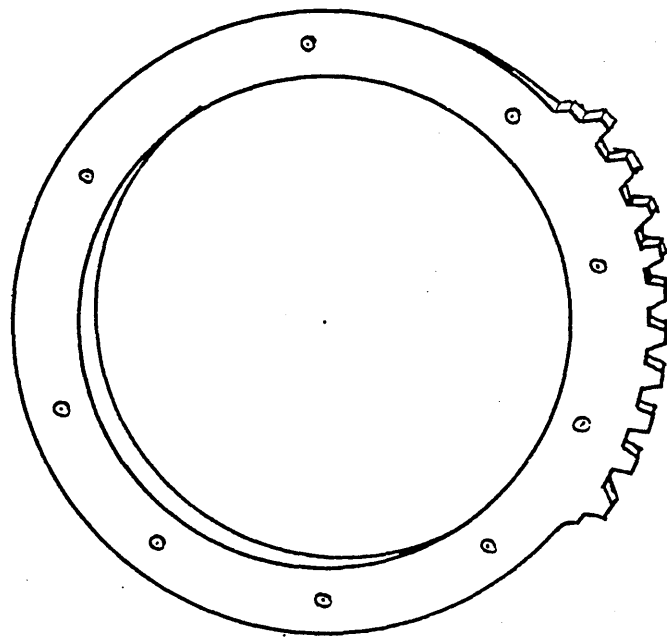


Fig.2-7 Form of As-U-Roll Cheek Piece and Rack

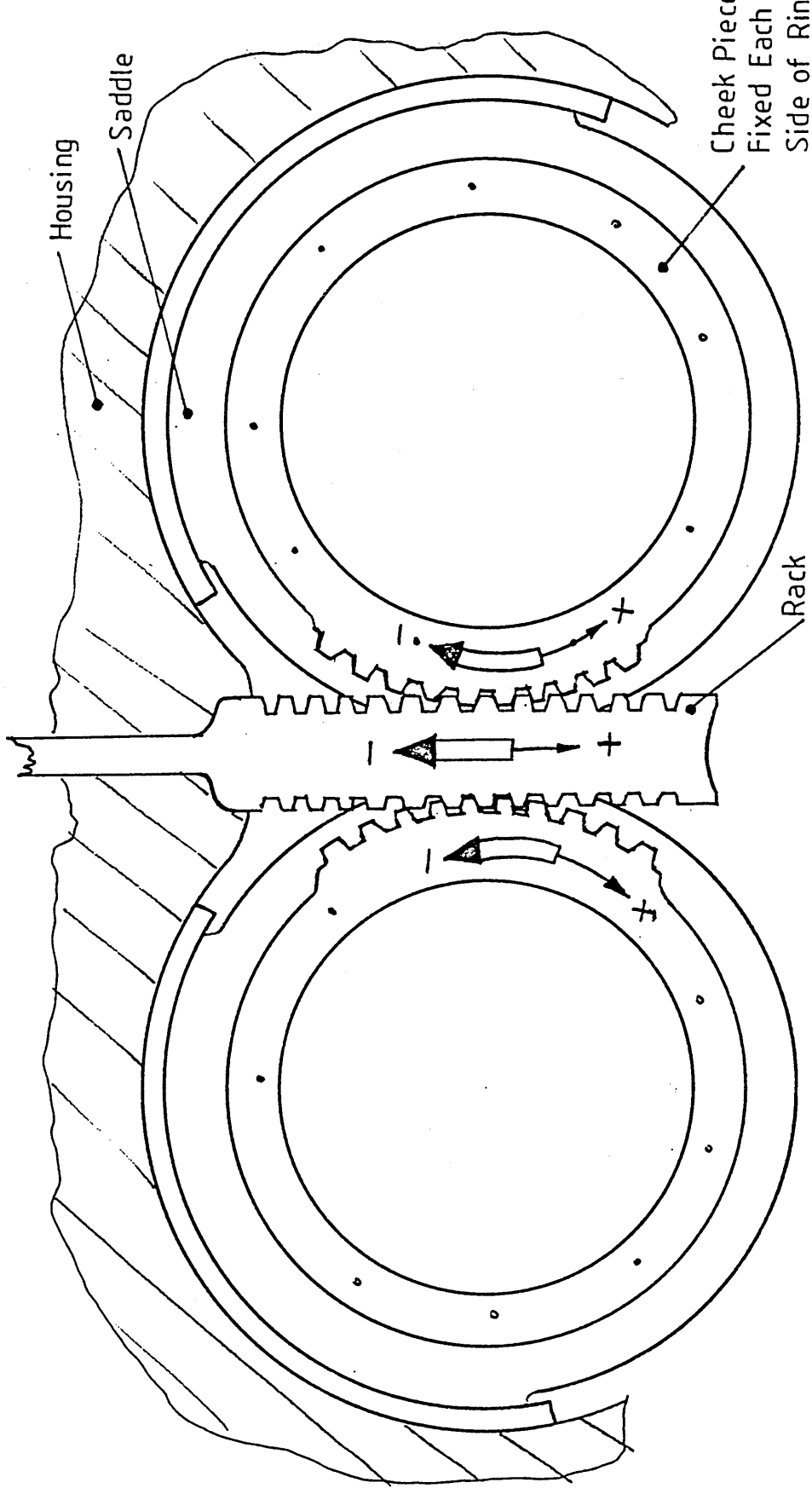


Fig. 2.8 As-U-Roll Rack and Ring Arrangement

concerned, so that its teeth mesh with the four appropriate check pieces (one on each side of the As-U-Roll rings at the corresponding saddles on shafts B and C). The mill operator can raise or lower each of the eight As-U-Roll racks independently, by operating electric solenoid valves. These supply a hydraulic motor for the selected As-U-Roll system, which raises or lowers the rack by a worm and rack arrangement.

As one As-U-Roll rack is raised or lowered, it rotates the As-U-Roll eccentric rings at the corresponding pair of saddles on shafts B and C via the check pieces (fig.2.8). Referring back to fig.2.6, this causes C3 to move around the fixed C1 on a circular path whose radius equals the eccentricity in the As-U-Roll ring. Since we are assuming that the screwdown system is not being operated at this time C2 will follow a "parallel" circular path to C3. Now C2 is the centre of the shaft and of the backing bearings on each side of the saddle under consideration. Therefore by moving one As-U-Roll rack only, the position of the backup roll assemblies B and C is changed, relative to the mill housing only adjacent to the saddle whose rack has been moved. Thus the roll is effectively bent, and this bending propagates down through the mill cluster onto the workroll. By manipulation of all eight racks, various bending profiles can be forced onto the workroll (see for example figure 2.9).

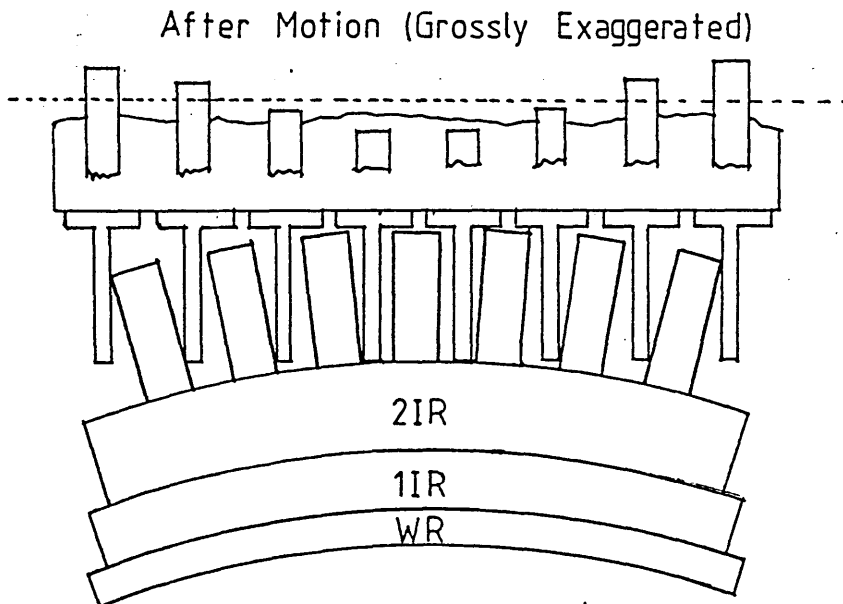
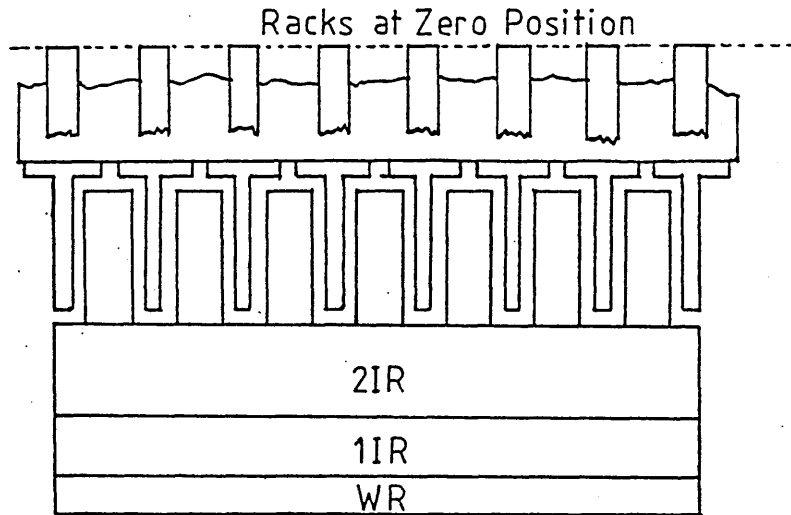


Fig.2.9 Effect of As-U-Roll Movement

It is worth reiterating that the design of the Sendzimir mill minimises interaction between gauge and shape control systems. When a shape change is made, only the As-U-Roll eccentric rings move, forcing a suitable profile onto the workrolls. The resultant change in gauges is extremely small, due to the small eccentricity in the As-U-Roll rings, and the fact that there are constraints upon the amount of As-U-Roll control possible (this will be discussed later). The automatic gauge control system is fast-acting compared with shape control, and if a shape change does cause a net gauge change visible to the AGC system, it will be corrected very quickly. On the other hand, when a gauge change is made, only the screwdown eccentric discs move (rotated by the shafts B and C) and as discussed in sub-section 2.3.3 above, the discs move an identical amount at each saddle. Thus the bending profile on the workroll is virtually unchanged, and an almost pure gauge change results.

#### 2.3.5 First Intermediate Rolls for Shape Control

Although the As-U-Roll system permits a much wider range of bending profiles to be forced onto the workrolls than is the case in a four-high mill, it is not as flexible as may at first appear. This is due to mechanical constraints upon the amount of bending which can be tolerated by the backup shafts B and C and the other rolls in the cluster under rotating conditions. The As-U-Roll actuators are set by the operator according to scales marked in ten arbitrary units. The manufacturers of the

mill and the mill engineers lay down a constraint that the position of any As-U-Roll actuator shall not deviate by more than  $1\frac{1}{2}$  of these units from the mean position of its two neighbours. Large gradients and sudden maxima and minima are therefore ruled out.

To allow much more freedom of control at the critical areas of the strip edges, a second means of shape control is provided. The first intermediate rolls O and P (in fig.2.1) are tapered off at the front of the mill, and Q and R at the rear as shown in figure 2.10. These tapers can be moved laterally into or out of the cluster as indicated in the figure. The upper and lower pairs of rolls are independently adjustable, thus allowing separate control of shape at the front and back edges of the strip. The motion is imparted to these rolls by means of internally threaded thimbles which run on external threads cut on non-rotating extensions coupled to the back ends of the first intermediate rolls. The thimbles are laterally constrained with respect to the mill housing, so that if the thimbles are rotated, the screw action of the threads will move the first intermediate rolls in or out. The drive to the thimbles is by chain from hydraulic motors controlled by switches on the mill operator's desk via solenoid valves. (Described in more detail in Chapter 4).

The control action obtainable by this method at the strip edges is very fine and very powerful. This is underlined by Urayama (19), although in Urayama's application it was actually desired to roll quarter buckle

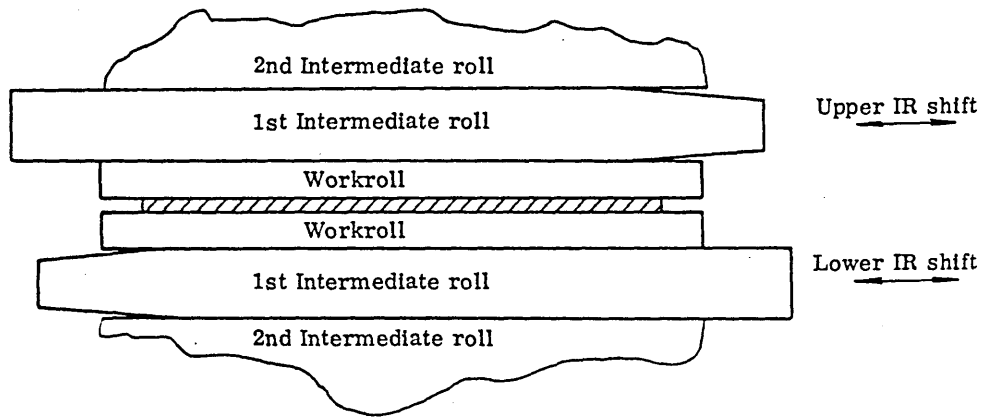


Fig.2.10 SENDZIMIR MILL FIRST INTERMEDIATE ROLL ADJUSTMENT

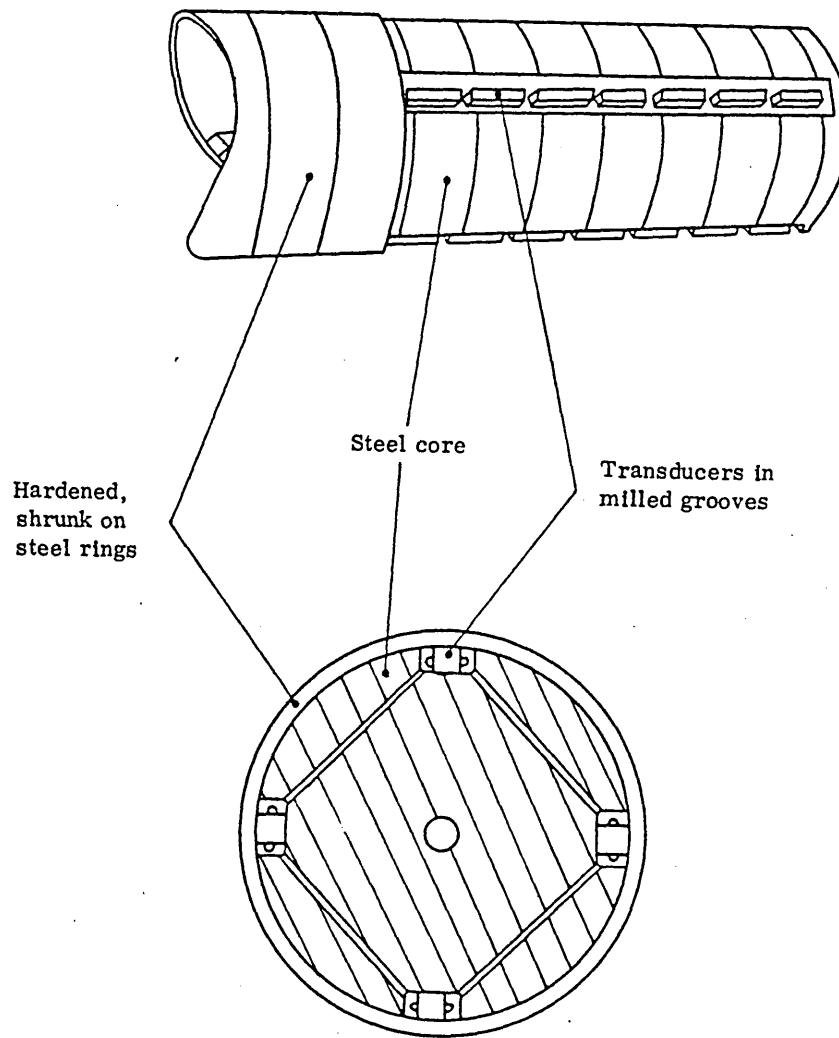


Fig.2.11 ASEA STRESSOMETER ROLL

into the strip, and it is known that the As-U-Roll system alone cannot produce two inflexions in the workroll, due to the mechanical constraints (20). Also, tapered intermediate rolls have recently been introduced for shape control in four-high mills by Hitachi (21), thus forming the six-high mill, which is making very rapid progress now in Japan.

The automatic shape control system for the Shepcote Lane mills will incorporate control of the As-U-Rolls and the first intermediate rolls, although initial effort has been directed at the As-U-Roll systems for various reasons which will become apparent.

#### 2.4 The ASEA Shapemeter System

To conclude this chapter, a brief description will now be given of the system which measures strip shape on the mills in question. The system comprises the transducer itself, which takes the form of a pass-line roll, and the electronics necessary to process the transducer signals and provide a shape display in the operator's pulpit.

##### 2.4.1 Description of the Stressometer Roll

One Stressometer measuring roll (4,5) is placed at each side of the mill, approximately 2.91m from the roll gap. Each roll takes the form of a solid core, having four axial grooves milled along it at equally spaced points about its circumference (figure 2.11). Each groove houses 31 modified "Pressductor" loadcells, which are installed to be slightly proud of the core surface and then machined to

the correct height. These transducers are then covered by 31 hardened steel rings which are shrink-fitted over the core so as to pre-stress the transducers. Each ring is 52mm wide, and is separated from its neighbours by small gaps of typically 20 to 40 microns. Each ring, with its group of four transducers therefore forms an independent measuring zone. The four transducers in each zone are connected together in such a way that the prestressing forces due to the shrunk-on steel ring, thermal effects, centrifugal force, bending of the roll due to strip tension and also stray magnetic effects are all effectively cancelled out. This leaves only the force on each zone due to the tension in the strip passing over it to be measured (because this affects only one transducer at a time, whereas the above mentioned are all common-mode effects).

The roll is mounted in roller bearings, and all the transducer signals are brought out by means of a multipole silver slipring and brush system at the rear of the mill.

#### 2.4.2 Description of the Signal Processing

The primary windings of the transducers in each zone are connected in series, and energized with a 2kHz signal. If the four transducers in a zone are labelled A,B,C and D sequentially around the roll, then the secondary windings (the transducers operate on the principle of magnetostriction) are connected in series as follows A(+), B(-), C(+), D(-). Therefore, when strip under tension is passing over the rotating roll, the output from

each zone will take the form of an amplitude modulated wave, having a carrier frequency of 2kHz, a modulating frequency dependent upon strip speed, amplitude which exhibits four pulses per revolution of the roll- alternatively less than and greater than the carrier amplitude, and of a magnitude dependent upon the load placed on the zone by the strip. This signal from each zone is fed to one channel of the signal processing electronics. Here, it is fed through phase-sensitive rectifiers and filters to obtain a direct voltage proportional to the radial force on the measuring zone.

In order to obtain good filtering characteristics, a variable time constant is used in the signal electronics. This is selected automatically as a function of strip speed (Table 2.1).

Strip Speed (m/s)	0-90% Response Time (s)
0.3 - 1	10.0
1 - 2	3.3
2 - 5	1.7
5 - 15	0.7
15 - 50	0.25

Table 2.1

Automatically Switched Filter Time  
Constants

Having obtained values  $F_x \Big|_{x=1,31}$  for the radial force exerted by the strip on each measuring zone (N), the processing proceeds as follows:

Let  $F_m$  = mean force (N)  
 $\sigma_x$  = stress in strip at zone x ( $Nm^{-2}$ )  
 $\sigma_m$  = mean stress ( $Nm^{-2}$ )  
 $\Delta\sigma_x \left\{ \begin{array}{l} = \text{deviation of stress at zone x from mean } (Nm^{-2}) \\ = \text{shape} \end{array} \right.$   
 $T$  = total strip tension (N)  
 $t$  = strip gauge (m)  
 $w$  = strip width (m)  
 $N$  = number of shapemeter rotors covered by the strip.

The parameters  $T$ ,  $t$  and  $w$  are available to the shapemeter electronics, therefore  $\sigma_m$  can be calculated as

$$\sigma_m = \frac{T}{w \cdot t} \quad (Nm^{-2})$$

also 
$$F_m = \frac{1}{N} \sum_{x=1}^N F_x \quad (N)$$

Now 
$$\frac{\sigma_m}{F_m} = \frac{\sigma_x}{F_x}$$

Therefore 
$$\sigma_x = F_x \cdot \frac{\sigma_m}{F_m} \Big|_{x=1,31} \quad (Nm^{-2})$$

The quantity  $\frac{\sigma_m}{F_m}$  is evaluated by the electronics, and so  $\sigma_x$  can be found for each zone. ( $Nm^{-2}$ )

Then finally

$$\Delta\sigma_x = \sigma_x - \sigma_m \Big|_{x=1,31} \quad (Nm^{-2})$$

The 31 values are then scaled in  $N \text{ mm}^{-2}$  and displayed to the mill operator by means of 31 edge-meters arranged side by side. The range of the display is  $\pm 200 N \text{ mm}^{-2}$  for each zone.

There is only one set of shapemeter electronics, and this is switched to whichever of the two Stressmeter rolls is at the output side of the mill.

## CHAPTER 3

### STATIC MATHEMATICAL MODEL OF THE MILL

#### 3.1 Introduction

This chapter considers the non-dynamic aspects of the mill stand itself, including the various actuator mechanisms described in section 2.3. The purpose of the model is to predict, from any possible combination of actuator movements, the magnitude of the effects upon the transverse internal stress distribution of the strip leaving the roll gap (fig.3.1). Clearly, for shape control considerations, the major emphasis is placed upon a perturbation analysis of the As-U-Roll and first intermediate roll taper effects upon the strip shape. However, it should be borne in mind that the settings of the screwdown and side eccentric systems affect the range of control of the shape control actuators by modifying the roll stack geometry. A unique feature of the present model is that it attempts rigorously to define these effects, by careful modelling of the complex mechanical mechanisms by which the distribution of rolling load throughout the cluster is affected when any of the mill's actuators is moved. In addition, every effort has been made to keep the model non-iterative, so that the long computation times associated with such models are avoided. Some details of the computer mechanisation of the model are given. The chapter concludes with the derivation of a gain matrix by which the mill can be represented in, for example, a state space derivation of a control scheme.

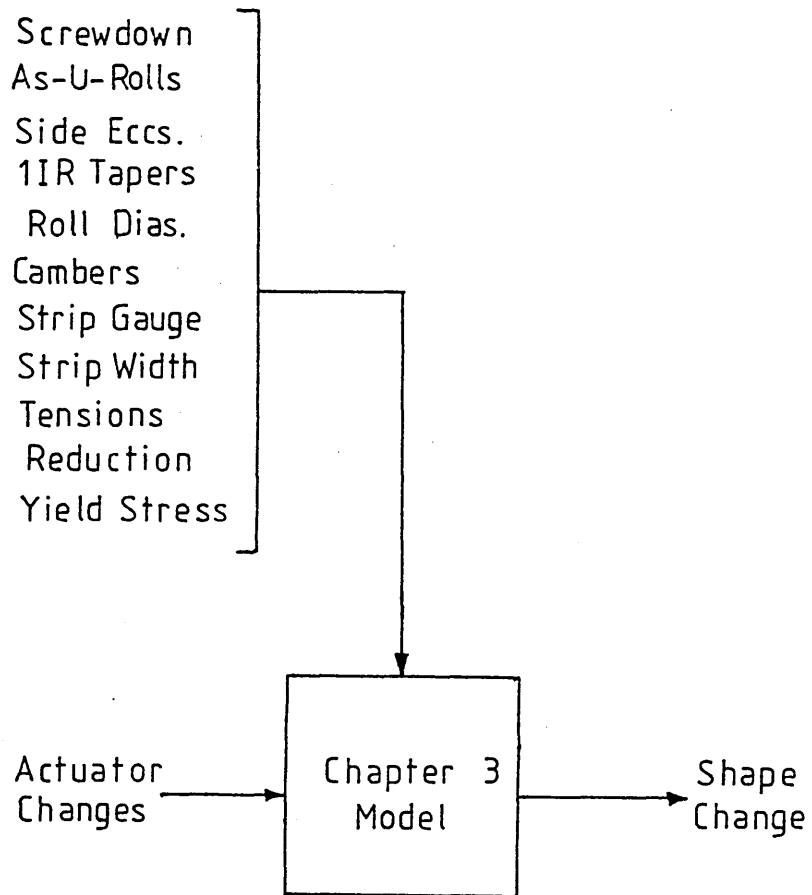


Fig.3-1 Function of Static Model

List of principal symbols, abbreviations and notations to be found in this chapter and Appendices 1 to 4

Subscripts (unless otherwise defined)

General subscripts used are:-

- B Quantity refers to backing bearings
- 2 Quantity refers to second intermediate rolls
- 1 Quantity refers to first intermediate rolls
- W Quantity refers to workrolls
- N Used as a count (i.e.  $N = 1, 2, 3, 4, \dots$  etc.)

Common second subscripts used are:-

- L Quantity refers to the Left-hand side or end
- R Quantity refers to the Right-hand side or end
- S Quantity refers to the area over the strip being rolled
- T Refers to the top half of the roll stack } (used
- B Refers to the bottom half of the roll-stack ) with  $L_I$ )
- o Indicates mill actuator datum positions (used with  $L_{s_1 s_2}$ )
- D Drive roll) (used with  $D_2$ )
- I Idler roll)

Main Variables and Abbreviations

$a_{BV_N}$  Motion of upper central backing shafts (roll B) towards centre of upper central second intermediate roll (J) at the  $N^{th}$  saddle from front of mill (i.e. due to motion of the  $N^{th}$  As-U-Roll rack). (m) (close approximation) (positive for roll B moving towards roll J).

AUR As-U-Roll

A )  
 $\lambda_x$ ) General functions defined in beams-on-elastic  
 B )  
 $\lambda_x$ ) foundations theory (Appendix 1)  
 )

B.O.E.F. Beams-on-Elastic Foundations

$c_s$  Camber off diameter of roll specified by subscript s. (m)

C )  
 $\lambda_x$ ) As A and B above  
 D )  
 $\lambda_x$ )  
 )

$D_s$  Maximum diameter (including camber) of roll specified by subscripts  $s$  (m)

$e$  Base of natural logarithms

$e_a, e_s, e_p$  Eccentricity of As-U-Roll rings, screwdown and side Eccentric Discs respectively (m)

$E$  Young's Modulus for all rolls ( $Nm^{-2}$ ).

$ECF$  Abbreviated form of "end-conditioning-force"

$E_{1s}$  ) Intermediate values defined in beams-on-elastic  
 $E_{2s}$  ) foundations theory (Appendix 1).  
 )

$F$  Value of concentrated force, subscripted as appropriate. (N) (positive downwards).

$F'_{Os}$  ) Values of force defined for roll specified by  
 $F''_{Os}$  ) subscript  $s$  in b.o.e.f. theory (N).  
 $F_{OAs}$  )  
 $F_{OBs}$  )

$\tilde{G}_p$  mill gain matrix ( $N\text{ mm}^{-2}$ )

$h_N$  Strip input gauge over the centre of the  $N^{\text{th}}$  shapemeter rotor covered by the strip. (m)

$H_N$  Strip output gauge corresponding to  $h_N$ . (m)

$h_i$  ) Strip general entry and exit gauges used in rolling  
 $h_o$  ) theory (m)  
 )

$I_s$  Second moment of area of roll specified by subscript  $s$ . Roll assumed cylindrical and of diameter  $D_s$  ( $m^4$ )

$J_B$  Number of backing bearings

$J_H$  Number of shapemeter rotor centres covered by strip

$J_R$  Number of rotors of shapemeter

$J_{sF}$  Number of concentrated forces taken to act on roll specified by subscript  $s$ . (Symmetrical about vertical centre-line of mill and equally-spaced).

- k Yield stress of strip in roll gap ( $\text{Nm}^{-2}$ ), variable as  $k(\phi)$
- $k_{s_1 s_2}$  Foundation modulus defined in b.o.e.f. theory (Appendix 1) for roll specified by subscript  $s_1$  resting on roll specified by subscript  $s_2$ . ( $\text{Nm}^{-2}$ )
- l Taper off base (i.e. uncambered) diameter of first intermediate rolls. (m)
- $L_t$  Length of IIR tapered portion (m)
- $L_B$  Length of each backing bearing. (m)
- $L_1$  Length of tapered section of first intermediate rolls which is slid into the cluster. (m)
- $L_R$  Width of each shapemeter rotor. (m)
- $L_S$  Strip Width. (m)
- $L_T$  Total roll length (m). (Length of non-tapered portion of IIRs).
- $L_U$  Unsupported length of workroll overhanging each edge of the strip. (m)
- LH Abbreviated form of "left-hand". Note that the "left-hand" end of any roll is at the front of the mill.
- $L_{s_1 s_2}$  Distance between centres of rolls specified by subscripts  $s_1$  and  $s_2$  (used in cluster angle and force analysis). (m)
- $M'_{As}$  )  
 $M''_{As}$  ) Various values of moment defined in the b.o.e.f. theory (Appendix 1) for roll specified by subscript  $s$ . (Nm) (Positive when clockwise on the left of a section - i.e. in the direction of the positive shearing force Q on the left of the section. Thus M is positive for a sagging beam).  
 $M'_{Bs}$  )  
 $M''_{Bs}$  )  
 $M'_{Os}$  )  
 $M''_{Os}$  )  
 $M_{OAs}$  )  
 $M_{OBs}$  )

$M_A$  As-U-Roll Rack position (operator's units)  
 (positive downwards)

$M_P$  side eccentric position (operator's units)

$M_S$  screwdown rack position ( " " )

$M_{s_1}$  Even number of points (symmetrical about the vertical  
 centre line of mill and equally spaced) at which  
 deflection is calculated for roll specified by  
 subscript  $s_1$ .

$P_B$  Pitch of backing bearings (m)

$P_T$  Total Rolling Load (N)

$P'$  Distributed Rolling Load ( $Nm^{-1}$ )

$q$  Value of uniformly-distributed loading,  
 subscripted as appropriate. ( $Nm^{-1}$ )(positive down-  
 wards)

$Q_{A_s}$  ) Values of shear defined in b.o.e.f. theory  
 $Q'_{A_s}$  ) (Appendix 1) for roll specified by subscript  $s$ . (N)  
 $Q''_{A_s}$  ) (Positive when acting upwards on the left of a section).  
 $Q_{B_s}$  )

$R$  Undeformed roll radius (m)

$R'$  Deformed roll radius (m)

$RH$  Abbreviated form of "right-hand"

$r_A, r_s, r_p$  Gain of As-U-Roll, screwdown and side eccentric  
 actuators (rad/operator's unit)

$s$  Normal rolling pressure ( $Nm^{-2}$ ) (Variable as  $s(\phi)$ ).

$T_i, T_o$  Entry & Exit Tensions (N)

$T'_i, T'_o$  " " Tension stresses ( $Nm^{-2}$ )

$t_N$  Peak value of triangular-distributed loading due to  
 backing bearing  $N$ . May be further subscripted  
 if the  $N^{th}$  bearing produces two triangular-  
 distributed loads. ( $Nm^{-1}$ ).

$TDL$  Abbreviated form of "triangular-distributed loading"

$UDL$  Abbreviated form of "uniformly-distributed loading"

WR Abbreviated form of "workroll"

w Strip width (m) used in rolling theory.

$x_{E_N}$  Distance of front edge of  $N^{\text{th}}$  backing bearing along second intermediate roll. Measured from front of mill. (A zero preceding the "N" indicates that the measurement is taken at zero As-U-Roll travel). (m)

$x_M \Big|_{M=1, M_s}$  Array of distances of the  $M_s$  points from the front of the mill. (m)

$x_{SF_N} \Big|_{N=1, J_{SF}}$  Distance from front of mill of point of application of  $N^{\text{th}}$  concentrated force acting on roll specified by subscript s. (m)

$y_{L_N}$  Deflection of workroll at LH edge of strip due to  $N^{\text{th}}$  element of array  $F_W(J_{WF})$ . (m)

$y_{R_N}$  Deflection of workroll at RH edge of strip due to  $N^{\text{th}}$  element of array  $F_W(J_{WF})$ . (m)

$y_{s x_M} \Big|_{M=1, M_s}$  Deflection of roll specified by subscript s at the section  $x_M$ . (m)

$Z_N$  A number of algebraic reduction factors used in section 3.9.21, defined as required.

$\delta_R$  p.u. Reduction of strip gauge due to rolling

$\Delta L_N \Big|_{N=1, J_H}$  Differential elongation (w.r.t. mean) of filament of strip corresponding to  $N^{\text{th}}$  covered shapemeter rotor centre from front of mill. (m)

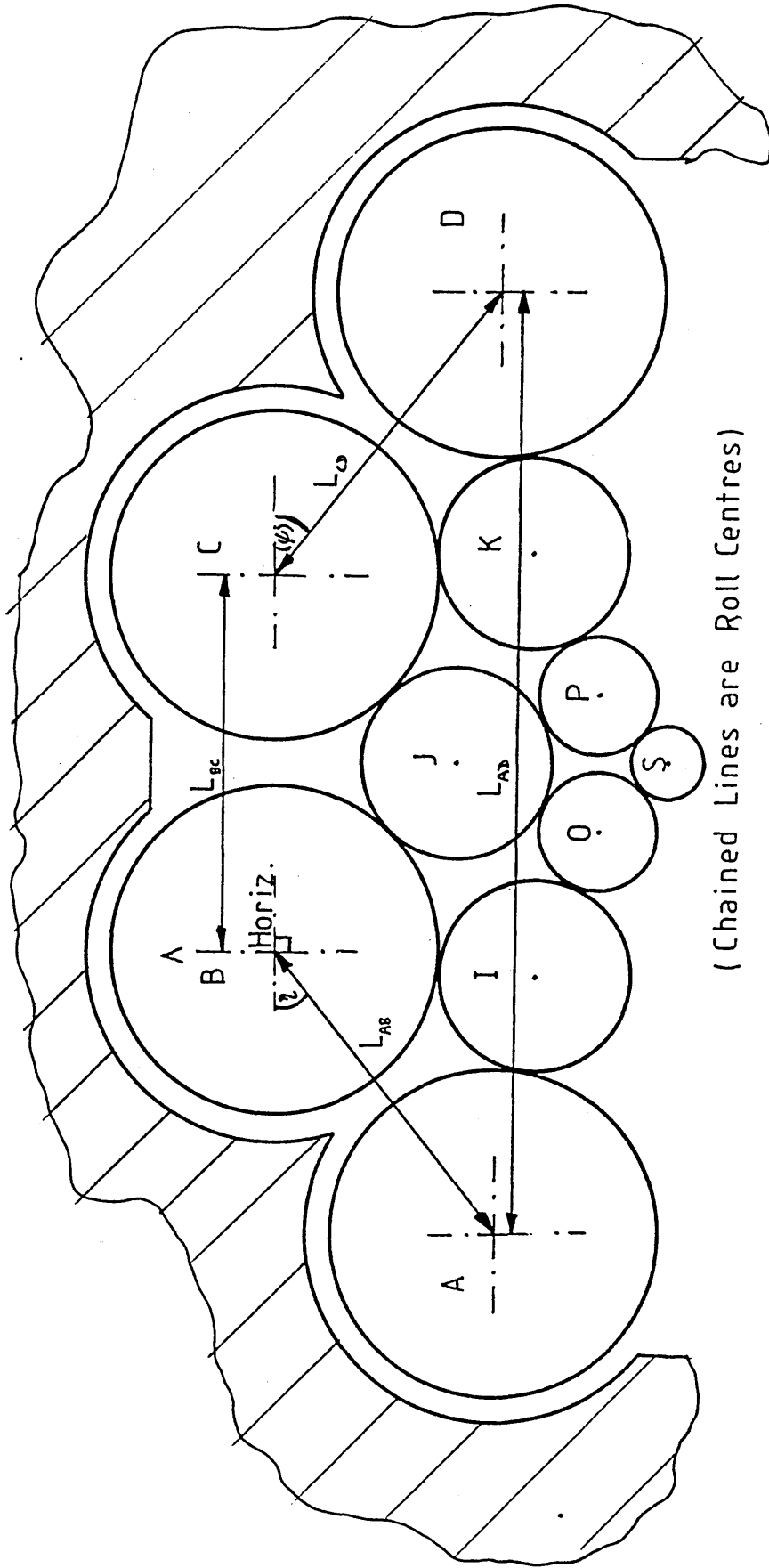
$\Delta \sigma_N \Big|_{N=1, J_H}$  Differential stress (shape) in the above filament. ( $\text{Nm}^{-2}$ )

$\theta_A, \theta_s, \theta_p$	Deviation of As-u-Roll, Screwdown and side eccentric rings/discs from datum position (rad). (positive when clockwise viewed from the front at shafts A,B,G,H)
$\theta_{L_N}$	Deflection angle corresponding to $y_{L_N}$ . (rad.)
$\theta_{R_N}$	Deflection angle corresponding to $y_{R_N}$ . (rad.)
$\theta_{W_{x_M}}$	Deflection angle corresponding to $y_{W_{x_M}}$ . (rad.)
$\theta_1 - \theta_8$ ) $\theta_{1R} - \theta_{8R}$ )	Cluster angles defined in figure 3.16 (rad.)
$\lambda_s$	See $E_{1s}$ ( $m^{-1}$ )
$\mu$	Co-efficient of friction in roll gap.
$\nu$	Poisson's Ratio for roll material.
$\phi_s, \phi_p$	"Rotation" of screwdown, side eccentric discs to achieve datum from "horizontal". (rad.)
$\phi$	Angle subtended at workroll centre by the arc of contact between exit plane and some plane of interest (rad.)
including:	
( $\phi_o$	= $\phi$ (exit plane) = 0(rad.)
( $\phi_i$	= $\phi$ (entry plane) = arc of contact of strip in roll gap (rad.)
( $\phi_n$	= neutral angle (rad.)
1IR	First Intermediate Roll
2IR	Second Intermediate Roll

### 3.2 Modelling of the Control Actuators

This section describes that part of the model which determines the effect upon the cluster geometry of moving the eccentric actuators (the first intermediate roll tapers are not discussed until section 3.8, as their effect is more sensibly included there). The next section considers the implications of the cluster geometry in terms of rolling load distribution.

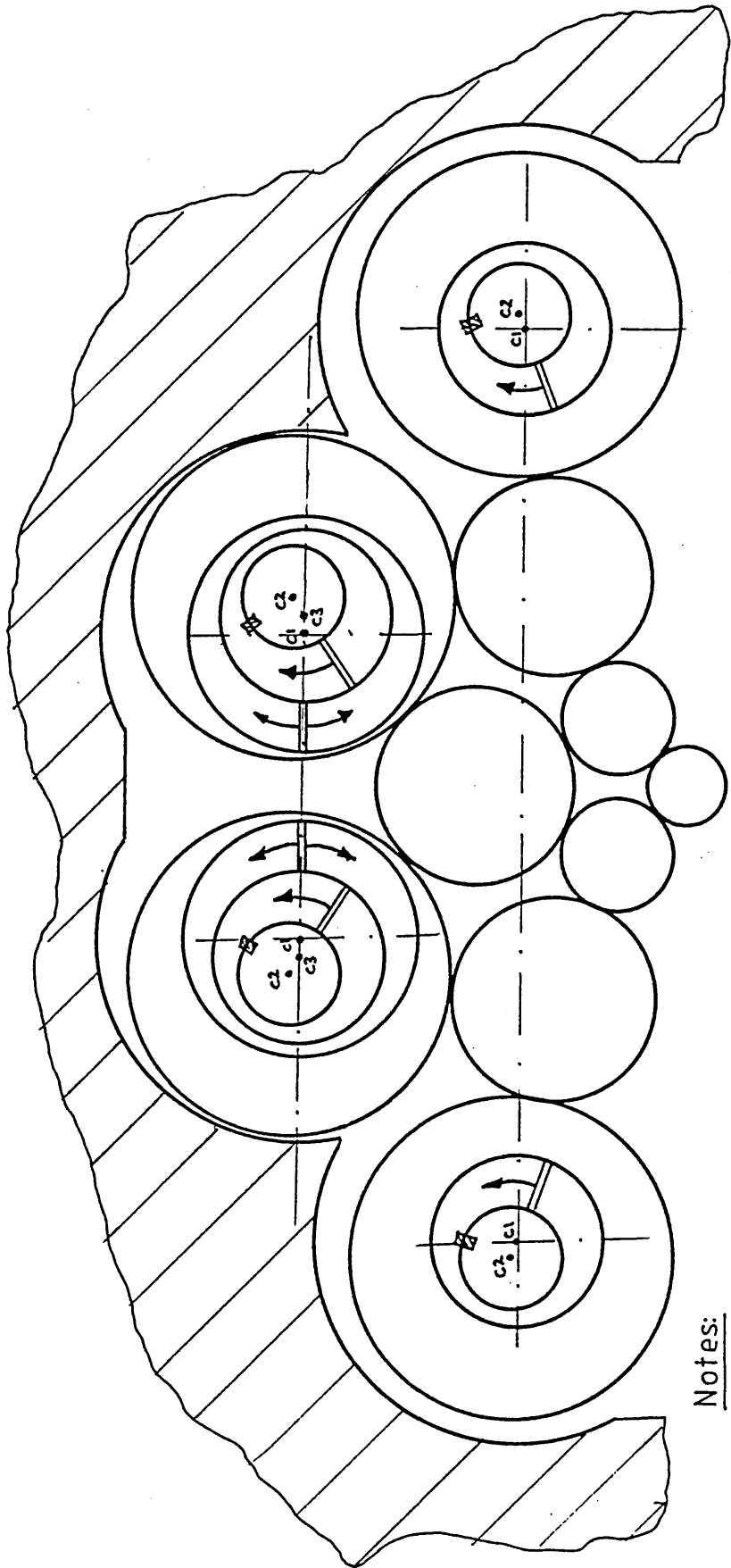
Consider first the upper half of the mill cluster. Section 2.3 has made it clear that when any of the eccentric actuators is moved (excepting here the push-up system, which acts only on the lower half of the roll stack) the centres of the backing shaft assemblies A to H (fig.2.1) will move relative to the fixed mill housing and relative to each other. Furthermore, perusal of sub-sections 2.3.3 and 2.3.4 (and the analysis below) will show that since the eccentrics at shafts B and C always move together, a line joining the centres of shafts B and C will remain horizontal at all times. Therefore, given a knowledge of the roll diameters, the set of five parameters shown in figure 3.2 is necessary and sufficient to specify the complete geometry of the upper half of the cluster. ( $\psi$  is itself a function of the other 5 parameters). Note that the roll diameters are modified by roll flattening under the influence of rolling load. These effects are included in section 3.4 (since they are so small as to make no appreciable difference to the cluster geometry effects under consideration here).



( Chained Lines are Roll Centres )

Fig.3.2 Parameters Which Fix Geometry of Upper Half of Cluster

Let us establish a datum position from which all actuator movements will be measured. The positions of the operating mechanisms for the screwdown, push-up and side eccentric systems are displayed to the mill operator on scales graduated in arbitrary units from zero to ten. The zero positions correspond to the fully open mill position (maximum roll gap) and these will be taken as the datum position. The As-U-Roll rack positions are displayed on scales of  $\pm 5$  divisions (+5 divisions being the position to which the rack is fully lowered), and the centre zero positions are taken as the datum here. The physical meaning of the datum position in terms of eccentric rotations is illustrated in figure 3.3. At each backing shaft position, C1 represents the (fixed) housing bore centre, C2 the centre of the backing bearing shaft assembly at the datum position and C3 (shafts B and C only) the centre of the inner diameter of the As-U-Roll eccentric ring. All eccentric movements in figure 3.3 have, of course, been grossly exaggerated for clarity, typical values of eccentricity being of the order of 9mm, 4.5mm and 1.5mm for the screwdown, side eccentric and As-U-Roll respectively (compared with the typical backing bearing diameter of 406mm). The various angles of rotation of the eccentric discs in fig.3.3 are defined below, and then the set of measurements between shaft centres (fig.3.2) is derived. At the datum position, the parameters shown in figure 3.2 will be referred to as  $L_{A_o B_o}$ ,  $L_{B_o C_o}$ ,  $L_{C_o D_o}$  and  $L_{A_o D_o}$ . These can be calculated from the known housing dimensions and the known rotations



Notes:

- i) Saddles Omitted for Clarity
- ii) Double Lines Indicate Heavy Side of Eccentrics
- iii) Chained Lines are Housing Bore Centres
- iv) Arrows Show Motion Away from Datum
- v) c1 - c3 as Fig.2.6

Fig.3.3 Eccentric Positions at Datum (Zero) State

of the eccentrics required to achieve the datum position (measured from the horizontal).

Consider one saddle of the backing shaft assembly B as shown with the eccentrics in the horizontal position in fig.3.4. The effect of moving the As-U-Roll eccentric ring only is illustrated in figure 3.5, and it is clear that since shaft C always moves as a mirror image of shaft B, then

$$L = \frac{1}{2} \cdot L_{BC}$$

Therefore,  $L_{BC} = 2(l_1 + e_A \cdot \cos \theta_A + e_s)$

Figure 3.6 shows the same situation with the addition of a screwdown rack movement causing a rotation of the screwdown eccentric ring of  $\phi_S$ , when

$$L_{BC} = 2(l_1 + e_A \cdot \cos \theta_A + e_S \cdot \cos \phi_S) \dots\dots\dots(3.1)$$

It can be shown that all other cases are a special case of equation 3.1. From figure 3.3 at the datum position,  $\theta_A=0$ , and therefore from (3.1)

$$L_{B_o C_o} = 2(l_1 + e_A + e_S \cdot \cos \phi_S) \dots\dots\dots(3.2)$$

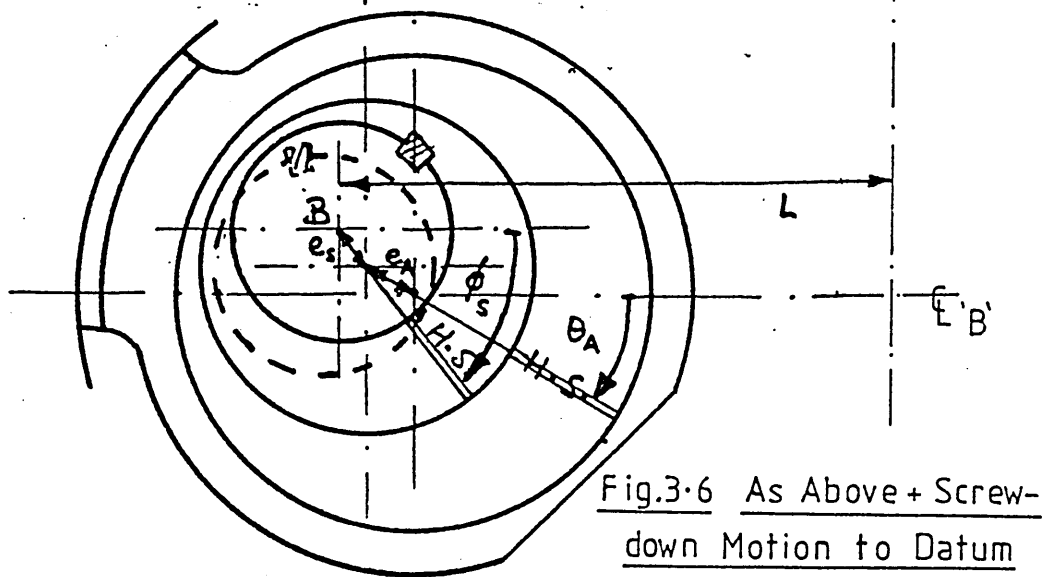
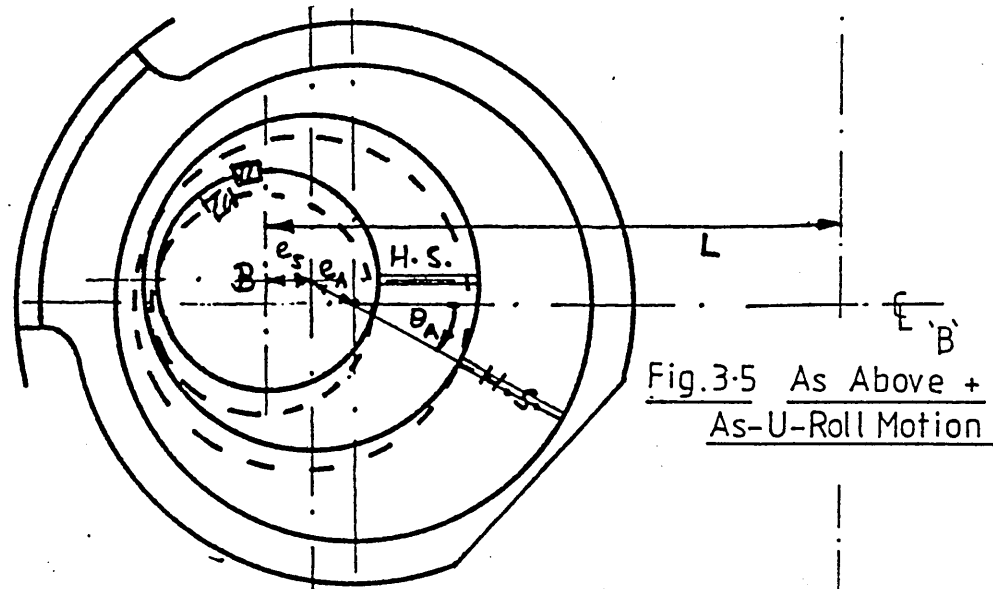
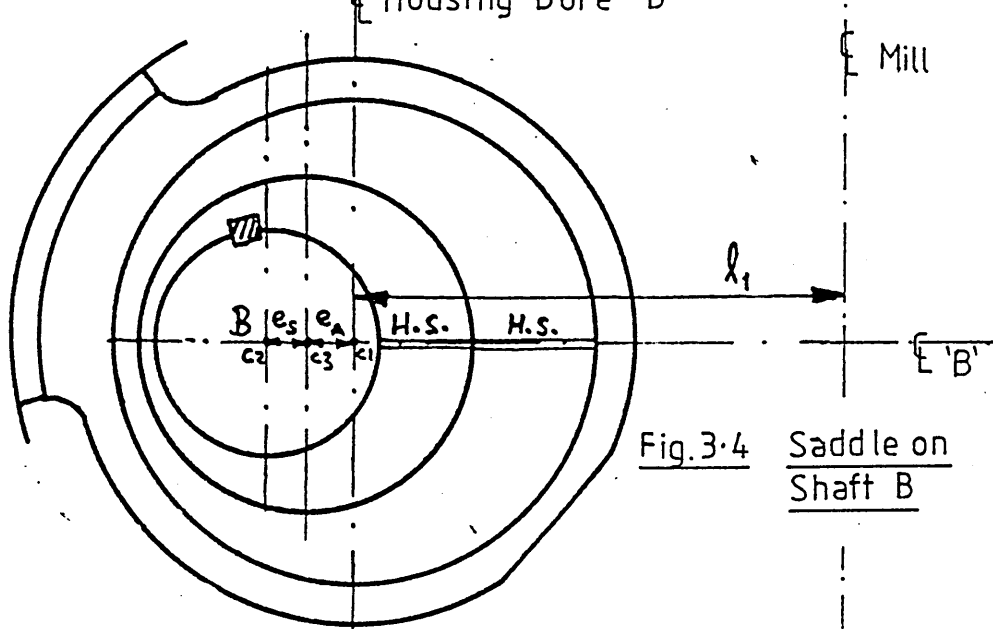
The situation at shaft A is shown in figure 3.7, whence

$$L = l_2 + e_p \cos \phi_p.$$

Now at the datum position, the magnitude of the right-hand side eccentric rotation will be the same as the left, therefore,

$$L_{A_o D_o} = 2L = 2(l_2 + e_p \cos \phi_p) \dots\dots\dots(3.3)$$

The situation pertaining to the derivation of  $L_{A_o B_o}$  (and



$L_{C_o D_o}$ ) is illustrated in figure 3.8. It can be shown that

$$l_4 = \sqrt{l_3^2 + (l_2 - l_1)^2}$$

and  $\alpha = \tan^{-1} \left[ \frac{l_3}{l_2 - l_1} \right]$

This gives rise to the geometrical figure shown in fig.3.9, where

$X_o$  is the centre of housing bore A.

$Y_o$  is the centre of the inner diameter of the As-U-Roll eccentric ring (and therefore also the outer diameter of the screwdown eccentric ring) at the datum point.

$Z_o$  is the centre of housing bore B.

Note: Since  $X_o$  and  $Z_o$  are saddle bore centres they are fixed with respect to the mill housing.

Applying the cosine rule to the triangle  $X_o Y_o Z_o$  in figure 3.9

$$L_{X_o Y_o} = \sqrt{l_4^2 + e_A^2 - 2.l_4 \cdot e_A \cos \alpha}$$

and also

$$\beta = \cos^{-1} \left[ \frac{L_{X_o Y_o}^2 + e_A^2 - l_4^2}{2 \cdot L_{X_o Y_o} \cdot e_A} \right] - \phi_S$$

Applying the cosine rule to the triangle  $X_o B_o Y_o$ ,

$$L_{X_o B_o} = \sqrt{L_{X_o Y_o}^2 + e_S^2 + 2 \cdot L_{X_o Y_o} \cdot e_S \cdot \cos \beta}$$

and the sine rule gives,

$$\gamma = \sin^{-1} \left[ \frac{e_S \sin \beta}{L_{X_o B_o}} \right]$$

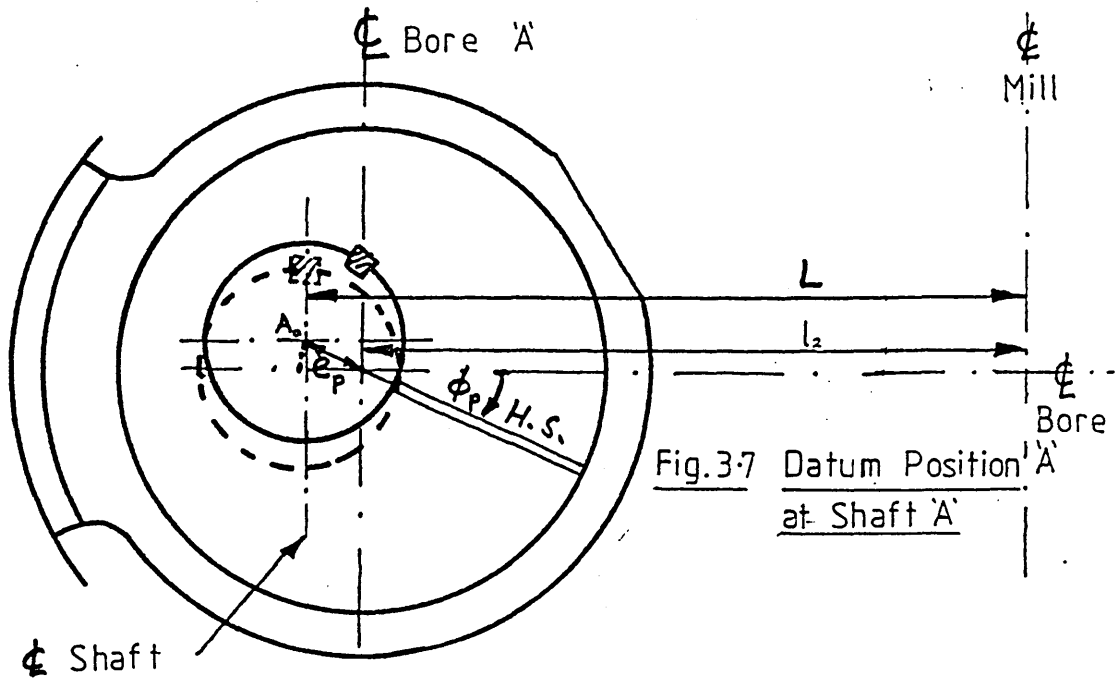


Fig.3.7 Datum Position 'A' at Shaft 'A'

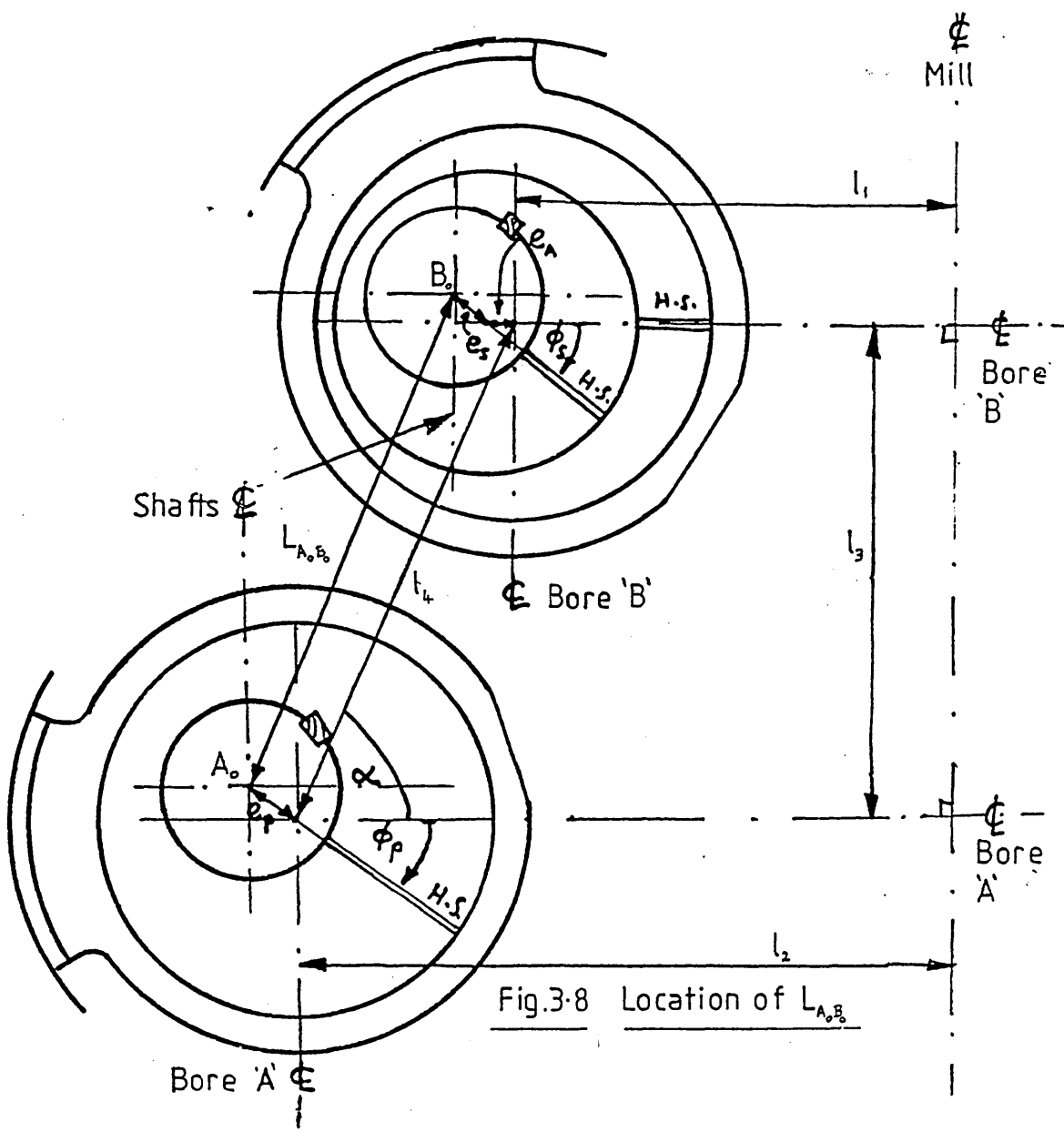
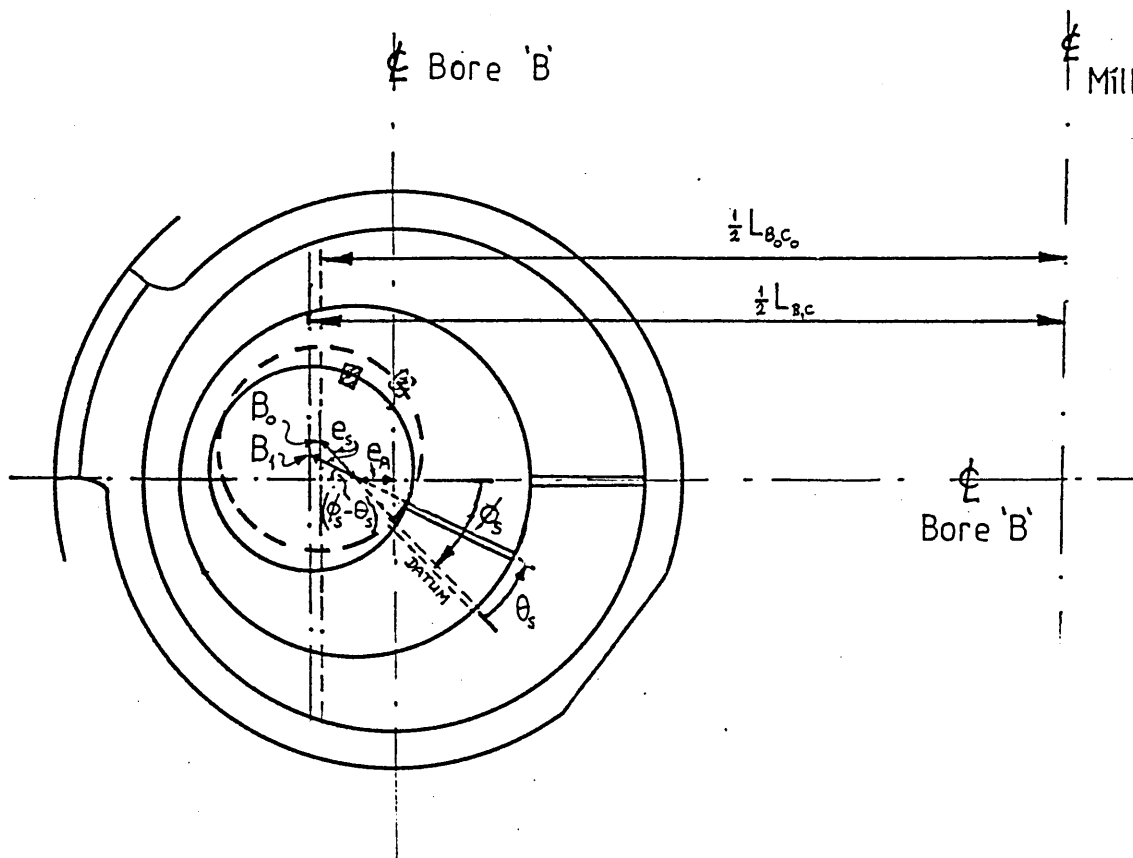
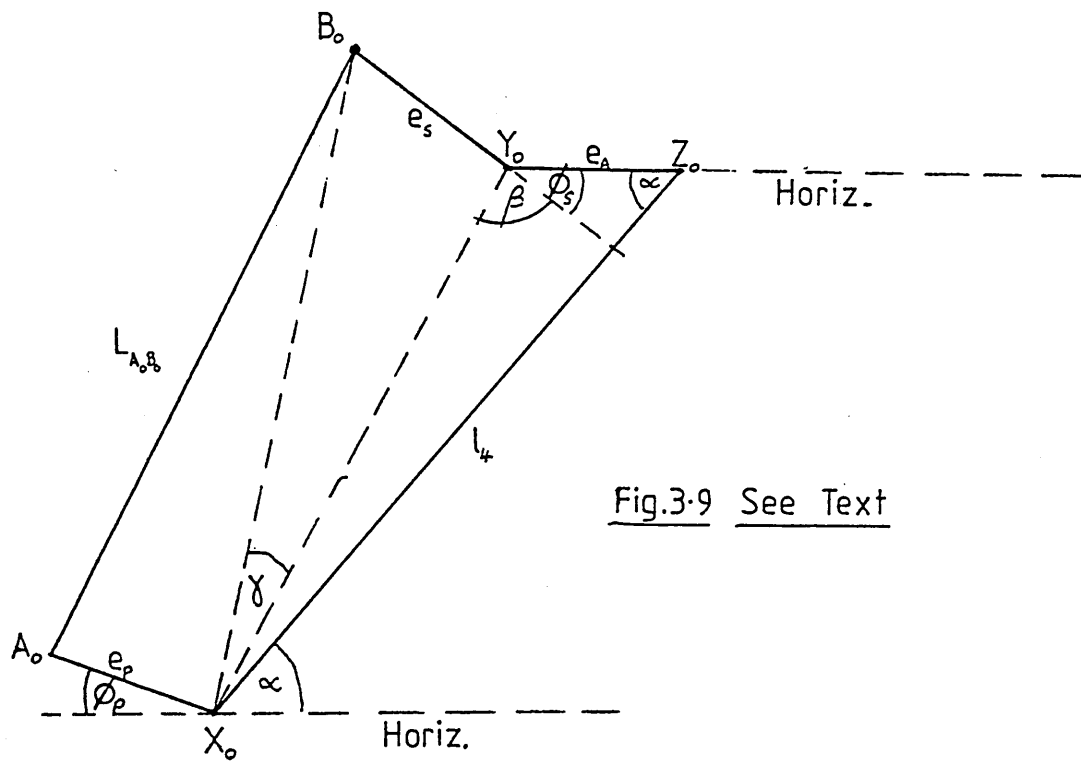


Fig.3.8 Location of  $L_{A_0B_0}$



Finally, applying the cosine rule in triangle  $A_o B_o X_o$

$$L_{A_o B_o} = \sqrt{L_{X_o B_o}^2 + e_p^2 - 2 \cdot L_{X_o B_o} \cdot e_p \cdot \cos(\beta + \phi_S - \phi_p - \gamma)} \dots (3.4)$$

and  $L_{C_o D_o} = L_{A_o B_o} \dots \dots \dots (3.5)$

The fully open mill position is now completely specified as the datum position by equations (3.2) to (3.5), since  $l_1$  to  $l_4$ ,  $\phi_S$  and the various eccentricities are known from the investigation of the plant drawings.

Having defined the datum configuration, we can now model the variations in the distances between the backing shaft assembly centres (figure 3.2) due to displacement of the actuators from their datum positions. The actuator positions are specified to the model in terms of the units displayed to the mill operators. These convenient arbitrary units are converted for use in the model using appropriate angular conversion constants calculated from mill drawings and plant tests.

For a screwdown rack position of  $M_S$  units indicated to the mill operator, the screwdown eccentrics will rotate through an angle of  $\theta_S$  radians from the datum as shown in figure 3.10 where

$$\theta_S = M_S \cdot r_S$$

Since the screwdown eccentric discs on shafts B and C always move in simultaneous contrarotation, it is clear that in figure 3.10,  $L_{B_1 C}$  will always remain parallel with  $L_{B_o C_o}$ .

Therefore,

$$L_{B_1C} = L_{B_0C_0} + 2e_S(\cos(\phi_S - \theta_S) - \cos\phi_S) \dots \dots \dots (3.6)$$

Equation 3.6 is valid for all possible practical values of  $\theta_S$  with the As-U-Roll racks at the datum position. However, we shall now modify it to take account of the movement of the As-U-Roll racks. In the general case this will yield a different value for  $L_{BC}$  at each saddle position on shafts B and C. However, the effect due to rotation of the As-U-Roll ring at any given saddle is small compared with the effect due to screwdown motion. This is because firstly the screwdown eccentricity is much greater than the As-U-Roll eccentricity, and secondly the rotation of the screwdown eccentric disc from the datum will also be greater in general than that of the As-U-Roll eccentric ring. Therefore, in calculating the distribution of rolling load throughout the cluster, the mean As-U-Roll rotation  $\bar{\theta}_A$  will be used where

$$\bar{\theta}_A = \frac{r_A}{8} \sum_{n=1}^8 M_{An} \quad \begin{array}{l} (n=1 \text{ refers to the front} \\ \text{As-U-Roll rack on the mill}) \end{array}$$

Note that in general  $\theta_{An} = r_A \cdot M_{An}$ , and the resulting sign of  $\theta_{An}$  specifies clockwise (+ve) or anti-clockwise rotation. Thus, positive (downward) motion of the As-U-Roll rack causes positive (clockwise) rotation of the ring at shaft B (see e.g. figure 2.8). This causes the backing shafts (and therefore the workroll) to move upwards (fig.3.5) which opens the roll gap. Therefore less reduction is taken at that area across the strip width and a positive change in differential

stress (tightening) results in the strip. The operators display of As-U-Roll rack position is wired to indicate positive rack motion upwards, from zero, so as to tie in with the shape display. Hence the equation for  $\theta_{An}$  above, yields the correct sign.

Motion of the As-U-Roll rack through an angle  $-\bar{\theta}_A$  from the datum will modify figure 3.10 to figure 3.11. Since  $L_{B_1Y_0}$  and  $L_{BY}$  are equal and parallel, the correction to  $\frac{1}{2}L_{B_1C}$  is given by

$$\text{correction} = -e_A (1 - \cos \bar{\theta}_A) \dots\dots\dots(3.7)$$

which is very small for all practical purposes, but is included for completeness. Therefore, combining (3.6) and (3.7) we have

$$L_{BC} = L_{B_0C_0} + 2e_S (\cos(\phi_S - \theta_S) - \cos \phi_S) - 2e_A (1 - \cos \bar{\theta}_A) \quad (3.8)$$

Equation (3.8) is valid for all practical values. (if  $\bar{\theta}_A$  is positive rather than negative, the cosine term being an even function, automatically compensates of course).

Considering now the side eccentrics, since the left and right hand units can be moved independently it is necessary to evaluate their separate effects. Figure 3.12 depicts a saddle on shaft A. For a "rack" position of  $M_{PL}$  units,

$$\theta_{PL} = r_P \cdot M_{PL}$$

The figure assumes that, for the present, shafts B and D are held at the datum position. From the figure (or more

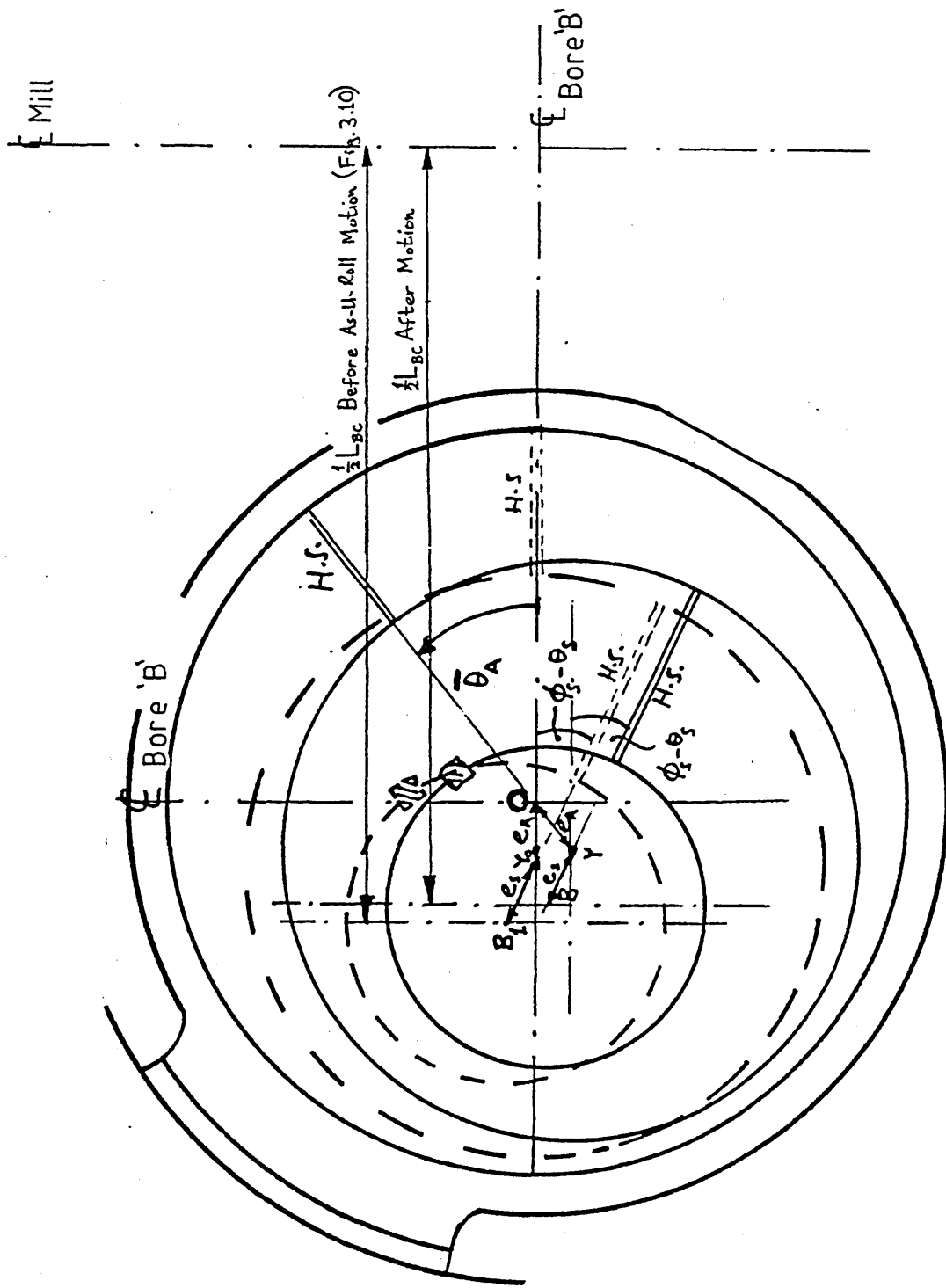


Fig.3.11 Effect of As-U-Roll Motion on  $L_{bc}$



clearly from figure 3.13),

$$L_{AA_o} = 2e_p \sin(\theta_{PL}/2) \dots\dots\dots(3.9)$$

which is valid for all practical values of  $\theta_{PL}$ .

Also since the datum position is symmetrical (Fig.3.3),

it can be seen that

$$\delta = \cos^{-1} \left[ \frac{L_{A_o D_o} - L_{B_o C_o}}{2 \cdot L_{A_o B_o}} \right] \dots\dots\dots(3.10)$$

Also from Fig. 3.12, by cosine rule,

$$L_{AD_o} = \sqrt{L_{A_o D_o}^2 + L_{AA_o}^2 + 2L_{A_o D_o} \cdot L_{AA_o} \cdot \sin(\phi_p - \frac{\theta_{PL}}{2})} \dots\dots\dots(3.11)$$

Equation (3.11) above is correct for all practical values of  $\theta_{PL}$ . Similarly at shaft D,

$$\theta_{PR} = M_{PR} \cdot r_p$$

and  $L_{DD_o} = 2 \cdot e_p \sin \frac{\theta_{PR}}{2} \dots\dots\dots(3.12)$

The combined effects of moving both side eccentrics can now be used to calculate the value of  $L_{AD}$ . Figure 3.13 illustrates the situation, whence the cosine rule applied to triangle  $A_o D_o A$  gives

$$\gamma = \cos^{-1} \left[ \frac{L_{A_o D_o}^2 + L_{AD_o}^2 - L_{AA_o}^2}{2 \cdot L_{AD_o} \cdot L_{A_o D_o}} \right]$$

Applying the cosine rule to triangle  $AD_o D$  gives

$$L_{AD} = \sqrt{L_{AD_o}^2 + L_{DD_o}^2 - 2 \cdot L_{AD_o} \cdot L_{DD_o} \cdot \sin(\frac{\theta_{PR}}{2} - \phi_p + \gamma)} \dots\dots\dots(3.13)$$

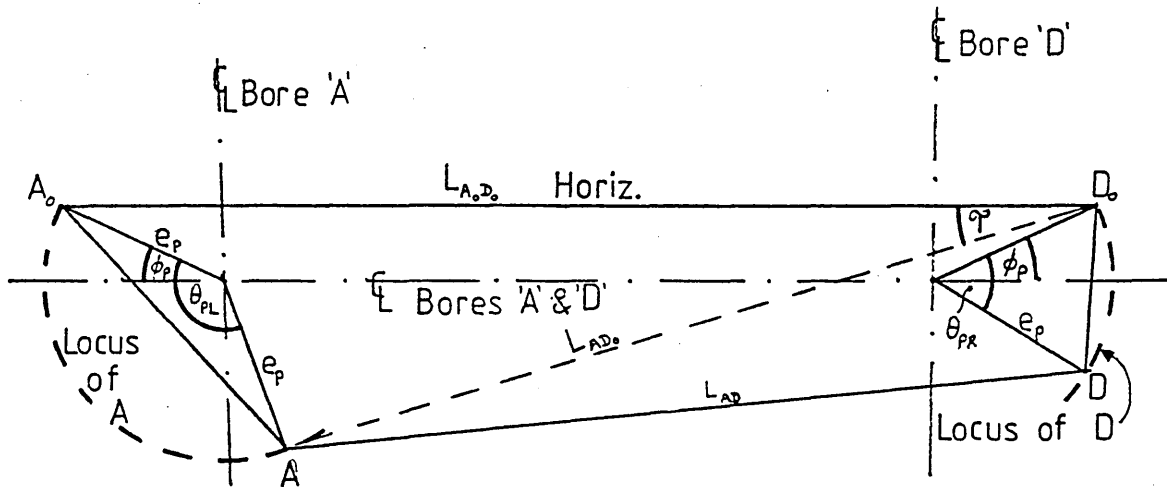


Fig.3.13 Displacement of Both Side Eccentrics

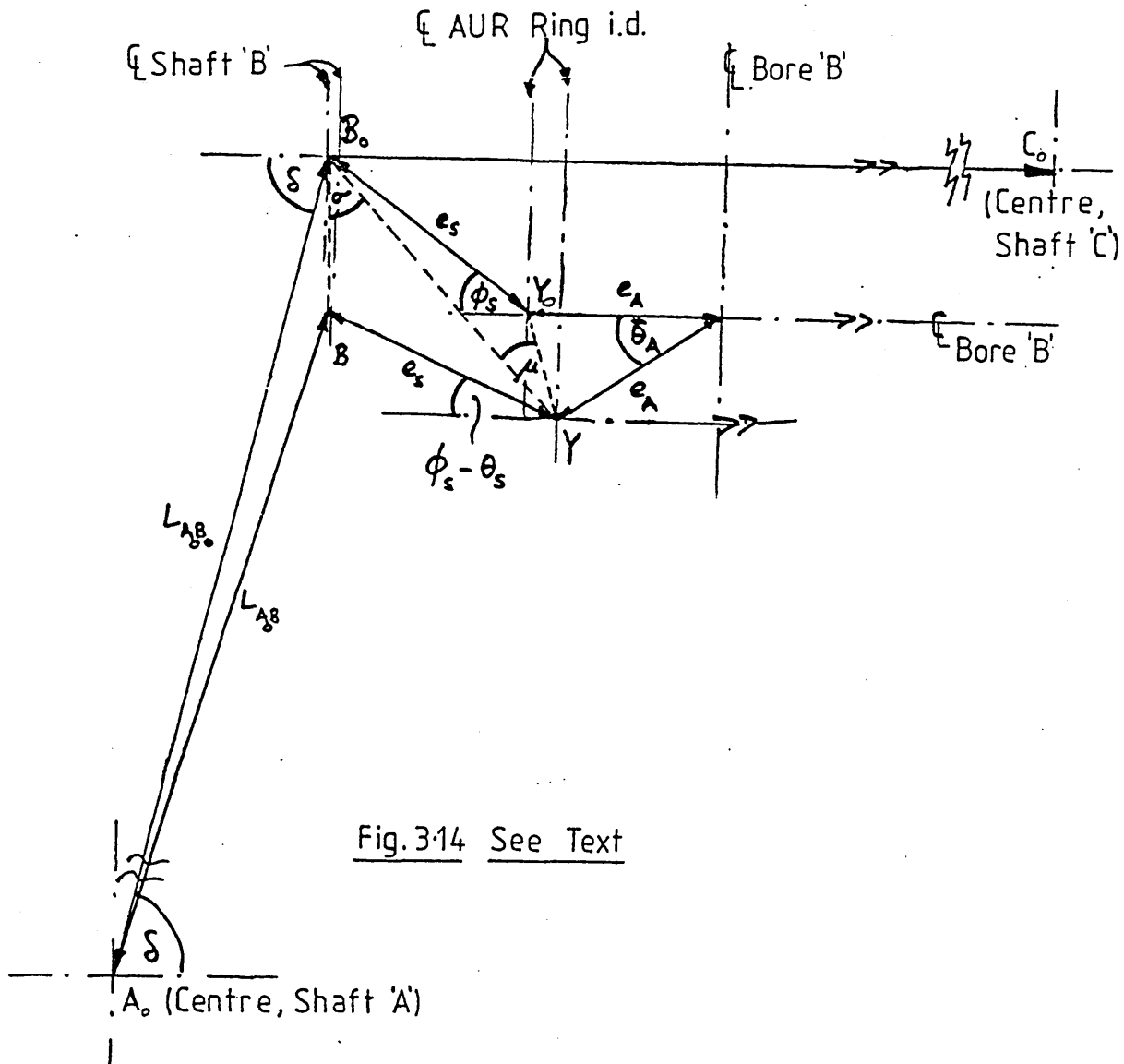


Fig.3.14 See Text

Note  $L_{A_0D_0}$  is given by equation (3.3)

$L_{AD_0}$  is given by equation (3.11)

$L_{AA_0}$  is given by equation (3.9)

$L_{DD_0}$  is given by equation (3.12)

Equation (3.13) can be shown to hold true for all possible practical combinations of  $\theta_{PR}$  and  $\theta_{PL}$ .

Having obtained general equations for  $L_{BC}$  (3.8) and  $L_{AD}$  (3.13) we now turn our attention to the somewhat more complex problem of  $L_{AB}$  and  $L_{CD}$ . Figure 3.14 comprises a geometrical figure which arises from the combination of the datum state of fig.3.10 and the final (general) state of fig.3.11. We assume that, for the present, shaft A (the left hand side eccentric) remains at its datum position. From figure 3.14, we see that (noting that  $\bar{\theta}_A$  as shown in the figure is negative)

$$L_{Y_0Y} = 2e_A \sin \frac{|\bar{\theta}_A|}{2}$$

Application of the cosine rule in triangle  $B_0Y_0Y$  then yields

$$L_{B_0Y} = \sqrt{L_{Y_0Y}^2 + e_S^2 + 2L_{Y_0Y}e_S \sin(\phi_S + \frac{|\bar{\theta}_A|}{2})} \quad \left| \bar{\theta}_A \leq \text{zero} \right.$$

$$\text{and } \mu = \cos^{-1} \left[ \frac{L_{B_0Y}^2 + L_{Y_0Y}^2 - e_S^2}{2L_{B_0Y} \cdot L_{Y_0Y}} \right]$$

Then from triangle  $BB_oY$

$$L_{BB_o} = \sqrt{L_{B_oY}^2 + e_S^2 + 2L_{B_oY}e_S \sin(\theta_S - \phi_S - \mu - \frac{|\bar{\theta}_A|}{2})} \Big|_{\bar{\theta}_A \leq \text{zero}}$$

$$\text{and } \sigma = \cos^{-1} \left[ \frac{L_{BB_o}^2 + L_{B_oY}^2 - e_S^2}{2L_{BB_o}L_{B_oY}} \right]$$

Finally, from triangle  $A_oB_oB$  we obtain similarly

$$L_{A_oB} = \sqrt{L_{A_oB_o}^2 + L_{BB_o}^2 - 2L_{A_oB_o}L_{BB_o} \sin(\delta + \sigma - \mu - \frac{|\bar{\theta}_A|}{2})} \Big|_{\bar{\theta}_A \leq \text{zero}}$$

..... (3.14)

(where  $L_{A_oB_o}$  is given by (3.4) and  $\delta$  by (3.10))

NOTE That if  $\bar{\theta}_A$  is positive rather than negative (i.e. the As-U-Roll ring is rotated clockwise) certain alterations are required in the above sequence of equations as follows:-

$L_{Y_oY}$  is calculated as before

$$L_{B_oY} = \sqrt{L_{Y_oY}^2 + e_S^2 + 2L_{Y_oY}e_S \sin(\frac{\bar{\theta}_A}{2} - \phi_S)} \Big|_{\bar{\theta}_A > \text{zero}}$$

$\mu$  is calculated using this value of  $L_{B_oY}$

$$L_{BB_o} = \sqrt{L_{B_oY}^2 + e_S^2 + 2L_{B_oY}e_S \sin(\phi_S - \theta_S - \mu - \frac{\bar{\theta}_A}{2})} \Big|_{\bar{\theta}_A > \text{zero}}$$

$\sigma$  is calculated using this value of  $L_{BB_o}$

It can be demonstrated by manipulation of figure 3.14, that for  $\bar{\theta}_A$  positive (rotating clockwise from the datum rather than anticlockwise as shown),  $L_{A_o B}$  is given by one of two equations depending upon whether B lies above or below the line  $B_o Y$ . Thus

$$L_{A_o B} = \sqrt{L_{A_o B_o}^2 + L_{B B_o}^2 - 2L_{A_o B_o} L_{B B_o} \sin(\sigma - \delta - \mu - \frac{\bar{\theta}_A}{2})} \dots (3.15)$$

$$\text{for } (\bar{\theta}_A > \text{zero}) \text{ and } (\phi_S - \theta_S) \geq (\mu - \frac{\pi}{2} + \frac{\bar{\theta}_A}{2})$$

or

$$L_{A_o B} = \sqrt{L_{A_o B_o}^2 + L_{B B_o}^2 - 2L_{A_o B_o} L_{B B_o} \sin(-\sigma - \delta - \mu - \frac{\bar{\theta}_A}{2})} \dots (3.16)$$

$$\text{for } (\bar{\theta}_A > \text{zero}) \text{ and } (\phi_S - \theta_S) < (\mu - \frac{\pi}{2} + \frac{\bar{\theta}_A}{2})$$

The equations for  $L_{AB}$  and  $L_{CD}$  can now be derived by considering these results in conjunction with the side eccentric motion evaluated previously. The geometrical figure arising from a combination of figures 3.12 and 3.14 is shown as figure 3.15, whence

$$\rho = \cos^{-1} \left[ \frac{L_{A_o B_o}^2 + L_{A_o B}^2 - L_{B B_o}^2}{2L_{A_o B_o} L_{A_o B}} \right]$$

where  $L_{A_o B_o}$  is given by (3.4)

$L_{A_o B}$  is given by (3.14, 3.15 or 3.16 as appropriate)

$L_{B B_o}$  is given in the derivation of  $L_{A_o B}$  above

and

$$L_{AB} = \sqrt{L_{AA_o}^2 + L_{A_o B}^2 - 2L_{AA_o} L_{A_o B} \sin(\frac{\theta_{PL}}{2} - \phi_p - \delta + \rho)} \dots (3.17)$$

(see conditions of validity below)

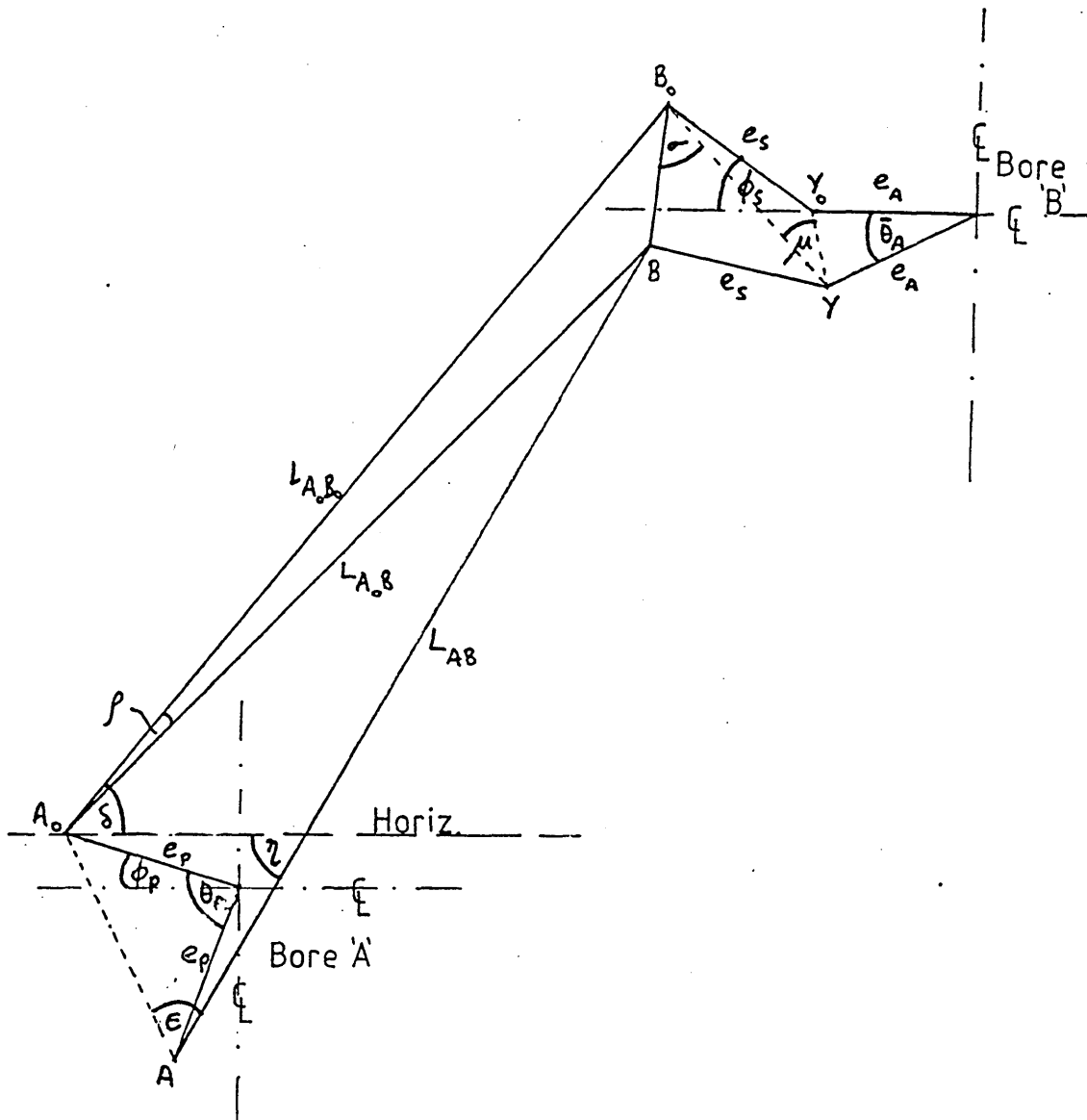


Fig.3-15 Overall Effect Pertaining to Derivation of  $L_{AB}$

where  $L_{AA_0}$  is given by (3.9)  
is given by (3.10)

Equation (3.17) is true only if point B lies below line  $A_0B_0$  or its projection beyond  $B_0$ . If the values of  $\theta_S$  and  $\bar{\theta}_A$  are such that B rises above this line, then

$$L_{AB} = \sqrt{L_{AA_0}^2 + L_{A_0B}^2 - 2L_{AA_0}L_{A_0B} \sin\left(\frac{\theta_{PL}}{2} - \rho_p - \delta - \beta\right)} \dots (3.18)$$

(see conditions of validity below)

Figure 3.15 can be drawn in many ways depending upon the relative magnitudes of  $\theta_{PL}$ ,  $\theta_S$  and  $\bar{\theta}_A$ . In fact over 15 permutations which could conceivably yield different solutions for  $L_{AB}$  were identified and analysed. All these permutations reduced to one of the two equations (3.17) or (3.18) according to the following conditions:-

For  $\bar{\theta}_A \leq \text{zero}$  (e.g. figs. 3.14 & 3.15) use (3.17)

For  $\bar{\theta}_A > \text{zero}$  (clockwise) and  $(\rho_S - \theta_S) \geq (\mu - \frac{\pi}{2} + \frac{\bar{\theta}_A}{2})$

If  $(\frac{\pi}{2} - \delta + \sigma - \mu - \frac{\bar{\theta}_A}{2}) \geq \text{zero}$  use (3.17)

otherwise use (3.18)

For  $\bar{\theta}_A > \text{zero}$  (clockwise) and  $(\rho_S - \theta_S) < (\mu - \frac{\pi}{2} + \frac{\bar{\theta}_A}{2})$

If  $(\frac{3\pi}{2} - \delta - \sigma - \mu - \frac{\bar{\theta}_A}{2}) \geq \text{zero}$  use (3.17)

otherwise use (3.18)

These apparently cumbersome conditions are trivially implemented in the computer model of course. It should also be pointed out that certain safeguards must be built into the model. For example, if the mean

rotation of the As-U-Rolls ( $\bar{\theta}_A$ ) was zero, then the quantity  $L_{Y_o Y}$  in the derivation of (3.14) would be zero (see figure 3.14). This would give an indeterminate result in the following equation for  $\mu$ . Therefore the condition  $\bar{\theta}_A=0$  must be trapped, and  $\mu$  set explicitly to a default value, which turns out to be  $\frac{\pi}{2} - \phi_S$ . Other similar situations are also trapped in this way.

The derivation of  $L_{CD}$  follows identical lines to that of  $L_{AB}$ .

$L_{C_o D_o}$  is given by (3.5) due to the symmetry of the datum position.

$\delta$  is given by (3.10)

$L_{DD_o}$  is given by (3.12)

$L_{CC_o}$  is given by the appropriate equation for  $L_{BB_o}$  since  $L_{CD}$  and  $L_{AB}$  are identically affected by As-U-Roll and Screwdown motion

$L_{D_o C}$  is given by (3.14), (3.15) or (3.16) as appropriate, for the same reason.

Then

$$\rho = \cos^{-1} \left[ \frac{L_{C_o D_o}^2 + L_{D_o C}^2 - L_{CC_o}^2}{2L_{C_o D_o} \cdot L_{D_o C}} \right]$$

and

$$L_{CD} = \sqrt{L_{DD_o}^2 + L_{D_o C}^2 - 2L_{DD_o} \cdot L_{D_o C} \sin\left(\frac{\theta_{PR}}{2} - \phi_p - \delta + \rho\right)}$$

.....(3.19)

or

$$L_{CD} = \sqrt{L_{DD_o}^2 + L_{D_o C}^2 - 2L_{DD_o} \cdot L_{D_o C} \sin\left(\frac{\theta_{PR}}{2} - \phi_p - \delta - \rho\right)}$$

.....(3.20)

as appropriate - using the same conditions as were used for deciding between (3.17) and (3.18).

The cluster geometry is fixed by the parameters shown in figure 3.2, and the only outstanding parameter is now the angle  $\gamma$ . This is also indicated in figure 3.15, whence from triangle  $AA_oB$

$$\epsilon = \cos^{-1} \left[ \frac{L_{AA_o}^2 + L_{AB}^2 - L_{A_oB}^2}{2L_{AA_o} L_{AB}} \right]$$

where

$L_{AA_o}$  is given by (3.9)

$L_{AB}$  is given by (3.17) or (3.18) as appropriate.

$L_{A_oB}$  is given by (3.14), (3.15) or (3.16) as appropriate

Thus 
$$\gamma = \frac{\pi}{2} - \phi_p + \frac{\theta_{PL}}{2} - \epsilon \dots\dots\dots(3.21)$$

The geometry-fixing parameters illustrated in figure 3.2 have now been completely specified for any combination of eccentric actuator settings as follows:-

$L_{BC}$  is given by (3.8)

$L_{AD}$  is given by (3.13)

$L_{AB}$  is given by (3.17) or (3.18) as appropriate

$L_{CD}$  is given by (3.19) or (3.20) as appropriate

$\gamma$  is given by (3.21).

### 3.3 Modelling of Roll Force Distribution in the Cluster

Considering still the upper half of the cluster, we shall now use the five cluster-fixing parameters derived in the previous section, together with knowledge of the roll diameter, to specify the various angles shown in figure 3.16. The distribution of rolling load will then be evaluated by resolution of forces. Note that roll-flattening effects are not included at this stage, as their influence upon the cluster angles is negligible.

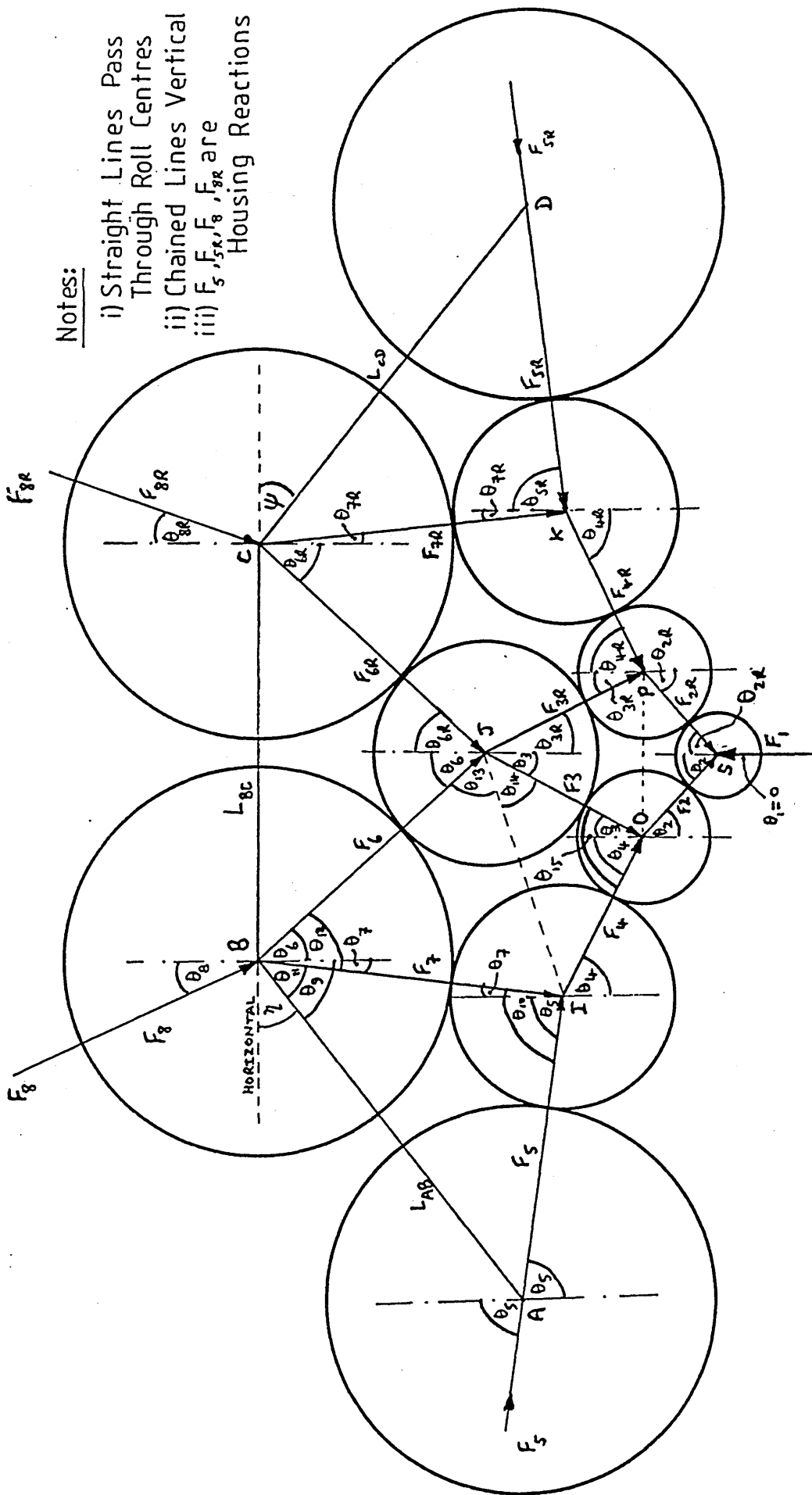
It should be noted at the outset that if the left and right hand side eccentrics are set differently, then  $L_{AB}$  and  $L_{CD}$  in figures 3.2 and 3.16 will be of different lengths, and  $L_{BC}$  and  $L_{AD}$  will not be parallel. The angles in the left-hand and right-hand halves of the cluster will therefore differ and must be calculated separately. The angles will be distinguished by adding a subscript "R" to those in the right-hand half. The angles of importance are  $\theta_1$  to  $\theta_8$  in figure 3.16, the other angles being intermediate values in the flow of calculation.

Since  $L_{BC}$  remains horizontal at all times, the cosine rule in triangle BCJ yields  $\theta_6$  and  $\theta_{6R}$  directly as

$$\theta_6 = \theta_{6R} = \frac{1}{2} \cos^{-1} \left[ 1 - \frac{2L_{BC}^2}{(D_B + D_{2I})^2} \right] \dots (3.22)$$

(where  $D_B$  and  $D_{2I}$  are the diameters of rolls (A-D) and J respectively

$$\begin{aligned} \text{now } \theta_9 &= \frac{\pi}{2} - \gamma \\ \text{and } \theta_{10} &= \cos^{-1} \left[ 1 - \frac{2L_{AB}^2}{(D_B + D_{2D})^2} \right] \end{aligned}$$



Notes:

- i) Straight Lines Pass Through Roll Centres
- ii) Chained Lines Vertical
- iii)  $F_5, F_6, F_7, F_8$  are Housing Reactions

Fig.3.16 Distribution of Rolling Load Through Roll Stack

and since triangle ABI is isosceles,

$$\theta_{11} = \frac{\pi - \theta_{10}}{2}$$

so that  $\theta_7$  is given by

$$\theta_7 = \theta_9 - \theta_{11} \dots \dots \dots (3.23)$$

and

$$\theta_5 = \theta_{10} - \theta_7 \dots \dots \dots (3.24)$$

Further, it is evident that

$$\theta_{12} = \theta_6 + \theta_7$$

And from triangle IBJ,

$$L_{IJ} = \frac{1}{2} \sqrt{(D_B + D_{2D})^2 + (D_B + D_{2I})^2 - 2(D_B + D_{2D})(D_B + D_{2I}) \cos \theta_{12}}$$

(where  $D_{2D}$  is the diameter of rolls I and K)

$$\text{and } \theta_{13} = \sin^{-1} \left[ \frac{(D_B + D_{2D}) \sin \theta_{12}}{2L_{IJ}} \right]$$

Now from triangle IJO

$$\theta_{14} = \cos^{-1} \left[ \frac{4L_{IJ}^2 + (D_{2I} + D_1)^2 - (D_{2D} + D_1)^2}{4L_{IJ}(D_{2I} + D_1)} \right]$$

(where  $D_1$  is the diameter of rolls O and P)

Therefore we can now obtain  $\theta_3$  as

$$\theta_3 = \pi - \theta_6 - \theta_{13} - \theta_{14} \dots \dots \dots (3.25)$$

Also from triangle IJO,

$$\theta_{15} = \cos^{-1} \left[ \frac{(D_{2I} + D_1)^2 + (D_{2D} + D_1)^2 - 4L_{IJ}^2}{2(D_{2I} + D_1)(D_{2D} + D_1)} \right]$$

$$\text{and } \theta_4 = \theta_{15} - \theta_3 \dots \dots \dots (3.26)$$

Insufficient information is so far available to allow calculation of  $\theta_2$ , because J is not necessarily vertically above S, therefore the triangle OJS does not contain the simple angles  $\theta_3$  and  $\theta_2$ . We therefore firstly calculate the angles in the right-hand half of the cluster which correspond to the left-half angles calculated so far:-

Initially, calculate the angle  $\psi$  which appears in figure 3.2 and 3.16, and corresponds with the left-half angle  $\eta$  (it will be easier to refer to figure 3.2 for this purpose).

Applying the cosine rule in triangle ABC, we can find

$$L_{AC} = \sqrt{L_{AB}^2 + L_{BC}^2 + 2L_{AB} \cdot L_{BC} \cdot \cos \eta}$$

(where the parameters on the right of the equation are evaluated in section 3.2).

The sine rule then gives

$$\hat{BCA} = \sin^{-1} \left[ \frac{L_{AB} \sin \eta}{L_{AC}} \right]$$

The cosine rule in triangle ACD then gives us

$$\hat{ACD} = \cos^{-1} \left[ \frac{L_{AC}^2 + L_{CD}^2 - L_{AD}^2}{2L_{AC} \cdot L_{CD}} \right]$$

$$\text{and then } \psi = \pi - \hat{BCA} - \hat{ACD}$$

Starting from the equation following (3.22) and replacing  $\eta$  by  $\psi$ , we now calculate  $\theta_{9R}$ ,  $\theta_{10R}$ ,  $\theta_{11R}$ ,  $\theta_{7R}$ ,  $\theta_{5R}$ ,  $\theta_{12R}$ ,  $\theta_{13R}$ ,  $\theta_{14R}$ ,  $\theta_{3R}$ ,  $\theta_{15R}$ , and  $\theta_{4R}$  using the same equations as before.

Now referring again to figure 3.16, from the isosceles

triangle OPJ we obtain  $L_{OP} = (D_{2I} + D_1) \sin \frac{(\theta_3 + \theta_{3R})}{2}$

and similarly, from triangle OPS,

$$L_{OP} = (D_1 + D_w) \sin \frac{(\theta_2 + \theta_{2R})}{2}$$

(where  $D_w$  = diameter of roll S)

so that we can write

$$\theta_2 = 2 \sin^{-1} \left[ \frac{L_{OP}}{D_1 + D_w} \right] - \theta_{2R} \dots \dots \dots (3.27)$$

Also, the vertical separation of J and S can be calculated twice over (using the left-side and right-side angles)

and equated, giving

$$\theta_{2R} = \cos^{-1} \left[ \cos \theta_2 + \frac{(D_{2I} + D_1)(\cos \theta_3 - \cos \theta_{3R})}{D_1 + D_w} \right] \dots (3.28)$$

Equations (3.27) and (3.28) are then solved simultaneously to obtain  $\theta_2$  and  $\theta_{2R}$  as

$$\theta_2 = 2 \tan^{-1} \left[ \frac{\sin x - \sqrt{4 \sin^2 \frac{x}{2} - y^2}}{y - 2 \sin^2 \frac{x}{2}} \right] \dots \dots \dots (3.29)$$

where  $x = 2 \sin^{-1} \left[ \frac{L_{OP}}{D_1 + D_w} \right]$

$$y = \frac{(D_{2I} + D_1)(\cos \theta_3 - \cos \theta_{3R})}{D_1 + D_w}$$

and from (3.28)

$$\theta_{2R} = \cos^{-1} (\cos \theta_2 + y) \dots \dots \dots (3.30)$$

Equations (3.22) to (3.26) and (3.29) and (3.30) have therefore specified the angles which most of the component of rolling load (shown in fig.3.16) make with the vertical. The exceptions are  $\theta_8$  and  $\theta_{8R}$  which cannot

yet be found, and  $\theta_1$  which is zero at all times since the rolling load is assumed for the present to act vertically through the workroll.

The distribution of rolling load throughout the cluster can now be specified. The force components  $F_1$  to  $F_8$  and  $F_{1R}$  to  $F_{8R}$  in figure 3.16 represent fractions of the total rolling load transferred between the various rolls as indicated. Let  $P_T$  represent the total rolling load transferred between the strip and the upper workroll, thus

$$F_1 = 1.0 P_T \quad \dots \dots \dots (3.31)$$

Vertical and horizontal resolution of forces at roll S (fig. 3.16) assuming equilibrium to exist, gives

$$F_1 = F_2 \cos \theta_2 + F_{2R} \cos \theta_{2R}$$

and  $F_2 \sin \theta_2 = F_{2R} \sin \theta_{2R}$

which, when solved simultaneously, and incorporating (3.31), gives

$$F_{2R} = \frac{\sin \theta_2}{\sin(\theta_2 + \theta_{2R})} \cdot P_T \quad \dots \dots \dots (3.32)$$

and  $F_2 = \frac{F_{2R} \cdot \sin \theta_{2R}}{\sin \theta_2} \quad \dots \dots \dots (3.33)$

Regarding the quantities  $F_3$  and  $F_4$  as balancing  $F_2$  at roll O, we can similarly solve for  $F_3$  and  $F_4$  by resolving in the direction of  $F_2$  and perpendicular to  $F_2$ , when we obtain

$$F_3 = \frac{F_2 \sin(\theta_4 - \theta_2)}{\sin(\theta_3 + \theta_4)} \quad \dots \dots \dots (3.34)$$

and 
$$F_4 = \frac{F_3 \sin(\theta_3 + \theta_2)}{\sin(\theta_4 - \theta_2)} \dots \dots \dots (3.35)$$

$F_{3R}$  and  $F_{4R}$  are found using  $F_{2R}$ ,  $\theta_{2R}$ ,  $\theta_{3R}$  and  $\theta_{4R}$  in the same equations.

In a similar manner, considering equilibrium at roll I, we obtain

$$F_7 = \frac{F_4 \sin(\theta_5 - \theta_4)}{\sin(\theta_5 + \theta_7)} \dots \dots \dots (3.36)$$

and 
$$F_5 = \frac{F_7 \sin(\theta_7 + \theta_4)}{\sin(\theta_5 - \theta_4)} \dots \dots \dots (3.37)$$

(The same equations will yield  $F_{7R}$  and  $F_{5R}$  as above).

Now consider roll J. It is known that  $\theta_6 = \theta_{6R}$  from previous discussion, therefore sufficient information is available to obtain  $F_6$  and  $F_{6R}$  by horizontal and vertical resolution as:

$$F_6 = \frac{F_3 \sin(\theta_6 - \theta_3) + F_{3R} \sin(\theta_6 + \theta_{3R})}{\sin 2\theta_6} \dots \dots (3.38)$$

and 
$$F_{6R} = F_6 + \frac{F_3 \sin \theta_3 - F_{3R} \sin \theta_{3R}}{\sin \theta_6} \dots \dots \dots (3.39)$$

The remaining unknown angles  $\theta_8$  and  $\theta_{8R}$  can now be found. At roll B, resolving perpendicular to  $F_8$  gives

$$F_7 \sin(\theta_7 + \theta_8) = F_6 \sin(\theta_6 - \theta_8)$$

leading to

$$\theta_8 = \tan^{-1} \left[ \frac{F_6 \sin \theta_6 - F_7 \sin \theta_7}{F_7 \cos \theta_7 + F_6 \cos \theta_6} \right] \dots \dots \dots (3.40)$$

and solution in the direction of  $F_8$  gives

$$F_8 = F_6 \cos(\theta_6 - \theta_8) + F_7 \cos(\theta_7 + \theta_8) \dots (3.41)$$

$\theta_{8R}$  and  $F_{8R}$  are of course obtainable by using  $F_{6R}$ ,  $F_{7R}$ ,  $\theta_{6R}$  and  $\theta_{7R}$  in the above equations. The reader may, if he so wishes, verify that the overall effect of reactions from the mill housing balances the rolling load i.e.

$$F_5 \cos \theta_5 + F_8 \cos \theta_8 + F_{8R} \cos \theta_{8R} + F_{5R} \cos \theta_{5R} = P_T$$

The various equations in this section therefore completely specify the geometry and overall load distribution pattern in the upper half of the mill cluster as shown in figure 3.16. A set of results is given below for screwdown rack at 8 operator's display units, left and right hand side eccentrics at 5 and 7 units respectively and mean As-U-Roll rack position at +1 unit.

$\theta_1 = 0$		$F_1 = P_T$	
$\theta_2 = 37.5^\circ$	$\theta_{2R} = 38.3^\circ$	$F_2 = 0.639P_T$	$F_{2R} = 0.628P_T$
$\theta_3 = 22.4^\circ$	$\theta_{3R} = 21.7^\circ$	$F_3 = 0.241P_T$	$F_{3R} = 0.228P_T$
$\theta_4 = 59.5^\circ$	$\theta_{4R} = 59.2^\circ$	$F_4 = 0.558P_T$	$F_{4R} = 0.551P_T$
$\theta_5 = 77.8^\circ$	$\theta_{5R} = 77.7^\circ$	$F_5 = 0.504P_T$	$F_{5R} = 0.495P_T$
$\theta_6 = 40.9^\circ$	$\theta_{6R} = 40.9^\circ$	$F_6 = 0.282P_T$	$F_{6R} = 0.294P_T$
$\theta_7 = 3.8^\circ$	$\theta_{7R} = 3.4^\circ$	$F_7 = 0.177P_T$	$F_{7R} = 0.176P_T$
$\theta_8 = 23.9^\circ$	$\theta_{8R} = 24.6^\circ$	$F_8 = 0.426P_T$	$F_{8R} = 0.438P_T$

Similar results are easily obtained for the lower half of the mill cluster by substituting the push-up rack position for the screwdown rack position, setting  $\bar{\theta}_A = \text{zero}$  (no As-U-Rolls in lower half) and applying the analysis from equation (3.5)ff.

Although this section has defined the overall pattern of load distribution, it is of course necessary to examine the way in which the load varies across the mill for shape control purpose. This is considered in a later section.

### 3.4 Rolling Load and Roll Flattening Calculations

In order to quantify the forces discussed in the previous section it is now necessary to obtain knowledge of the rolling load ( $P_T$ ). On a four-high mill, this can be had from loadcells placed between the mill screws and backup roll chocks. In the Sendzimir mill it would be difficult (not to mention extremely costly) to obtain a direct measurement of rolling load, and only an indirect indication is available. This takes the form of indication of the differential pressure in the hydraulic screwdown cylinders. From knowledge of the cylinder dimensions, this can be converted to rack-pull in some convenient units (e.g. MN). The mill manufacturers then provide a rule-of-thumb conversion from rack-pull to rolling load. Accurate measurement of rolling load is therefore unavailable.

The measurement of rolling load is not however necessary for operation of the on-line control scheme, but only for use in the static mill model (which is run off-line). The value of rolling load used in the static model is calculated using a rolling load model, and can be represented in functional form as

$$P_T = f(w, h_i, h_o, T_i, T_o, k, \mu, E, \nu, R)$$

(where the various symbols are defined at the beginning of the chapter).

The drawback is that since no accurate measure of mill rolling load is available, it is not easy to assess the accuracy of the value of  $P_T$  thus calculated. For this reason, steps have been taken to allow the use of a rolling load model which is well tested, but which has often been rejected in the past, for models requiring rapid execution, on the grounds of computational difficulties.

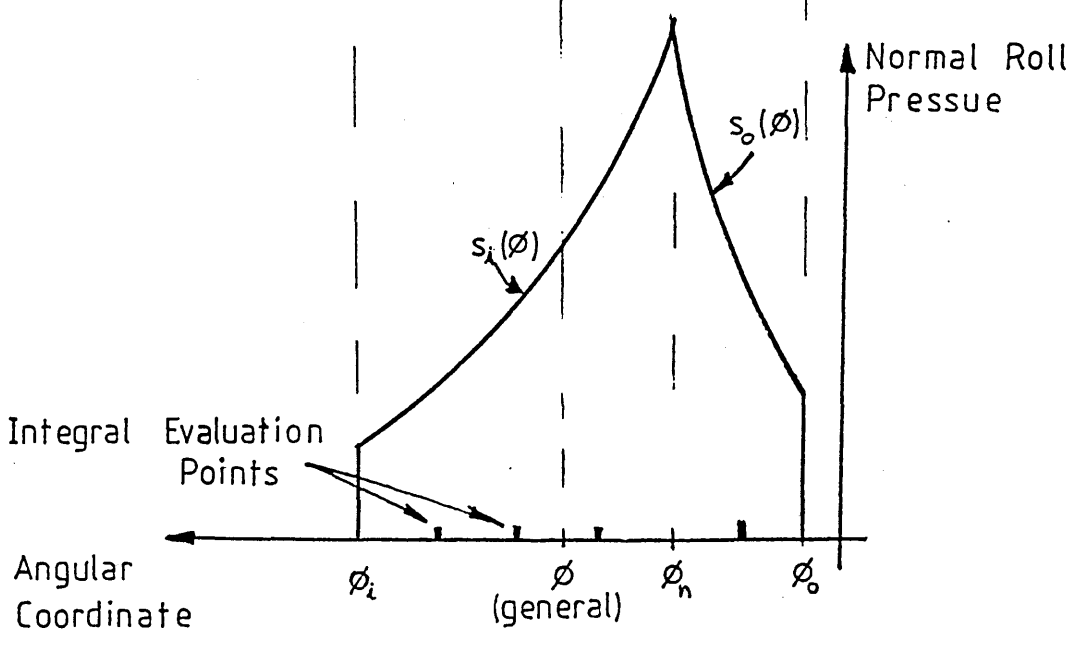
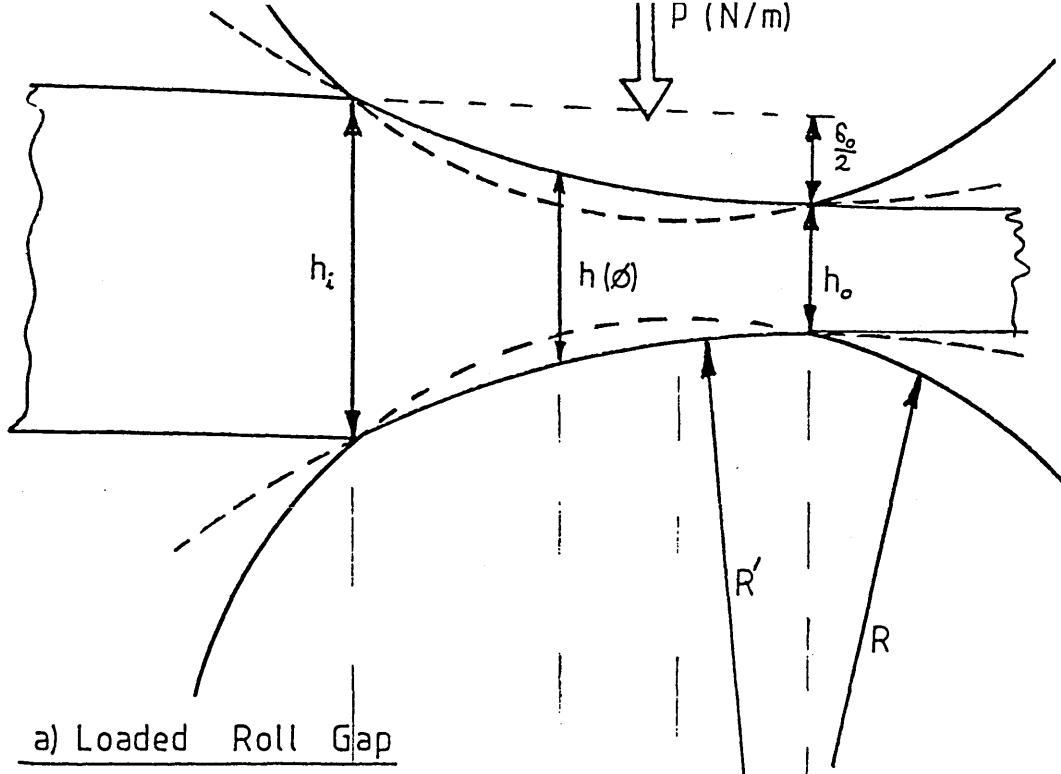
The "yardstick" as it were, by which the accuracy of cold rolling models has traditionally been judged, is the work of Orowan (22), although this work itself is not suitable for efficient computer mechanization. The work of Orowan set this standard of accuracy by removing arbitrary simplifications imposed by previous models. Due to the need for more rapidly evaluated models, various workers have simplified the theory by judicious re-incorporation of some of the simplifying factors, made possible by the understanding of Orowan's work. Typical examples are given in (23) to (27), but the most widely accepted of these from an accuracy point of view is probably the theory of Bland and Ford (23). Unfortunately Bland and Ford's model involves iterative solution of implicit simultaneous equations; which renders it, at first sight, unsuitable for use in models (such as the present static model - see later sections) requiring

several rolling load evaluations. To overcome this difficulty, Bryant and Osborn (26) have proposed an explicit solution by introducing further simplifications and Carlton, Edwards and Thomas (28) have subsequently extended this work. Despite the simplifications, the model of Bryant and Osborn compares acceptably with the more accurate models under certain conditions, and has been used by other workers in the area under discussion(14).

The author has removed some of the objections to the use of Bland and Fords' model (in a mill off-line static model) by the use of a fast, but little known, algorithm for solution of the equations. (Note that for applications requiring on-line calculation of rolling load, such as mill scheduling and automatic set up systems, this method would probably still not be fast enough under stringent timing constraints). The algorithm involves the use of a modification to the secant method, which can have a greatly beneficial effect upon the solution time under certain conditions - in the case of this static model, convergence to within 0.5% is achieved after typically only two iterations through the process outlined below.

Bland and Ford's model assumes that the arc of contact remains circular during rolling, as depicted in figure 3.17. The deformed roll radius is given by Hitchcock (29) as

$$R' = R \left( 1 + \frac{cP'}{\delta_o} \right) \quad (m) \quad \dots \dots \dots (3.42)$$



b) Normal Roll Pressure Curve

Fig. 3-17

where  $c \triangleq \frac{16(1-\nu^2)}{\pi E}$

Figure 3.17 shows the loaded roll gap as envisaged by Bland and Ford, where  $\phi$  is a general angle subtended at the roll centre by the exit plane and some plane of interest. A function  $H(\phi)$  is defined

$$H \triangleq 2 \cdot \sqrt{\frac{R'}{h_0}} \cdot \tan^{-1} \sqrt{\frac{R'}{h_0}} \cdot \phi \dots \dots \dots (3.43)$$

The value ( $H_n$ ) of  $H$  at the neutral angle (where slip of strip against rolls is zero) is given explicitly from a different formula, after which the position of the neutral angle is found from

$$\phi_n = \sqrt{\frac{h_0}{R'}} \cdot \tan \left[ \sqrt{\frac{h_0}{R'}} \cdot \frac{H_n}{2} \right]$$

Figure 3.17 also depicts the pressure distribution throughout the roll gap and according to Bland and Ford the normal roll pressure to the exit side of the neutral plane is given by

$$s_o(\phi) = \frac{k(\phi) \cdot h(\phi)}{h_0} \cdot \left(1 - \frac{T'_o}{k_o}\right) \cdot e^{\mu H(\phi)} \dots \dots \dots (3.44a)$$

and to the entry side, by

$$s_i(\phi) = \frac{k(\phi) \cdot h(\phi)}{h_i} \cdot \left(1 - \frac{T'_i}{k_i}\right) \cdot e^{\mu(H_i - H(\phi))} \dots \dots \dots (3.44b)$$

where  $k(\phi)$ ,  $k_i$  and  $k_o$  are known from curves of yield stress against reduction,  $h(\phi)$  is easily found as  $h = h_0 + 2R'(1 - \cos\phi)$  and  $T'_i$  and  $T'_o$  are the input and exit tension stresses corresponding to the known tension values

$T_i$  and  $T_o$ . The values of  $H(\phi)$  are found from equation (3.43).

The specific rolling load is then found as a function of the area under the curve of figure 3.17(b).

Namely

$$P' = R' \left[ \int_0^{\phi_n} s_o(\phi) \cdot d\phi + \int_{\phi_n}^{\phi_i} s_i(\phi) \cdot d\phi \right] \dots \dots (3.45)$$

Equation (3.45) is solved by the author using a piecewise Simpson's rule integration procedure, taking one intermediate point midway between 0 and  $\phi_n$ , and three intermediate points in the interval  $\phi$  to 0 where greater accuracy is desirable. These points are indicated in fig. 3.17(b), and equations (3.44)(a) and (b) are used as appropriate to calculate the corresponding values of  $s_o$  or  $s_i$ .

Clearly, the magnitude of the value of  $P'$  given by (3.45), must be consistent with the value of  $P'$  used in (3.42) and an iterative procedure is therefore necessary. The system is solved by a fast modification of the secant method which is used to solve a rearranged version of equation 3.42, thus

$$f(R') = R(1 - \frac{cP'}{\delta_o}) - R' = 0 \quad (3.46)$$

The secant method (see for example (30), (31)) requires two starting values of the function. These must lie one at either side of the solution and are found by taking  $R' = 1.25R$  as an initial guess and using a forcing procedure to obtain via equations (3.45) and (3.46) two

values,  $f(R')_1$ , being positive and  $f(R')_2$  being negative.

The next estimate for  $R'$  is then found by using the

secant method, i.e.

$$R'_n = R'_{n-1} - \frac{f(R')_{n-1} (R'_{n-1} - R'_{n-2})}{f(R')_{n-1} - f(R')_{n-2}} \dots \dots (3.47)$$

equations (3.45) and (3.46) then give  $P'_n$  &  $f(R')_n$

If  $|R'_n - R'_{n-1}| < \epsilon \cdot R'_{n-2}$  (where  $\epsilon$  = convergence limit)

then  $P'_n$  is taken as the solution. Otherwise, the

parameters are updated according to the modification to

the secant method as follows;

If  $f(R')_n$  and  $f(R')_{n-1}$  are of opposite sign

then

$$R'_{n-2(\text{new})} = R'_{n-1}$$

$$f(R')_{n-2(\text{new})} = f(R')_{n-1}$$

otherwise

$$f(R')_{n-2(\text{new})} = \frac{f(R')_{n-2} f(R')_{n-1}}{f(R')_{n-1} + f(R')_n}$$

and  $R'_{n-2}$  remains unchanged.

In either case,  $R'_{n-1(\text{new})} = R'_n$

$$f(R')_{n-1(\text{new})} = f(R')_n$$

and the procedure is repeated from equation (3.47).

When convergence is achieved, the final values are taken to be

$$R' = R'_n$$

$$P' = P'_n$$

so that total rolling load is given by

$$P_T = P'.w \quad (N) \quad \dots \dots \dots (3.48)$$

The magnitudes of the various rolling load components given by equations (3.31) to (3.41) may now be calculated by substitution of (3.48) into (3.31) to (3.41).

Now, for purposes of calculating the roll bending in the mill cluster due to movements of the control actuators, the rolls are each treated as a beam resting on an elastic foundation formed by the surrounding rolls. Although this analysis is covered in a later section, it is convenient to introduce it here.

The theory used is Hetenyi's theory of beams on elastic foundations, which is given in reference (32). Since the roll bending model cannot be understood without knowledge of this theory, it has been considered prudent to include the basic derivations and results in Appendix 1 of this thesis. The calculation of deflection of a beam on an elastic foundation cannot proceed without a knowledge of the "foundation modulus" (see section A1.1). The magnitude of the foundation modulus is dependent upon rolling load as will be seen from its derivation given in Appendix 2. Therefore, having a knowledge of the distributed loading acting upon any given pair of rolls (from the load components calculated

above, acting on a width equal to the strip width) the methods of Appendix 2 can now be used to give the roll flattening between any pair of touching rolls, and the appropriate foundation modulus also.

### 3.5 Philosophy of Roll Stack Deflection Model

The foregoing sections have fixed, in terms of the actuator settings, the basic roll stack geometry (section 3.2), the distribution of rolling load throughout the cluster (section 3.3) and the magnitude of the mean loading at each roll interface (section 3.4). In addition, the methods of Appendix 2 have given values of roll flattening and the foundation modulus (required by Hetenyi's theory of beams on elastic foundations) for each interface. The following sections give details of how this information is used to predict the transverse workroll profile (and hence strip shape) due to any combination of the mill actuator settings.

In an attempt to achieve relatively simple calculations and fast computation times, certain simplifying assumptions have been made, and these are stated as they occur, together with justifications. At this stage, it is helpful to consider an overall flowchart of the roll deflection model, which is given in figure 3.18. The results of the actuator modelling will be used in section 3.6 to give the magnitude and distribution of the loading acting upon roll J (fig.3.16) due to movement of the eight As-U-Roll actuators in any specified manner. A major assumption is then made, in that the effects of

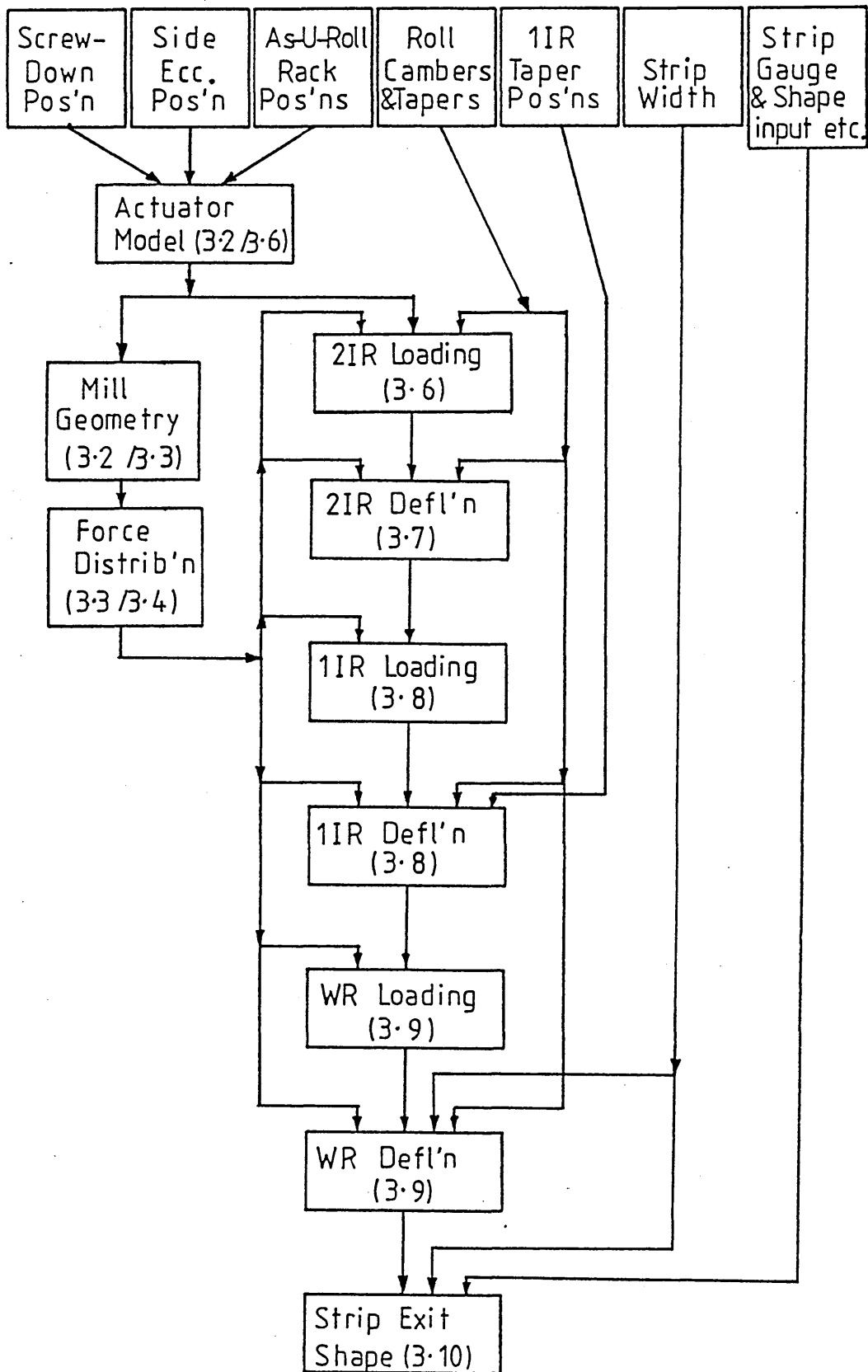


Fig.3.18 Fundamental Flow of Deflection Calculations

control actuator movements for purposes of shape correction, whilst causing differential loadings across the mill of sufficient magnitude to cause the desired roll bending, do not make a significant change to the total rolling load. This assumption is numerically substantiated later, and has two major advantages so far as complexity and speed of calculation in the model are concerned.

Firstly, it removes the need to iterate several times around each roll interface due to the local feedback mechanism between roll force and roll bending and flattening. Secondly, it becomes possible to assume that any feasible path between the As-U-Rolls and the roll gap can be used for calculation without reference to the other rolls in the cluster, due to the fact that the iterations around the entire roll stack (which would otherwise have been necessary) are obviated. Thus, the only path considered in this analysis is from the As-U-Rolls to roll B (fig. 3.16), then to roll J and then O and finally to the workroll, S. The deviations of the lines of action of the various forces from the vertical (the angles  $\theta$  in fig.3.16) are allowed for in the analysis.

Having calculated the loading on roll B, the theory of beams on elastic foundations is used to obtain the resulting deflection profile of roll J, which is modified by any camber existing on roll J (section 3.7 and Appendix 4). The profile is then converted into a loading pattern acting upon the first intermediate roll O (section 3.8) modified by any camber on roll O, and by

the amount of first intermediate roll tapers slid into the mill. This process is continued until a workroll deflection is obtained (when strip width is taken into account)(section 3.9). Finally, section 3.10 combines known input strip dimensions with the calculated workroll deflection profile to yield strip shape.

### 3.6 Calculation of the Loading Pattern on the Upper Central Second Intermediate Roll

We now consider a set of As-U-Roll actuator movements and define the manner in which it affects the roll J in figure 3.16. The starting point of this analysis is the distance by which displacement of the As-U-Roll rack at any given backing saddle moves the backing shaft radially relative to the central second intermediate roll (abbreviated to 2IR in future). The sense of this displacement is indicated in figure 3.19, and more detail is shown in figure 3.20. Note the assumption in figure 3.20 that for this purpose point V, is effectively fixed on the circumference of roll B. This is justified on the grounds that the As-U-Roll motion only is being considered, and the maximum value of  $L_{B_1B}$  due to full scale As-U-Roll travel has been calculated to be of the order of 0.7mm, which is much more than will ever occur in practice. This is then greatly attenuated at point V due both to the fact that  $R_B$  is typically almost twice  $R_{2I}$ , and the fact that the angle  $\widehat{VBB_1}$  is very obtuse in any case.

The length  $L_{BC}$  is given by equation (3.8), and it can be seen that

$$\theta_C = \cos^{-1} \left[ \frac{L_{BC}}{2(R_B + R_{2I})} \right]$$



Now, in figure 3.20, only As-U-Roll motion is involved in moving point  $B_1$  to point B. Therefore  $B_1 Y_O YB$  is a parallelogram so that

$$L_{B_1 B} = L_{Y_O Y} = 2e_A \sin \frac{|\theta_A|}{2}$$

and  $\widehat{Y_O YU} = \widehat{B_1 B U_1}$

where  $B_1 \equiv$  centre of shaft B at the saddle in question, considering screwdown motion only

and  $B \equiv B_1$  plus As-U-Roll motion

The cosine rule in triangle  $B_1 VB$  then gives

$$L_{B_1 V} = \sqrt{R_B^2 + L_{B_1 B}^2 + 2R_B L_{B_1 B} \sin \left[ \frac{|\theta_A|}{2} + \theta_C \right]} \dots (3.49)$$

Rearrangement of figure 3.20 will show that equation (3.49) is also correct for values of  $\theta_A$  and  $\theta_S$  such that B falls above the line  $B_1 V$ . However, for the case  $\theta_A$  rotating clockwise, thus taking BY above  $B_1 Y_C$ , it is necessary to use

$$L_{B_1 V} = \sqrt{R_B^2 + L_{B_1 B}^2 + 2R_B L_{B_1 B} \sin \left[ \frac{|\theta_A|}{2} - \theta_C \right]} \dots (3.50)$$

Finally, the motion of the shaft B along BV (i.e. towards the centre of the 2IR) is given, to a very good approximation, by

$$a_{BV} = L_{B_1 V} - R_B \dots (3.51)$$

where  $a_{BV}$  will be called the "attempted motion" towards the 2IR, and is considered positive for motion of B towards

the centre of roll J,  $L_{B_1V}$  being given by (3.49) or (3.50) as appropriate.

This value  $a_{BV}$  is calculated for the As-U-Roll motion at each of the eight As-U-Roll positions, thus giving a set of 8 such values. Note that the set need only contain one value per As-U-Roll rack, as shafts B and C always move by an identical amount. These displacements  $a_{BV}$  are, however, restricted by the rolling load pushing up through the roll stack, and hence a loading profile results along the roll J.

Figure 3.21 illustrates the general situation at a backing bearing on shafts B or C where the As-U-Roll racks have been raised at each side of the bearing, but the front rack has been raised more than the rear. Together with figure 3.22 it shows how the As-U-Roll racks are used to place a bending profile onto the 2IRs. Note that fig. 3.22 has been chosen to illustrate seven out of the eight possible loading configurations which can exist at a backing bearing (the eighth being the case where racks N and N+1 are both moved upwards equally). The 2IR is assumed to be able to respond to the negative loadings (e.g. c and d in fig. 3.22) because of the upward-acting effect of the rolling load. I.e. since the motion of the As-U-Roll racks has caused bearings c and d to move away from the 2IR, the rolling load pushing upwards from below the 2IR will cause it to follow bearings c and d as if they had the capability of pulling it upwards. Returning now to fig. 3.21, we calculate the loading required in the following manner.

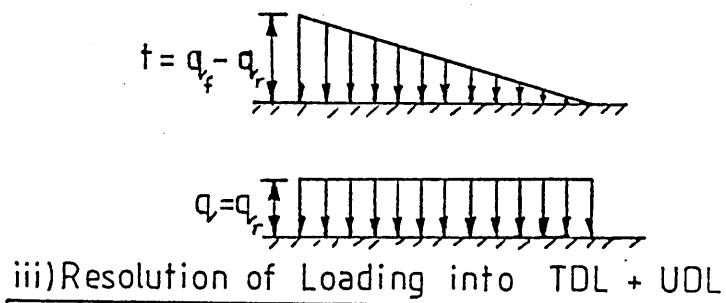
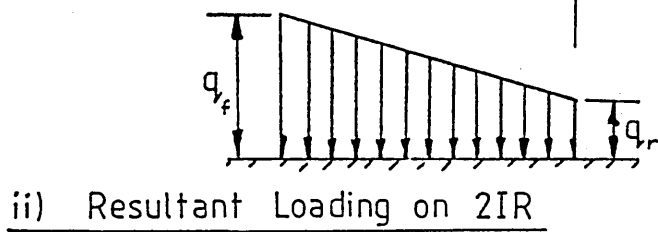
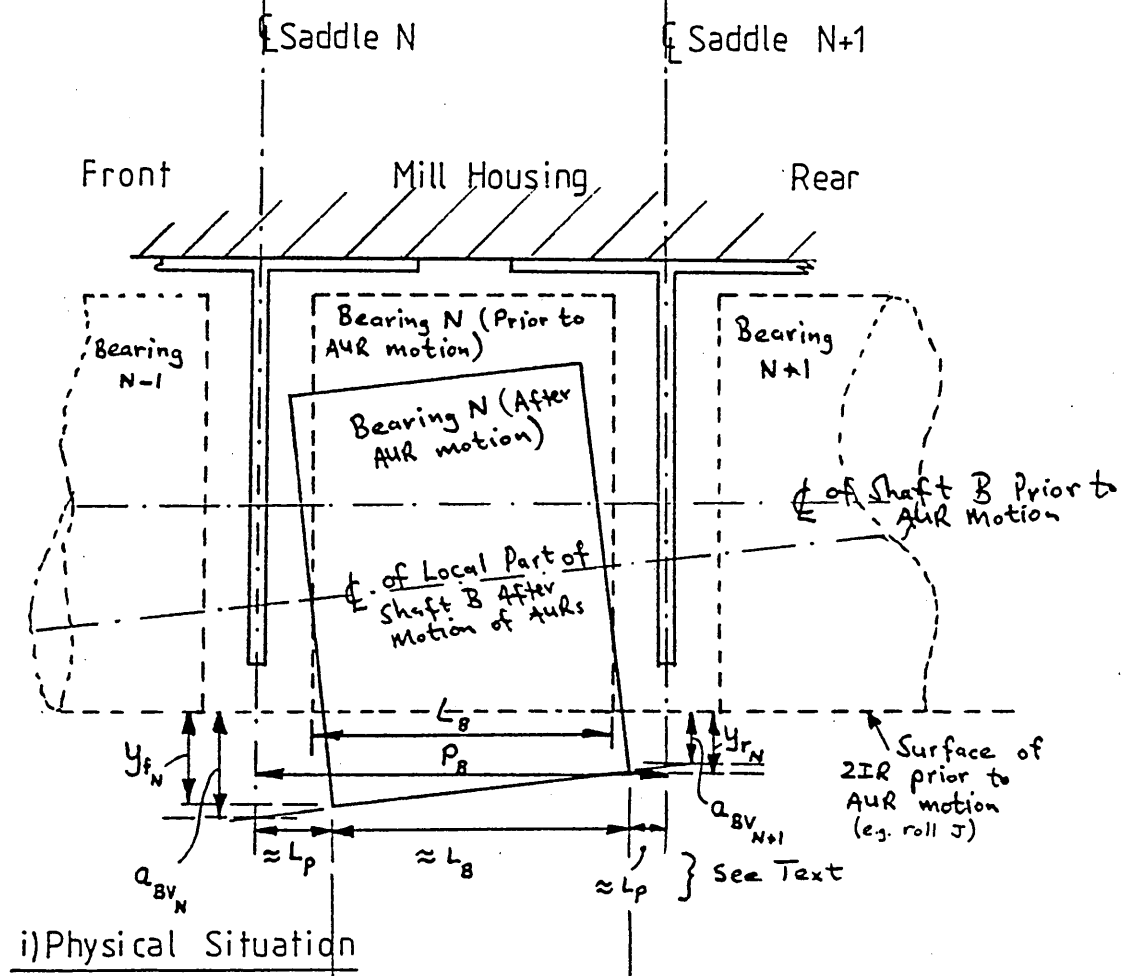
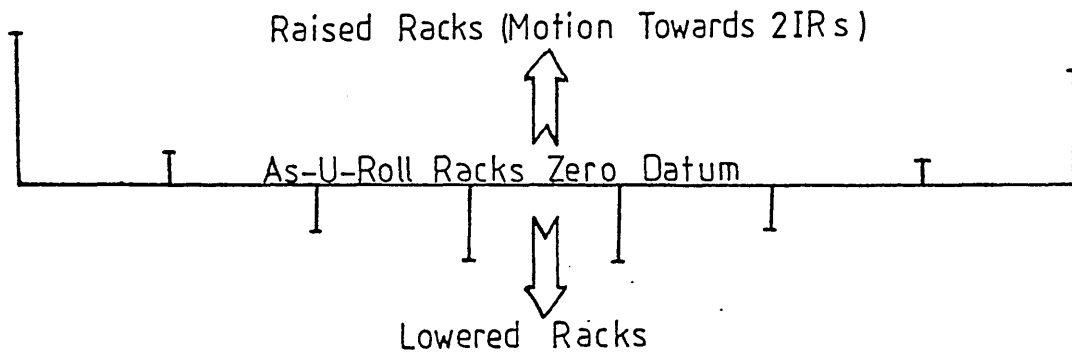
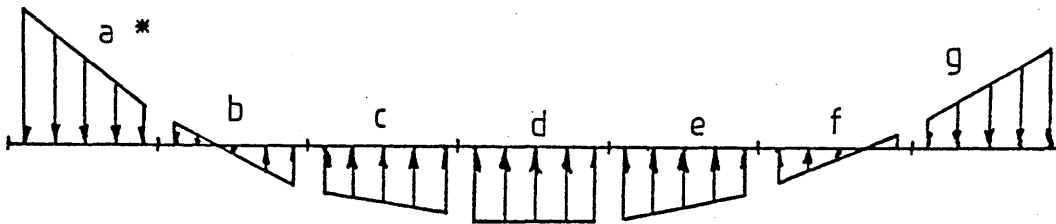


Fig.3-21 Positive Motion of Adjacent As-U-Roll Racks

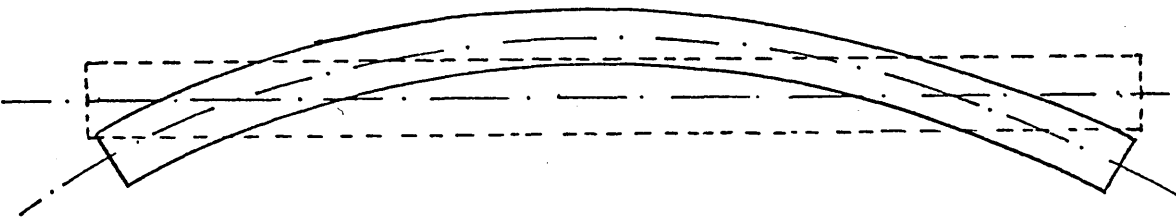


i) Rack Movements from Datum



("h" - not shown - is the inverse of "d")  
 \* "a" corresponds to fig. 3.21

ii) Loading on 2IR due to (i)



iii) Resultant Form of 2IR Bending

Fig. 3.22 Effect of a Complete Set of As-U-Roll Movements

The distance  $L_p$  between each edge of the backing bearing and the centre-line of the adjacent saddle is assumed to be equal at the front and rear of the bearing, and also to be independent of As-U-Roll motion (these assumptions are, for all practical purposes, entirely valid; bearing in mind the physical dimensions of the plant - a more rigorous analysis has been carried out, but was found to be completely unnecessary). Thus,

$$L_p \approx \frac{P_B - L_B}{2} \dots \dots \dots (3.52)$$

Also, it is easily shown from fig.3.21 (bearing in mind that the quantities  $a_{BV_N}$  and  $a_{BV_{N+1}}$  as shown are both positive) that

$$y_{f_N} = a_{BV_N} - \frac{L_p}{P_B} (a_{BV_N} - a_{BV_{N+1}}) \dots (3.53)$$

and

$$y_{r_N} = a_{BV_N} - \frac{L_p + L_B}{P_B} (a_{BV_N} - a_{BV_{N+1}}) \dots N=1, \dots J_B$$

where  $J_B$  = number of backing bearings.

It will be seen from fig. 3.22 (ii) that there are eight possible loading conditions for any given backing bearing (labelled "a" to "h" in the figure). Re-drawing of fig. 3.21 for each of these conditions shows that the pair of equations (3.53) need be re-written in only three forms to cover all eight cases, thus,

$$\left. \begin{aligned}
 y_{fN} &= a_{BV_N} - \frac{L_p}{P_B} \cdot |a_{BV_N} - a_{BV_{N+1}}| \\
 y_{rN} &= a_{BV_N} - \frac{L_p + L_B}{P_B} \cdot |a_{BV_N} - a_{BV_{N+1}}|
 \end{aligned} \right\} \begin{array}{l} \dots \dots (3.54) \\ N=1, \dots J_B \\ \text{cases "a", "c"} \\ \text{and "h"} \end{array}$$

$$\left. \begin{aligned}
 y_{fN} &= a_{BV_N} + \frac{L_p}{P_B} \cdot |a_{BV_N} - a_{BV_{N+1}}| \\
 y_{rN} &= a_{BV_N} + \frac{L_p + L_B}{P_B} \cdot |a_{BV_N} - a_{BV_{N+1}}|
 \end{aligned} \right\} \begin{array}{l} \dots \dots (3.55) \\ N=1, \dots J_B \\ \text{cases "d", "e"} \\ \text{and "g"} \end{array}$$

For cases b and f, two triangular loadings result as shown in fig. 3.23 (for case f). Here,

$$\left. \begin{aligned}
 y_{fN} &= \frac{L_f}{L_f + L_p} a_{BV_N} \\
 y_{rN} &= a_{BV_{N+1}} \left[ 1 - \frac{L_p}{P_B - L_p - L_f} \right]
 \end{aligned} \right\} \begin{array}{l} \dots \dots (3.56) \\ N=1, \dots J_B \\ \text{cases "b" and "f"} \end{array}$$

where  $L_f$  (see fig. 3.23) is given by

$$L_f = \frac{|a_{BV_N}| \cdot [P_B - L_p] - |a_{BV_N}| \cdot L_p}{|a_{BV_N}| + |a_{BV_{N+1}}|} \dots \dots (3.57)$$

(from similar-triangles' geometry)

The different cases are easily distinguished in the computer model by consideration of the relative signs and magnitudes of the appropriate pair of  $a_{BV}$  values. Note

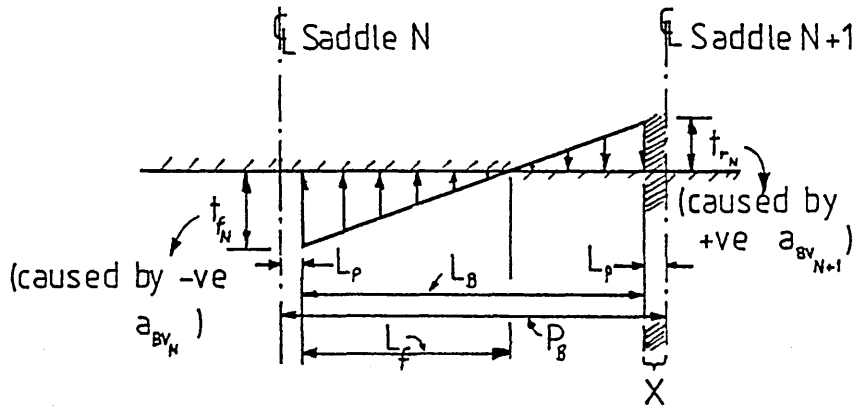


Fig.3.23 Loading due to Case "f" (in fig.3.22)

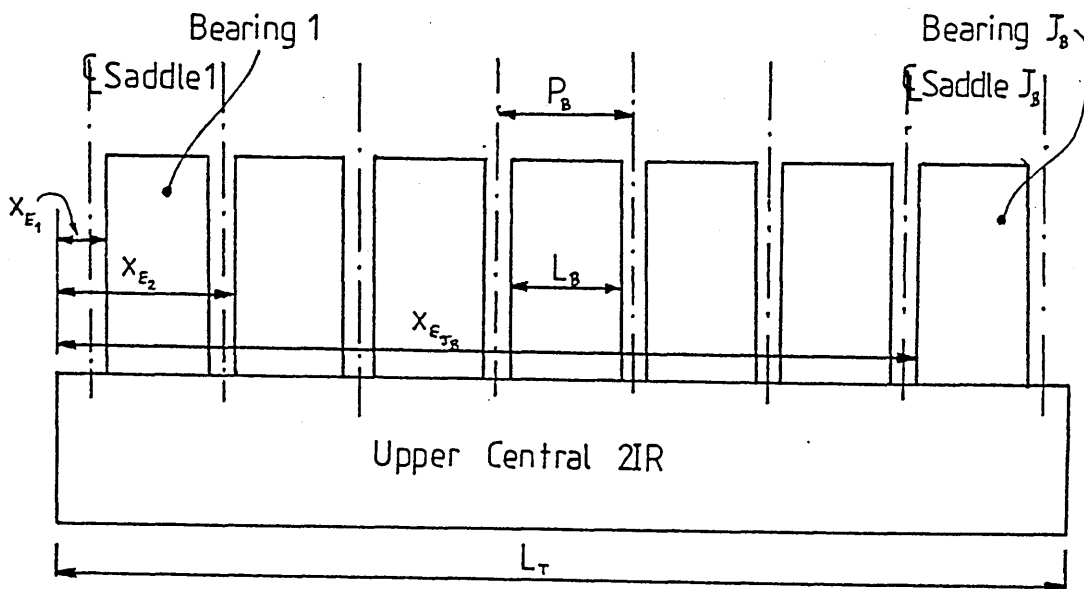


Fig.3.24 Backing Bearing Positions

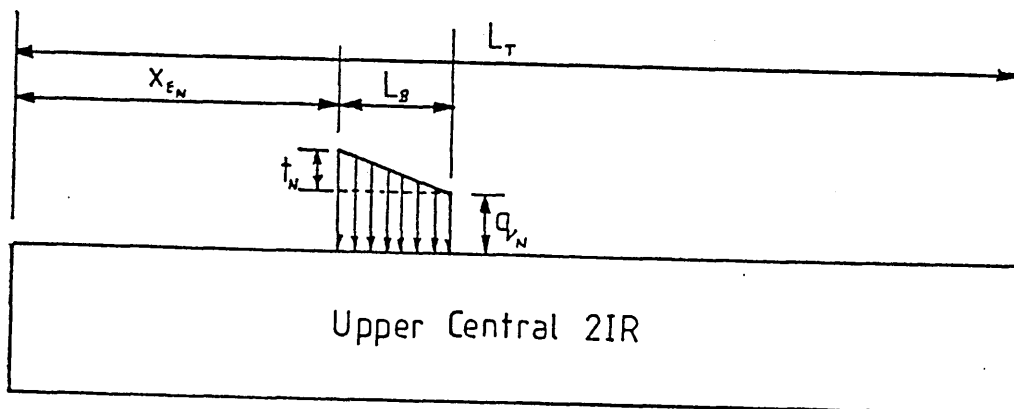


Fig.3.25 Loading due to As-U-Roll Action at Bearing N

however, that apparent occurrences of cases "b" and "f" identified by this method may be erroneous. For example, consider  $a_{BV_N}$  negative and  $a_{BV_{N+1}}$  positive. This leads to the assumption of case "f" (e.g. fig. 3.23). However, if  $a_{BV_{N+1}}$  is only very slightly positive, the "zero crossing" of the loading may occur in the region labelled X in the figure. In this case, the loading is not of the form of case "f", but rather case "e" (fig.3.22). In a similar way, apparent occurrences of case "b" may in reality be "a" or "c", and case "f" may also really be case "g". These occurrences are all trapped in the model by simple geometric tests. However, the region  $L_P$  is small (typically some 29mm) compared with  $P_B$  (about 227mm on the mills under consideration) so that this trapping and changing case is rarely called into action.

Knowing these "attempted motions" towards (or away from) the second intermediate rolls at each end of every backing bearing, we must now evaluate the beams-on-elastic-foundations constant ("foundation modulus")  $k_{B2}$  so that the loading applied to the second intermediate roll can be found from an equation of the form

$$q = k_{B2} \cdot y \quad (\text{Nm}^{-1}) \quad (\text{c.f. equation (A1.1) -Appendix 1})$$

An estimate of rolling load  $P_T$  has already been obtained (equation (3.48)), and reference to figure 3.16 shows that the component of this passing between roll J and the backing shaft assembly B is designated  $F_6$ . Furthermore,  $F_6$  is given by equation (3.38) so that the overall load transmitted via the path B-J is therefore

known (typically  $0.28P_T$  - see end of section 3.3)

The foundation modulus can therefore be found by the methods of **Appendix 2** as

$$k_{B2} = \frac{f_1}{\ln(f_2) + \ln(D_B + D_{2I}) - \ln(F_6/L_T)} \quad (Nm^{-2}) \dots (3.58)$$

where  $f_1 = \frac{\pi E}{2(1-\nu^2)} \quad (Nm^{-2})$

$$f_2 = \frac{\sqrt[3]{e^2 \pi E}}{4(1-\nu)^2} \quad (Nm^{-2})$$

Now consider again fig. 3.21, and the relevant pair of equations (3.53). The magnitude of the uniformly distributed loads and triangular distributed load shown in fig. 3.21 (ii) and (iii) are now given as

$$q_{fN} = k_{B2} y_{fN} \quad (Nm^{-1})$$

$$q_{rN} = k_{B2} y_{rN} \quad (Nm^{-1})$$

$$\text{and therefore } \left. \begin{aligned} q_N &= k_{B2} y_{rN} \quad (Nm^{-1}) \\ t_N &= k_{B2} (y_{fN} - y_{rN}) \quad (Nm^{-1}) \end{aligned} \right\} \dots \dots \dots (3.59) \quad N=1, \dots, J_B$$

Note however, that the TDL given by  $t_N$  is reversed in sense compared with fig. A.1.7 (Appendix 1) in that the maximum magnitude of the loading occurs at the left rather than at the right. A flag is set in the computer model to indicate this fact, which is taken into account in the 2IR deflection model (next section).

Equations (3.59) may be generalized in the same way as before, thus:-

$$\left. \begin{aligned} q_N &= k_{B2} y_{r_N} \quad (Nm^{-1}) \\ t_N &= k_{B2} (y_{f_N} - y_{r_N}) \quad (Nm^{-1}) \end{aligned} \right\} \begin{array}{l} \dots \dots \dots (3.60) \\ N=1, \dots J_B \\ \text{cases "a", "d", "e"} \\ \text{and "h"} \end{array}$$

(with flags set for "reversed"  $t_N$  in cases "a" and "e")  
 (note  $t_N=0$  in cases "d" and "h")

$$\left. \begin{aligned} q_N &= k_{B2} y_{f_N} \quad (Nm^{-1}) \\ t_N &= k_{B2} (y_{r_N} - y_{f_N}) \quad (Nm^{-1}) \end{aligned} \right\} \begin{array}{l} \dots \dots \dots (3.61) \\ N=1, \dots J_B \\ \text{cases "c" and "g"} \end{array}$$

Cases "b" and "f" in fig. 3.22 each resolve into two TDL's as shown in fig. 3.23, which will be called  $t_{f_N}$  and  $t_{r_N}$  where, in each case,

$$\left. \begin{aligned} q_N &= 0 \\ t_{f_N} &= k_{B2} y_{f_N} \quad (Nm^{-1}) \\ t_{r_N} &= k_{B2} y_{r_N} \quad (Nm^{-1}) \end{aligned} \right\} \begin{array}{l} \dots \dots \dots (3.62) \\ N=1, \dots J_B \\ \text{cases "b" and "f"} \end{array}$$

(with flags set for "reversed"  $t_N$  in the case of  $t_{f_N}$ ).

Note that in equations (3.53) to (3.62), the sign conventions are automatically maintained, so that we finally obtain downward-acting loadings positive. Also,  $t_{f_N}$  and  $t_{r_N}$  are set to zero in (3.60) and (3.61).



### 3.7 Upper Central Second Intermediate Roll Deflection Calculation

The previous section has specified loadings acting on roll J in figure 3.16 along the path denoted  $F_6$ . We now wish to evaluate the deflection of roll J due to these loadings, and eventually to apply this to roll 0 along the path denoted by  $F_3$ . We must therefore apply some form of compensation to account for the fact that  $F_6$  and  $F_3$  are not colinear. It will be recalled from earlier sections in this chapter that the angles  $\theta_6$  and  $\theta_{6R}$  are always equal. Also, from the previous section, it will be appreciated that loadings along the path of  $F_6$  due to As-U-Roll motion (NOT to be confused with the general rolling load component  $F_6$  itself) for shape control, are exactly duplicated by an identical set of loadings acting along the path of  $F_{6R}$ . Thus for a general loading of, say,  $q_N$  ( $Nm^{-1}$ ) given by one of the equations (3.60) to (3.62) for a certain setting of the As-U-Roll racks, there will be a total downward acting loading of  $2 q_N \cos \theta_6$  ( $Nm^{-1}$ ) on roll J (in addition to the rolling load before the As-U-Rolls were set). The component of this which acts in the direction of  $F_3$  is then given by  $2 q_N \cos \theta_6 \cos \theta_3$ . Therefore a transformation of this type is made upon all the loadings given by (3.60) to (3.62):

$$\left. \begin{aligned}
 q_{N \text{ effective}} &= q_N \cdot T_2 & (Nm^{-1}) \\
 t_{N \text{ effective}} &= t_N \cdot T_2 & (Nm^{-1}) \\
 t_{fN \text{ effective}} &= t_{fN} \cdot T_2 & (Nm^{-1}) \\
 t_{rN \text{ effective}} &= t_{rN} \cdot T_2 & (Nm^{-1})
 \end{aligned} \right\} \dots \dots \dots (3.64)$$

N=1, .. J<sub>B</sub>

where  $T_2 = 2 \cos \theta_6 \cos \theta_3$

and  $\theta_6$  is given by equation (3.22)

$\theta_3$  is given by equation (3.25)

N.B. The values  $q_N$ ,  $t_N$ ,  $t_{f_N}$  and  $t_{r_N}$  below must now be read as  $q_{N_{\text{effective}}}$ ,  $t_{N_{\text{effective}}}$  etc.—i.e. as the transformed values.

The foundation modulus  $k_{21}$  for the beam formed by roll J resting upon the foundation formed by roll 0 is given by the methods of Appendix 2 as

$$k_{21} = \frac{f_1}{\ln(f_2) + \ln(D_{2I} + D_1) - \ln(F_3/L_T)} \quad (\text{Nm}^{-2}) \dots (3.65)$$

where  $f_1$  and  $f_2$  are as given in equation (3.58)ff,

$F_3$  is given by equation (3.34)

Other constants which will be required in the analysis are as follows

$$I_2 = \frac{\pi D_{2I}^4}{64} \quad (\text{m}^4)$$

$$\lambda_2 = \sqrt[4]{\frac{k_{21}}{4EI_2}} \quad (\text{m}^{-1})$$

$$E_{12} = \frac{0.5 e^{\lambda_2 L_T}}{\sinh(\lambda_2 L_T) + \sin(\lambda_2 L_T)}$$

$$E_{22} = \frac{0.5 e^{\lambda_2 L_T}}{\sinh(\lambda_2 L_T) - \sin(\lambda_2 L_T)}$$

The general functional abbreviations

$$A_{\lambda x} = e^{-\lambda x} (\cos(\lambda x) + \sin(\lambda x))$$

$$B_{\lambda x} = e^{-\lambda x} \sin(\lambda x)$$

$$C_{\lambda x} = e^{-\lambda x} (\cos(\lambda x) - \sin(\lambda x))$$

$$D_{\lambda x} = e^{-\lambda x} \cos(\lambda x) \quad \text{will also be widely}$$

employed. To avoid too much complication, the effects of roll camber have been omitted from this section, but are described separately in Appendix 4.

The 2IR is now considered to be divided into an even number ( $M_2$ ) of equal sections across the mill, and the deflection of the roll will be calculated at a point corresponding to the centre of each section. The distances of these points from the LH end of the roll (i.e. the front of the mill) are therefore given by

$$x_M = \frac{L_T(2M-1)}{2M_2} \quad (\text{m}) \text{ for } M=1, \dots, M_2 \quad \dots \dots (3.66)$$

The components of loading (UDL and TDL) due to each backing bearing are now considered in turn, applying the theory of beams on elastic foundations for each, and evaluating the resulting deflection at all the  $M_2$  points ( $x_M$ ) along the 2IR for each. The total deflection profile of the 2IR is finally found by algebraically summing the deflections found for all the components of all the  $J_B$  loadings at each of the  $M_2$  points. As an example, consider the loading due to the  $N^{\text{th}}$  backing bearing shown in fig.3.26.

We will consider firstly the UDL, magnitude  $q_N(\text{Nm}^{-1})$  due to this bearing. Applying the procedure of Appendix 1, section A1.4, the sequence of computation is as follows.

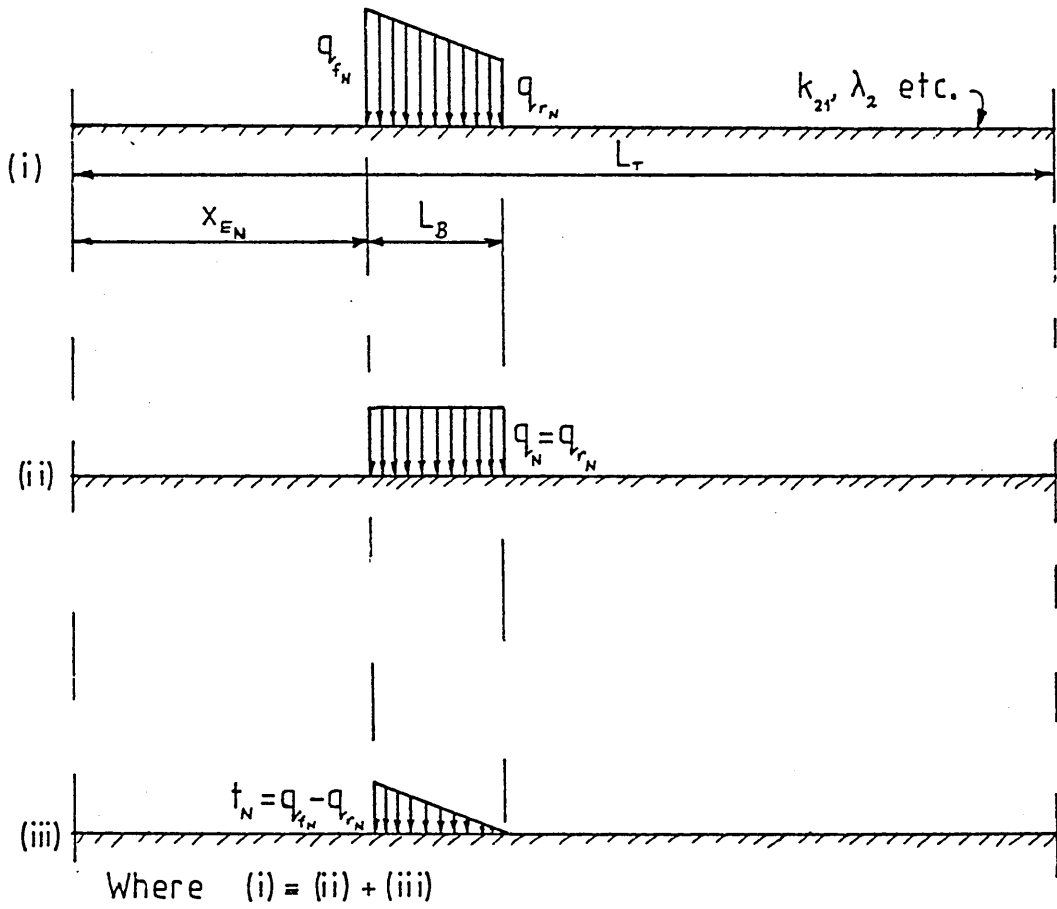


Fig.3-26 Resolution of fig.3-25 into UDL + TDL

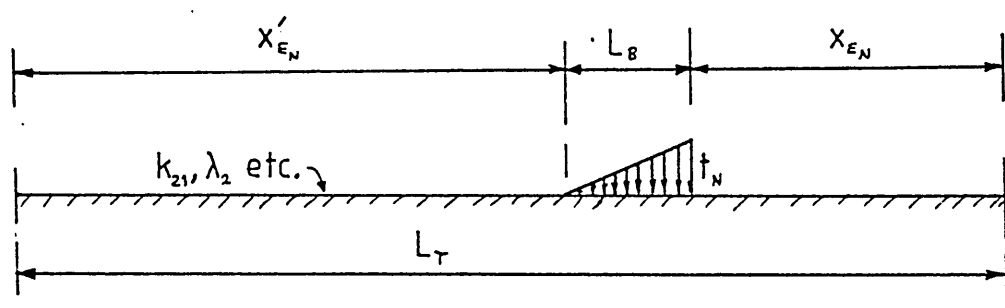


Fig. 3-27 Reversal of fig.3-26 (iii)

We firstly evaluate the moments and shears due to this UDL (acting on an infinitely long 2IR) at points corresponding to the ends of the actual 2IR. For this, equations (A1.21), (A1.25), (A1.22) and (A1.26) are used. Thus: (but see also Appendix 4, where the effect of roll camber is considered).

$$M_{A_2} = \frac{-q_N}{4\lambda_2^2} \cdot (B\lambda_2 \cdot x_{E_N} - B\lambda_2 \cdot (x_{E_N} + L_B)) \quad (\text{Nm})$$

$$M_{B_2} = \frac{q_N}{4\lambda_2^2} \cdot (B\lambda_2 \cdot (L_T - x_{E_N}) - B\lambda_2 \cdot (L_T - x_{E_N} - L_B)) \quad (\text{Nm})$$

$$Q_{A_2} = \frac{q_N}{4\lambda_2} \cdot (C\lambda_2 \cdot x_{E_N} - C\lambda_2 \cdot (x_{E_N} + L_B)) \quad (\text{N})$$

$$Q_{B_2} = \frac{q_N}{4\lambda_2} \cdot (C\lambda_2 \cdot (L_T - x_{E_N}) - C\lambda_2 \cdot (L_T - x_{E_N} - L_B)) \quad (\text{N})$$

Equations A1.40 then give

$$M'_{A_2} = 0.5(M_{A_2} + M_{B_2}) \quad (\text{Nm})$$

$$M''_{A_2} = 0.5(M_{A_2} - M_{B_2}) \quad (\text{Nm})$$

$$Q'_{A_2} = 0.5(Q_{A_2} - Q_{B_2}) \quad (\text{N})$$

$$Q''_{A_2} = 0.5(Q_{A_2} + Q_{B_2}) \quad (\text{N})$$

The end-conditioning forces (ECFs), which need to be applied to cause the portion of the infinite beam under consideration to behave precisely as if it were the 2IR of length  $L_T$  with free ends, subjected to the UDL  $q_N$  as shown in fig.3.26(ii), are then found using equations (A1.41) and (A1.42) as

$$F'_{O_2} = 4E_{12} \left[ Q'_{A_2} (1+D\lambda_2 L_T) + \lambda_2 \cdot M'_{A_2} \cdot (1-A\lambda_2 L_T) \right] \quad (N)$$

$$M'_{O_2} = \frac{-2E_{12}}{\lambda_2} \left[ Q'_{A_2} \cdot (1+C\lambda_2 L_T) + 2\lambda_2 \cdot M'_{A_2} \cdot (1-D\lambda_2 L_T) \right] \quad (Nm)$$

$$F''_{O_2} = 4E_{22} \left[ Q''_{A_2} (1-D\lambda_2 L_T) + \lambda_2 \cdot M''_{A_2} \cdot (1+A\lambda_2 L_T) \right] \quad (N)$$

$$M''_{O_2} = \frac{-2E_{22}}{\lambda_2} \left[ Q''_{A_2} (1-C\lambda_2 L_T) + 2\lambda_2 M''_{A_2} \cdot (1+D\lambda_2 L_T) \right] \quad (Nm)$$

And then

$$F_{OA_2} = F'_{O_2} + F''_{O_2} \quad (N)$$

$$F_{OB_2} = F'_{O_2} - F''_{O_2} \quad (N)$$

$$M_{OA_2} = M'_{O_2} + M''_{O_2} \quad (Nm)$$

$$M_{OB_2} = M'_{O_2} - M''_{O_2} \quad (Nm)$$

The deflection of the 2IR at each of the  $M_2$  points along the roll is then given for  $F_{OA_2}$  by equation (A1.7) (but see also Appendix 4, where the effect of roll camber is considered).

$$y_{2_{x_M}} = \frac{F_{OA_2} \lambda_2}{2 k_{21}} \cdot A \lambda_2 x_M \quad (m) \text{ for } M=1, \dots, M_2 \dots (3.67)$$

where  $k_{21}$  is given by (3.65)

and the  $x_M$  are given by (3.66)

Similarly the deflection due to  $F_{OB_2}$  is given by

$$y_{2_{x_M}} = \frac{F_{OB_2} \lambda_2}{2 k_{21}} A \lambda_2 (L_T - x_M) \quad (m) \text{ for } M=1, \dots, M_2 \dots (3.68)$$

Equation A1.11 gives the deflections due to the moments:-

For  $M_{OA_2}$ ,

$$y_{2x_M} = \frac{M_{OA_2} \lambda_2^2}{k_{21}} B_{\lambda_2 x_M} \quad (m) \quad \text{for } M=1, \dots, M_2 \quad \dots (3.69)$$

and for  $M_{OB_2}$ ,

$$y_{2x_M} = \frac{M_{OB_2} \lambda_2^2}{k_{21}} B_{\lambda_2 \cdot (L_T - x_M)} \quad (m) \quad \text{for } M=1, \dots, M_2 \quad \dots (3.70)$$

2

Note that the sign here is positive (rather than negative as might at first be expected) because of the sense in which  $M_{OB_2}$  is taken to act (c.f. figs. A1.5 and A1.8).

The four components of deflection calculated above are then algebraically summed at each of the  $M_2$  points to give the 2IR deflection profile due to the ECFs for the UDL:-

$$y_{2x_M} = \frac{\lambda_2}{2 k_{21}} \left[ F_{OA_2} A_{\lambda_2 \cdot x_M} + F_{OB_2} A_{\lambda_2 \cdot (L_T - x_M)} \right] + \frac{\lambda_2^2}{k_{21}} \left[ M_{OA_2} B_{\lambda_2 x_M} + M_{OB_2} B_{\lambda_2 (L_T - x_M)} \right] \quad (m) \quad \text{for } M=1, \dots, M_2 \quad \dots (3.71)$$

Next, the deflection profile due to the UDL itself must be found at each of the  $M_2$  points along the 2IR. Here, equations A1.19, A1.15 or A1.23 are used, depending upon whether the point  $x_M$  falls to the left of the loading,

or to the right of the loading respectively:-

$$y_{2_{x_M}} = \frac{q_N}{2 k_{21}} \left[ D\lambda_2(x_{E_N} - x_M) - D\lambda_2(x_{E_N} - x_M + L_B) \right] \quad \text{for } 0 \leq x_M < x_{E_N} \quad (m) \dots (3.72)$$

or

$$y_{2_{x_M}} = \frac{q_N}{2 k_{21}} \left[ 2^{-D}\lambda_2(x_M - x_{E_N}) - D\lambda_2(x_{E_N} + L_B - x_M) \right] \quad \text{for } x_{E_N} \leq x_M \leq (x_{E_N} + L_B)$$

or

$$y_{2_{x_M}} = -\frac{q_N}{2k_{21}} \left[ D\lambda_2(x_M - x_{E_N}) - D\lambda_2(x_M - x_{E_N} - L_B) \right] \quad \text{for } (x_{E_N} + L_B) < x_M \leq L_T$$

The total 2IR deflection due to the UDL of fig 3.26 (ii) is then found by summing the results of equations (3.71) and (3.72) at each of the  $M_2$  points:-

$$y_{2_{x_M}} = \left[ (y_{2_{x_M}} \text{ due to eqn.3.71}) + (y_{2_{x_M}} \text{ due to equn.3.72}) \right] (m) \quad \text{for } M=1, \dots, M_2 \quad \dots (3.73)$$

To this result must now be added the effect of the TDL (fig.3.26 (iii)). It will be recalled that Appendix 1 considers results only for TDLs whose non-zero end is to the right, and the TDL of fig.3.26 (iii) does not conform

to this pattern. A simple method of overcoming this problem is to use a mapping which conceptually "reverses" the roll and TDL as shown in fig. 3.27 the mapping being

$$x'_{E_N} = L_T - x_{E_N} - L_B \quad (m) \quad \dots \dots (3.74)$$

This is applied by the computer model in response to the flags set at equations (3.60) and (3.62).

The procedure below is then applied using  $x'_{E_N}$  throughout (as shown), and when the total 2IR deflection profile due to the TDL has been found (equation 3.77) the mapping is reversed by equation (3.78) so that the roll reverts to the "correct way round".

As in the case of the UDL above, the whole procedure of Appendix 1, section A1.4 is applied. Equations A1.33, A1.37, A1.34 and A1.38 yield the moments and shears at points corresponding to the roll-ends on an infinite beam as:-

$$M_{A_2} = \frac{-t_N}{8\lambda_2^3 L_B} \left[ A\lambda_2^{x'_{E_N}} - A\lambda_2(x'_{E_N} + L_B) - 2\lambda_2^{L_B} B\lambda_2(x'_{E_N} + L_B) \right] \quad (Nm)$$

$$M_{B_2} = \frac{-t_N}{8\lambda_2^3 L_B} \left[ A\lambda_2(L_T - x'_{E_N}) - A\lambda_2(L_T - x'_{E_N} - L_B) + 2\lambda_2^{L_B} \cdot B\lambda_2(L_T - x'_{E_N} - L_B) \right] \quad (Nm)$$

$$Q_{A_2} = \frac{-t_N}{4\lambda_2^2 L_B} \left[ B\lambda_2^{x'_{E_N}} - B\lambda_2(x'_{E_N} + L_B) + \lambda_2^{L_B} C\lambda_2(x'_{E_N} + L_B) \right] \quad (N)$$

$$Q_{B_2} = \frac{t_N}{4\lambda_2^2 L_B} \left[ B\lambda_2(L_T - x'_{E_N}) - B\lambda_2(L_T - x'_{E_N} - L_B) - \lambda_2^{L_B} \cdot C\lambda_2(L_T - x'_{E_N} - L_B) \right] \quad (N)$$

Equations A1.40, A1.41 and A1.42 are then applied as above to give the ECFs  $F_{OA_2}$ ,  $F_{OB_2}$ ,  $M_{OA_2}$  and  $M_{OB_2}$  due to the TDL. The deflection profile of the 2IR due to the ECFs for the TDL is then found as before (c.f. equation 3.71) as

$$y_{2_{x_M}} = \frac{\lambda_2}{2k_{21}} \left[ F_{OA_2}^A \lambda_2 x_M + F_{OB_2}^A \lambda_2 (L_T - x_M) \right] + \frac{\lambda_2^2}{k_{21}} \left[ M_{OA_2}^B \lambda_2 x_M + M_{OB_2}^B \lambda_2 (L_T - x_M) \right] \quad (m) \text{ for } M=1, \dots, M_2 \dots (3.75)$$

Where  $F_{OA_2}$ ,  $F_{OB_2}$ ,  $M_{OA_2}$  and  $M_{OB_2}$  are evaluated for the TDL of magnitude  $t_N$ .

The deflection due to the TDL itself must now be found at each of the  $M_2$  points along the 2IR. Equations A1.31, A1.27 or A1.35 are used, depending upon whether the point  $x_M$  is to the left of the loading of fig.3.27 under it, or to the right of it. Thus,

$$y_{2_{x_M}} = \frac{t_N}{4\lambda_2 k_{21} L_B} \left[ C_{\lambda_2}(x'_{E_N} - x_M) - C_{\lambda_2}(x'_{E_N} + L_B - x_M) - 2\lambda_2 L_B D_{\lambda_2}(x'_{E_N} + L_B - x_M) \right] \text{ for } 0 \leq x_M < x'_{E_N} \quad (m) \text{ for } M=1, \dots, M_2 \dots (3.76)$$

or

$$y_{2_{x_M}} = \frac{t_N}{4\lambda_2 k_{21} L_B} \left[ C_{\lambda_2}(x_M - x'_{E_N}) - C_{\lambda_2}(x'_{E_N} + L_B - x_M) - 2\lambda_2 L_B D_{\lambda_2}(x'_{E_N} + L_B - x_M) + 4\lambda_2(x_M - x'_{E_N}) \right] \text{ for } x'_{E_N} \leq x_M \leq (x'_{E_N} + L_B)$$

or

$$y_{2_{x_M}} = \frac{t_N}{4\lambda_2 k_{21} L_B} \left[ C_{\lambda_2}(x_M - x'_{E_N}) - C_{\lambda_2}(x_M - x'_{E_N} - L_B) + 2\lambda_2 L_B D_{\lambda_2}(x_M - x'_{E_N} - L_B) \right] \text{ for } (x'_{E_N} + L_B) < x_M \leq L_T$$

The total 2IR deflection profile due to the TDL of fig.3.27 is then found by summing the results of equations (3.75) and (3.76) at each of the  $M_2$  points, i.e.

$$y_{2_{x_M}} = \left[ (y_{2_{x_M}} \text{ due to eqn.3.75}) + (y_{2_{x_M}} \text{ due to eqn.3.76}) \right] \text{ (m)}$$

for  $M=1, \dots, M_2 \dots \dots (3.77)$

Now if the TDL had to be "reversed" as in this example, the order of the  $M_2$  points must now be reversed to "correct" the mapping which was made at (3.74) above. This is accomplished by:-

$$y'_{2_{x_M}} = y_{2_{x_M}} \text{ (m) for } M=1, \dots, M_2 \quad \left. \begin{array}{l} ) \\ ) \\ ) \\ ) \\ ) \\ ) \end{array} \right\} \dots \dots (3.78)$$

then

$$y_{2_{x_M}} = y'_{2_{x_{(M_2+1-M)}}} \text{ (m) for } M=1, \dots, M_2 \quad \left. \begin{array}{l} ) \\ ) \\ ) \\ ) \\ ) \\ ) \end{array} \right\}$$

The final deflection profile of the 2IR due to the loading of fig. 3.25 (c.f. fig.3.26 (i)) is then found by summing the contributions due to the UDL and the TDL at each of the  $M_2$  points, thus

$$y_{2_{x_M}} = \left[ (y_{2_{x_M}} \text{ due to eqn. 3.73}) + (y_{2_{x_M}} \text{ due to eqn.3.78}) \right] \text{ (m)}$$

for  $M=1, \dots, M_2 \dots (3.79)$

The overall deflection profile of the 2IR due to all As-U-Roll rack movements is found by applying the above procedure to each of the  $J_B$  loadings caused by the backing bearings, and summing all the results at each

of the  $M_2$  points along the roll. Note, however, the following points (refer to fig. 3.22 (ii)):-

NOTE A When a loading acts "upwards" (such as in cases c, d and e), it is treated as if it in fact acted downwards (i.e. as above), and the sign conventions in the b.o.e.f. theory will automatically give the correct sign to the deflection profile.

NOTE B When a TDL acts the "correct" way round (i.e. with its non-zero end on the right, such as cases c and g), the mapping of equation (3.74) is not applied. The subsequent analysis continues, using  $x_{E_N}$  rather than  $x'_{E_N}$ . Equation (3.78) is also not applied, and the results of equation (3.77) are used directly in equation (3.79).

NOTE C The cases b and f, where the backing bearing is tilted about its horizontal axis, are treated as follows.

Consider case f as depicted in fig. 3.23. Here we have two TDLs. The first acts over a length of roll  $L_f$  given by equation (3.57), and the second over a length of roll  $(L_B - L_f)$  (from fig. 3.23). Furthermore, the position of the LH end of the first loading is already known from the appropriate value of  $x_{E_N}$  given by equation (3.63), and the position of the LH end of the second loading will be known as  $x_{E_{N_2}}$  where  $x_{E_{N_2}} = x_{E_N} + L_f$ .

The 2IR deflection profile due to a loading of this form is therefore found by firstly applying the previous TDL analysis (i.e. from equation (3.74) onwards) to the

LH part (i.e. using  $t_{fN}$  instead of  $t_N$ , and  $L_f$  instead of  $L_B$ ) and storing the deflection profile yielded by equation (3.78). The analysis is then applied a second time for the RH part (i.e. using  $t_{rN}$  instead of  $t_N$ ,  $(L_B - L_f)$  instead of  $L_B$  and  $x_{E_{N_2}}$  instead of  $x_{E_N}$ ), but this time the loading is the "correct" way round and so NOTE B above applies also. The deflection profile given for this RH part by equation (3.77) is then summed with that previously stored for the LH part to give the total 2IR deflection profile due to the loading of fig.3.23 as

$$y_{2_{x_M}} = \left[ \begin{array}{l} (y_{2_{x_M}} \text{ for the LH part of loading, due to eqn.3.78}) \\ + (y_{2_{x_M}} \text{ for RH part of loading, due to eqn.3.77}) \end{array} \right] \text{ (m)}$$

. . . . . (3.80)

This is then added into the overall total deflection profile for the 2IR in the same way as the profile due to any other backing bearing (note that equation (3.79) is not needed here, as UDL is zero).

For a loading of the form shown in case b (fig.3.22 (ii)), precisely the same method is used, i.e. applying equation (3.74), etc. and obtaining the result at equation (3.80). The b.o.e.f. sign convention will automatically compensate for the fact that case f is the inverse of case b.

To sum up, the final deflection profile of the upper central 2IR due to the  $J_B$  loadings transferred from the backing bearings is given by

$$y_{2x_M} = \left[ \sum_{N=1}^{J_B} \left[ \begin{array}{l} \text{Deflection at section } x_M \text{ due} \\ \text{to UDL from bearing N} \end{array} \right] \right. \quad (m)$$

$$+ \left. \left[ \begin{array}{l} \text{Deflection at section } x_M \text{ due} \\ \text{to TDL from bearing N} \end{array} \right] \right] \quad \left. \begin{array}{l} \text{for} \\ M=1, \dots, M_2 \\ \dots \dots \dots (3.81) \end{array} \right.$$

where the deflection at  $x_M$  due to the UDL

is zero for cases b and f  
or is given by equation (3.73) for all other cases.

and the deflection at  $x_M$  due to the TDL

is zero for cases d and h  
or is given by equation (3.77) for cases c and g  
or is given by equation (3.78) for cases a and e  
or is given by equation (3.80) for cases b and f.

### 3.8 Treatment of the First Intermediate Rolls

The second intermediate roll deflection profile given by equation (3.81) in the previous section will now be converted into a system of loadings acting upon the upper first intermediate roll labelled "0" in fig.3.16. The system of loadings is then used to calculate a similar deflection profile for roll 0. The effects of roll camber are left out of the discussion for the present only, so as not to complicate matters any further, as are the effects of the tapered-off ends of the first intermediate rolls used for shape control. The inclusion of both these effects is described separately in Appendix 4.

#### 3.8.1 Conversion of the Upper Central 2IR Deflection Profile into a System of Loadings Acting on the First Intermediate Roll '0'

The simplest system of loadings which can be envisaged to give accurate results is a set of concentrated forces, and this is the system which has been adopted. In order to simplify the calculations a condition is imposed that the number of concentrated forces chosen ( $J_{1F}$ ) should be an integer sub-multiple of the number of sections along the roll at which the 2IR deflection is known ( $M_2$ ), whilst remaining large enough to yield a smooth and meaningful deflection profile of the 1IR. (Typical values used in the model are  $M_2 = 100$ ,  $J_{1F} = 20$ ). As in the case of the  $x_M$  values (equation 3.66), the  $J_{1F}$  forces are taken to act at the centres of equal divisions of the 1IR so that the points of application of the forces from the front of the mill are given by

$$x_{1F_N} = \frac{L_T(2N-1)}{2J_{1F}} \text{ (m) for } N=1, \dots, J_{1F} \dots (3.82)$$

The relationship between the  $N^{\text{th}}$  of these forces from the front of the mill, and the deflection values given by (3.81) is shown in fig, 3.28 (assuming the ratio between the typical values of  $M_2$  and  $J_{1F}$  as given above). The local values of UDL due to each deflection value are found from equation (A1.1) in Appendix 1., as

$$q_{x_M} = k_{21} y_{2_{x_M}} \quad (Nm^{-1}) \quad \text{for } M=1, \dots, M_2 \dots (3.83)$$

where the  $y_{2_{x_M}}$  are given by equation (3.81),

and the local value of concentrated force due to each value of deflection is therefore given by

$$q_{x_M} \cdot \frac{L_T}{M_2} = \frac{k_{21} y_{2_{x_M}} L_T}{M_2} \text{ (N) for } M=1, \dots, M_2 \dots (3.84)$$

The value of the  $N^{\text{th}}$  concentrated force  $F_{1N}$  is then computed as the sum of the appropriate  $\frac{M_2}{J_{1F}}$  values of local concentrated force given by (3.84). Thus

$$F_{1N} = \frac{k_{21} L_T}{M_2} \cdot \left( \frac{NM_2}{J_{1F}} + \frac{(N-1)M_2}{J_{1F}} \right) y_{2_{x_Q}} \text{ (N) for } N=1, \dots, J_{1F} \dots (3.85)$$

where the  $y_{2_{x_Q}}$  are the appropriate results of equation (3.81).

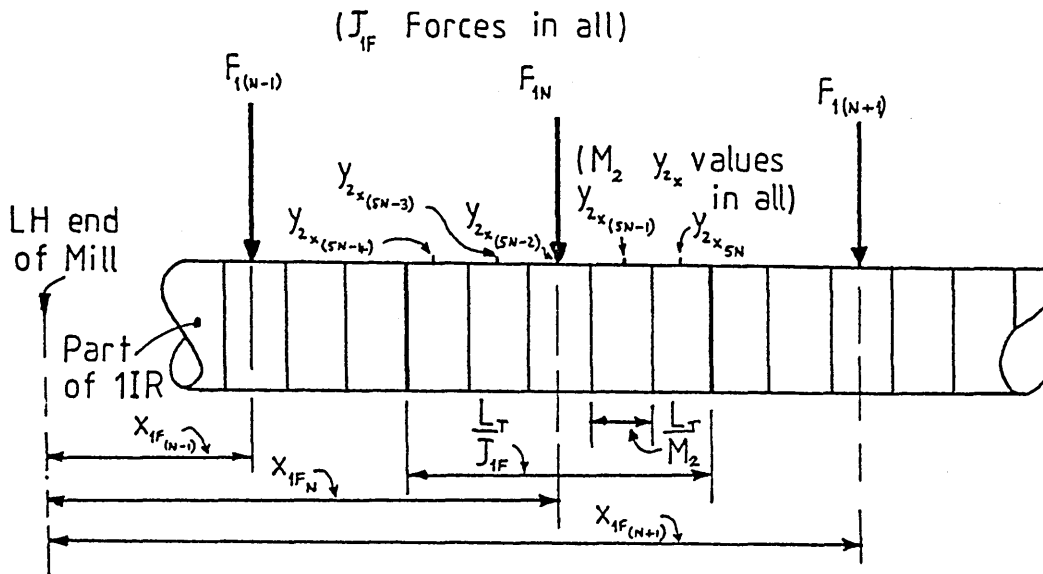


Fig.3-28 Relationship Between  $N^{\text{th}}$  Concentrated Force Taken to act on 1IR, & Surrounding Values of 2IR Deflection (For Case  $M_2/J_{1F} = 5$ )

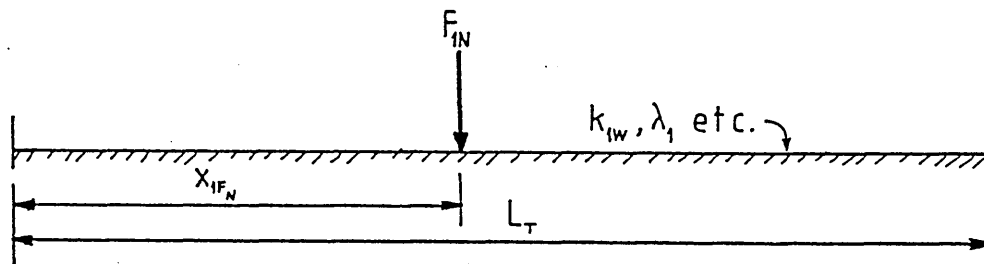


Fig. 3-29  $N^{\text{th}}$  Conc. Force Acting on 1IR

Now, as in the case of the 2IR considered in the previous section, we must make compensation for the fact that we eventually wish to apply a loading along the path denoted  $F_2$  in fig. 3.16, from information pertaining to the path denoted by  $F_3$ ; the problem being that  $F_3$  and  $F_2$  are not colinear. Strictly, we should calculate the loadings on path  $F_4$  also, and resolve forces as before to obtain the fraction of the loadings due to  $F_3$  and  $F_4$  which should be considered to yield the correct magnitude of  $F_2$ . However, due to the mill geometry it was thought that a change in As-U-Roll actuators would provide a much greater percentage change in the direction of  $F_3$  than in the direction of  $F_4$ . Therefore the effect of changes in  $F_4$  is ignored, and the vertical change acting upon roll 0 becomes  $F_{1N} \cos \theta_3$  for one of the forces given by equation (3.85). The component of this acting in the direction of  $F_2$  is then given by  $F_{1N} \cos \theta_3 \cos \theta_2$ . Therefore a transformation is carried out upon the forces given by (3.85):

$$\left. \begin{aligned} F_{1N}^{\text{effective}} &= F_{1N} \cdot T_1 \\ & \dots \dots \dots (3.86) \end{aligned} \right\} \begin{array}{l} (N) \\ N=1, \dots, J_{1F} \end{array}$$

where  $T_1 = \cos \theta_3 \cos \theta_2$

and  $\theta_3$  is given by equation (3.25)

$\theta_2$  is given by equation (3.29)

The values of  $F_{1N}$  below must now be read as

$F_{1N}^{\text{effective}}$  - i.e. as the transformed values.

Note that the assumption above concerning changes in  $F_4$  has been called into some doubt by recent model results at the time of writing. There is therefore scope for more work in this area, whereby in addition to the present work a diagram such as figures 3.19 and 3.20 could be drawn and analysed for the motion of the backing bearings on shaft B relative to roll I (rather than J). This would give, by identical methods to those used in sections 3.6 and 3.7, a deflection profile for roll I. The proper values of loading upon the roll O would then be found from a combination of  $F_{1N}$  values given by (3.85) for the loading due to roll J, and another set of  $F_{1N}$  values for the loading due to roll I along the path  $F_4$ . The required modifications to the static model program are not particularly difficult in order to achieve this (the model being well-structured), but time has not yet permitted it to be carried out.

### 3.8.2. Evaluation of First Intermediate Roll Deflection Profile

The 1IR (O in fig.3.16) is now treated as a beam subjected to the system of forces given by (3.86), and resting upon an elastic foundation formed by the upper workroll (WR). The foundation modulus ( $k_{1w}$ ) for the 1IR/WR interface must therefore be found. The methods of Appendix 2 give us

$$k_{1w} = \frac{f_1}{\ln(f_2) + \ln(D_1 + D_w) - \ln(F_2/L_T)} \quad (\text{Nm}^{-2}) \quad \dots (3.87)$$

where  $f_1$  and  $f_2$  are given by (3.58)ff

$F_2$  is given by equation (3.33)

Other required constants are

$$I_1 = \frac{\pi D_1^4}{64} \quad (\text{m}^4)$$

$$\lambda_1 = \sqrt[4]{\frac{k_{1w}}{4EI_1}}$$

$$E_1 = \frac{0.5 e^{\lambda_1 L_T}}{\sinh(\lambda_1 L_T) + \sin(\lambda_1 L_T)}$$

$$E_{21} = \frac{0.5 e^{\lambda_1 L_T}}{\sinh(\lambda_1 L_T) - \sin(\lambda_1 L_T)}$$

The effect of each of the  $J_{1F}$  forces is now investigated in turn, using the procedure of Appendix 1, section 4. Consider as an example the  $N^{\text{th}}$  concentrated force from the front of the mill ( $F_{1N}$ ) shown in fig.3.29.

Firstly, equations A.9 and A.10 are used to specify the moments and shears which would be produced by  $F_{1N}$  at points on an infinitely long beam which correspond with the ends of the WR:- (see also Appendix 4)

$$M_{A_1} = \frac{F_{1N}}{4\lambda_1} \cdot C_{\lambda_1 x_{1F_N}}$$

$$M_{B_1} = \frac{F_{1N}}{4\lambda_1} \cdot C_{\lambda_1 (L_T - x_{1F_N})}$$

$$Q_{A_1} = \frac{F_{1N}}{2} \cdot D_{\lambda_1 x_{1F_N}}$$

$$Q_{B_1} = \frac{-F_{1N}}{2} \cdot D_{\lambda_1 (L_T - x_{1F_N})}$$

Equations (A1.40), (A1.41) and (A1.42) are then applied using  $k_{1w}$ ,  $E_{11}$ ,  $E_{21}$ ,  $\lambda_1$  etc. to yield the ECFs  $F_{OA_1}$ ,  $F_{OB_1}$ ,  $M_{OA_1}$  and  $M_{OB_1}$ .

The deflection profile of the lIR due to the combined effect of these ECFs is then found as before (c.f. equation (3.71)):-

$$y_{1x_M} = \frac{\lambda_1}{2k_{1W}} \cdot \left[ F_{OA_1} \cdot A_{\lambda_1 x_M} + F_{OB_1} \cdot A_{\lambda_1 (L_T - x_M)} \right] + \frac{\lambda_1^2}{k_{1W}} \left[ M_{OA_1} \cdot B_{\lambda_1 x_M} + M_{OB_1} \cdot B_{\lambda_1 (L_T - x_M)} \right] \quad (m) \dots (3.88)$$

for  $M=1, \dots, M_1$

Note that  $M_1$  need not be the same as  $M_2$  used previously, but it must nevertheless be an even number. If  $M_1$  differs from  $M_2$  the new  $x_M$  values are given by using  $M_1$  in equation (3.66) rather than  $M_2$ .

The deflection profile of the lIR caused by  $F_{1N}$  itself is found by applying equation (A1.7) as:-

$$y_{1x_M} = \frac{F_{1N} \lambda_1}{2k_{1W}} \cdot A_{\lambda_1 |x_{1F_N} - x_M|} \quad (m) \dots \dots \dots (3.89)$$

for  $M=1, \dots, M_1$

The total deflection profile of the lIR due to the  $N^{th}$  concentrated force is then found by summing the results of equations (3.88) and (3.89) at each of the  $M_1$  points:-

$$y_{1x_M} = \left[ (y_{1x_M} \text{ due to eqn. (3.88)}) + (y_{1x_M} \text{ due to eqn. (3.89)}) \right] (m)$$

$\vdots$   
 $\dots \dots \dots (3.90)$

for  $M=1, \dots, M_1$

and the overall deflection of the lIR due to all the  $J_{1F}$  forces is then found by summing all the  $J_{1F}$  results of

equation (3.90) at each of the  $M_1$  points:-

$$y_{1x_M} = \left[ \begin{array}{c} J_{1F} \\ \text{Deflection due to } F_{1N} \text{ at} \\ \text{section } x_M \\ N=1 \end{array} \right] \quad \begin{array}{l} (m) \\ \text{for} \\ M=1, \dots, M_1 \end{array} \quad \dots \dots (3.91)$$

Where the deflection in question is given by (3.90).

The effects of roll cambers and the lateral positions of the llR tapers on this result are evaluated in Appendix 4.

### 3.9 Treatment of the Upper Workroll

The deflection profile at the first intermediate roll given by equation (3.91) in the previous section will now be converted into a system of loadings acting upon the upper workroll labelled "S" in fig.3.16. The system of loadings is then used to calculate the workroll profile. The effects of roll camber are omitted at this stage, as this section will be found quite complex enough without them! Appendix 4 gives the means by which they are included in the model.

#### 3.9.1 Conversion of the llR Deflection Profile Into a System of Loadings acting on the Upper WR

As in section 3.8.1 above, a system of  $(J_{WF})$  concentrated forces is chosen to act (at points  $x_{WF_N}$ ) on the workroll. The value  $J_{WF}$  chosen for the WR need not be the same as  $J_{1F}$  used for the llR, but it must be an integer sub-multiple of  $M_1$ . Equation (3.82) yields the points of application of the forces as



This is then colinear with F<sub>1</sub> (the rolling load), so that the transformation upon the forces given by equation (3.93) is given by,

$$F_{WN \text{ effective}} = F_{WN} \cdot T_W \quad (N) \quad \dots \dots \dots (3.94)$$

where  $T_W = \cos \theta_2 + \cos \theta_{2R}$

and  $\theta_2$  is given by equation (3.29)

$\theta_{2R}$  is given by equation (3.30)

The values of F<sub>WN</sub> below must now be read as F<sub>WN effective</sub>.

### 3.9.2. Evaluation of WR Deflection Profile

The situation here is more complex than that of section 3.8.2 due to the fact that the upper WR is not supported over its entire length. The presence of the strip being rolled means that the ends of the upper WR are completely unsupported as shown in fig. 3.30 (the Sendzimir mill having no neck bearings.) This in turn means that all the rolls in the cluster are in fact more firmly supported over the strip than at the ends, which calls into question the practice of using a single value of foundation modulus ( $k_{21}$  or  $k_{1W}$  above) over the entire mill width. The practice is defended on the grounds that it is a relatively simple assumption, and it should be accurate enough for present requirements since loadings which are not directly over the strip, and occur high up in the cluster, will have relatively small effects on the strip compared with forces which are directly over it.

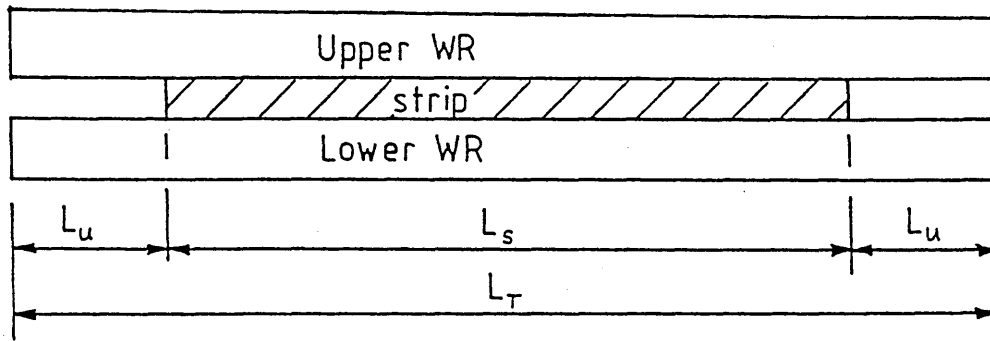


Fig.3-30 Strip in Roll Bite

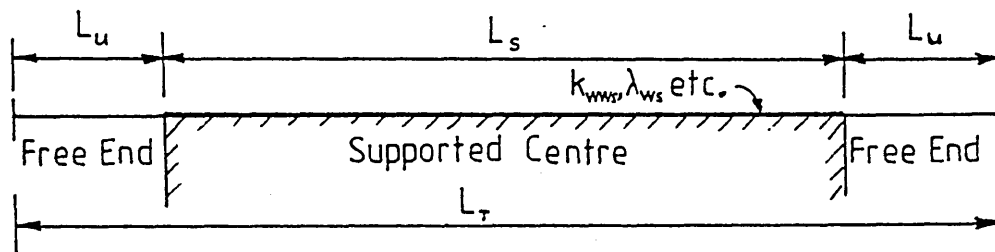


Fig.3-31 B.O.E.F. Diagram for Upper WR

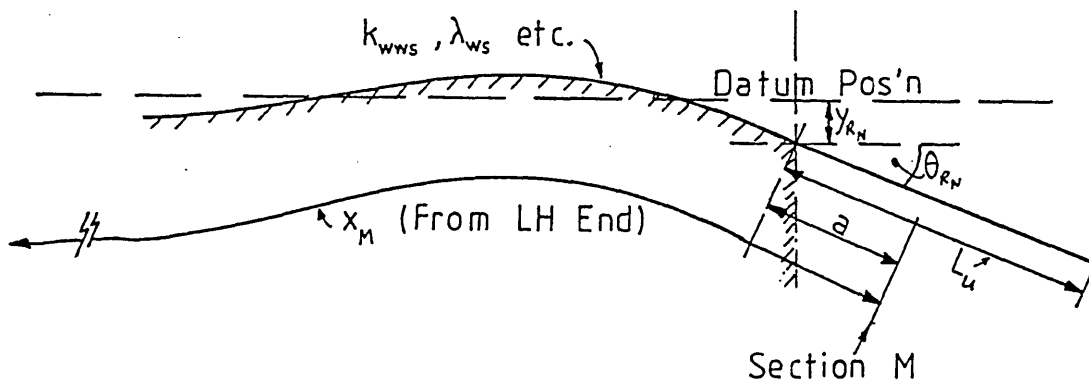


Fig.3-32 RH End of WR with  $y_{RN}$  and  $\theta_{RN}$  Positive

Future work is clearly possible in this area, should the need ever become apparent.

In view of the points outlined above, it is clearly not possible to use a foundation modulus which covers the entire length of the WR. The WR is considered as a beam subjected to the loadings specified by equation (3.94) and supported as shown in fig. 3.31 where  $L_S$  is the strip width. The foundation modulus must only be evaluated for the supported section. For the purposes of this calculation, it is assumed that the upper WR rests directly upon the lower to remove variable plastic effects due to the strip (this approximation could also be removed in future if desired).

Thus, from Appendix 2, we obtain

$$k_{WWS} = \frac{f_1}{\ln(f_2) + \ln(2D_W) - \ln(P_T/L_S)} \quad (\text{Nm}^{-2}) \dots (3.95)$$

where  $f_1$  and  $f_2$  are given by (3.58)ff

$P_T$  is the rolling load given by (3.48)(N)

$L_S$  is strip width (m)

Other required constants are

$$I_W = \frac{\pi D_W^4}{64} \quad (\text{m}^{-1})$$

$$\lambda_{WS} = \sqrt{4 \frac{k_{WWS}}{4EI_W}} \quad (\text{m}^{-1})$$

$$E_{1WS} = \frac{0.5 e^{\lambda_{WS} L_S}}{\sinh(\lambda_{WS} L_S) + \sin(\lambda_{WS} L_S)}$$

$$E_{2WS} = \frac{0.5 e^{\lambda_{WS} L_S}}{\sinh(\lambda_{WS} L_S) - \sin(\lambda_{WS} L_S)}$$

Also, from figure 3.31,

$$L_u = 0.5 (L_T - L_S) \quad (m) \quad . . . . . (3.96)$$

The deflection profile of the WR due to the  $J_{WR}$  forces specified by equation (3.94) must now be calculated. The point of application of each force ( $x_{WF_N}$ ) is examined, and the method of calculating WR deflection depends upon whether the corresponding force ( $F_{WN}$ ) acts over the LH unsupported end, over the RH unsupported end, or directly over the strip. These three cases are considered separately below.

The deflection is calculated at  $M_W$  points along the workroll due to each of the  $J_{WF}$  forces, using the results summarised at the end of the appropriate sub-section below (depending upon the point of application of the force under consideration), and the results at each of the  $M_W$  sections are summed as before to obtain the total bending profile of the upper WR. The value of  $M_W$  need not be the same as either  $M_2$  or  $M_1$ , but must remain an even number. If  $M_W$  is different from  $M_2$  or  $M_1$ , the new  $x_M$  values are found by using  $M_W$  in equation (3.66). The effect of WR camber is evaluated in Appendix 4.

#### 3.9.2.1 WR Deflection due to a force acting on the LH unsupported end

The free LH end of the WR under these conditions is treated as an elastically mounted cantilever according to the theory developed in Appendix 3. Most of the necessary equations for the deflection under this condition therefore exist in that Appendix. There are however, two outstanding problems worthy of note, and requiring special solution.

THE FIRST problem is to specify the deflection of the RH unsupported end of the WR due to the force acting on the LH end. It may be suggested that this is irrelevant as far as strip shape is considered, but nevertheless it will be considered for completeness, and in case a full-width WR deflection profile should be required for some future purpose.

If the value of  $\theta_{R_N}$  given by equation (A.3.14) is non-negative, then the deflection is easily specified by considering the RH end to remain straight as shown in fig. 3.32 whence it can be seen that the deflection of the RH end is given by

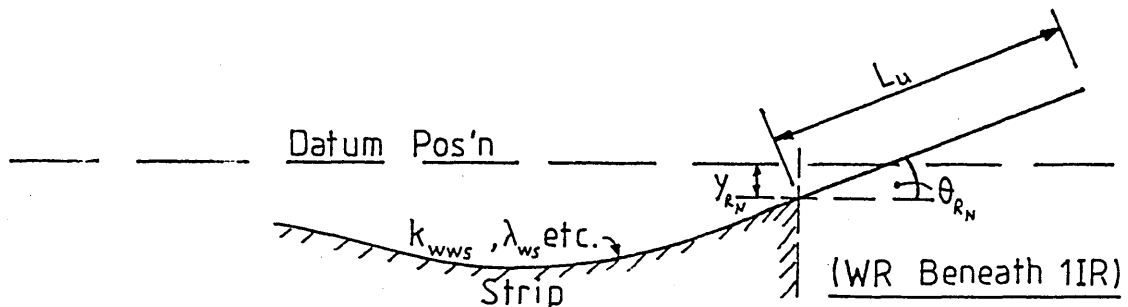
$$y_{W_{x_M}} = y_{R_N} + a \cdot \sin \theta_{R_N} \quad (m) \quad \dots \dots \dots (3.97)$$

$$\text{for } (L_U + L_S) < x_M \leq L$$

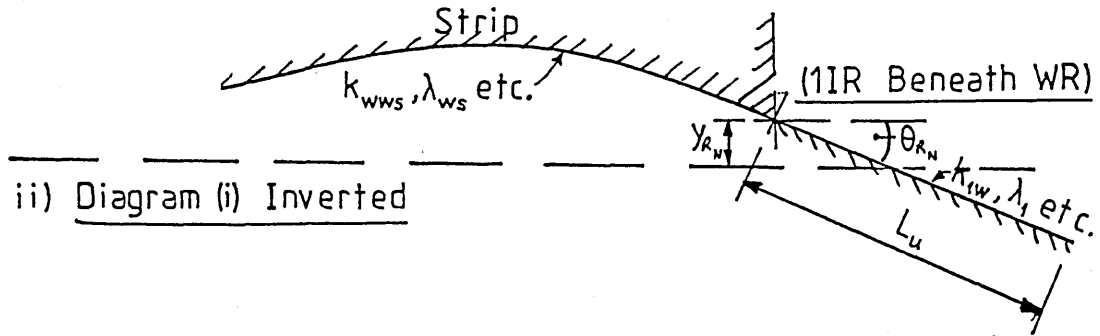
$$\text{and } M=1, \dots, M_W$$

$$\text{where } a = x_M - L_U - L_S$$

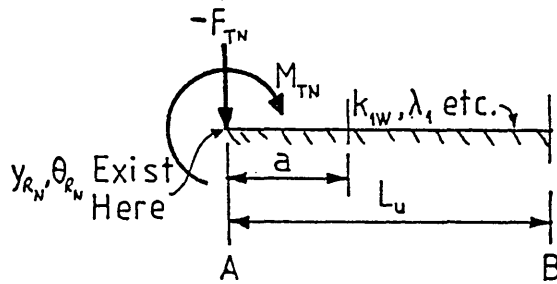
If however, the value of  $\theta_{R_N}$  is negative, this approach would result in the RH end of the WR continuing upwards in a straight line as shown in fig. 3.33(i). This is impossible, as the presence of the lIRs above would stop it from happening. The problem is overcome by assuming that if  $\theta_{R_N}$  is negative, then the RH end of the WR will "bounce" back off the lIR until the angle  $\theta$  again becomes positive, after which the straight-line approach can again be used. This is achieved by regarding the values of  $y_{R_N}$  and  $\theta_{R_N}$  (fig.3.33(i)) as having



i) Case  $y_{RN}$  Positive,  $\theta_{RN}$  Negative



ii) Diagram (i) Inverted



iii) Equivalent B.O.E.F. Diagram for RH End of (ii)

Fig.3.33 "Free" RH End of WR with  $\theta_{RN}$  Negative

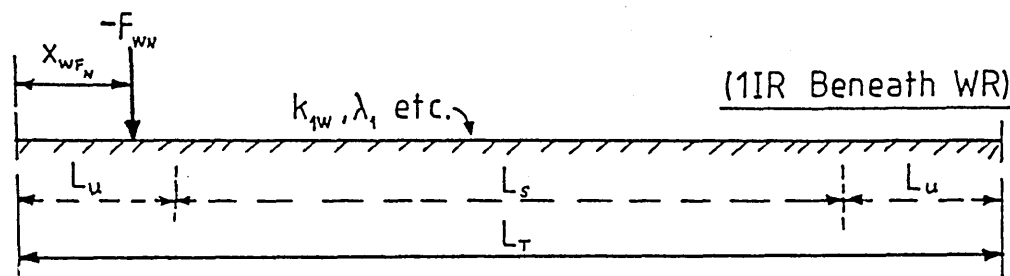


Fig.3.34 Method of Handling WR with Negative  $F_{wN}$  on LH End

been caused by some unknown values of force and moment acting on the RH end at the point where it joins the supported section (i.e. at the point where  $y_{R_N}$  and  $\theta_{R_N}$  exist. The mill is now considered temporarily to be inverted so that the situation is as shown in fig.3.33(ii). The RH "unsupported" end of the WR now "rests" on an elastic foundation formed by the lIR, and the beam diagram for this appears in fig.3.33(iii), where  $F_{TN}$  and  $M_{TN}$  are the unknown force and moment "transmitted" from the supported section of the roll due to the  $N^{\text{th}}$  concentrated force acting on the LH end. Simultaneous equations can be formed and solved for  $F_{TN}$  and  $M_{TN}$  (see below), and the deflection profile for the beam of fig.3.33(iii) can then be evaluated in the usual way (but for the RH end of the WR above the lIR). As soon as a section is reached where the angle of deflection changes sign so that the WR tends to move away from the lIR, the "bounce" is considered to be complete, and the "straight line" approach is adopted for the remainder of the roll to the extreme RH end. The analysis is as follows.

Consider the case shown in fig.3.33(i) where  $y_{R_N}$  is positive but  $\theta_{R_N}$  is negative. If the mill is now considered to be inverted so that the WR is above the lIR, these values will change sign (fig.3.33(ii)). The RH end of the WR is now drawn as in fig. 3.33(iii), where  $F_{TN}$  and  $M_{TN}$  cause the known values of  $y_{R_N}$  and  $\theta_{R_N}$ . The constants for the beam of fig.3.33(iii) are given by equation (3.87)ff, the fact that the system is inverted being immaterial.

Fig.3.33(iii) bears obvious similarity to fig.A.3.3 and the equations for  $y_{L_N}$  and  $\theta_{L_N}$  in Appendix 3 (equations (A.3.12) and (A.3.13)) can therefore be employed to obtain expressions for  $y_{R_N}$  and  $\theta_{R_N}$  in fig.3.33(iii). Firstly, the appropriate ECFs ( $F_{OA_R}$ ,  $F_{OB_R}$ ,  $M_{OA_R}$  and  $M_{OB_R}$ ) must be found in the usual way:-

$$M_{A_R} = \frac{-F_{TN}}{4\lambda_1} - \frac{M_{TN}}{2} \quad (Nm)$$

$$M_{B_R} = \frac{-F_{TN}}{4\lambda_1} \cdot C\lambda_1 L_U + \frac{M_{TN}}{2} \cdot D\lambda_1 L_U \quad (Nm)$$

$$Q_{A_R} = \frac{-F_{TN}}{2} - \frac{M_{TN}\lambda_1}{2} \quad (N)$$

$$Q_{B_R} = \frac{F_{TN}}{2} D\lambda_1 L_U - \frac{M_{TN}\lambda_1}{2} \cdot A\lambda_1 L_U \quad (N)$$

Equations (A.1.40), (A.1.41) and (A.1.42) are then applied (using  $k_{1W}$ ,  $\lambda_1$  etc.) to give the ECFs. (But note that  $F_{TN}$  and  $M_{TN}$  are unknown, see below).

Now applying equations (A.3.11) and (A.3.13)

$$-y_{R_N} = \frac{\lambda_1}{2k_{1W}} \cdot (-F_{TN} + F_{OA_R} + F_{OB_R} \cdot A\lambda_1 L_U) + \frac{\lambda_1^2}{k_{1W}} \cdot M_{OB_R} \cdot B\lambda_1 L_U \quad (m)$$

. . . . . (3.98)

$$-\theta_{R_N} = \frac{\lambda_1^2}{k_{1W}} \cdot F_{OB_R} \cdot B\lambda_1 L_U + \frac{\lambda_1^3}{k_{1W}} \cdot (M_{TN} + M_{OA_R} - M_{OB_R} \cdot C\lambda_1 L_U) \quad (rad)$$

. . . . . (3.99)

Note that  $-y_R$  and  $-\theta_R$  must be used, as the "inversion" of the mill has changed their signs.

Now, in these two equations,  $y_{R_N}$  and  $\theta_{R_N}$  are known from the previous application in Appendix 3 of equations (A.3.12) and (A.3.14),  $k_{1W}$ ,  $\lambda_1$  and  $L_U$  are also known. However,  $F_{OA_R}$ ,  $F_{OB_R}$ ,  $M_{OA_R}$  and  $M_{OB_R}$  are functions of  $F_{TN}$  and  $M_{TN}$  which are as yet unknown.

In the equations for these variables above, let,

$$Z_1 = \lambda_1 L_U$$

$$Z_2 = A_{Z1} \quad Z_3 = B_{Z1} \quad Z_4 = C_{Z1} \quad \text{and} \quad Z_5 = D_{Z1}$$

$$\text{giving } M_{A_R} = \frac{-F_{TN}}{4\lambda_1} - \frac{M_{TN}}{2} \quad (\text{Nm})$$

$$M_{B_R} = \frac{-F_{TN}}{4\lambda_1} \cdot Z_4 + \frac{M_{TN}}{2} \cdot Z_5 \quad (\text{Nm})$$

$$Q_{A_R} = \frac{-F_{TN}}{2} - \frac{M_{TN}}{2} \cdot \lambda_1 \quad (\text{N})$$

$$Q_{B_R} = \frac{F_{TN}}{2} \cdot Z_5 - \frac{M_{TN}}{2} \cdot \lambda_1 \cdot Z_2 \quad (\text{N})$$

Now applying equations (A.1.41) and rearranging,

$$M'_{A_R} = \frac{1}{4} \left[ \frac{-F_{TN}}{2\lambda_1} \cdot (1+Z_4) - M_{TN} \cdot (1-Z_5) \right] \quad (\text{Nm})$$

$$M''_{A_R} = \frac{1}{4} \left[ \frac{-F_{TN}}{2\lambda_1} \cdot (1-Z_4) - M_{TN} \cdot (1+Z_5) \right] \quad (\text{Nm})$$

$$Q'_{A_R} = \frac{1}{4} \left[ -F_{TN} \cdot (1+Z_5) - M_{TN} \cdot \lambda_1 \cdot (1-Z_2) \right] \quad (\text{N})$$

$$Q''_{A_R} = \frac{1}{4} \left[ -F_{TN} \cdot (1-Z_5) - M_{TN} \cdot \lambda_1 \cdot (1+Z_2) \right] \quad (\text{N})$$

$$\begin{aligned}
\text{Now let } Z_6 &= 1+Z_2 & Z_7 &= 1-Z_2 \\
Z_8 &= 1+Z_4 & Z_9 &= 1-Z_4 \\
Z_{10} &= 1+Z_5 & Z_{11} &= 1-Z_5
\end{aligned}$$

Applying equations (A1.41) then yields:-

$$F'_{O_R} = E_{11} \left[ -F_{TN}(Z_{10}^2 + \frac{Z_7 Z_8}{2} - 2M_{TN}\lambda_1 \cdot Z_7) \right] \quad (N)$$

$$F''_{O_R} = E_{21} \left[ -F_{TN} (Z_{11}^2 + \frac{Z_6 Z_9}{2} - 2M_{TN}\lambda_1 \cdot Z_6) \right] \quad (N)$$

$$M'_{O_R} = E_{11} \left[ \frac{F_{TN}Z_8}{\lambda_1} + M_{TN} (Z_{11}^2 + \frac{Z_7 Z_8}{2}) \right] \quad (Nm)$$

$$M''_{O_R} = E_{21} \left[ \frac{F_{TN}Z_9}{\lambda_1} + M_{TN} (Z_{10}^2 + \frac{Z_6 Z_9}{2}) \right] \quad (Nm)$$

$$\text{Now let } Z_{12} = Z_{10}^2 + \frac{Z_7 Z_8}{2} \quad Z_{13} = Z_{11}^2 + \frac{Z_6 Z_9}{2}$$

$$Z_{14} = Z_{11}^2 + \frac{Z_7 Z_8}{2} \quad Z_{15} = Z_{10}^2 + \frac{Z_6 Z_9}{2}$$

Application of equations (A.1.42) then gives the ECFs as

$$\begin{aligned}
F_{O_A_R} &= F_{TN} (-E_{11} \cdot Z_{12} - E_{21} \cdot Z_{13}) & & ) \\
&+ 2\lambda_1 \cdot M_{TN} (-E_{11} \cdot Z_7 - E_{21} \cdot Z_6) & (N) & ) \\
F_{O_B_R} &= F_{TN} (-E_{11} \cdot Z_{12} + E_{21} \cdot Z_{13}) & & ) \\
&+ 2\lambda_1 \cdot M_{TN} (-E_{11} \cdot Z_7 + E_{21} \cdot Z_6) & (N) & ) \\
M_{O_A_R} &= \frac{F_{TN}}{\lambda_1} (E_{11} \cdot Z_8 + E_{21} \cdot Z_9) + M_{TN} (E_{11} \cdot Z_{14} + E_{21} \cdot Z_{15}) & (Nm) & ) \\
M_{O_B_R} &= \frac{F_{TN}}{\lambda_1} (E_{11} \cdot Z_8 - E_{21} \cdot Z_9) + M_{TN} (E_{11} \cdot Z_{14} - E_{21} \cdot Z_{15}) & (Nm) & ) \\
\end{aligned} \quad (3.100)$$

Equations (3.100) can now be substituted into equations (3.98) and (3.99) above, which after rearrangement into matrix form gives

$$\begin{bmatrix} \frac{\lambda_1 z_{16}}{2k_{1W}} & \frac{\lambda_1^2 z_{17}}{k_{1W}} \\ \frac{\lambda_1^2 z_{18}}{k_{1W}} & \frac{\lambda_1^3 z_{19}}{k_{1W}} \end{bmatrix} \cdot \begin{bmatrix} F_{TN} \\ M_{TN} \end{bmatrix} = \begin{bmatrix} y_{RN} \\ \theta_{RN} \end{bmatrix}$$

$$\text{where } z_{16} = E_{11} \cdot (z_6 z_{12} - 2z_3 z_8) + E_{21} \cdot (z_7 z_{13} + 2z_3 z_9) + 1$$

$$z_{17} = E_{11} \cdot (z_6 z_7 - z_3 z_{14}) + E_{21} \cdot (z_6 z_7 + z_3 z_{15})$$

$$z_{18} = E_{11} \cdot (z_3 z_{12} - z_8 z_9) + E_{21} \cdot (-z_3 z_{13} - z_8 z_9)$$

$$z_{19} = E_{11} \cdot (2z_3 z_7 - z_9 z_{14}) + E_{21} \cdot (-2z_3 z_6 - z_8 z_{15}) - 1$$

The matrix equation is easily solved to give

$$F_{TN} = \frac{\lambda_1^2}{k_{1W} z_{20}} \cdot (\lambda_1 \cdot y_{RN} \cdot z_{19} - \theta_{RN} \cdot z_{17}) \quad (N) \quad \dots \dots (3.101)$$

$$M_{TN} = \frac{\lambda_1}{2 \cdot k_{1W} z_{20}} \cdot (\theta_{RN} \cdot z_{16} - 2\lambda_1 \cdot y_{RN} \cdot z_{18}) \quad (Nm) \quad \dots \dots (3.102)$$

$$\text{where } z_{20} = \frac{\lambda_1^4}{k_{1W}^2} \cdot \left[ \frac{z_{16} z_{19}}{2} - z_{17} z_{18} \right] \quad (N^{-2})$$

These values are then substituted back into equations (3.100) give the values of the ECFs for fig.3.33(iii).

The deflection and angle at any section "a" in fig.3.33(iii) can now be found from equations similar to (A.39) and (A.3.10):-

$$\begin{aligned}
 -y_{W_a} = & \frac{\lambda_1}{2k_{1W}} \cdot \left[ (-F_{TN} + F_{OA_R}) A \lambda_1^a + F_{OB_R} A \lambda_1^{(L_U - a)} \right] \\
 & + \frac{\lambda_1^2}{k_{1W}} \cdot \left[ (M_{TN} + M_{OA_R}) B \lambda_1^a + M_{OB_R} B \lambda_1^{(L_U - a)} \right] \quad (m) \\
 & \text{for } 0 < a \leq L_U \quad \dots \dots (3.103)
 \end{aligned}$$

where  $a = x_M - L_S - L_U$  on the R.H.S.

$$\begin{aligned}
 -\theta_a = & \frac{\lambda_1^2}{k_{1W}} \left[ (F_{TN} - F_{OA_R}) B \lambda_1^a + F_{OB_R} B \lambda_1^{(L_U - a)} \right] \\
 & + \frac{\lambda_1^3}{k_{1W}} \left[ (M_{TN} + M_{OA_R}) C \lambda_1^a - M_{OB_R} C \lambda_1^{(L_U - a)} \right] \quad (\text{Rad.}) \\
 & \text{for } 0 < a \leq L_U \quad \dots \dots (3.104)
 \end{aligned}$$

Where "a" on the R.H.S. will be given by  $a = x_M - L_S - L_U$

for  $M=1, \dots, M_W$

Note the introduction of minus signs on the LHS of each equation to "re-invert" the mill to its correct state.

Now as soon as a value of "a" is reached where  $\theta_a$  becomes positive (say  $a=a'$ ), then the "bounce" of the WR off the LIR is considered complete as it is heading downwards again. Equation (3.103) is now suspended, and subsequent deflection values are calculated by the "straight-line" principle (c.f. equation (3.97) as

$$y_{W_{X_M}} = y_{W_{a'}} + (X_M - a') \sin \theta_{a'} \quad (m) \quad \dots \dots (3.105)$$

for  $a' < X_M \leq L_U$

and  $M=1, \dots, M_W$

THE SECOND problem of note occurs when the original force on the LH unsupported WR end is negative, i.e. in figs. A.3.1 and A.3.2  $F_{WN}$  acts upwards rather than downwards. Under this condition, equation (A.3.8) cannot be used to specify the deflection of the LH end of the WR (for the same reason that equation (3.97) could not be used for the RH end with a negative  $\theta_{RN}$  value above). The procedure of "inverting" the mill is therefore once more adopted, but in this case it would be of little value to specify separate cases for the portion of the WR over the strip, and the RH end, and so the entire WR width is considered in a single step. Figure 3.34 depicts the situation with the WR resting above the lIR.

The deflection profile of the WR due to the force  $F_{WN}$  is then found in the same way as was the lIR deflection profile due to any given force in section 3.8.2. i.e.

$$M_{A_W} = \frac{-F_{WN}}{4\lambda_1} \cdot C_{\lambda_1} x_{WF_N} \quad (\text{Nm})$$

$$M_{B_W} = \frac{-F_{WN}}{4\lambda_1} \cdot C_{\lambda_1} (L_T - x_{WF_N}) \quad (\text{Nm})$$

$$Q_{A_W} = \frac{-F_{WN}}{2} \cdot D_{\lambda_1} x_{WF_N} \quad (\text{N})$$

$$Q_{B_W} = \frac{F_{WN}}{2} \cdot D_{\lambda_1} (L_T - x_{WF_N}) \quad (\text{N})$$

Equations (A.1.40), (A.1.41) and (A.1.42) are then applied using  $k_{1W}$ ,  $\lambda_1$ , etc. to give the ECFs  $F_{OA_W}$ ,  $F_{OB_W}$ ,  $M_{OA_W}$  and  $M_{OB_W}$ , after which the deflection at each of the  $M_W$  sections across the roll is found by (c.f. equation (3.90)):-

$$\begin{aligned}
 -y_{W_{x_M}} = & \frac{\lambda_1}{2k_{1W}} \left[ -F_{WN} \cdot A \lambda_1 |x_{WR_N} - x_M| + F_{OA_W} \cdot A \lambda_1 x_M + F_{OB_W} \cdot A \lambda_1 (L_T - x_M) \right] \\
 & + \frac{\lambda_1^2}{k_{1W}} \left[ M_{OA_W} \cdot B \lambda_1 x_M + M_{OB_W} \cdot B \lambda_1 (L_T - x_M) \right] \quad (m) \\
 & \text{for } M=1, \dots, M_W
 \end{aligned}$$

. . . . . (3.106)

Note that  $-y_{W_{x_M}}$  is found so as to "re-invert" the mill to its correct state.

We have now completely specified the deflection at the  $M_W$  points along the WR resulting from the application of a concentrated force  $F_{WN}$  to the unsupported LH end of the WR. The results are summarised below for convenience.

For the  $N^{th}$  concentrated force ( $F_{WN}$ ) from the front of the mill,

- A) If  $F_{WN}$  is negative (i.e. acting upwards, away from the roll gap),

For  $0 \leq x_M \leq L_T$ ,  $y_{W_{x_M}}$  is given by equation (3.106)

- B) If  $F_{WN}$  is non-negative

For  $0 \leq x_M < x_{WF_N}$   $y_{W_{x_M}}$  is given by equation (A.3.8a)

For  $x_{WF_N} \leq x_M < L_U$   $y_{W_{x_M}}$  is given by equation (A.3.8b)

For  $L_U \leq x_M \leq (L_U + L_S)$   $y_{W_{x_M}}$  is given by equation (A.3.9)

For  $(L_U + L_S) < x_M \leq L_T$  IFF  $\theta_{R_N}$  given by equation (A.3.14) is positive for  $F_{WN}$ , then

$y_{W_{x_M}}$  is given by equation (3.97)  
 (using  $y_{R_N}$  and  $\theta_{R_N}$  given by  
 (A.3.12) and (A.3.14))

OTHERWISE

$y_{W_{x_M}}$  is given by equation (3.103) up to and including the first value of  $x_M$  (say X) for which equation (3.104) gives  $\theta_{x_M}$  positive. For all values of  $x_M$  to the right of this point,

$y_{W_{x_M}}$  is given by equation (3.105) where  $a' = X$

Note that since the value of  $F_{WN}$  affects every one of these results, the whole procedure must be repeated for every value of N, and the resulting  $y_{W_{x_M}}$  values summed at each of the  $M_W$  points to give the total WR deflection profile due to all the elements of the array of  $J_W$  forces which act over the unsupported LH end ( $J_U$  in number).

3.9.2.2. WR Deflection due to a force acting on the RH unsupported end

This case is a mirror-image of the case considered in section 3.9.2.1 and is treated as such. Therefore, the analysis of section 3.9.2.1 is used after replacing

$x_{WF_N}$  with  $(L_T - x_{WF_N})$

Thus  $x_{WF_N}$  and the  $x_M$  values are effectively measured from the RH end of the roll rather than the left, and the situation becomes identical to that of section 3.9.2.1.

The final set of  $M_W$  values of  $y_W$  at  $x_M$  which result from the application of section 3.9.2.1 must then be reversed in order (using the method of equation (3.78)) to correct for the "mirror-image" approach.

### 3.9.2.3. WR deflection due to a force acting directly over the strip

For the portion of the WR over the strip (fig.3.35) this is the "normal" situation. The same method as used in section 3.8.2 therefore applies giving

$$M_{A_S} = \frac{F_{WN}}{4\lambda_{WS}} \cdot C \lambda_{WS} (x_{WF_N} - L_U) \quad (Nm)$$

$$M_{B_S} = \frac{F_{WN}}{4\lambda_{WS}} \cdot C \lambda_{WS} (L_S - x_{WF_N} + L_U) \quad (Nm)$$

$$Q_{A_S} = \frac{F_{WN}}{2} \cdot D \lambda_{WS} (x_{WF_N} - L_U) \quad (N)$$

$$Q_{B_S} = \frac{-F_{WN}}{2} \cdot D \lambda_{WS} (L_S - x_{WF_N} + L_U) \quad (N)$$

where  $\lambda_{WS}$  is given following equation (3.95).

Equations (A.1.40), (A.1.41) and (A.1.42) (using  $k_{WWS}$ ,

$\lambda_{WS}$  etc.) then give the ECFs  $F_{OA_S}$ ,  $F_{OB_S}$ ,  $M_{OA_S}$  and  $M_{OB_S}$ .

The resulting equations for deflection and angle are then

$$y_W = \frac{\lambda_{WS}}{2k_{WWS}} \left[ F_{WN} \cdot A \lambda_{WS} |x_{WF_N} - x_M| + F_{OA_S} \cdot A \lambda_{WS} (x_M - L_U) \right. \\ \left. + F_{OB_S} \cdot A \lambda_{WS} (L_U + L_S - x_M) \right] \\ + \frac{\lambda_{WS}^2}{k_{WWS}} \left[ M_{OA_S} \cdot B \lambda_{WS} (x_M - L_U) + M_{OB_S} \cdot B \lambda_{WS} (L_U + L_S - x_M) \right] \quad (m)$$

for  $L_U \leq x_M \leq (L_U + L_S)$  and  $M=1, \dots, M_W \dots$  (3.107)

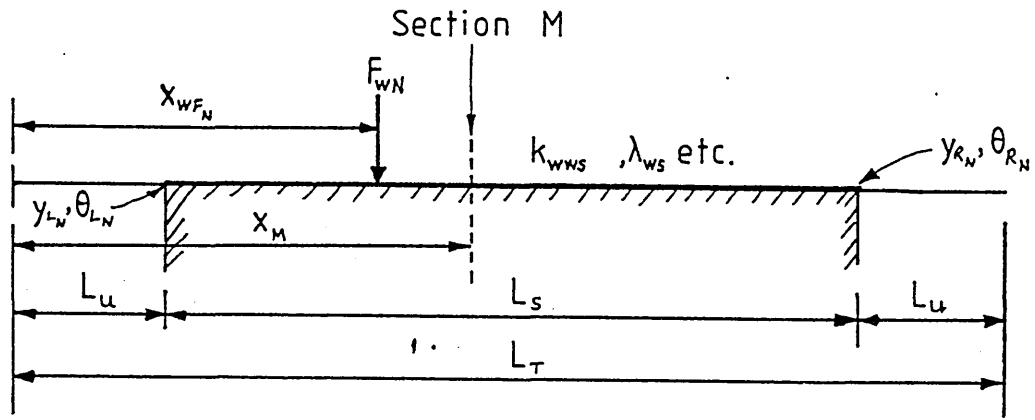


Fig.3-35 Conc. Force Acting on Portion of WR Over Strip

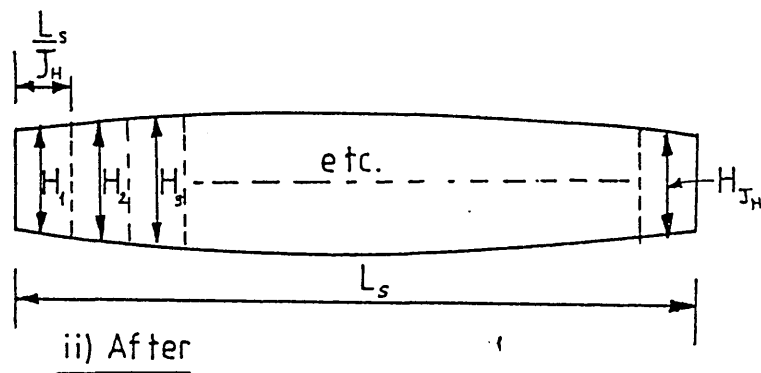
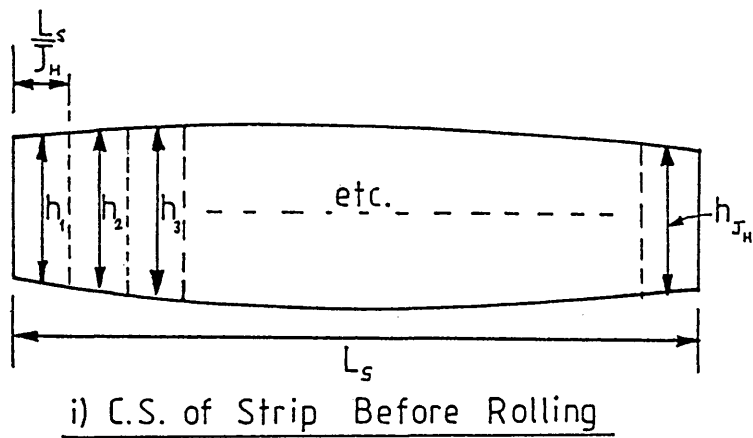


Fig.3-36 Effect of Rolling Upon Gauge Profile

$$\theta_{W x_M} = \frac{\lambda_{WS}}{k_{WWS}} \left[ F_{WN} \cdot Z \cdot B \lambda_{WS} |x_{WF_N} - x_M|^{-F_{OA_S}} \cdot B \lambda_{WS} (x_M - L_U) \right. \\ \left. + F_{OB_S} \cdot B \lambda_{WS} (L_U + L_S - x_M) \right] \\ + \frac{\lambda_{WS}^3}{k_{WWS}} \left[ M_{OA_S} \cdot C \lambda_{WS} (x_M - L_U) - M_{OB_S} \cdot C \lambda_{WS} (L_U + L_S - x_M) \right] \quad (\text{rad}) \quad \dots (3.108)$$

$$\text{for } L_U \leq x_M \leq (L_U + L_S)$$

$$\text{and } M=1, \dots, M_W$$

where  $Z = +1$  for  $L_U \leq x_M < x_{WF_N}$

$$Z = -1 \text{ for } x_{WF_N} \leq x_M \leq (L_U + L_S)$$

(Note that these equations could be compared also with equations (A.3.9) and (A.3.10), except that here there is zero moment and the force does not act at the LH end of the supported section).

By inserting  $x_M = L_U$  and  $x_M = (L_U + L_S)$  into these equations we obtain  $y_{L_N}$ ,  $\theta_{L_N}$  and  $y_{R_N}$ ,  $\theta_{R_N}$  as indicated in fig.17 (c.f. Appendix 3 following equation (A.3.10)) due to the  $N^{\text{th}}$  force from the front of the mill:-

$$y_{L_N} = \frac{\lambda_{WS}}{2k_{WWS}} \left[ F_{WN} \cdot A \lambda_{WS} (x_{WF_N} - L_U) + F_{OA_S} + F_{OB_S} \cdot A \lambda_{WS} L_S \right] \\ + \frac{\lambda_{WS}^2}{k_{WWS}} \cdot M_{OB_S} \cdot B \lambda_{WS} L_S \quad (m) \quad \dots \dots (3.109)$$

$$y_{R_N} = \frac{\lambda_{WS}}{2k_{WWS}} \left[ F_{WN} \cdot A \lambda_{WS} (L_U + L_S - x_{WF_N}) + F_{OA_S} \cdot A \lambda_{WS} L_S + F_{OB_S} \right] \\ + \frac{\lambda_{WS}^2}{k_{WWS}} \cdot M_{OA_S} \cdot B \lambda_{WS} L_S \quad (m) \quad \dots \dots (3.110)$$

$$\theta_{L_N} = \frac{\lambda_{WS}^2}{k_{WWS}} \left[ F_{WN} \cdot B \lambda_{WS} (x_{WF_N} - L_U) + F_{OB_S} \cdot B \lambda_{WS} L_S \right] \\ + \frac{\lambda_{WS}^3}{k_{WWS}} \left[ M_{OA_S} - M_{OB_S} \cdot C \lambda_{WS} L_S \right] \quad (rad.) \\ \dots \dots (3.111)$$

$$\theta_{R_N} = \frac{\lambda_{WS}^2}{k_{WWS}} \left[ -F_{WN} \cdot B \lambda_{WS} (L_U + L_S - x_{WF_N}) - F_{OA_S} \cdot B \lambda_{WS} L_S \right] \\ + \frac{\lambda_{WS}^3}{k_{WWS}} \left[ M_{OA_S} \cdot C \lambda_{WS} L_S - M_{OB_S} \right] \quad (rad.) \\ \dots \dots (3.112)$$

The deflection at any section of the WR where  $x_M$  falls over the strip has been given by equation (3.107) but the question of the unsupported WR ends remains. For the RH end, the situation is absolutely identical to that discussed in section 3.9.2.1, above (figs.3.32 and 3.33) i.e.  $y_{W_{x_M}}$  is given by equation (3.97) (using  $y_{R_N}$  and  $\theta_{R_N}$ )

if the result of (3.112) is non-negative or by equations (3.103) and (3.105) (with the ECFs corresponding to the force  $F_{WN}$  under investigation) if the result of (3.112) is negative.

For the LH unsupported end, if  $\theta_{L_N}$  (given by equation (3.111) is negative, then the mirror image of fig. 3.32 applies, and it is easily shown that

$$y_{W_{x_M}} = y_{L_N} - (L_U - x_M) \sin \theta_{L_N} \quad (m) \quad (3.113)$$

for  $0 \leq x_M < L_U$

and  $M=1, \dots, M_W$

If, however,  $\theta_{L_N}$  is positive, then the situation is the mirror-image of fig.3.33 and the analysis leading to equations (3.103) and (3.105) can be applied after replacing

$$\theta_{R_N} \text{ with } -\theta_{L_N}$$

and  $y_{R_N}$  with  $y_{L_N}$

and using  $a = L_U - x_M$

It is then necessary to apply the analysis for INCREASING "a" (i.e. decreasing  $x_M$ ) so that the position can be found where the WR "bounces back" off the LIR. This will be the value of  $x_M$  for which  $\theta_a$  (given by equation (3.104)) becomes positive again (say point a') after which equation (3.103) is suspended and  $y_{W_{x_M}}$  is then calculated by equation (3.105) for the remaining values of  $x_M$  until the extreme LH end of the roll is reached.

The deflection of the WR has now been completely specified due to the action of a concentrated force  $F_{WN}$  acting over the strip. The results are summarised below for convenience.

For  $0 \leq x_M < L_U$  IFF  $\theta_{L_N}$  given by equation (3.111) is negative, then

$y_{W_{x_M}}$  is given by equation (3.113)

OTHERWISE

$y_{W_{x_M}}$  is given by equation (3.103) (using

$$a = L_U - x_M, \theta_{R_N} = -\theta_{L_N}, y_{R_N} = y_{L_N}$$

and the corresponding values of  $F_{TN}$  and  $M_{TN}$  given by equations (3.101)

and (3.102)). The analysis must begin at the value of  $x_M$  nearest the top of of the range (i.e.  $x_M \approx L_U$ ) and continue for decreasing  $x_M$  until the section is reached (say  $x_M = X$ )

where  $\theta_{x_M}$  (given by (3.104) with

values as above) becomes positive.

For all subsequent  $x_M$  values (i.e.  $x_M < X$ ):-

$y_{W_{x_M}}$  is given by equation (3.105) written as  $y_{W_{x_M}} = y_{W_X} + (X - x_M) \sin \theta_X$

For  $L_U \leq x_M \leq (L_U + L_S)$   $y_{W_{x_M}}$  is given by equation (3.107)

For  $(L_U + L_S) < x_M \leq L$  IFF  $\theta_{R_N}$  given by equation (3.112) is

positive then

$y_{W_{x_M}}$  is given by equation (3.97)

### OTHERWISE

$y_W$  is given by equation (3.103)  
 $x_M$  using the appropriate values of  
 $F_{TN}$  and  $M_{TN}$  given by equations  
(3.101) and (3.102) up to and  
including the section (say  
 $x_M = X$ ) for which equation  
(3.104) gives  $\theta_{x_M}$  positive.  
 $y_W$  For all  $x_M > X$ , is given by  
 $x_M$  equation (3.105) using  $a' = X$

### 3.10 Calculation of Strip Shape

The analysis of strip shape changes in response to roll gap geometry changes forms a literature in its own right (see for example (37)-(39)). However, for the purposes of the present model, the philosophy of relative simplicity is maintained in this area, also and a purely geometric approach is taken. Any of the more complex methods could be used instead if desired.

Consider a piece of strip having the cross-sectional gauge profile shown in fig. 3.36(i), where the strip is divided across its width into  $J_H$  equal filaments, and the  $h$  values are measured at the centre of each.  $J_H$  is an odd number so as to give a gauge measurement at the centre of the strip. Let the gauge profile after rolling be as shown in fig. 3.36(ii), where the measurements are taken at the same points, and zero width-wise spread is assumed. Further, consider the piece of strip to have a length  $l_0$ .

prior to rolling, and after rolling let it be slit lengthwise into  $J_H$  filaments as shown in fig.3.37. If the reduction of gauge profile between figs. 3.36(i) and (ii) is not uniform across the width of the strip, then the filaments of fig.3.37(ii) will have non-uniform lengths as shown.

Assuming zero internal stress prior to rolling, no lateral spread, and conservation of volume during rolling, we can say that for the  $N^{\text{th}}$  filament,

$$l_0 h_N = L_N H_N \quad (\text{m}^2)$$

$$\therefore L_N = l_0 \cdot \frac{h_N}{H_N} \quad (\text{m}) \text{ for } N=1, \dots, J_H \quad \dots \dots (3.114)$$

Also, the mean length of the rolled filaments is given by

$$\bar{L} = \frac{l_0}{J_H} \cdot \sum_{N=1}^{J_H} \frac{h_N}{H_N} \quad (\text{m}) \quad \dots \dots (3.115)$$

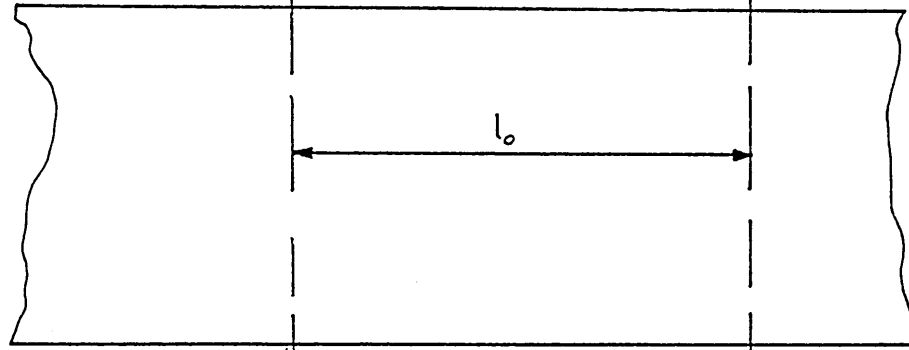
During normal rolling, the filaments obviously cannot extend relative to each other in the way shown in fig.3.37(ii), but are either stretched or compressed so as to conform to the length  $\bar{L}$ . This amount of stretching is called differential elongation, and is here defined as

$$\Delta L_N = \bar{L} - L_N \quad (\text{m}) \text{ for } N=1, \dots, J_H \quad \dots \dots (3.116)$$

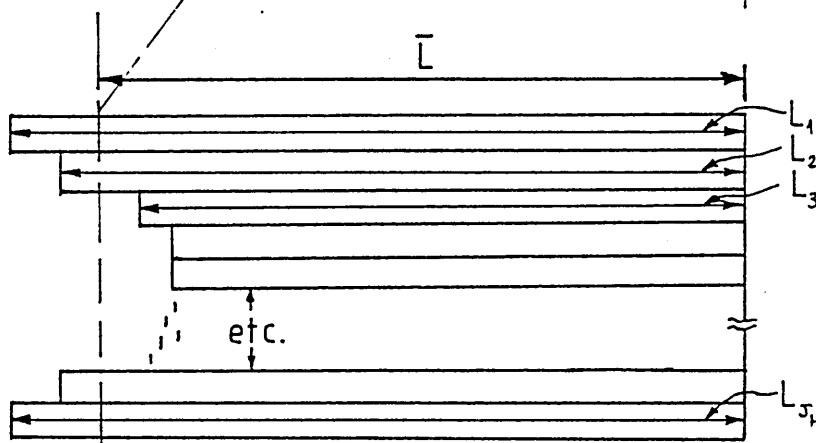
so that for a filament which is stretched (i.e. the strip is tight)  $\Delta L$  is positive. The differential strain in each filament is then defined as

$$\Delta \epsilon_N = \frac{\Delta L_N}{\bar{L}} \quad \text{for } N=1, \dots, J_H$$

and therefore the differential stress distribution across the strip is given by



i) Section of Strip Prior to Rolling



ii) Same Section Slit into Filaments After Rolling

Fig. 3-37 Effect of Rolling Upon Length

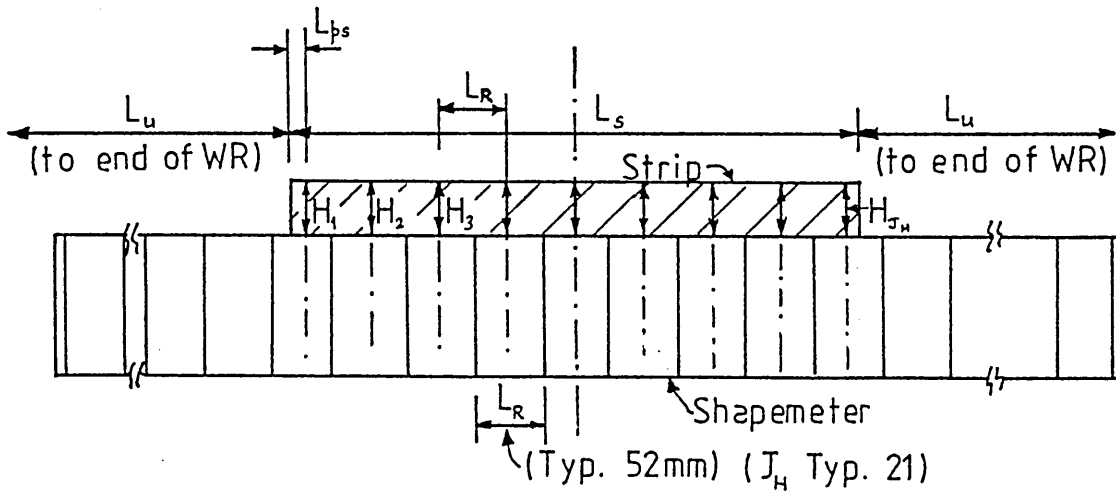


Fig. 3-38 Strip Passing Over Shapemeter Roll

$$\Delta\sigma_N = E_S \cdot \Delta\varepsilon_N \quad (\text{Nm}^{-2}) \text{ for } N=1, \dots, J_H \quad \dots \dots (3.117)$$

where  $E_S =$  Youngs Modulus for the strip ( $\text{Nm}^{-2}$ )

This quantity of differential stress is a measure of strip shape, and is displayed by the ASEA Stressometer shapemeters on the Sendzimir mill in question.

Substituting (3.114), (3.115) and (3.116) into (3.117) gives

$$\Delta\sigma_N = E_S \cdot \left[ 1 - \frac{J_H h_N}{J_H \sum_{Q=1}^{J_H} \frac{h_Q}{H_Q}} \right] \quad (\text{Nm}^{-2}) \quad \dots \dots (3.118)$$

for  $N=1, \dots, J_H$

Thus, shape is positive where the strip is tighter than the mean, and negative where it is slacker. For strip to have "perfect" shape, this internal stress distribution equation should give  $\Delta\sigma_N = 0$  for all  $N$ . Non-zero values of  $\Delta\sigma_N$  lead to the internal stresses in the strip forming "latent" (bad) shape. If these stresses grow large enough to overcome the section modulus of the material, then the strip will visibly buckle, forming "manifest" (bad) shape (see section 1, chapter 1.).

The input gauge profile of the strip ( $h_N$  in equation (3.118)) is known either from an estimate of the characteristics of the incoming strip (on the first pass) or by reading the output gauge profile stored at a number of points during the previous pass. The output gauge profile ( $H_N$ ) is calculated as follows, using the knowledge of the mean output gauge (from the plant instrumentation) and the WR profile generated by the model:-

The values of  $\Delta\sigma_N$  given by equation (3.118) must be given at points which coincide with the centres of the rotors on the ASEA Stressometer, if any simple model/plant comparison is to be made. Let the shapemeter have  $J_R$  rotors of width  $L_R$ (m). Note that  $J_R$  is an odd number (31 for the present Z mill) so as to place a rotor centre at the strip centre. Fig.3.38 shows the strip passing over the segmented shapemeter roll. The number of shapemeter rotors covered by the strip is given by

$$\frac{L_S}{L_R} \dots \dots \dots (3.119)$$

which will probably not be an integer at this stage, but must be made such. Since  $J_R$  is an odd integer, and fig. 3.38 is symmetrical about its vertical centre-line, then the number of shapemeter rotor centres covered by the strip ( $J_H$ ) must also be odd. An integerised version of (3.119) is obtained by truncating its fractional part:-

$$i_H = \frac{L_S}{L_R} \left| \begin{array}{l} \text{fractional part} \\ \text{set to zero.} \end{array} \right.$$

This is then tested to ascertain whether it is even or odd (e.g. by dividing by 2 and testing for a remainder). Consideration of fig. 3.38 shows that if  $i_H$  is even, then  $J_H = i_H+1$ ; whereas if  $i_H$  is odd it needs no alteration. Therefore

$$\begin{array}{l} J_H = i_H \quad \text{for } i_H \text{ odd} \\ \text{or } J_H = i_H+1 \text{ for } i_H \text{ even} \end{array} \left. \begin{array}{l} ) \\ ) \\ ) \\ ) \end{array} \right. \dots \dots \dots (3.120)$$

The value of  $L_{ps}$  in fig. 3.38 is then found by

$$L_{ps} = \frac{L_S - L_R (J_H - 1)}{2} \quad (m) \quad (3.120)$$

The distance from the LH end of the mill at which the  $N^{\text{th}}$  value of gauge must be calculated to coincide with a shapemeter rotor centre, can then be found as

$$x_N = L_U + L_{ps} + (N-1)L_R \quad (m) \quad \text{for } N=1, \dots, J_H \quad \dots (3.121)$$

Now the WR deflection is known at  $M_W$  points along the roll (from section 3.9), also measured from the front of the mill, but it is most improbable that the  $J_H$  values of  $x_N$  given by (3.121) will correspond precisely with values from the set of  $M_W$  values of  $x_M$  used in section 3.9 to find  $y_W$ . To find WR deflection at points corresponding to (3.121) therefore, a curve could be fitted to the  $M_W$  values of  $y_W$  previously calculated for the WR (section 3.9) and the  $J_H$  values of  $y_{x_N}$  read off it. Fitting a single high-order curve and interpolating in this way, is prone to numerical inaccuracies however, and the method employed instead (see below) is more accurate, although somewhat laborious to set down on paper. (The computer mechanization is quite simple of course).

For each  $x_N$  value given by (3.121), a search is made through the  $M_W$  values (at which WR deflection is known) until the nearest value of  $x_M$  to  $x_N$  is found. The  $x_M$  values on either side of this value (i.e.  $x_{M-1}$  and  $x_{M+1}$ )

are also taken; so that three values of  $x_M$  are considered, with the value of  $x_N$  falling within the range of the three. A quadratic of the form  $y = ax^2 + bx + c$  is then fitted to the three points. We therefore have

$$y_{W_{x_{M-1}}} = a_N x_{M-1}^2 + b_N x_{M-1} + c_N$$

$$y_{W_{x_M}} = a_N x_M^2 + b_N x_M + c_N$$

$$y_{W_{x_{M+1}}} = a_N x_{M+1}^2 + b_N x_{M+1} + c_N$$

which are simultaneously solved to give

$$b_N = \frac{\begin{bmatrix} y_{W_{x_{M-1}}} & -y_{W_{x_{M+1}}} \end{bmatrix} \begin{bmatrix} x_M^2 - x_{M-1}^2 \end{bmatrix} + \begin{bmatrix} y_{W_{x_M}} & -y_{W_{x_{M-1}}} \end{bmatrix} \begin{bmatrix} x_{M+1}^2 - x_{M-1}^2 \end{bmatrix}}{\begin{bmatrix} x_{M-1} & -x_{M+1} \end{bmatrix} \begin{bmatrix} x_M^2 - x_{M-1}^2 \end{bmatrix} + \begin{bmatrix} x_M & -x_{M-1} \end{bmatrix} \begin{bmatrix} x_{M+1}^2 - x_{M-1}^2 \end{bmatrix}}$$

$$a_N = \frac{y_{W_{x_M}} - y_{W_{x_{M+1}}} - b_N \cdot \begin{bmatrix} x_M - x_{M-1} \end{bmatrix}}{x_M^2 - x_{M-1}^2}$$

$$c_N = y_{W_{x_{M+1}}} - a_N \cdot x_{M+1}^2 - b_N x_{M+1}$$

The WR deflection corresponding to the point  $x_N$  measured from the front of the mill (i.e. corresponding to a shapemeter rotor centre) is then given by

$$y_{W_{x_N}} = a_N x_N^2 + b_N x_N + c_N \quad (m) \quad \text{for } N=1, \dots, J_H \dots \dots (3.122)$$

where the  $x_N$  are given by (3.121).

(Note that if a value of  $x_N$  should fall so close to one end of the WR that the nearest  $x_M$  value is the last on the roll, then the end three values of  $x_M$  are used).

Since the number of forces taken to act on the WR ( $J_{WF}$ ) and the number of points at which deflection of the WR was calculated ( $M_W$ ) were chosen to be large enough to give a smooth deflection profile, the fitting of a quadratic to any three consecutive points will introduce negligible errors.

When rolling strip in a four-high rolling mill, the conditions around the roll-bite are such that if a bending profile is forced onto the upper WR, then the lower WR will always adopt the inverse profile. The strip will therefore always look symmetrical about its horizontal axis. It is thought however, that this condition will not apply in a Sendzimir mill, since the lower WR is not free to deflect to the same extent. Therefore, if the incoming strip has the gauge profile of fig. 3.39(i) and good shape, to maintain the good shape whilst imparting a per-unit reduction  $\delta_R$  the roll-bite must adopt in the limit the profile shown in fig. 3.39(ii) (neglecting elastic recovery of gauge and the lower WR camber). As has been mentioned previously, although fig. 3.39(ii) looks extreme, it is grossly exaggerated as  $c_S$  is some four or five orders of magnitude less than  $L_T$ . Due to this relatively minute lateral bending of the strip, it is expected that it will elastically recover after rolling

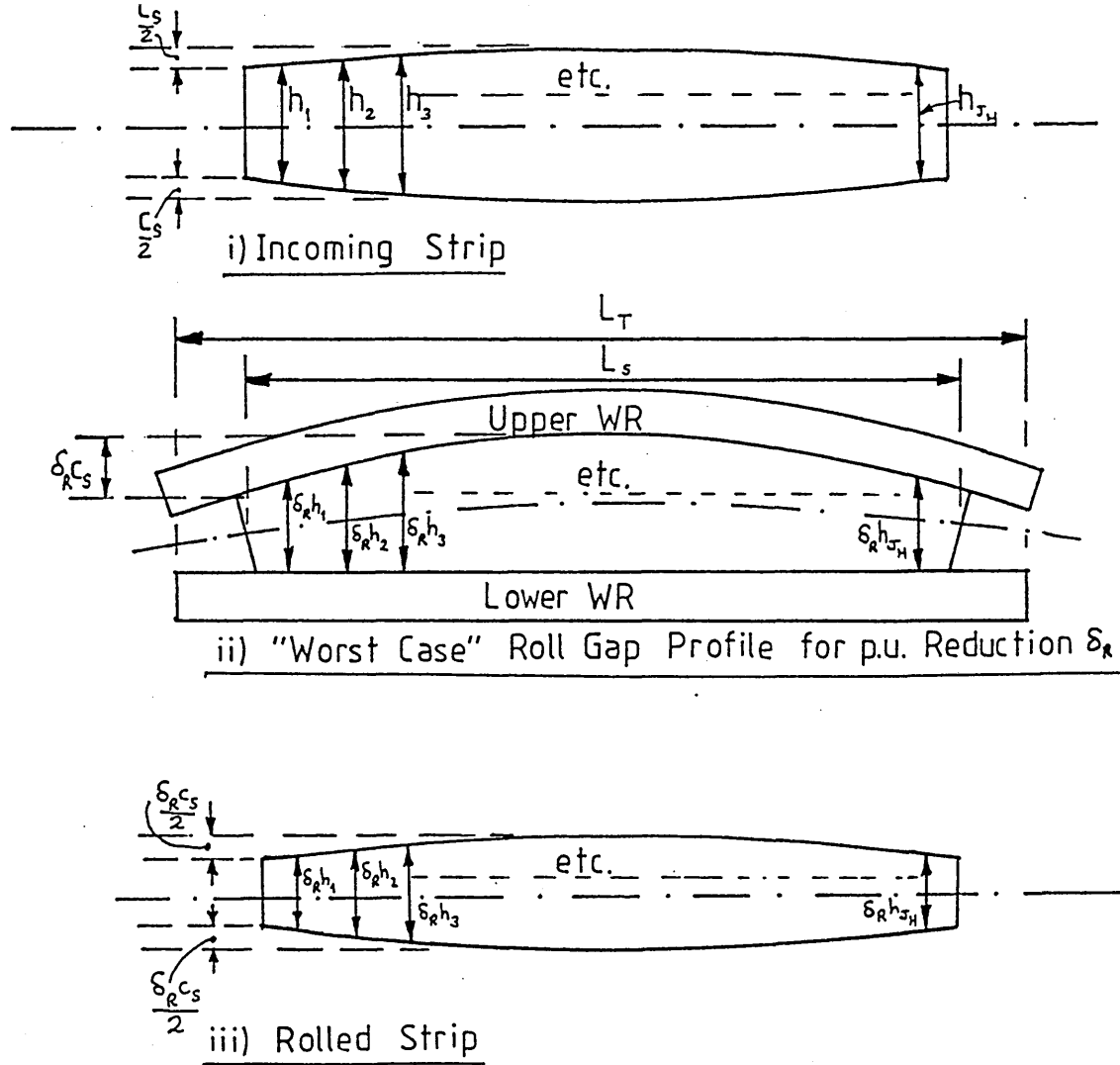


Fig.3:39 Profile Changes Assumed During Rolling

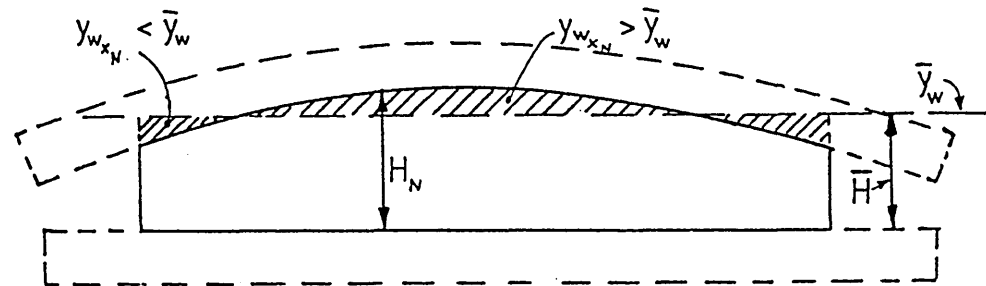


Fig.3:40 Pertaining to Strip Exit Gauge Calculation

to the profile of fig. 3.39(iii), and so the good shape will be maintained.

The output gauge vector (H) for use in equation (3.118) is therefore found by considering the roll-bite profile to be as per fig.3.39(ii). The mean output gauge H is known from the mill instrumentation, and the mean upper WR deflection for the  $J_H$  points across the strip can be found by

$$\bar{y}_W = \frac{1}{J_H} \cdot \sum_{N=1}^{J_H} y_{W_{x_N}} \quad (m)$$

where the  $y_{W_{x_N}}$  are given by (3.122).

We now assume that this mean value of WR deflection corresponds to the mean output gauge as shown in fig.3.40. The  $J_H$  values of  $H_N$  are then found by superimposing the deviation of the WR deflection from the mean onto H at each point:-

$$H_N = \bar{H} + \bar{y}_W - y_{W_{x_N}} \quad (m) \quad \text{for } N=1, \dots, J_H \quad \dots \dots (3.123)$$

Equation (3.118) can now be used with the results of equations (3.120) and (3.123) and the known input gauge profile, to give the change in strip shape (due to all the actuator movements) at points across the strip which coincide with the centres of all the covered shape-meter rotors. If the incoming strip has "perfect" shape (all  $\Delta\sigma_{IN} = 0$ ) then equation (3.118) gives absolute shape

after rolling. Otherwise, the stress profile given by (3.118) must be superimposed on that existing in the strip to obtain absolute shape. (This is thought to be the best simple approximation which can be made). The incoming shape must be estimated on the first pass, but on each subsequent pass the shapemeter output stored at a number of intervals during the preceding pass can be used.

### 3.11 The Computer Model and the Mill Gain Matrix

It is not proposed to enter into great detail concerning the actual algorithms and flowcharts of the model, since the previous discussion of the static model itself covers, in one way or another, all that would be said. Suffice it to say that the model is fundamentally a computer mechanization of the pseudo-flowchart shown in figure 3.18, and as such it contains all the necessary programming to implement all the equations developed in sections 3.2 to 3.10 inclusive and appendices 1 to 4 inclusive. The language of the model is FORTRAN (with DEC additions).

The model started life mounted on an ICL1903 installation, where it was overlaid to run in 32k of memory. By force of circumstance, it presently resides on a Digital PDP11/70 installation under the RSTS/E operating system. This limits user memory to 28k, and no amount of overlaying could achieve this. Therefore, the program is split into two parts called ZMODEL and ZMODL2. The structure of each part is broken down into a large number

of function and subroutine subprograms, but no details of these will be given here. The model can be run either interactively from a terminal, or in a batch mode. The overall function of each half of the model is as follows.

Programme ZMODEL requires as input data:

Young's Modulus and Poisson's Ratio for the rolls.

The length of the rolls.

The maximum (i.e. barrel-centre) diameter of every roll in the top half of the cluster (this allows for example, different diameters of the outer second intermediate rolls and the central second intermediate rolls - which is normal practice).

The camber taken off these diameters for every roll.

The length and magnitude of first intermediate roll tapers fitted.

The geometry of the mill housing and backing bearings in the form of various plant dimensions, eccentricities, pitch circle radii, length and pitch of backing bearings etc.

Number of backing bearings (variable so as to allow application to any 20-high Z mill).

Strip width.

Strip annealed gauge and yield stress.

Entry and Exit gauges and tensions for the present pass.

Setting of Screwdown rack (in operator's divisions).

Setting of all eight As-U-Roll racks (perturbation) (operator's divisions).

Setting of both side eccentrics (in operator's divisions).

Setting of upper and lower first intermediate roll tapers.

Clearly, much of this data will not be varied from one run of the model to the next. Therefore such data are fixed at the beginning of the programme, and are only alterable by editing the appropriate file. The remainder of the data are input from the keyboard or batch file in answer to programme prompts.

The output data from ZMODEL includes the following (and much more besides!):-

All input data for verification.

Rolling load predicted by the roll force model, together with accuracy indication.

All force components and angles shown on figure 3.16.

B.O.E.F. foundation moduli.

Forms and magnitudes of loadings transferred via the backing bearings.

All data required by the second half of the model is then written onto a disc file and the first programme terminates with a suitable prompt to the user or batch control programmes to run the second half of the model.

Programme ZMODL2 requires as input data:

All the data stored on disc by ZMODEL (which is checked for sensible values as it is read in automatically).

The number of points along the various rolls at which deflection is to be calculated.

The numbers of forces to be calculated to act on each roll.

Options for graph plotting and shape calculation (see below).

The output from ZMODL2 includes:-

Tables of deflection values taken along the 2IR, 1IR and WR.

Optional graphs plotted on a CIL plotter to include any or all of the workroll deflection profiles due to each force acting upon the workroll, the total workroll deflection profile, and an amplified version of the deflection over the strip width.

Tables of roll gap magnitude vs. distance across the mill, together with strip gauges and shape. These may optionally be given at the shapemeter rotor centres, at eight points across the mill, or at eight points across the strip (see below).

One set of model results occupies typically seven sheets of 120 character line-printer paper, and cannot therefore readily be reproduced in a form suitable for direct inclusion in this thesis. However, selected results and sample graphs are discussed below.

Now for the purposes of a control scheme design, what we require is a gain matrix for the mill. This takes the form of a matrix of shape sensitivities to actuator movements. The initial work on the control system (Chapter 6) assumed for simplicity a system of eight As-U-Roll actuators controlling the shape at eight points measured across the mill, yielding obviously an  $8 * 8$  system. The mill matrix for such a system ("Plant matrix") is given as

$$\tilde{G}_p = \begin{bmatrix} g_{11} & g_{12} & g_{13} \cdots \cdots \cdots g_{18} \\ g_{21} & g_{22} & g_{23} \cdots \cdots \cdots g_{28} \\ \cdot & \cdot & \cdot & \cdot \\ \cdot & \cdot & \cdot & \cdot \\ \cdot & \cdot & \cdot & \cdot \\ g_{81} & g_{82} & g_{83} \cdots \cdots \cdots g_{88} \end{bmatrix}$$

where  $g_{ij}$  represents the shape gain of the  $j^{\text{th}}$  As-U-Roll actuator from the front of the mill, at the  $i^{\text{th}}$  section of strip from the front of the mill (in units of shape change per unit rack displacement,  $Nm^{-2}/m$ . However,  $Nmm^{-3}$  is a more practical unit).

To obtain such a matrix, the entire static model is run eight times in succession. Each time, one As-U-Roll rack only is moved by a given small amount. The vector of eight shape values across the strip given by the run is then divided by the As-U-Roll motion thus giving the column of the gain matrix corresponding to the As-U-Roll which was moved. Therefore eight runs give the entire matrix.

For practical control schemes however (see chapter 6), the matrix will not be  $8 \times 8$ , but will be of size  $N \times 8$  where  $N$  is the number of covered shapemeter rotors. Nevertheless, the same procedure applies, and each of the eight runs of the model will yield an  $N$ -vector for one column of  $\tilde{G}_p$ , where  $\tilde{G}_p$  is now:-

$$\tilde{G}_P = \begin{bmatrix} \xi_{11} & \xi_{12} \dots \dots \dots \xi_{18} \\ \xi_{21} & \xi_{22} \dots \dots \dots \xi_{28} \\ \cdot & \cdot & & \cdot \\ \cdot & \cdot & & \cdot \\ \cdot & \cdot & & \cdot \\ \xi_{N1} & \xi_{N2} \dots \dots \dots \xi_{N8} \end{bmatrix} \quad (Nmm^{-3}) \dots (3.124)$$

### 3.12 Discussion of Results

Very many runs of this static mill model have been carried out for various purposes, but it is not intended to present here a vast anthology of results. Rather, the mill gain matrices produced by the model will be discussed (since these are its major raison d'être). Furthermore, the matrices for only a limited range of parameters will be considered - namely those most relevant to the present studies.

Many model parameters were held constant during all the runs to be described, and these are as follows (based upon practical values in the main):-

For roll material, Young's modulus =  $203 \cdot 10^9 \text{ Nm}^{-2}$

Poisson's Ratio = 0.3      Length of roll barrels = 1.7m

Roll diamters (m):- (zero roll cambers were used for these runs)

Sacking Bearings	0.405	
All Second Inter.Rolls	0.235	
First Inter.Rolls	0.137	Plus a section 0.559 m long tapered at 2mm/m off diameter.
Workrolls	0.09	

## Mill Geometry

Separation of central backing shaft centres (e.g. B & C)

$$= 0.419\text{m}$$

Separation of outer backing shaft centres (e.g. A & D)

$$= 1.094\text{m}$$

Separation of central and outer backing shaft centres

$$(e.g. A \& B) = 0.423\text{m}$$

Number of backing bearings = 7

Length of barrel of each bearing = 0.171m

Pitch of bearings = 0.221m

Screwdown disc eccentricity =  $8.89 \times 10^{-3}\text{m}$

As-U-Roll ring eccentricity =  $1.55 \times 10^{-3}\text{m}$

Side eccentric disc eccentricity =  $4.44 \times 10^{-3}\text{m}$

## Miscellaneous

Amount of first inter-roll tapers in play = 0

Strip incoming gauge =  $2.4 \times 10^{-3}\text{m}$

Strip incoming camber = 0

Roll gap coefficient of friction = 0.06

Young's Modulus for strip =  $203 \times 10^9 \text{ Nm}^{-2}$

Other model parameters were perturbed to investigate their effects, but the values unless otherwise stated were as follows:-

Screwdown Position = 0 (Datum)

Side Eccentric Positions = 0 (Datum)

As-U-Roll positions = 0 (Datum) except for the single As-U-Roll perturbed to produce the appropriate column of the gain matrix, which is moved to -0.54 operator's divisions..

Strip width = 1.61m (to give all 31 shapemeter rotors covered)

Annealed gauge of strip =  $2.4 \times 10^{-3}\text{m}$

(Cont'd.)

Yield stress curve = INCO curve of yield stress vs.reduction  
for EN304 stainless steel.

Exit strip gauge =  $2.05 \cdot 10^{-3} \text{m}$

Back Tension =  $134 \cdot 10^3 \text{N}$

Front Tension =  $191 \cdot 10^3 \text{N}$

This set of data yields the cluster angles and force components (see fig.3.16) below, which may be compared with those given in section 3.3 (following equation (3.41)).

$\theta_1 = 0^\circ$	$F_1 = P_T$
$\theta_2 = 40.3^\circ$	$F_2 = 0.655 P_T$
$\theta_3 = 23.3^\circ$	$F_3 = 0.219 P_T$
$\theta_4 = 59.7^\circ$	$F_4 = 0.591 P_T$
$\theta_5 = 78.3^\circ$	$F_5 = 0.536 P_T$
$\theta_6 = 40.8^\circ$	$F_6 = 0.266 P_T$
$\theta_7 = 4.4^\circ$	$F_7 = 0.191 P_T$
$\theta_8 = 22.2^\circ$	$F_8 = 0.423 P_T$

(the cluster is symmetrical under these conditions so the right-half values are identical).

The rolling load  $P_T$  is calculated as  $3.25 \cdot 10^6 \text{N}$  under these conditions, with a deformed workroll radius of  $50.9 \cdot 10^{-3} \text{m}$ , This represents a fairly light loading for this mill.

The gain matrix corresponding to this standard set of data, and evaluated at eight points across the strip is given in Appendix 5 (section A5.8). Every element in the matrix has been treated with a simple scalar multiplier (the same for each element) to give these values. This was done in the light of early plant tests, to give values in closer agreement with reality than

the untreated model. The multiplier is 0.0054. One possible reason for this requirement is the simplistic approach to the calculation of the actual strip shape (equation (3.118)) in which Young's modulus is used as a multiplier. It is very probable that, due to the plastic nature of the rolling process, a value of gradient on the portion of the stress-strain curve above the yield point should be used rather than Young's modulus (which is, of course, the gradient below the yield point). For the material in question, this upper portion of the curve flattens out very significantly, and the factor given above is quite feasible. All the matrices to be discussed have been processed in this way to allow direct comparison.

The matrix of A5.8 may be compared with that given in A5.9 which was derived by Gunawardene for similar conditions (Ref.16, section 6.6, p.151). It can be seen that the two models are in good basic agreement, although the present model's computer execution time is only a small fraction of that of Gunawardene's model. Furthermore, it can be seen that the matrix produced by the present model exhibits the absolute symmetry which is expected under the conditions for which it was run (i.e.  $g_{ij} = g_{(9-i), (9-j)}$ ), whereas numerical errors in Gunawardene's model have disrupted this to some extent in the matrix of A5.9. This is due to the much greater computational complexity of Gunawardene's model - which does, however, pay off in other respects (see later).

Another feature of the matrix is that, as expected, vertical columns sum to zero (within rounding errors); since shape is displayed with respect to mean the average value across the strip (down the column) must be zero. The horizontal rows should also sum to zero (if each As-U-Roll is moved by the same amount, a pure gauge change will result - not a shape change), but this is not actually the case, small errors being present. The discrepancy is due to numerical errors, but is generally less than the errors in the matrix of A5.9. One unusual feature common to both models is that As-U-Roll number 2 appears to have a greater effect upon the portion of strip nearer to As-U-Roll number 1 than does As-U-Roll number 1 itself (i.e.  $g_{12} > g_{11}$ ). This is at first sight, incorrect, and has not been conclusively observed on the plant, but a tentative explanation is possible (this applies to the present model, i.e. to the matrix given in A5.8) and is now proffered.

Figures 3.41(a) to 3.41(d) give the workroll deflection graphs produced by the model during calculation of the matrix of A5.8. Graph (a) is the deflection due to motion of As-U-Roll 1 only, graph (b) is for As-U-Roll 2 only, etc. As-U-Rolls 8,7,6 and 5 simply produced mirror images of the graphs for As-U-Rolls 1,2,3 and 4 respectively. Consider graphs (c) and (d), and notice that the deflection profiles are extremely similar both in form and magnitude, being simply shifted laterally to coincide with the appropriate As-U-Roll position. This is due to the fact that for both these As-U-Rolls there is

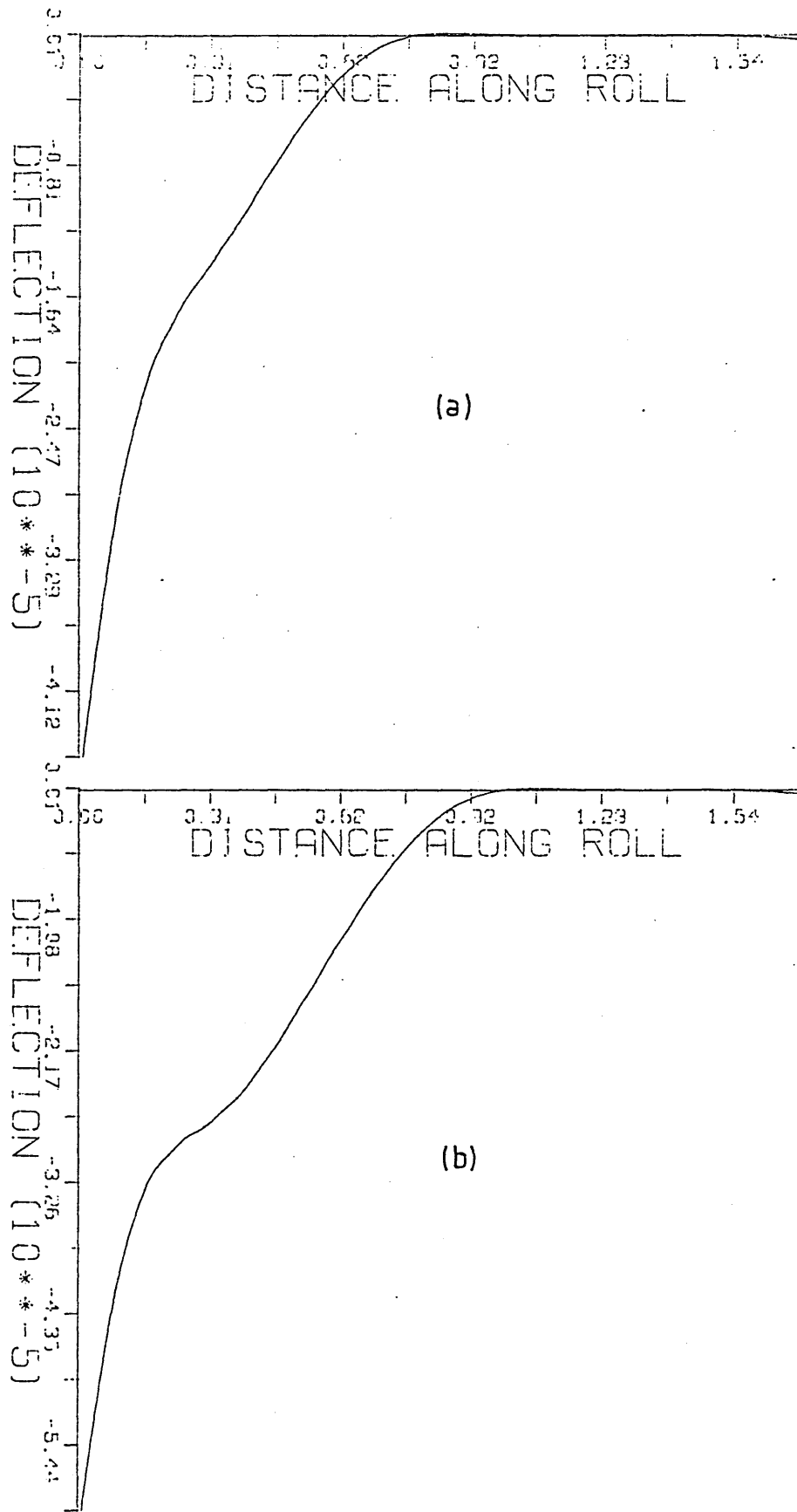


Fig. 3-41 Workroll Deflections for 1.61m Strip

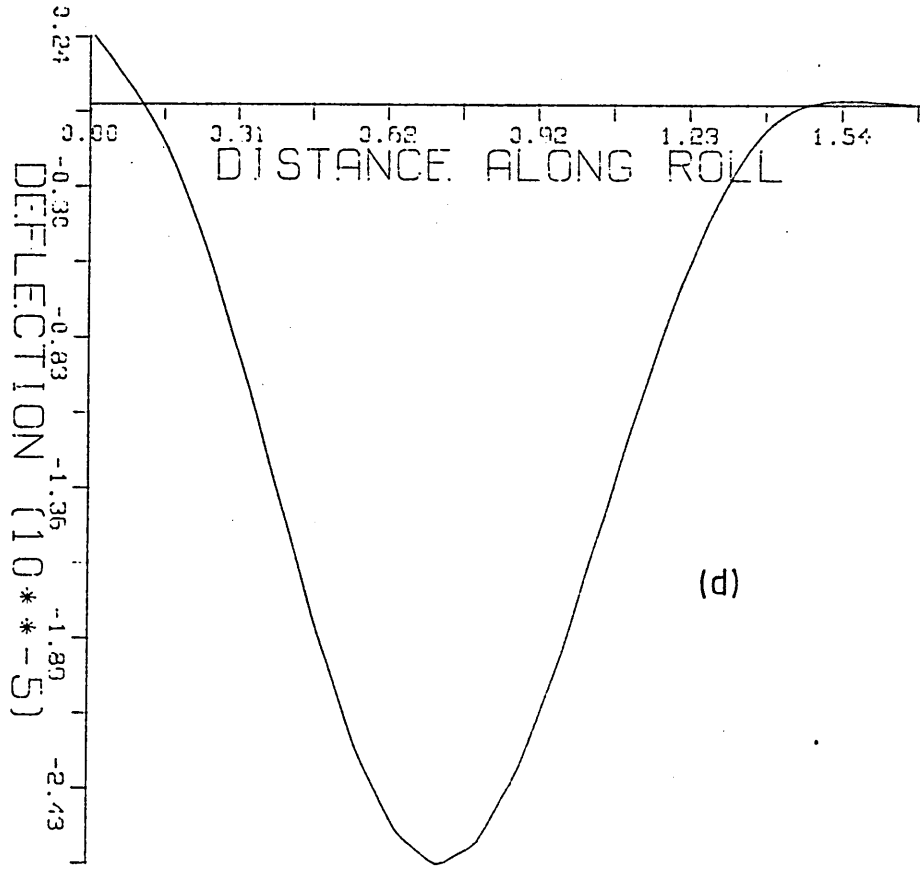
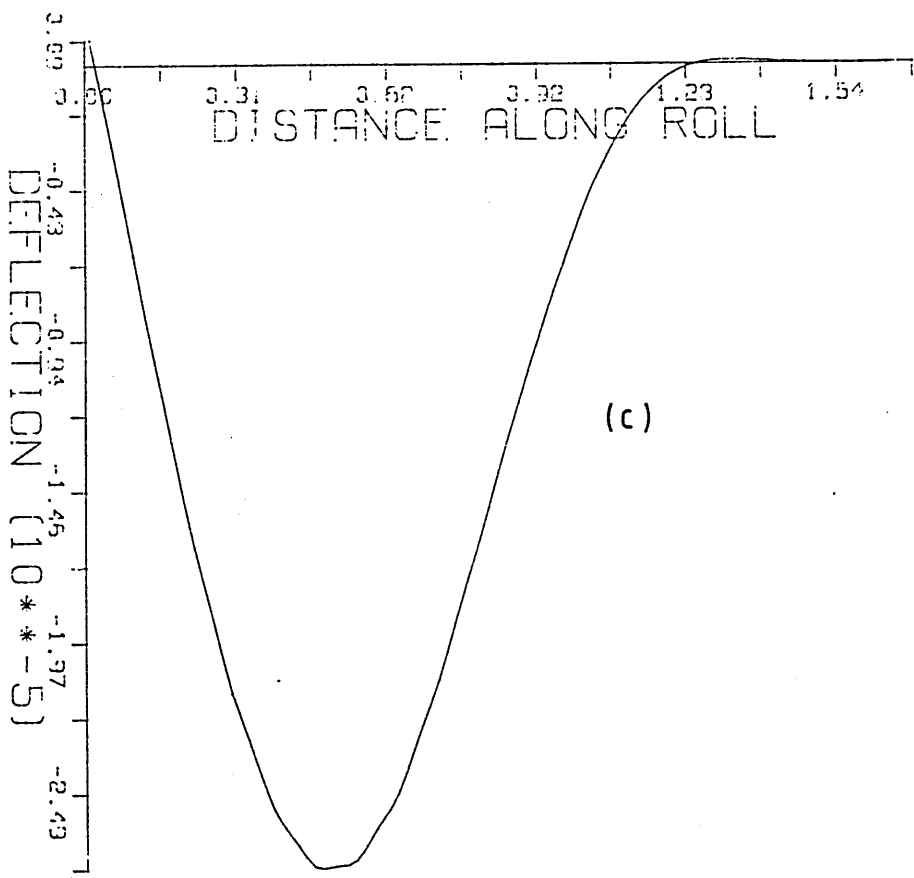


Fig. 3-41 Contd.

plenty of strip to either side of the As-U-Roll location, and the strip edges have no effect therefore. Consider now graph (b). Here, the edge of the strip becomes significant. It is placed at 0.045m on the horizontal scale, whilst As-U-Roll 2 is at 0.275m. The downward motion of the As-U-Roll rack will therefore cause a certain amount of force on that part of the workroll which is unsupported to the left of the strip edge. This is treated as a cantilever and is expected to deflect much more than when strip is present (as will be seen by comparing the maximum deflection of graph (b) with graphs (c) or (d)). Graph (b) exhibits two distinct portions to the deflection. The portion over the strip (from about 0.15m to 0.92m) exhibits similar behaviour to the right-hand portions of graphs (c) and (d), tending to "bottom out" at approximately  $-2.8 \times 10^{-5}$ m. The cantilevered portion, however, deflects more easily and causes thinning of the strip edge as it runs into the supported portion thus building up the entire graph. Now, in graph (a), As-U-Roll 1 is virtually coincident with the strip edge. Therefore, its influence on the supported portion of the strip is not as great as that of As-U-Rolls 2,3 and 4. The "supported" portion of the deflection curve, such as it is, appears to "bottom out" therefore at say  $-1.5 \times 10^{-5}$ m. However, the As-U-Roll (1) is not actually over the unsupported portion of the workroll (as would be the case for narrower strips) and its influence on the cantilevered portion is therefore not much greater than that of As-U-Roll 2. The net effect consequently is that the maximum deflection due to As-U-Roll 2 is greater than

that due to As-U-Roll 1, hence the entries in the gain matrix. It is stressed that the Author does not have great confidence in this "explanation", and clearly more work is possible in this area.

The 8 x 8 matrix discussed above is of little practical use, and was included simply to allow comparison with the work of Gunawardene. The practical matrix for 1.61m strip is actually 31\*8 (i.e. shape calculated at each covered shapemeter rotor) and is given in Appendix 5, section A5.10. The same comments apply as for the matrix of A5.8, which in fact describes precisely the same conditions (for example, row 1 of the A5.8 matrix lies at a position on the strip between rows 2 and 3 of the A5.10 matrix, whilst row 4 of A5.8 is almost coincident with the position on the strip of row 14 of A5.10, etc.). This is the matrix which will later be used to represent the plant in simulation studies (Chapter 7, section 7.5).

The model was run to produce such matrices for several different strip widths. Sections A5.11 and A5.12 of Appendix 5 give the matrices for 1.3m strip (25 covered rotors) and 0.99m strip (19 covered rotors) respectively. For an identical rolling schedule except for narrower material, the rolling load would be expected to reduce. This is found to be the case, the rolling loads for 1.61m wide, 1.3m wide and 0.99m wide strip being  $3.25 \cdot 10^6 \text{ N}$ ,  $2.53 \cdot 10^6 \text{ N}$  and  $1.81 \cdot 10^6 \text{ N}$  respectively as given by the model. As the strip becomes narrower, the roll flattening therefore reduces. The elastic foundation constants are

therefore somewhat reduced, which implies that a given deflection forced onto the second intermediate rolls by the As-U-Rolls, will produce lower loadings upon the other rolls in the cluster, and less deflection of the strip. The elements in the gain matrices would therefore be expected to reduce as one progresses from section A5.10 to A5.12. It appears initially however, that this is not the case, as the eye automatically begins to scan the matrices from element  $g_{11}$ . However, we can only directly compare the actions of As-U-Roll racks which are well over the strip for every width considered, so that strip edge effects are excluded. This limits the comparison to columns 3,4,5 and 6 of the matrices. In addition, we can similarly only compare the shape at rotors which are not much affected by As-U-Rolls other than 3,4,5 and 6 for the same reason. This limits us to the middle 11 rows or so of each matrix. Thus only the central 11 rows and 4 columns may be compared fairly. When comparison is limited in this manner, it can be seen that the gains do in fact decrease with decreasing strip width. For example, taking the middle row and column 4 in each matrix (A5.10, A5.11 and A5.12) as the strip width decreases 1.61m, 1.3m, 0.99m; the gain decreases  $1.18Nmm^{-3}$ ,  $0.93Nmm^{-3}$ ,  $0.58Nmm^{-3}$ . The reason for the large gain increases in other parts of the matrix (e.g. element  $g_{11}$ ) is that as the strip becomes narrower, the outer As-U-Rolls do not lie over the strip at all, but over the unsupported (cantilevered) sections of the upper workrolls. There is consequently only a relatively small

resistance to deflection, and some very large deflections indeed are given by the model at the workroll ends. The effect of this is to bend the cantilevered sections over the strip edges like a lever, giving much greater reductions in the edge zones than might be expected, and therefore higher gains. That having been said, it must be admitted that these peripheral gains are thought to be much too high under these conditions. There are various reasons for this, but one of the main inaccuracies in the model is probably the manner in which loadings on the unsupported workroll ends are calculated and handled (section 3.9), and it has already been said that further work is required in this area. Also, no facility has so far been included in the model to allow for the ends of the upper and lower workrolls coming into contact when rolling narrow strip. This would also reduce these large peripheral gains, as the leverage effects of the cantilevered roll ends on the strip edges would be greatly reduced. The lack of confidence in the mill matrices for very narrow strip is not a serious problem however, as most of the control system design and simulation (see later chapters) uses wider strips. Where narrow-strip matrices were required, the extreme elements were intuitively adjusted to more believable values. The strip width was held at 1.61m for all the remaining model runs reported in this section.

The next area of investigation was the effect of strip hardness. The annealed gauge of the strip was changed to 4.0mm, whilst the incoming gauge was maintained at 2.4mm.

This had the effect of simulating a much harder material, as a 40% reduction of the material must have occurred before the present pass. The input yield stress according to the model changed from  $278 \cdot 10^6 \text{Nm}^{-2}$  to  $1087 \cdot 10^6 \text{Nm}^{-2}$  due to this alteration. It would be expected, all other things remaining unchanged, that the rolling load would need to increase accordingly, and this was the case. The model gave a load of  $8.2 \cdot 10^6 \text{N}$  as opposed to the previous  $3.25 \cdot 10^6 \text{N}$ . For harder materials then, any given loading has less effect, and the gains are therefore expected to decrease and this was found to be the case. The gain matrix is not reproduced here as it is similar to A5.10 in structure; suffice it to say that all elements experienced a reduction of 2 to 5% compared with section A5.10. There was a tendency for the lower reductions to occur in the body of the matrix, but this was not exclusive.

The next parameter to be changed was the reduction taken during the pass. Two runs will be considered. Firstly, an output gauge of 1.7mm instead of 2.05mm (an increase of 100% in reduction) and secondly an output gauge of 2.25mm (a decrease in reduction of about 60%). The rolling loads were given by the model as  $5.9 \cdot 10^6 \text{N}$  and  $1.8 \cdot 10^6 \text{N}$  respectively. By the argument used previously to explain the effect of narrower strip widths, the gains would be expected to increase for higher reductions and decrease for lower reductions. This was observed to occur. For the higher reductions, all gains increased by an amount 18 to 20% uniformly distributed around the

matrix. For the lower reductions, a similarly distributed reduction of 6 to 8% was noted.

For an increase in (front) tension on the strip, the same reduction should require a lower rolling load. This is confirmed by the model. However, sufficiently large tension changes to cause meaningful load changes were not possible (due to pulling the neutral angle outside the roll gap for example), and therefore the effects on the gain matrices are not clear. From the previous arguments, it would be expected that higher front tensions (lower rolling load) would decrease the gains. However, with a tension of  $286 \cdot 10^3 \text{N}$  instead of  $191 \cdot 10^3 \text{N}$ , the rolling load decreased by some 0.8%, and the gains appeared actually to increase. Since the percentages involved (typically 0.008%) are negligible, no further analysis was attempted.

Finally, the effects of changing the cluster geometry bear a mention. As an example, if the screwdown rack and each side eccentric rack are moved from the datum positions to +5 operator's divisions (half scale), the model gives the following geometry (see fig.3.16):-

$\theta_1 = 0^\circ$	$F_1 = P_T$
$\theta_2 = 38.1^\circ$	$F_2 = 0.635 P_T$
$\theta_3 = 22.1^\circ$	$F_3 = 0.236 P_T$
$\theta_4 = 59.6^\circ$	$F_4 = 0.557 P_T$
$\theta_5 = 78.3^\circ$	$F_5 = 0.502 P_T$
$\theta_6 = 41.1^\circ$	$F_6 = 0.290 P_T$
$\theta_7 = 3.6^\circ$	$F_7 = 0.180 P_T$
$\theta_8 = 24.3^\circ$	$F_8 = 0.437 P_T$

The rolling load  $P_T$  is still  $3.25 \cdot 10^6 \text{N}$ .

As a result, the gains are reduced by 7 to 11%. The reason for this is simply one of force resolution - more of the effort produced by the As-U-Rolls goes into the mill housing rather than the strip for this geometry.

To sum up, the results have in general confirmed the correct qualitative operation of the model. Chapter 5 describes an attempt to verify the quantitative operation. The resultant gain matrices for wide strips appear to be realistic enough to use in plant simulations and control system design (nothing more reliable being available). The model is very much faster in execution than that of Gunawardene (16), but results of the latter model appear more plausible for narrow strips at present.

CHAPTER 4

DYNAMIC MATHEMATICAL DESCRIPTION  
OF THE PLANT

## CHAPTER 4

### DYNAMIC MATHEMATICAL DESCRIPTION OF THE PLANT

#### 4.1 Introduction

In order to carry out a control scheme design, it is necessary to know the plant transfer functions. Compared with the static model, the dynamic description of the plant is fairly straightforward. The mill cluster itself is considered to be non-dynamic, and is represented only by the gain matrix relating shape changes to actuator changes (see Chapter 3). That is to say, when an actuator moves, the response at the roll gap is taken to be instantaneous.

This chapter therefore develops transfer function representations for the remaining elements of the plant; namely the As-U-Roll actuators, the first intermediate roll lateral motion, the dynamic transfer of strip shape from the roll gap to the shapemeter and the shapemeter system itself. The controller dynamics are considered in Chapter 6.

#### 4.2 The As-U-Roll Actuators

Figure 4.1 gives a schematic representation of the manual system of As-U-Roll control which has always existed on the mills in question. The mill operator is provided with a separate "Raise-Off-Lower" switch for each of the eight actuators, and a position transducer (in the form of a linear variable potentiometric type of transducer) supplying a meter indicating the actuator's position to the operator on an arbitrary scale of  $\pm 5$

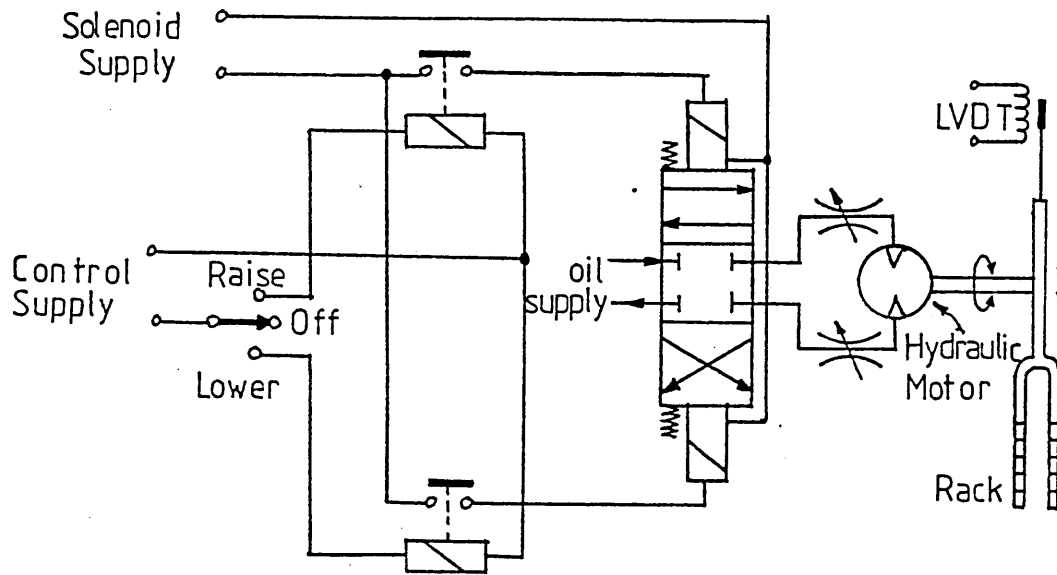
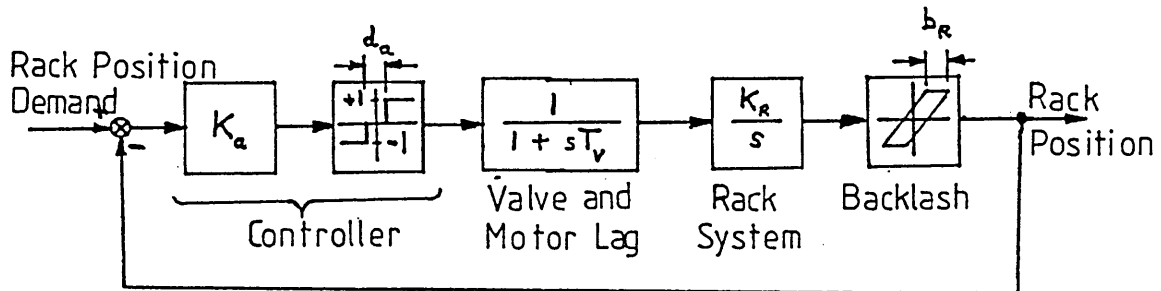


Fig. 4.1 Manual As-U-Roll Control Schematic



Where:

$K_a = 0.0625$	OR	$0.333$
$d_a = 5 \text{ mm}$		$5 \text{ mm}$
$T_v = 0.5 \text{ s}$		$0.05 \text{ s}$
$K_R = 16 \text{ mm/s}$		$8 \text{ mm/s}$
$b_R = 5 \text{ mm}$		$3 \text{ mm}$
(demonstration)		(actual)

Fig. 4.2 Closed Loop Control Block Diagram

divisions. Whenever the operator engages the "Raise" or "Lower" switch positions, the As-U-Roll rack moves at a nominally constant rate, i.e. the system is "bang-bang". For each As-U-Roll the operator's switch controls relays which, in turn, energize hydraulic solenoid valves feeding a hydraulic motor. This motor is geared onto the As-U-Roll rack.

Clearly, closed-loop control of these actuators is desirable if they are to form part of an automatic scheme. The optimum means of providing such control would be to replace the bang-bang elements with a proportional servo valve system, but this was not possible for financial reasons. Therefore a simple closed-loop system around the existing plant has been incorporated in the system software. This takes the form of figure 4.2. The transfer function of the hydraulic valve (time constant) has been estimated from plant tests (see Chapter 5.). The transfer function of the rack is an integrator whose gain is found from the rack velocity. Although this velocity is nominally fixed, the hydraulic supplies to the hydraulic motors are fitted with variable restrictions in each direction, so that in practice each rack may raise and lower at different rates. Furthermore, the hydraulic supply to these motors is not rated to drive all eight actuators simultaneously, therefore the rate at which any actuator moves will change depending upon how many other actuators are moving at the same time. The "demonstration" rack gain given in the figure is a value obtained for one actuator moving alone before

the plant engineers slowed down its response at the Author's request, - the "actual" value was then obtained (see Chapter 5, section 5.4.1). Some backlash is to be expected in the rack mechanism, and this is therefore also shown in figure 4.2. The "actual" magnitude of the backlash has also been estimated from plant tests. The controller simply takes the form of a small proportional gain and an imposed dead-band to prevent system hunting (which would shorten the life expectancy of the mechanical components). The initial selections of controller gain and dead-band were made by digital and analogue dynamic simulations discussed in Chapter 7.

For the purposes of control system design and simulation (see Chapters 6 and 7) the non-linear As-U-Roll system has been replaced by a second order system which gives a comparable response to the system of fig.4.2 under simulated conditions. The resultant system is described by

$$g_a(s) = \frac{K'_a w_a^2}{s^2 + 2\zeta_a w_a s + w_a^2} \dots \dots (4.1)$$

where

$K'_a = 1.0$	or	$K'_a = 1.0$
$w_a = 1.95 \text{ rad/s}$		$w_a = 0.4 \text{ rad/s}$
$\zeta_a = 0.85$		$\zeta_a = 1.0$

(for "demonstration" system)      (For "actual" system)

and  $s =$  Laplace Operator

Figure 4.3 shows a step response as an example of the representation of the non-linear system by equation (4.1). The reason for using the somewhat unreal values of the "demonstration" system is to illustrate where the lack of fit occurs at the origin of figure 4.3. For the "actual" values, the fit is much better in this area as the effective dead-band width ( $d_a/K_a$ ) is much smaller. (However, the fit at the "top" of the characteristic is not quite so good).

Since the actuators are not mutually interactive, the block diagram matrix ( $\tilde{G}_a$ ) is simply  $\tilde{G}_a = g_a(s) \cdot \tilde{I}_B$  where  $g_a(s)$  is given by the "actual" values in equation (4.1) and  $\tilde{I}_8$  is the identity matrix (8 square).

It is also worth reiterating at this point that constraints are imposed by the mill manufacturer upon the relative positioning of adjacent As-U-Roll actuators. This is designed to prevent attempts at excessive backing shaft bending gradients, or excessively sharp maxima or minima in the bending profile - any of which could damage the mill. The means of ensuring compliance with these constraints are discussed in detail in Chapter 8 (section 8.2).

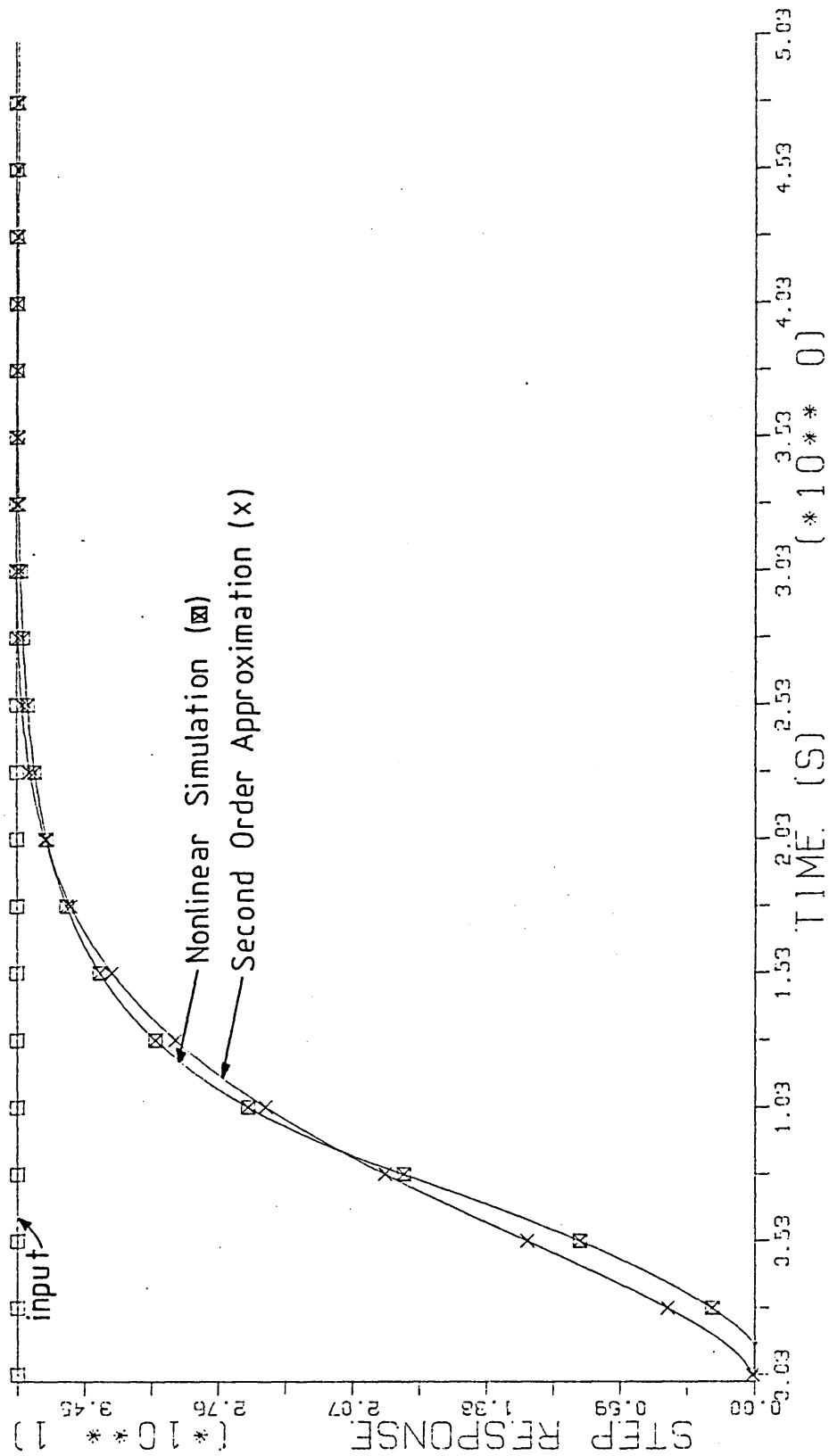
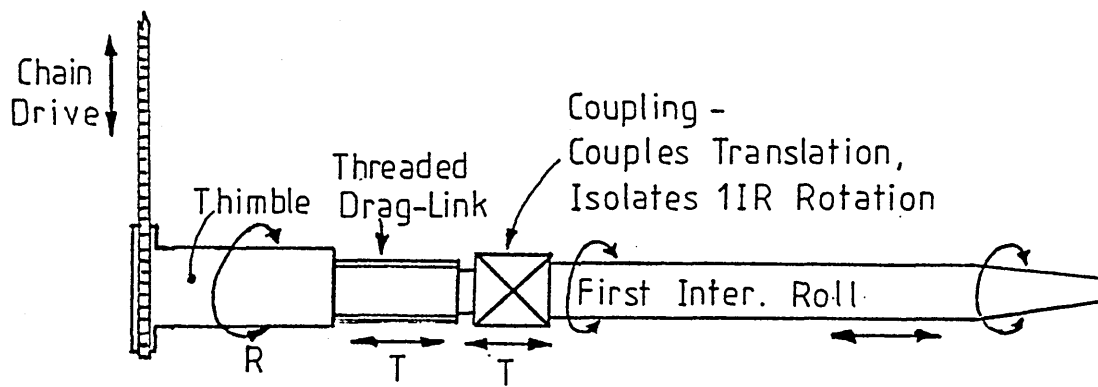


Fig.4.3 Comparison of As-U-Roll Model Step Responses (Demonstration System)

### 4.3 First Intermediate Roll Lateral Adjustment Actuators

The manual system for control of the first intermediate roll lateral positions is very similar in concept to that previously described for the As-U-Roll systems. Again the operator is provided with three position switches ("In-Off-Out") which control "constant" speed hydraulic motors (about 590rpm) via relays and hydraulic valves. The major differences are that the drive is not directly transmitted to the rolls, but is fed via quite long runs of chain drive and gear trains (overall reduction ratio about 18.7:1) which drive an internally threaded thimble (see figure 4.4). This thimble is rotated by the chain drive (at about 31.5rpm) and engages a non-rotating threaded section coupled to the end of the first intermediate roll, which is therefore moved into or out of the threaded thimble depending upon the thimble's direction of rotation. The pitch of the thread is about 6mm, giving a lateral velocity of 3.15mm/s. In addition, the position indication device is more complex. A selsyn transmitter is driven by one of the intermediate shafts in the chain drive system. This is cabled to a matching selsyn receiver mounted at the front of the mill. The shaft of the receiver drives via a gear train onto a leadscrew arrangement, which linearly moves an indicating pointer visible to the mill operator. Apart from these differences (mechanical drive arrangement and transducer), the system can be represented by the same schematic diagram and block diagram (minus the controller and feedback) as the As-U-Roll system (figs.4.1 and 4.2).

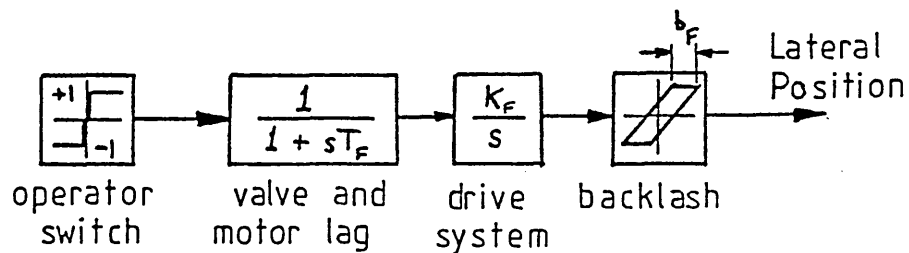


Key:

R - Rotation Only

T - Translation Only

Fig.4.4 First Intermediate Roll - Lateral Drive



Where:

$$T_F = 0.1 \text{ s}$$

$$K_F = 3.15 \text{ mm/s}$$

$$b_F = 0.5 \text{ mm (estimated)}$$

Fig.4.5 Block Diagram

However, the coarse-pitch chain drive system gives rise to greater backlash than in the As-U-Roll system. Nevertheless, when this backlash is referred to lateral first intermediate roll motion, its effect is greatly attenuated by the reduction gearing giving the system shown in figure 4.5.

The automatic scheme for these actuators takes the same form as fig.4.2, but extra transducers had to be introduced onto the plant to avoid the conversion of the selsyn signals (for financial reasons). These were of potentiometric type, of rugged construction so as to withstand the plant environment.

#### 4.4 Transfer of Strip Shape Between Mill and Shapemeter

Consider initially a gauge (thickness) change occurring at the roll gap. If this is to be measured by a gauge transducer some distance downstream of the mill, then a transport lag (distance/velocity lag) would exist between the gauge changes at the roll gap and at the transducer. Consider now a change in mill exit tension. Such a change would have instantaneous effects both at the roll gap and at a downstream tensiometer. Since a change in strip shape is conceptually a hybrid of these two cases, it is to be expected that some transport lag will exist between the mill and the shapemeter, but that this will not necessarily be of the magnitude expected due to strip velocity and the distance of the shapemeter from the roll gap. An ancient principle due to St. Venant (referenced in (36)) suggests that stresses

existing at some section across a steel strip, will decay to zero (given that the strip is not subjected to external stresses also) within say one-and-one-half strip widths of the section. We can therefore postulate a transfer function for the strip between the roll gap and shapemeter of the form

$$g_s(s) = \frac{e^{-sT_{s1}}}{1 + sT_{s2}} \dots \dots \dots (4.2)$$

where  $T_{s1}$  = distance/velocity lag for distance from mill to shapemeter minus  $l\frac{1}{2}$ \*strip width

$T_{s2}$  = time constant for the build-up of the differential tension readings to the maximum

For plant values, this suggests

$$T_{s1} \approx \frac{2.9 - 1.5w}{v} \quad (s) \dots \dots \dots (4.3)$$

$$T_{s2} \approx 0.3 \frac{w}{v} \quad (s)$$

where  $w$  = strip width (m)  
 $v$  = strip velocity ( $ms^{-1}$ )

Plant trials (see Chapter 5) have been carried out to test the validity of equations (4.3).

As in the case of the As-U-Roll actuators, there is assumed to be no interaction between the transfer functions of each "ribbon" of strip corresponding to one shapemeter rotor (although there

will in reality be some small cross-coupling) so that the overall transfer function matrix  $\tilde{G}_s(s)$  contains one independent  $g_s(s)$  per covered shapemeter rotor. Further work is possible in this area which is very complex if treated rigorously, and is not yet well understood judging by the dearth of available literature on the subject.

#### 4.5 The Shapemeter System

The electronics of the shapemeter system are fairly complex, and therefore no attempt has been made to derive a transfer function by analysis of the circuitry. Perusal of the shapemeter manuals indicates that the system gain is switched under various conditions, but this must clearly be done in order only to maintain the same input-output calibration under all conditions. Therefore this function is "transparent" to the user, and need not be included in the transfer function.

The system is apparently representable by two cascaded first-order lags, one of which is of fixed time constant and the other of switched time constant according to strip speed. The latter is always much greater than the fixed time constant, and therefore a representation (relating measured shape to strip shape) of

$$g_m(s) \approx \frac{1}{1 + sT_m} \dots \dots \dots (4.4)$$

will be used, where

$$T_m = 4.35 \quad (0.3 < v \leq 1.0 \text{ ms}^{-1})$$

$$T_m = 1.43 \quad (1.0 < v \leq 2.0 \text{ ms}^{-1})$$

$$T_m = 0.74 \quad (2.0 < v \leq 5.0 \text{ ms}^{-1})$$

$$T_m = 0.3 \quad (5.0 < v \leq 15.0 \text{ ms}^{-1})$$

$$T_m = 0.19 \quad (15.0 < v \leq 30.0 \text{ ms}^{-1})$$

(All time constants in seconds) (c.f. Table 2.1, Chapter 2).

The shapemeter rotors do not interact with each other, so that the overall transfer function matrix  $\tilde{G}_m(s)$  simply contains one  $g_m(s)$  per rotor.

PLANT TESTING FOR MODEL VALIDATION

5.1 Introduction

In work such as the present project, heavily reliant upon modelling, it is a general principle that any mathematical model purporting to represent a physical plant or system, should be checked against the plant or system to confirm its accuracy. This laudable intent however, cannot always be accomplished for a variety of reasons - unobservable plant, safety constraints, financial constraints etc., (which indeed are often the reasons for modelling in the first place). Nevertheless, it is certainly good policy to validate models wherever possible.

That having been said, anyone who has understood the preceeding two chapters will realise that there are great difficulties in validation of some of these models, and rigorous validation is virtually impossible. Logging equipment valued at well over £100000 has been employed (some of it specifically designed and constructed by the author) in efforts to prove the validity of the models, and this chapter describes these efforts and their results.

It should be pointed out that at the time of writing, plant tests are still being carried out further to refine the models, and results are therefore to some extent open-ended.

## 5.2 Test Instrumentation and Set-Up

Various configurations of test equipment have been employed from time to time, but figure 5.1 gives a good indication of the type of systems used.

The equipment was installed in the mill computer room, where most of the required signals were available. Brief details of the equipment shown in the figure are given here for interest (other equipment was also used as required).

Signal Isolation - Direct Current Isolator (DCI) units to isolate up to 2kV, designed by B.S.C. Sheffield Labs. and built by outside contractors. Multi-range inputs for  $\pm 10V$  d.c. output.

Signal Conditioning - Operational amplifier units connected to patch panels allowing various configurations, gains and filters to be selected. 24-channel units designed by B.S.C. Sheffield Labs. and built by outside contractors, 32-channel unit designed and built by the author.

32-Channel Analogue Multiplexer Unit - Accepts up to 32 analogue inputs in the range  $\pm 10V$  d.c.

Simultaneously samples and holds, then sequentially outputs to a single output channel.

Single-Shot, or repeated sampling up to 10Hz.

Designed and built by the author.

14-Channel Instrumentation analogue magnetic tape recorders - Type SE7000 (Thorn EMI Datatech).

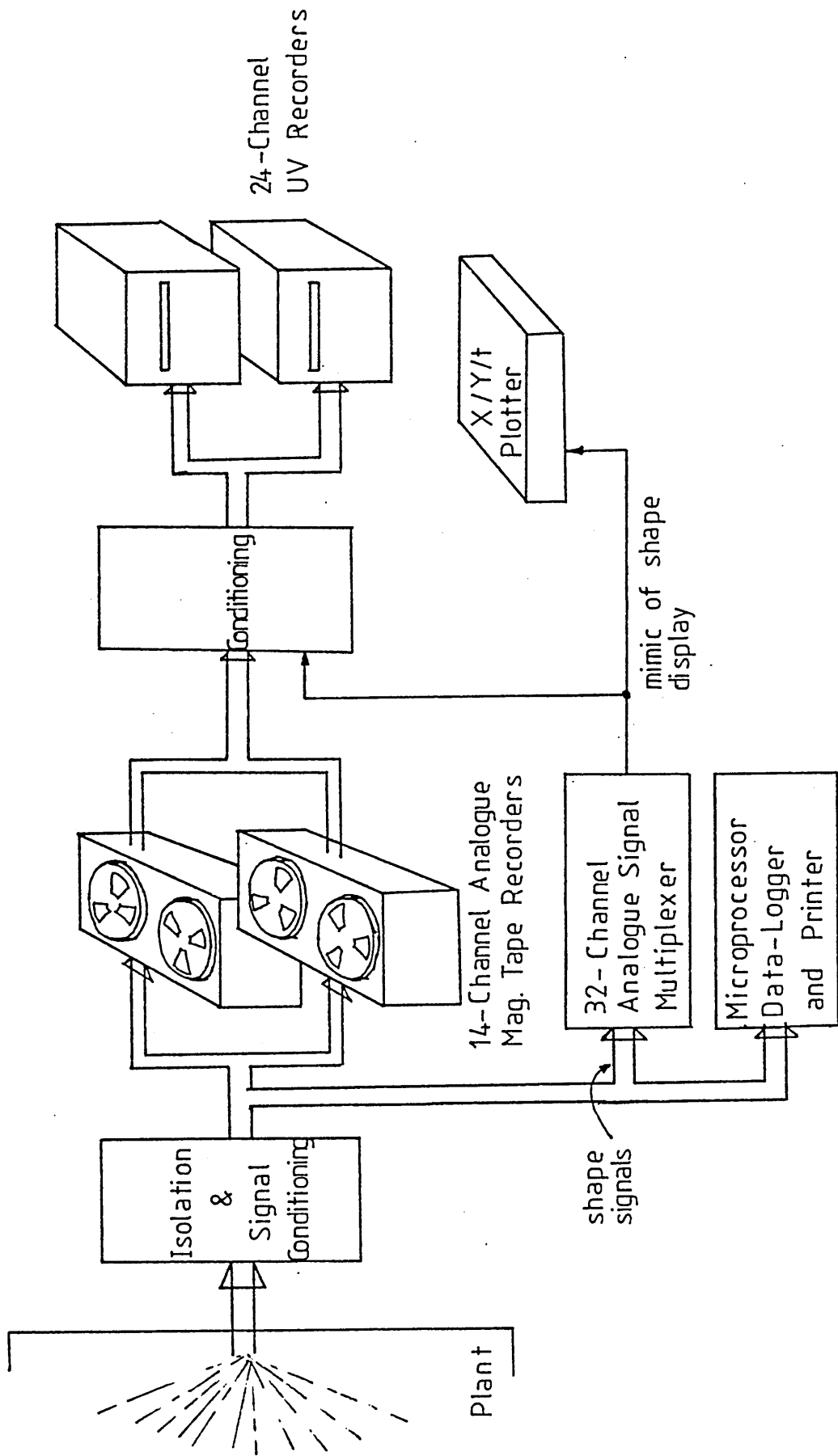


Fig. 5.1 Configuration of Data Logging Equipment

(Thorn EMI Datatech).

X-Y-t Analogue Plotter - Linseis - Type LY1800 or Bryans-26000.

Microprocessor - based data logger - Uses a single-board microcomputer marketed by J.B. Microsystems Ltd. (see Appendix 7), software developed by B.S.C. Sheffield Laboratories (by engineers supervised by the author).

The plant connections, and also the interconnections between the various items of instrumentation, were made in such a manner that the set of recorded parameters could easily be changed for different investigations.

A typical set of logged signals comprises:-

All eight As-U-Roll rack positions (continuous)

Upper and Lower First Intermediate Roll Lateral Positions (continuous)

Strip shape at 31 points across the mill multiplexed to a single channel so as to mimic the operator's display (sampled at a rate appropriate to the purpose of the trial).

Strip speed (continuous)

Tensions

Gauges

Strip Width

Other signals as appropriate

### 5.3 Static Model Validation

The aim of these tests was to obtain a steady shape in the strip, make a small measured movement of a single As-U-Roll actuator, and record the effect upon strip shape. So long as records were made of the schedule being rolled; the actuator settings for screwdown, As-U-Rolls, side eccentrics and first intermediate rolls; tensions, speed and other mill parameters, then the same small As-U-Roll change should be able to be run via the static mill model, to produce a good approximation to the shape change observed on the mill. These small As-U-Roll changes could be made during normal mill production on the early passes of multi-pass coils without harming the eventual end product.

As an aside, it may occur to the reader that correlation methods of identification (see for example (40)) could well be employed here. In fact, correlation equipment and pseudo random binary sequence generators were available at B.S.C. Sheffield Laboratories; but since the principal action of the actuators is that of an integrator, and since significant non-linearities were thought to exist in the system, and also it would not be easy to interface a PRBS with the "bang-bang" mill systems, this approach was rejected.

In practice, it proved exceedingly difficult to obtain a change of shape on the plant (by the above means) which could be definitely tied down to As-U-Roll motion and no other cause. This was basically due to two effects. Firstly small random variations of the shape display occur continuously at a frequency which is too low and irregular to

be ascribed to normal "noise". Their origin is therefore either in the strip itself, or due to sporadic electromagnetic effects from other parts of the plant. In either case, their magnitude is significant compared with the changes in shape which can be deliberately introduced without risk of damaging the (very expensive) material being rolled on the mill. The second problem was that the mill operators were only prepared to make these deliberate As-U-Roll disturbances on the first or second pass of a multi-pass coil, so that plenty of opportunity existed to correct the deliberate errors thus introduced. On such passes, the strip is often travelling very slowly, when the shapemeter readings may not be accurate. Furthermore, it was not possible to convince the mill operator to allow the "error" introduced to remain long enough for a steady-state to be achieved before he felt obliged to correct it again, fearing damage to the rolled material. In fact, up to the time of writing, no really satisfactory result has been achieved, in spite of many efforts spaced over a period of some four or five years!

Typical of the results obtained is the following set. It does tend to confirm the philosophy of the model, as will be seen in the ensuing discussion, but there are areas of doubt which are unresolved.

## Trial Parameters

### Rolls:

$D_B = 405\text{mm}$

$D_{2D} = 235\text{mm}$  ( $D_{2I}$  assumed, no record available)

$D_1 = 134\text{mm}$ , with 584mm length tapered off diameter  
at 2.5mm/m

$D_w = 84\text{mm}$  (top), 101mm (bottom)

Cambers:- 0.15mm (top idler), 0.36mm (bottom idler),  
0.1mm (workrolls - assumed)  
0.15mm (first intermediate rolls)

Strip Material: EN304 stainless 1.016m wide,  
annealed gauge 2.95mm, input gauge 1.52mm, exit gauge 1.29mm

### Mill Setup:

Front tension 450 kN, back tension 425 kN, screwdown  
position 4.5 operator's divisions, both side eccentrics  
4.2 divisions, pushup system 9.8 divisions, upper/lower  
first intermediate roll tapers positioned 110mm/100mm  
over the strip respectively. As-U-Roll positions  
(operator's divisions) prior to test, 2.0, 1.1, -0.2,  
-1.6, -1.7, -0.5, 0.8, 2.0

### Test:

As-U-Roll 4 moved from -1.6 div. to -3.6 div.

Shapemeter Rotor	Before Test	After Test	Change	Model Change
(6)	(-3.0)	(-2.9)	(+0.1)	-
7	+0.1	+0.2	+0.1	-0.4
8	-	-	-	+0.01
9	-2.0	-2.1	-0.1	+0.03
10	-1.7	-1.8	-0.1	-0.14
11	-0.7	-0.8	-0.1	-0.34
12	0.4	0.1	-0.3	-0.54
13	0.6	0.3	-0.3	-0.64
14	1.1	0.8	-0.3	-0.68
15	1.3	1.1	-0.2	-0.64
16	1.5	1.2	-0.3	-0.53
17	1.0	0.8	-0.2	-0.38
18	2.1	2.0	-0.1	-0.18
19	0.8	0.7	-0.1	+0.04
20	0.1	0.1	0.0	+0.26
21	-0.4	-0.3	+0.1	+0.48
22	-0.9	-0.8	+0.1	+0.67
23	-1.1	-0.8	+0.3	+0.85
24	-0.2	0.0	+0.2	+1.00
25	+0.2	+0.7	+0.5	+1.14
(26)	(-1.5)	(-1.1)	(+0.4)	-

Table 5.1 Comparison of Plant and Static Model Shape Values  
(All units are operator's divisions)

Note that in table 5.1, rotors 6 and 26 were partially covered by the strip edges, and therefore gave very low readings. Calculations based upon strip width show that for a centrally-tracking strip these rotors should be covered by only 27% or so, and therefore should not be included in the shape display reading (see Chapter 8, section 8.6 for a discussion on this point). No reading is available for rotor 8, due to a fault in the equipment at the time of the trial. (A crude interpolation based upon the mean of the neighbouring values would give - 0.1 div. both before and after the test).

As would be expected, in the fourth column of table 5.1, the shapemeter rotors nearest to the position of As-U-Roll 4 (rotor 14 is below As-U-Roll 4) show a loosening of the strip, which gradually reduces and then changes to a tightening as one moves away from rotor 14 towards the strip edges (so as to preserve the mean level). It is likely that the apparently excessive tightening at the rear of the strip (rotors 23 to 25) is due to a first intermediate roll movement, which was made by the operator before the steady-state readings (given in the third column of the table) had been achieved at the shapemeter.

The static mill model was run with the same set of mill and strip data, and the same change was applied to As-U-Roll 4. The resulting predictions of shape change in the strip are given in the right-hand column of table 5.1. It is known (see chapter 3) that there are inaccuracies in the static model at the strip edges for the case of narrow strips (which is the case here) and this is borne out by the predictions for rotor 7 and rotors 20 to 25, the errors being due to the very large deflections predicted for the workroll ends which are not over the strip, as discussed in Chapter 3. (As an aside, the model predicted that the front end of the workroll would deflect by approximately 0.7mm under these conditions). If these areas of significant doubt are excluded, it can be seen that the form of the model results is in accord with the experimental results, with the maximum loosening of the strip at rotor 14. However, the gain of the model appears from this test to be too great by a factor of, say, two. Much of this error can be attributed to non-linearity in the mill.

The As-U-Roll change of -2 divisions represents 20% of full-scale, and therefore no longer constitutes a "small change". In table 5.2, the column of the mill gain matrix produced by the model whilst calculating the right-hand column of table 5.1, is compared with the 19-rotor small-change version taken from column 4 of the matrix given in Appendix 5, section A5.12. Indeed, if the ratio of the "small-change" to "large-change" column entries of table 5.2 is applied as a multiplier to correct the corresponding entry in the right-hand column of table 5.1, many of the entries for rotors 11 to 19 become identical to the plant trial results.

Thus, although there are many uncertainties and inaccuracies, the plant tests tend to confirm the predictions of the small-signal gain matrices, except at the areas of the strip edges. The edge-effects are much more apparent for narrower strip widths, and the model is therefore only to be trusted for wide strip.

Rotor Number	Column 4 of "small-change" gain matrix (from section A5.12)	Column 4 of "large-change" gain matrix (from the present model run)
7	1.07	0.72
8	0.21	-0.01
9	-0.04	-0.05
10	0.07	0.25
11	0.30	0.62
12	0.55	0.98
13	0.69	1.16
14	0.74	1.23
15	0.71	1.16
16	0.58	0.95
17	0.41	0.68
18	0.18	0.32
19	-0.07	-0.07
20	-0.33	-0.46
21	-0.59	-0.86
22	-0.83	-1.21
23	-1.05	-1.53
24	-1.23	-1.81
25	-1.39	-2.06

Table 5.2 Comparison of Model Gains

#### 5.4 Dynamic Model Verification

This section describes the tests carried out to identify the transfer functional parameters of the various dynamic items of the plant, as modelled in Chapter 4.

##### 5.4.1. The As-U-Roll Actuators

Using the magnetic tape and UV recorders shown in fig.5.1, it was a relatively simple matter to move the As-U-Roll actuators whilst recording their positions. When such a test was first carried out it was found that the eight actuators moved at very different rates, a range of speeds of 3:1 being apparent. The plant engineers therefore adjusted the hydraulic flow regulators to achieve more closely matched actuator velocities. The resultant response of a single actuator is shown in figure

## 5.2 for the manual control system of fig.4.1

From figure 5.2, it is clear that the response is primarily that of an integrator, having a gain of approximately 10mm/s. However, due to hydraulic flow-limiting, this gain varies according to the number of actuators moving at any given time. If all eight actuators should move together for example the gain will be of the order of 6.5mm/s. For simulation purposes a compromise value of 8mm/s was therefore selected.

Due to the difficulty of recording the instant at which the As-U-Roll rack was asked to move by moving the RAISE-OFF-LOWER switch (since the switches, solenoids and valves were remote from the recording gear and on a lower floor), estimation of the time constant of the hydraulic components ( $T_v$  in figure 4.2, Chapter 4) and the rack backlash ( $b_R$  in figure 4.2) was postponed until the automatic system was capable of closed loop control of the actuators. (The controlling digital outputs would then be cabled from a position immediately adjacent to the recording gear). This is described in section 5.4.4 below.

### 5.4.2. First Intermediate Roll Lateral Adjustment Actuators

At the time of writing, effort has been concentrated upon automatic control of the As-U-Rolls, with control of the first inter. rolls to be added later. One reason for this is the lack of easily calibrated instrumentation around these rolls, and the difficulty of providing readily zeroed position transducers. The existing transducers are driven from a leadscrew arrangement running via a gear train

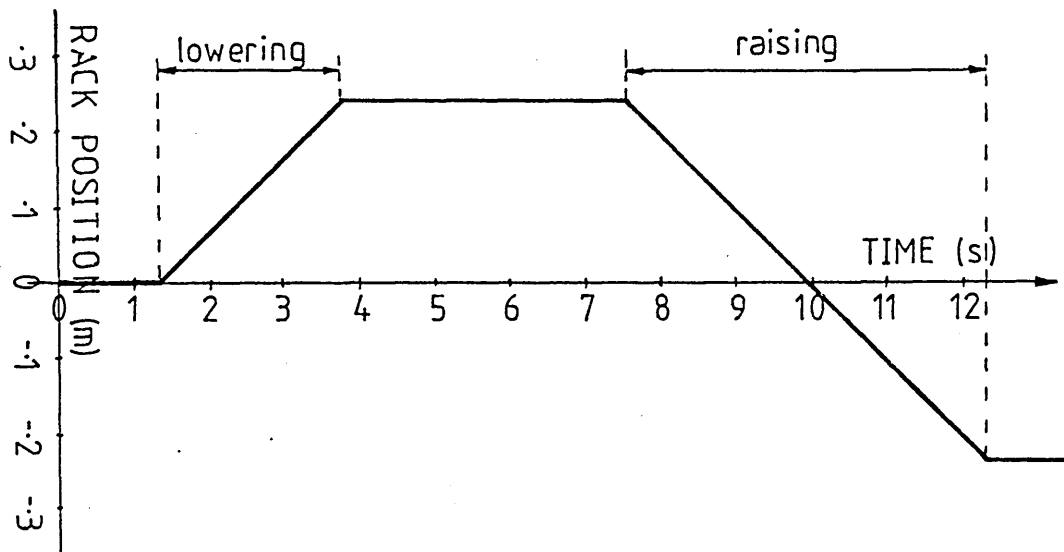


Fig. 5.2 Motion of One As-U-Roll Rack

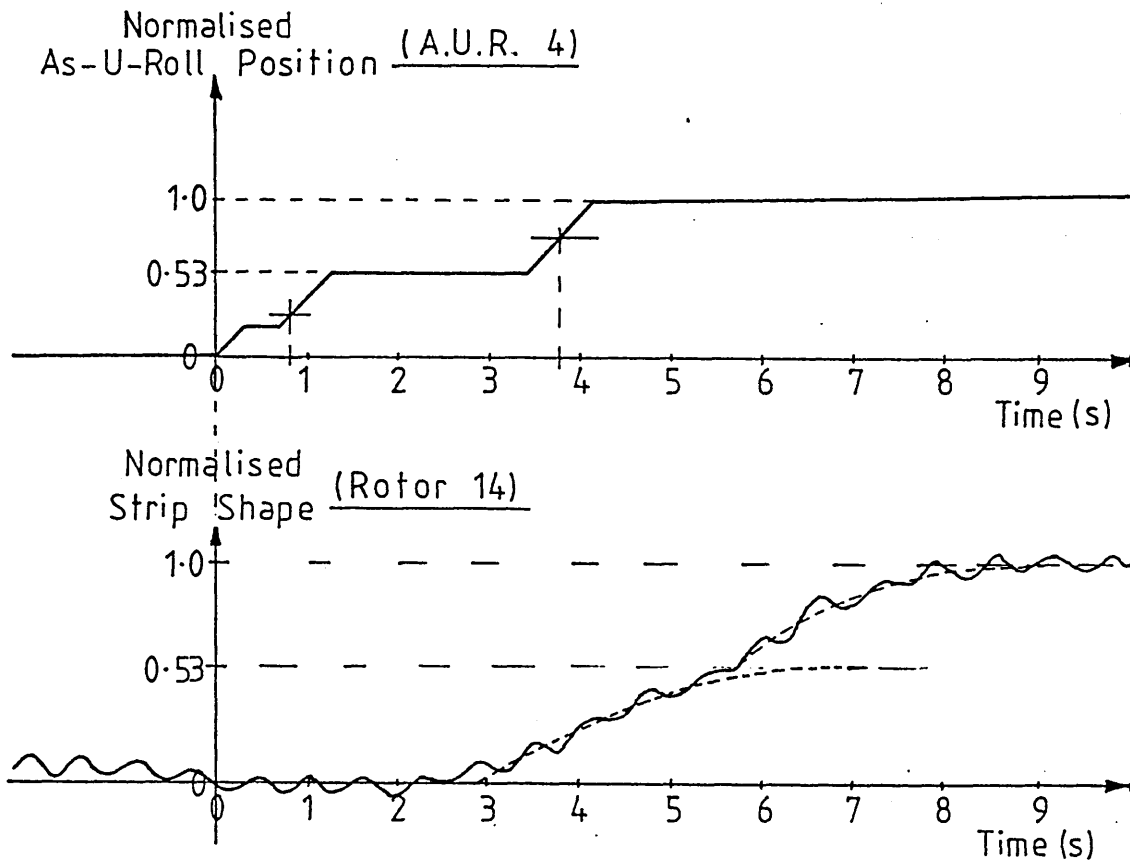


Fig. 5.3 As-U-Roll Motion & Shape Response

from a selsyn receiver, and any measurement of backlash using this arrangement would be misleading. For the present then, a value of 0.5mm is estimated, although this may turn out to be rather high. Nevertheless, since the first intermediate roll dynamics are not under active consideration (at the time of writing) in simulation work or controller design, the value will pass for the present.

The integrator gain was measured by recording the speed of the hydraulic motor using an optical tachometer, and then dividing this down by the various gear ratios and thread pitch effects in the drive train (see section 4.3 in Chapter 4) giving an overall figure of  $3.15\text{mm s}^{-1}$ .

The valve and motor time constant is roughly estimated also, for the reasons given above (see fig.4.5). More accurate results will be obtained as soon as they are required for simulation purposes.

#### 5.4.3. The Transfer of Strip Shape Between the Mill and Shapemeter (Including the Shapemeter Dynamics)

Since the only way of measuring the dynamics of strip shape is by using the shapemeter, it is not possible to separate the dynamics of the shapemeter itself from those of the transfer of strip shape between the roll gap and the shapemeter. Furthermore, since the As-U-Roll actuators move at only say 10mm/s maximum it is also impossible to inject a true step change in strip shape into the system. These two factors, taken together with the random shape variations discussed in section 5.3, make this particular identification exercise inordinately difficult, and in the end it is perhaps one area where at

least the philosophy of the modelling simply has to be taken on trust (which is somewhat unfortunate, since it is also one of the areas most open to inaccuracy and incorrect assumption!).

The test method employed was to make deliberate changes to a single As-U-Roll rack, of as large a magnitude as was deemed permissible, during the first or second pass of a coil (exactly as was done in the attempts to verify the static model). The rotors of the shapemeter which corresponded most closely to the area of strip directly below the As-U-Roll in question were added to the continuous magnetic tape record. Thus, recordings were obtained which contained a reasonably large As-U-Roll movement (albeit a ramp, rather than a step) and the time-amplitude responses of the shapemeter rotors most closely related to the As-U-Roll being moved.

Figure 5.3 shows a typical recording, and is a tracing of a UV recording obtained during plant trials. It shows the mill operator's movement of As-U-Roll number 4, and the corresponding response (according to the shapemeter) of shapemeter rotor 14. Several points should be noted.

- a) The "stepped" nature of the injected (i.e. As-U-Roll) signal is entirely typical of these trials. The mill operators were loth to inject such large changes in a single ramp.
- b) The shapemeter signal has been passed through a 100ms first-order filter to attenuate the ripple to the level shown.

- c) The shapemeter signal "zero" level was estimated from 30cm or so of chart preceding the event in figure 5.3.
- d) The shapemeter signal "final" level is estimated from the figure. No other information is available, as the operator induced a change on another pair of As-U-Rolls after 9.5s, and the shapemeter signal then began to decrease again.

Turning now to an analysis of the figure, if we regard the two initial movements of the As-U-Roll as a single change, then we have two distinct changes, one from 0 to 0.53 and the other from 0.53 to 1.00 on the normalized scale (the total actual movement was 2 operator's divisions, i.e. 40% of f.s.d, and the shape response 3% of f.s.d.). If these levels are translated to the shapemeter rotor trace, we can in fact see the two resulting responses postulated by the dashed lines. (Although, in truth, a straight line approximation would have been just as valid for the first of the two!). Support for assuming the presence of two separate responses in this manner comes from the fact that the time of 2.8 seconds, between the "starts" of the dashed responses, corresponds fairly closely with the time of 2.9 seconds marked on the As-U-Roll trace at the centre-points of each ramp (again considering the two small initial ramps as a single event).

If the transport delay is measured from the ramp centre-points in the As-U-Roll trace, to the start of the corresponding dashed response drawn on the shapemeter trace, then we obtain 2.1 seconds for the first response

and 1.9 seconds for the second response. If we assume a transport delay given by  $e^{-sT_{s1}}$ , from section 4.4

$$T_{s1} = \frac{2.9 - x.w.}{v} \quad \text{where } w = \text{strip width (m)}$$

= 1.016 for this trial

$v = \text{strip speed (ms}^{-1}\text{)}$

= 1.833 for this trial

then we obtain  $x$  as  $-0.75$ . The negative value implies a transport lag longer than the pure distance/velocity lag between the roll gap and the shapemeter, by 75% of the strip width. This is not reconcilable with the present understanding of the system, and an alternative explanation must exist. This presumably will include the fact that a ramp is injected, rather than a step, but even measuring from the ends of the ramps, the value of  $T_{s1}$  is still 1.6 seconds, giving  $x \approx 0$ . This implies that a shape change does not propagate away from the roll gap, and should be treated in the same way as a gauge change so far as its dynamics are concerned.

If this is the case, then the shapemeter should measure a straightforward stepchange in shape. Now the shapemeter time constant for a strip speed of  $1.83 \text{ ms}^{-1}$  is 1.43s (from the table following equation (4.4) in the previous chapter). If the two dashed responses of figure 5.3 are plotted on a sheet of graph paper, together with the step response of the shapemeter (assuming the shapemeter to be represented by  $\frac{1}{1+1.43s}$ ), then the two responses lie one on either side of the shapemeter response. This does initially suggest that step changes are being

measured, but it must be borne in mind that the time constant of the exponential rise in measured shape expected from equations (4.2) and (4.3) can be very small. For the values used in the trial, equation (4.3) predicts a time constant of approximately 0.17s. This would be entirely swamped by the shapemeter dynamics, and so cannot be discussed further.

It should be pointed out that other trials have yielded similarly puzzling results also, whilst still others have supported the theories of Chapter 4, section 4.4, concerning the propagation of shape from the mill to the shapemeter. It is concluded that more variables affect this problem than was anticipated (for example, strip tension may have an effect), but due to the difficulties in executing a well-controlled trial, with well-scaled results and low noise disturbances, the proposed model will be accepted for simulation purposes.

#### 5.4.4. Closed Loop Controlled As-U-Rolls

As mentioned in section 4.2, the As-U-Roll actuators must be closed-loop position controlled in the overall scheme, and this is done as per figure 4.2. The design and implementation of the controller are discussed in sections 7.6 and 8.5 respectively.

During the early commissioning of these systems step responses were obtained for these closed-loops, and figure 5.4 depicts one such, with the control loop being executed every 50 ms by the microcomputer system. The deadband in

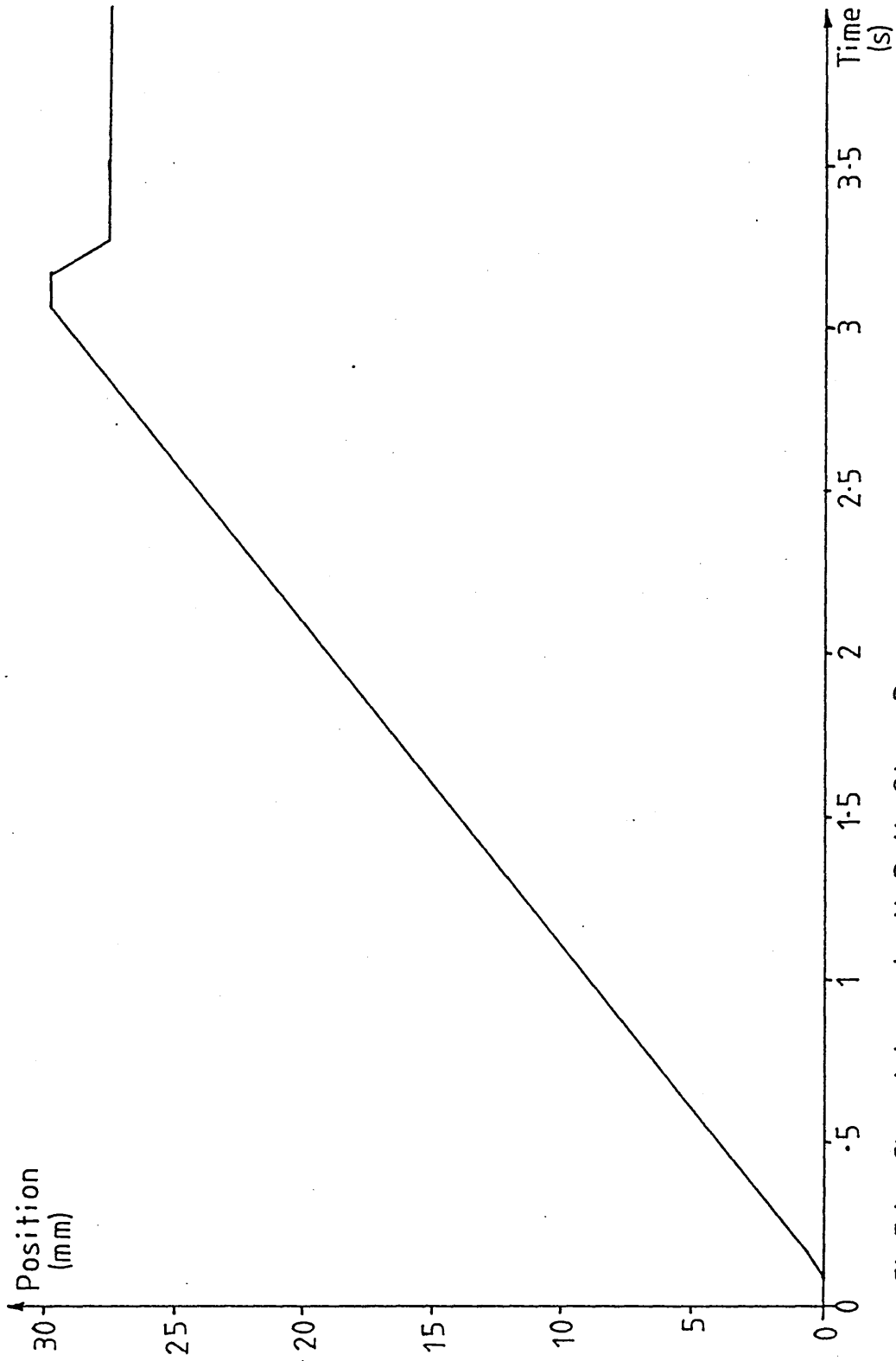


Fig.5.4 Closed Loop As-U-Roll Step Response

the controller was tuned in order to obtain a response which occasionally exhibited a little overshoot (as in the figure); but usually settled on the final value immediately, thus saving wear on the mechanical components. The deadband selected was of total width 0.833mm in figure 4.2. Therefore, including the effect of the gain  $k_a$ , the total effective deadband was 2.5mm or  $\pm 1.25\%$  of total rack travel.

In the figure (5.4), the command for the As-U-Roll to raise was issued by the microcomputer at time=0. It can be seen therefore, that a deadtime of approximately 89ms existed. This constitutes the time taken for the various relays and hydraulic valves to operate. When the rack was returned to the zero position and the test repeated, the deadtime amounted to approximately 107ms. For the first test, the rack had previously been moved to zero from the negative direction, and for the second test from the positive direction. The differences in these deadtimes, of 18ms, may therefore be tentatively ascribed to the presence of rack backlash. The measurements are very imprecise however, due to the difficulty in distinguishing from plant recording the exact instant at which the rack begins to move, in the presence of measurement noise pickup. Nevertheless, for a rack velocity of  $10\text{mm s}^{-1}$ , this gives a backlash of 0.18mm. Allowing some time for acceleration of the rack from rest, an estimate of 0.3mm was reached (see fig.4.2, "actual" values).

It is not particularly clear from figure 5.4, but some very slight evidence of rack acceleration was present, which appeared to be complete after approximately 190ms. If a first-order lag approximation for the valve and hydraulic motor is made (see fig.4.2) this leads to a time constant estimation of say 50ms (visible acceleration complete two time constants after start of motion, and some time for pressure build-up to overcome stiction etc before that).

CHAPTER 6  
CONTROL SYSTEM DESIGN

6.1 Introduction

This Chapter describes the design of the control scheme itself. Since this scheme is to be implemented on the plant, the design must be practically applicable. After much discussion with the present author concerning the operation of the Sendzimir mill, and the requirements of such a control scheme, Fotakis and Grimble ((17),(18)) developed the basic principle of the scheme to be used. Their work is acknowledged wherever appropriate, but their results given in (17) and (18) are not immediately applicable in practice. Therefore, although the design principles of Fotakis and Grimble are preserved intact, the present author has re-worked a number of aspects of the scheme so as to achieve a practically realisable system. The most important of the author's contributions are in the area of parameterization of the measured strip shape signals, and the expansion of the square system of Fotakis and Grimble (in which eight shape measurements were considered throughout for convenience in matching the number of As-U-Roll actuators) to a non-square system coping with a variable number of measured shape signals, depending upon the width of strip being rolled.

6.2 Parameterization of Shape Measurements

The shapemeter devices used on the Sendzimir mills in question, are furnished with thirty one measuring zones across the mill width. Clearly, for different widths of strip being processed, there will be a different

number of measuring zones registering the strip shape. In fact, in the present application, this number may lie in the range seventeen to thirty one. This variable number of plant measurement signals, if used directly, would pose problems to the control system. It is therefore desirable to reduce the number of signals representing the measured shape to a number of parameters which is independent of the number of signals involved. This may be done by fitting a series of polynomials to the strip shape measurements as described below.

From observations of the plant during rolling, and the recordings referred to in Chapter 5, it was found that a typical shape of strip produced on the mill before the automatic system was introduced took the form of a central maximum of internal stress together with two internal stress minima more or less symmetrically placed on either side of the maximum (figure 6.1). It is consequently possible to represent this shape to a reasonable degree of accuracy using fourth order polynomials. Higher order behaviour has, however, been noted, and the effects of this are discussed in Chapter 8 (section 8.6). It does not affect what follows.

Let  $P_i(w_j)$  be an  $i^{\text{th}}$  order polynomial (whose form will be chosen later) in  $w$ , evaluated at the value of  $w$  given in the  $j^{\text{th}}$  element of a vector  $\underline{w}$ , and write  $P_{ij} = P_i(w_j)$  for short, where

$i$  = order of polynomial,  $i=1,4$

$j$  = section across strip width,  $j=1,N$  where

$N$  = number of covered shapemeter rotors.

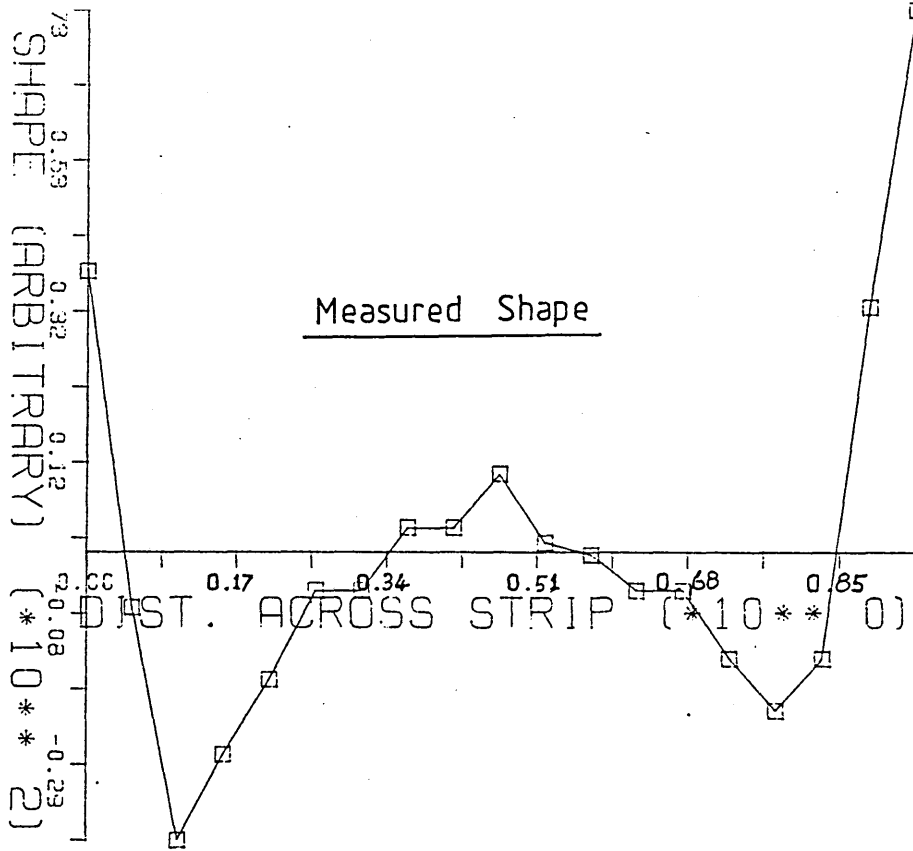


Fig.6-1 Typical Shape

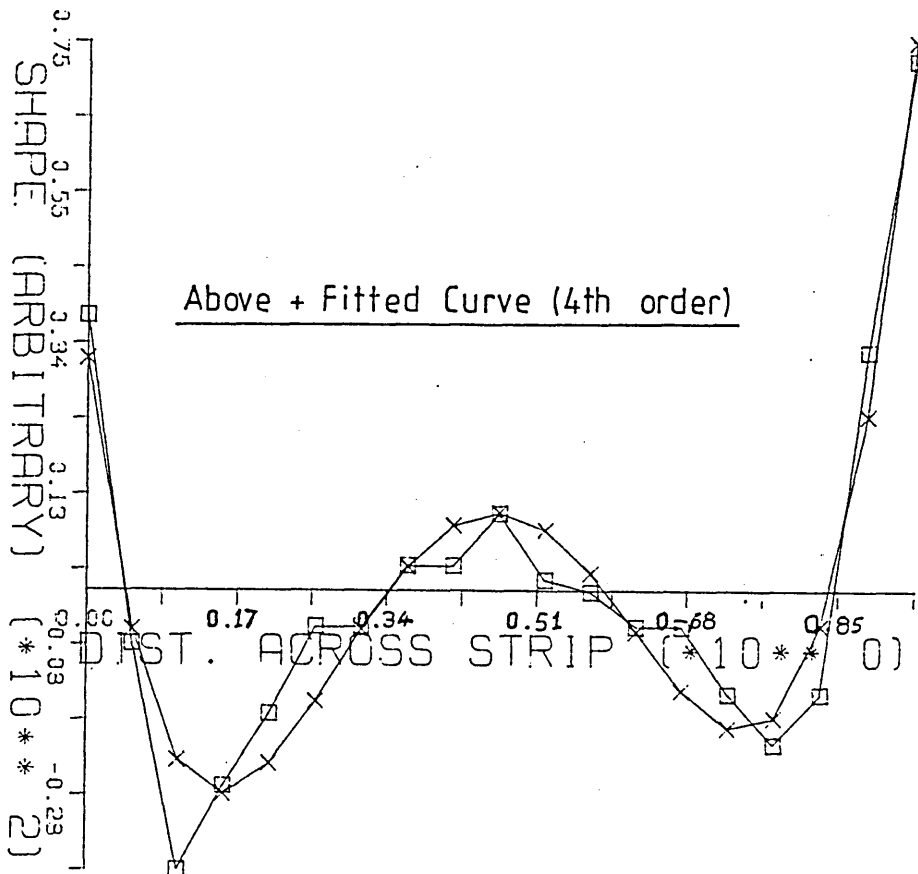


Fig.6-2 Fit to a Typical Shape

Note that the zeroth order polynomial ( $i=0$ ) is not required. (since shape is always measured as deviation from the mean there will never be any zeroth order offset).

Let the vector  $\underline{y}_m \in \mathbb{R}^N$  represent  $N$  measured values of strip shape.

Let the vector  $\hat{\underline{y}}_m \in \mathbb{R}^4$  represent the four parameter values corresponding to  $\underline{y}_m$  (assuming a 4<sup>th</sup> order fit for the present).

Thus,

$$\begin{aligned} y_{m_1}(t) &= P_{11}\hat{y}_{m_1}(t) + P_{21}\hat{y}_{m_2}(t) + P_{31}\hat{y}_{m_3}(t) + P_{41}\hat{y}_{m_4}(t) + \delta_1 \\ &\vdots \\ y_{m_N}(t) &= P_{1N}\hat{y}_{m_1}(t) + P_{2N}\hat{y}_{m_2}(t) + P_{3N}\hat{y}_{m_3}(t) + P_{4N}\hat{y}_{m_4}(t) + \delta_N \end{aligned} \quad (6.1)$$

where  $\underline{\delta} \in \mathbb{R}^N$  represents a vector of fitting errors.

In matrix form, we rewrite equations (6.1) as

$$\underline{y}_m(t) = \tilde{X}_0^T \hat{\underline{y}}_m(t) + \underline{\delta} \quad (6.2)$$

where  $\tilde{X}_0$  is given by  $x_{ij} = P_{ij}$ ,  $i=1,4$ ,  $j=1,N$

We therefore have the problem of determining  $\hat{\underline{y}}_m(t)$  given  $\underline{y}_m(t)$  and  $\tilde{X}_0$ , so as to minimise the fitting error  $\underline{\delta}$ . This is accomplished by linear regression (least-squares), when it can be shown (see for example (44)) that the best estimate for  $\hat{\underline{y}}_m(t)$  to minimise  $\underline{\delta}$  is given by

$$\hat{\underline{y}}_m(t) = (\tilde{X}_0 \tilde{X}_0^T)^{-1} \tilde{X}_0 \underline{y}_m(t) \quad (6.3)$$

(Note the interchange of  $\tilde{X}_0$  and  $\tilde{X}_0^T$  compared with the standard classic equation, due to the form of (6.2)).

Now, there is likely to be much computation involved in the calculation of  $(\tilde{X}_0 \tilde{X}_0^T)^{-1}$  in equation (6.3) for a general  $\tilde{X}_0$  matrix. However, this is greatly reduced if the set of polynomials  $P_i$   $\left| \begin{array}{l} \\ i=1,4 \end{array} \right.$  is chosen to contain only orthogonal polynomials. In this case, from the definition of orthogonality,

$$\sum_{j=1}^N P_{kj} P_{1j} = 0 \quad \left| \begin{array}{l} \\ k \neq 1 \end{array} \right.$$

and it therefore follows that all off-diagonal elements of the matrix  $(\tilde{X}_0 \tilde{X}_0^T)$  are zero. The required matrix  $(\tilde{X}_0 \tilde{X}_0^T)^{-1}$ , which will be called  $\tilde{L}$ , is therefore given simply by

$$l_{ik} = \left[ (\tilde{X}_0 \tilde{X}_0^T)^{-1} \right]_{ik} = \frac{1}{\sum_{j=1}^N P_{ij}^2} \quad \left| \begin{array}{l} \\ i=k, i=1,4 \\ k=1,4 \end{array} \right. \quad (6.4)$$

$$= 0 \quad \left| \begin{array}{l} \\ i \neq k \end{array} \right.$$

if a set of orthogonal polynomials from first to fourth order is chosen for the  $P_i(w_j)$ .

There are many such sets of polynomials in the literature, but one set in particular has a number of astonishing properties. This is the set of Chebyshev polynomials, and it can be shown (see ref.(45)) that one such property is that if a function is approximated by

a number of different sets of polynomials, of equal degree, then the least maximum fitting error will always exist when the Chebyshev polynomials are used. This is called the "minimax" approximation, (but is to be had only at the expense of a larger mean square error than other methods). Grimble and Fotakis chose the Chebyshev polynomials for parameterization in their work because of the minimax benefit, but unfortunately these polynomials are not practically suited to the problem in hand for other reasons which will now be discussed.

The Chebyshev polynomials are orthogonal over the following set of N discrete points equally spaced in the angular domain:-

$$\underline{\theta} = \left[ 0, \frac{\pi}{N-1}, \frac{2\pi}{N-1}, \dots, \frac{(N-2)\pi}{N-1}, \pi \right]^T, \text{ but are not}$$

orthogonal over equally-spaced points in the linear domain as assumed by Fotakis and Grimble.

When translated into the linear domain as

$w_j = \cos \theta_j$  we obtain

$$\underline{w} = \left[ 1, \cos\left(\frac{\pi}{N-1}\right), \dots, \cos\left[\frac{(N-2)\pi}{N-1}\right], -1 \right]^T \text{ for the same N points.}$$

$$\text{i.e. } w_j = \cos \left[ \frac{(j-1)\pi}{N-1} \right]_{j=1, N}$$

Thus, for say twenty one covered shapemeter rotors (N=21 above), the Chebyshev polynomials would require data at points across the strip (normalized to lie in (-1,1)) the first few of which would be given by

$$\underline{w} = (-1, -0.9877, -0.9511, -0.8910, -0.8090, \text{etc.})^T$$

(for  $j=$  21, 20, 19, 18, 17 etc.)

. . . . (6.5)

whereas the shapemeter rotor centres for twenty one covered rotors similarly normalised would lie at evenly spaced points in the linear domain:-

$$\underline{w} = (-1, -0.9, -0.8, -0.7, -0.6 \text{ etc})^T \dots \dots (6.6)$$

(see (6.7)below)

Clearly the values in (6.5) are not those which occur in practice (6.6), and correct interpolation of (6.6) to the Chebyshev points would be out of the question for reasons both of accuracy at the extreme ends of the vector  $\underline{w}$  and the expense involved in terms of computational effort. We therefore reject the Chebyshev polynomials in favour of a set of polynomials which, whilst retaining the properties of orthogonality to allow the use of the simple equation (6.4), will operate on data given at equally spaced points across the strip in the linear domain.

As an aside at this point, it is to be noted that for  $N$  covered shapemeter rotors, the vector  $\underline{w}$  of equally spaced points in the linear domain, normalized in  $\underline{w} \in (-1,1)$ , is given by

$$w_j = \frac{2(j-1)}{N-1} - 1 \quad \left| \dots \dots (6.7) \right.$$

$j=1, N$

(by which the values of (6.6) were enumerated)

Returning to the choice of polynomials, the author, together with Dr. John Barrett (46), decided that the Gram polynomials were a much better choice. These may be constructed by applying the Gram-Schmidt orthogonalization method to the sequence  $1, w, w^2, w^3$  etc. (47), but for computer usage the present author prefers to use a set of recurrence relationships. A suitable recurrence relation is given in (48) after Forsythe, and takes the form

$$P_i = P_i(w) = (w - \gamma_i)P_{i-1}(w) - \delta_i P_{i-2}(w) \quad \left. \dots (6.8) \right|_{i=1,4}$$

subject to  $P_0(w) = 1, \quad P_{-1}(w) = 0$

$$\text{where } \gamma_i = \frac{\sum_{j=1}^N w_j P_{i-1,j}^2}{\sum_{j=1}^N P_{i-1,j}^2}$$

$$\delta_i = \frac{\sum_{j=1}^N w_j P_{i-1,j} P_{i-2,j}}{\sum_{j=1}^N P_{i-2,j}^2}$$

Now let  $\Sigma^k \triangleq \sum_{j=1}^N (w_j^k)$

then for  $w_j$  equally spaced in  $(-1,1)$ , which is our concern,

$$\sum^1 = \sum^3 = \sum^5 \text{ etc.} = 0$$

and it will be found in the recurrence relations (6.8) that this leads to  $\gamma_i = 0$  for all  $i$ . This simplifies the recurrence relations sufficiently to obtain the first four polynomials explicitly as:

$$\begin{aligned} x_{o_{1j}} &= P_1(w_j) = w_j \\ x_{o_{2j}} &= P_2(w_j) = w_j^2 - \frac{1}{N} \sum^2 \\ x_{o_{3j}} &= P_3(w_j) = w_j^3 - w_j \cdot \frac{\sum^4}{\sum^2} \dots (6.9) \\ x_{o_{4j}} &= P_4(w_j) = w_j^4 + w_j^2 \cdot \left[ \frac{\sum^2 \sum^4 - N \sum^6}{N \sum^4 - (\sum^2)^2} \right] + \left[ \frac{\sum^2 \sum^6 - (\sum^4)^2}{N \sum^4 - (\sum^2)^2} \right] \end{aligned}$$

$$\text{where } \sum^k = \sum_{j=1}^N (w_j^k) \text{ as above, } j=1,2,\dots,N$$

In practice, the first two polynomials are calculated explicitly, and the remainder by the recursion.

Appendix 5 gives examples of the  $\tilde{X}_o^T$  matrix generated by (6.9) at the points given by (6.7) for a fourth order fit, and  $N=8$  (to allow direct comparison with the matrix of Fotakis and Grimble given in (49)) and for the more practical case of  $N=21$ . The matrix  $(\tilde{X}_o \tilde{X}_o^T)^{-1} \tilde{X}_o^T = \tilde{L}$  is also given for each case. (Where  $x_{o_{ij}} = P_{ij}$  as above).

To check the accuracy of fit using these polynomials, an arbitrarily selected vector of measured plant values  $\underline{y}_m$  for  $N=19$  covered shapemeter rotors was taken (see fig.6.1). Using the Gram polynomials (6.9), the estimated parameter values  $\hat{\underline{y}}_m$  corresponding to  $\underline{y}_m$  were calculated using equation (6.3). An "estimate" of the measured shape  $\hat{\underline{y}}_E$  was then obtained using  $\hat{\underline{y}}_E = \tilde{\underline{X}}_o^T \hat{\underline{y}}_m$  (c.f. equation (6.2)) and the result is plotted on top of the original data (of fig.6.1) in figure 6.2.

It can be shown that for a large number of points  $N$ , the Gram polynomials approximate to the Legendre polynomials in suitably normalised form. The Legendre polynomials are calculated by a much simpler recursion than (6.8) (see for example (50)) and these were therefore also tried on figure 6.2 to see if  $N \in (17, 31)$  was large enough to allow their use instead. However, the lack of fit was not encouraging, and therefore the Gram polynomials are retained.

### 6.3 Target Shape for the Control System

The purpose of the control scheme is to maintain the strip shape at some desired form of internal stress distribution in the face of varying plant conditions. In line with the work of Fotakis and Grimble, this is achieved by parameterizing the measured shape values (at regular intervals in time) using equation (6.3), and controlling the resulting vector of parameter values. A set of four reference parameter values at which the resultant vector of (6.3) should be held constant (assuming again a fourth order fit) must therefore be given,

but how are these to be provided?

In one mode of operation, the mill operator can press a button labelled "hold present shape", in case some shape is transiently achieved which is considered desirable for some particular reason. In this case, the vector of parameter values given by (6.3) (at the instant the button is pressed) is used as the reference vector, for the remainder of the current pass through the mill (unless the 'hold' mode is cancelled by the operator in the meantime). This mode was installed in response to mill personnels' suggestions.

Of greater interest, and more conventional for control purposes, is the case where a certain "target shape" is specified to the controller from the outset. For reasons of plant operation, this may differ on pass number 1 of a coil from subsequent passes, but in general the desired shape laid down by the plant personnel takes the following form. For all strip widths, the extreme outer rotors covered by the strip should be at -1.0 units on the operators' shape display (which is arbitrarily scaled from +5.0 to -5.0 units). The next rotor towards the strip centre from each edge should be at -0.5 units. All the remaining rotors should be as near to zero as possible - they will have to be at some small positive value in practice of course, as shape is displayed with respect to mean tension. It is therefore necessary to determine the parameter values which correspond with these ideal shapes. To do this, the vector  $\underline{y}_m$  used in the previous section is calculated

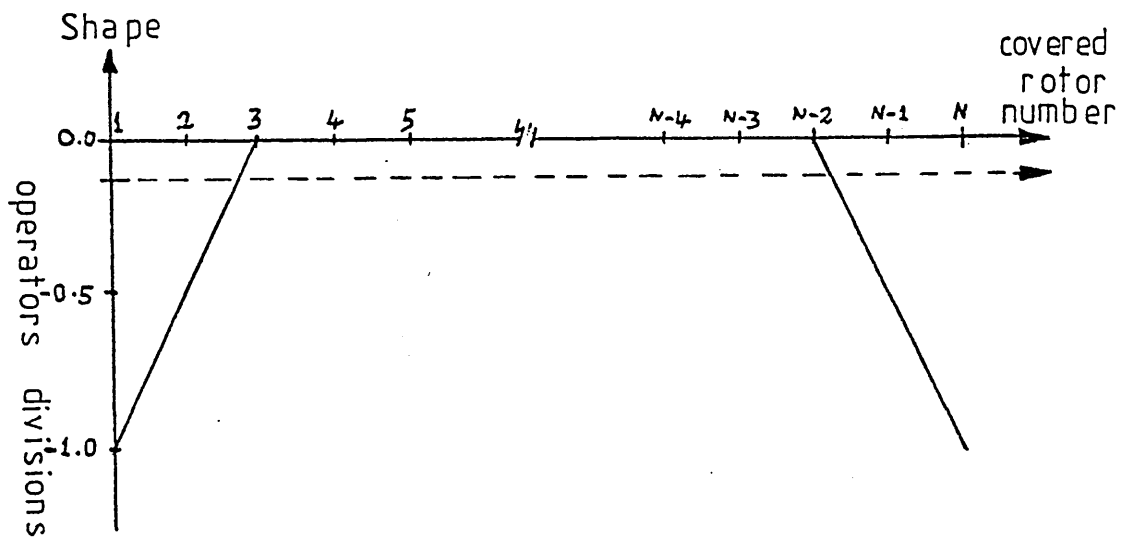
as follows. For a strip width corresponding to N covered shapemeter rotors, ideally

$$\begin{array}{ll}
 y_{m_1} = -1.0 \text{ div.} & y_{m_N} = -1.0 \text{ div.} \\
 y_{m_2} = -0.5 \text{ div.} & y_{m_{N-1}} = -0.5 \text{ div.} \\
 y_{m_j} = 0 \text{ div.} & \left. \begin{array}{l} \\ \\ \end{array} \right| j = 3, N-2
 \end{array}$$

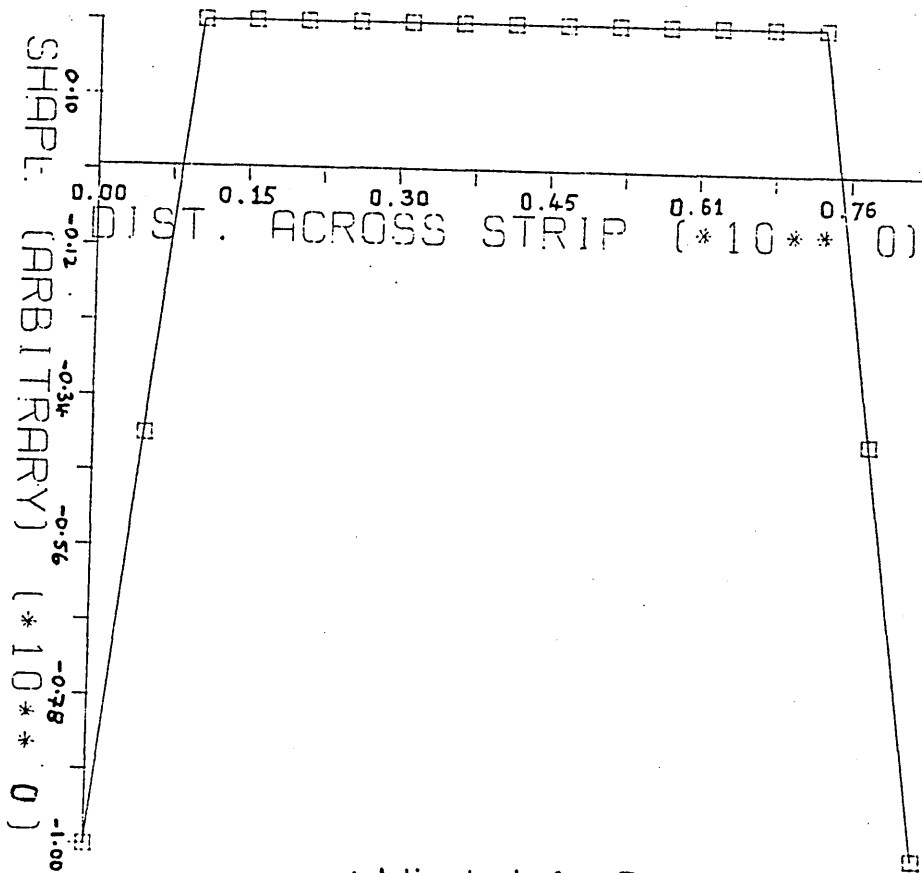
giving the form of figure 6.3(i). However, since shape is displayed with respect to the mean, the horizontal zero axis in fig. 6.3(i) must be moved downwards (as shown by the dashed line) until the sum of the values at rotors 1,2,N-1 and N balances the sum of the values at rotors 3 to N-2. If the extreme end values are to be maintained at a true level of -1.0 division, it can be shown, by a trivial exercise in geometry, that the target shape having zero mean is then given by

$$\begin{array}{ll}
 y_{m_1} = -1.0 \text{ div.} & y_{m_N} = -1.0 \text{ div.} \\
 y_{m_2} = -\frac{N-6}{2N-6} \text{ div.} & y_{m_{N-1}} = -\frac{N-6}{2N-6} \text{ div.} \\
 y_{m_j} = \frac{3}{N-3} \text{ div.} & \left. \begin{array}{l} \\ \\ \end{array} \right| j=3, N-2
 \end{array} \quad \dots(6.10)$$

The reader may verify that  $y_{m_1} + y_{m_2} + y_{m_{N-1}} + y_{m_N} + (N-4)y_{m_j} = 0$



(i) Original Specification



(ii) Adjusted for Zero Mean  
(17 Rotors)

Fig.6.3 Idealized Strip Shape Target

Thus, for 17 covered rotors, (see figure 6.3(ii))..

$$y_{m_1} = y_{m_{17}} = -1.0 \text{ div.} \quad y_{m_2} = y_{m_{16}} = -0.393 \text{ div.}$$

$$y_{m_3} \text{ to } y_{m_{15}} = +0.214 \text{ div.}$$

Whilst for 31 covered rotors,

$$y_{m_1} = y_{m_{31}} = -1.0 \text{ div.} \quad y_{m_2} = y_{m_{30}} = -0.446 \text{ div.}$$

$$y_{m_3} \text{ to } y_{m_{29}} = +0.107 \text{ div.}$$

Whilst employing these values to obtain the corresponding parameter values  $\hat{y}_m$  from equation (6.3) using appropriate  $\tilde{X}_0$  matrices given by (6.9), it was noted that the resulting values for seventeen or thirty one covered rotors were not greatly different, especially in the fourth order parameter. Therefore similar values for all possible cases of covered rotors (N= all odd numbers from 17 to 31 inclusive) were calculated, and the mean value of each parameter was selected. Figure 6.4 shows the fitting errors introduced by this practice for the case of seventeen covered rotors - the worst case due to the lowest number of points making the ideal shape least attainable of all cases by a fourth order curve. However, were this shape to be obtained in practice the plant personnel would certainly not object (since such a flat shape is not easily attained under manual control). Zero mean is automatically retained due to non-use of the zeroth-order polynomial.

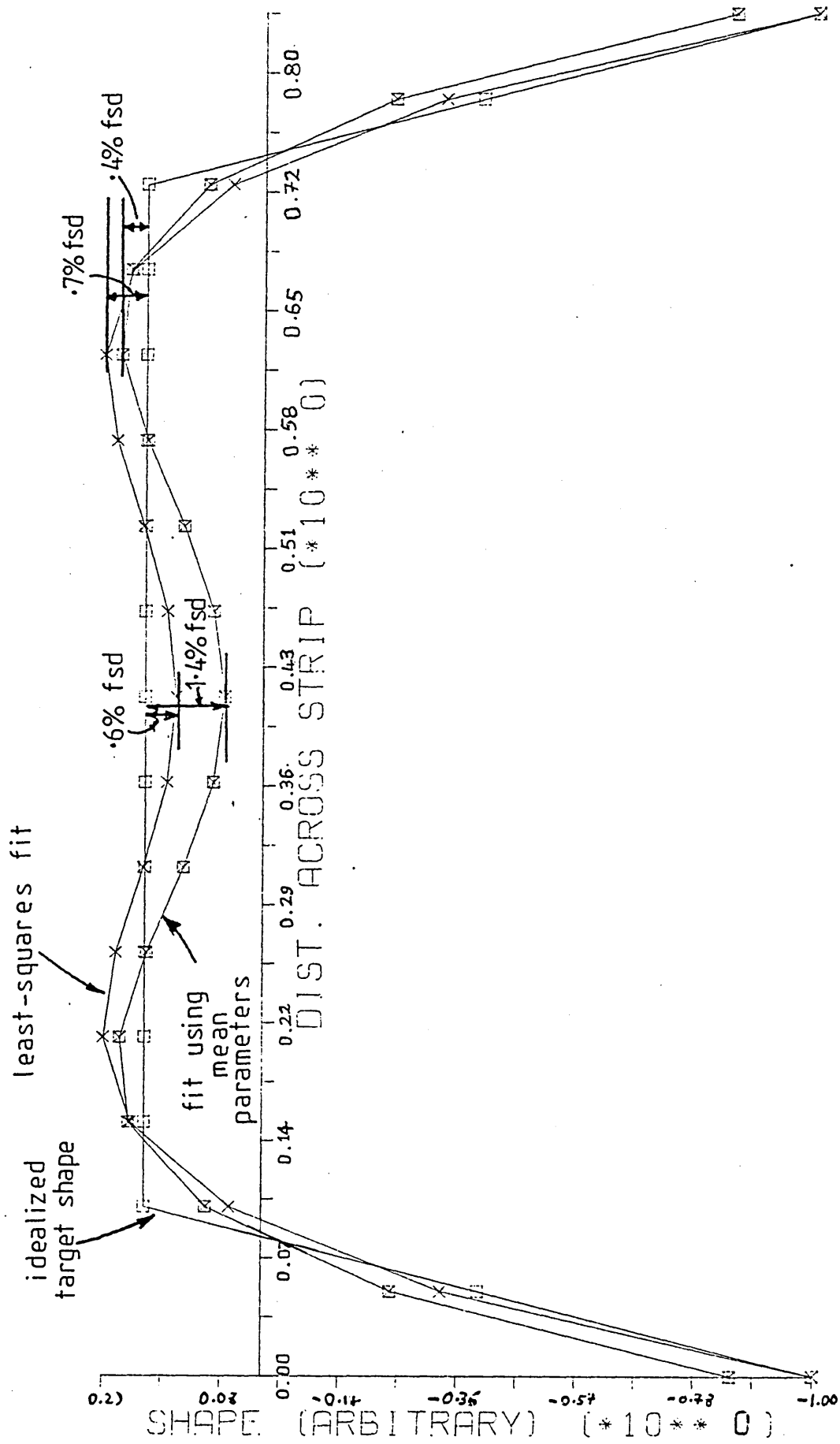


Fig.6-4 Fourth Order Approximation to Target Shape (17 Rotors)

This use of a single target vector for any strip width is a significant discovery by the Author as it completely removed any need to select target shapes according to strip width, thus saving on computing time and storage of data.

#### 6.4 Control System Philosophy

Since we have here a plant with up to 31 shape measurements, plus measurements of speed, tension, width, gauges etc.; and we need to control eight As-U-Roll actuators and two sets of first intermediate roll actuators, a multivariate design would seem appropriate. However, the mill matrix  $\tilde{G}_p$  given by the static model has some unusual properties which must be considered. Due to the symmetrical nature of the mill, given that the left and right hand side eccentrics are set at equal points, a movement of As-U-Roll 1 will cause an identical shape change from front to rear of the strip as the same movement of As-U-Roll 8 would from the rear to the front. Thus if the mill matrix is partitioned

$$\tilde{G}_p = ( \underline{g}_1 \ \underline{g}_2 \ \underline{g}_3 \ \underline{g}_4 \ \underline{g}_5 \ \underline{g}_6 \ \underline{g}_7 \ \underline{g}_8 )$$

where the  $\underline{g}_i$  are all N-vectors, then  $\underline{g}_8 = \underline{g}_1$  with the order of elements reversed,  $\underline{g}_7 = \underline{g}_2$  with the order of elements reversed and so on. Also, since shape is displayed with respect to mean, the elements of each of the  $\underline{g}_i$  vectors must sum to zero. Furthermore, if all eight As-U-Roll actuators were to be changed by the same amount, then no shape change would occur (only a very

small gauge change), therefore every row of  $\tilde{G}_p$  also sums to zero. These properties mean that for the case where the strict inverse of  $\tilde{G}_p$  is defined (i.e. for  $N=8$ ) the matrix will be singular and the inverse therefore meaningless. In the general case of  $\tilde{G}_p$  as an  $N \times 8$  matrix, the natural inverse could be found (see for example Lanczos (51)) but this too would have no significance. This problem would appear to rule out the direct use of the Characteristic Locus (MacFarlane and Kouvaritakis (52)) or Inverse Nyquist Array (Rosenbrock (53)) methods, as these would both produce a controller highly dependent upon  $\tilde{G}_p^{-1}$  due to the fact that all the interactions in the system occur in  $\tilde{G}_p$ . Optimal control methods applied to a state-space representation of the system could be considered (54), but would be expected to be sensitive to parameter variations due to the presence of non-linear elements. The method chosen by Fotakis and Grimble and maintained here, is therefore to linearise the plant and use the parameterization of the measured signals (given correctly by the present author in section 6.2 above) to introduce a measure of redundancy which can be used to obtain an invertible transformed system (see below). This can then be compensated by its inverse so as to form four identical single-loop systems which can be treated by classical concepts (e.g. Bode diagram) to obtain the required controllers.

## 6.5 Control System Design

Figure 6.5 depicts the control system in block diagram form. The actuator transfer functions  $\tilde{G}_a(s)$ , mill matrix  $\tilde{G}_p$ , strip  $\tilde{G}_s(s)$ , shapemeter  $\tilde{G}_m(s)$  and parameterization  $\tilde{X}_o$  matrices have all been previously defined. The matrix  $\tilde{L}$  which compensates for the fact that the Gram polynomials are only orthogonal (rather than orthonormal) has also been defined as  $\tilde{L} = (\tilde{X}_o \tilde{X}_o^T)^{-1}$  (if the Gram polynomials were orthonormal  $\tilde{L}$  would reduce to the unit matrix). The means of providing the reference parameters  $\underline{y}_r$  has also been discussed.

Having controlled (in some manner) the four parameters  $\hat{\underline{y}}_m$  by operating upon the error vector  $\underline{e} = \underline{y}_r - \hat{\underline{y}}_m$ , we obtain the control vector  $\underline{u}_p \in R^4$  (assuming the use of fourth order polynomial fitting). This must be deparameterized so as to give suitable control signals to the eight As-U-Roll actuators (note that the control of the first intermediate roll lateral adjustment will be included at a later date). This could be achieved in a number of ways. There are, however, constraints upon the motion of the As-U-Roll actuators relative to each other which are imposed by the mill manufacturer (see Chapter 8, section 8.2), and therefore the As-U-Roll actuator positions are constrained to lie on a smooth curve. For this reason, and to be consistent with the method of parameterizing strip shape discussed in section 6.2 above it was decided to use the appropriate  $\tilde{X}_o^T$  matrix for this purpose. Now, since the location of the As-U-Roll actuators

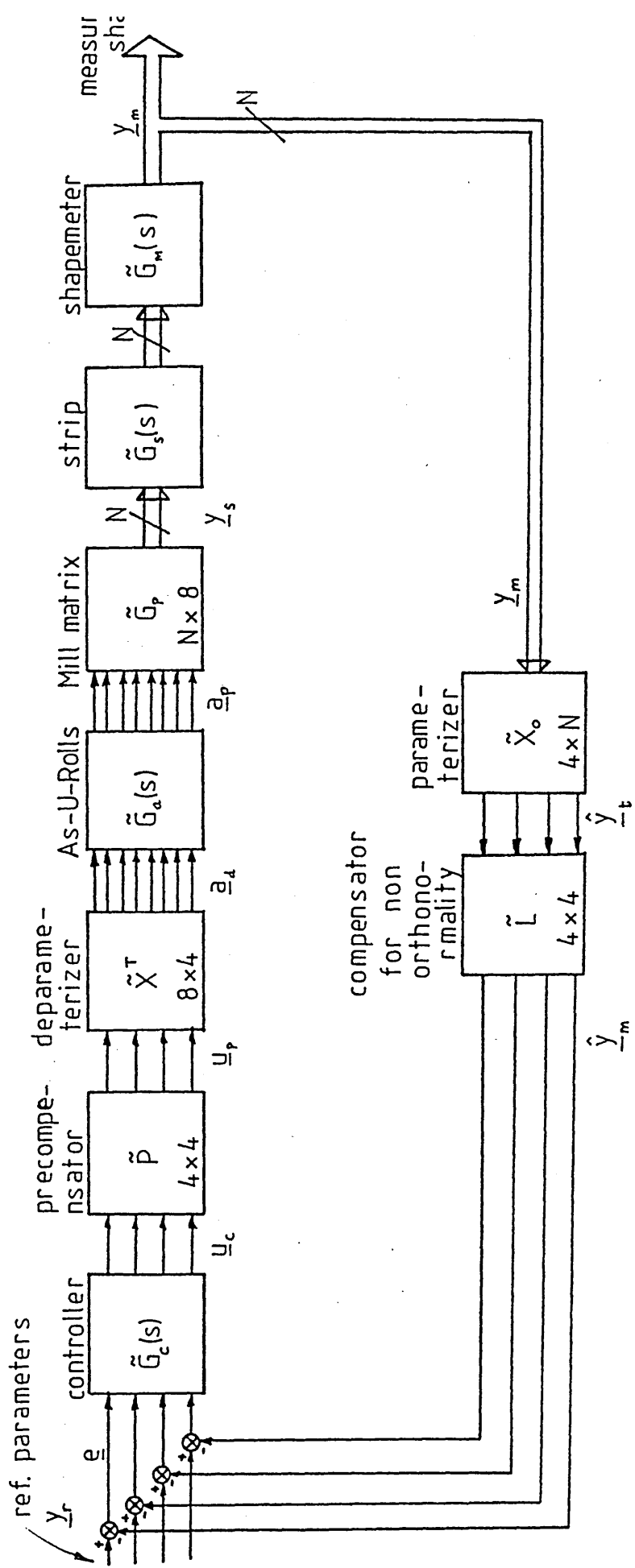


Fig. 6.5 Control Scheme Block Diagram (Fourth Order Parameterization)

is fixed relative to the mill housing and shape measurement points, it would seem sensible that a constant deparameterization matrix could be used.

Referring back to equation (6.2), if the fitting error  $\underline{\delta}$  has been minimized in a least squares regression, then

$$\underline{y}_m \approx \tilde{X}_o^T \hat{\underline{y}}_m$$

In the same way, on figure 6.5, the  $\underline{u}_p$  are (controlled) parameter estimates for the actual control signals  $\underline{a}_d$ , and we therefore write

$$\underline{a}_d = \tilde{X}^T \underline{u}_p \quad \dots \dots \dots (6.11)$$

where  $\tilde{X}^T$  is calculated according to the method of equation (6.9) with  $N=8$  and therefore  $j=1,8$ . This gives  $\tilde{X}$  as a  $4 \times 8$  matrix, so that  $\tilde{X}^T$  is  $8 \times 4$  (which is dimensionally correct).

It can therefore be seen from the block diagram that we now have the entire knowledge of the transformed plant given by

$$\underline{y}_m(s) = \frac{z(s)}{p(s)} \cdot \tilde{L} \cdot \tilde{X}_o \cdot \tilde{G}_p \cdot \tilde{X}^T \cdot \underline{u}_p(s) \quad \dots \dots \dots (6.12)$$

which is a four input, four output system.

where  $p(s)$  and  $z(s)$  are the poles and zeros respectively of  $g_m(s), g_s(s), g_a(s)$ .

Now, let the transformed plant matrix be given by

$$\tilde{G}_T = \tilde{L} \tilde{X}_o \tilde{G}_p \tilde{X}^T \quad \dots \dots \dots (6.13)$$

(Note that we are about to investigate the symmetry properties of  $\tilde{G}_T$  and so we can now consider  $\tilde{X}$  rather than  $\tilde{X}_0$  for convenience).

Let  $\tilde{X}$  be partitioned into  $(\tilde{X}_1 \tilde{X}_2)^T$  such that  $\tilde{X}_1$  contains the low order (first and second) terms and  $\tilde{X}_2$  the high order (third and fourth) terms. (Thus  $\tilde{X}_1$  and  $\tilde{X}_2$  are both  $2 \times 8$  matrices).

The transformed plant matrix (6.13) can then be expressed in partitioned form as

$$\tilde{G}_T = \tilde{L} \begin{bmatrix} \tilde{X}_1 \\ \tilde{X}_2 \end{bmatrix} \tilde{G}_p \begin{bmatrix} \tilde{X}_1^T & \tilde{X}_2^T \end{bmatrix} = \tilde{L} \begin{bmatrix} \tilde{X}_1 \tilde{G}_p \tilde{X}_1^T & \tilde{X}_1 \tilde{G}_p \tilde{X}_2^T \\ \tilde{X}_2 \tilde{G}_p \tilde{X}_1^T & \tilde{X}_2 \tilde{G}_p \tilde{X}_2^T \end{bmatrix} \dots (6.14)$$

The contents of the four terms in the partitioned matrix (6.14) are identical to those found by Fotakis(56) and Grimble, but note that the notation of  $\tilde{X}$  and  $\tilde{X}^T$  is interchanged here due to the conventions of polynomial evaluation adopted, and the matrix  $\tilde{L}$  is omitted from Fotakis and Grimble's work as they assumed their polynomials to be orthonormal (giving  $\tilde{L} = \tilde{I}^4$ ), which is not the case in practice.

During calculation of the matrix  $\tilde{G}_T$  by (6.14) using various versions of the plant matrix  $\tilde{G}_p$ , Fotakis and Grimble noted that the two blocks on the diagonal of (6.14) namely  $\tilde{X}_i \tilde{G}_p \tilde{X}_i^T$  tended to become diagonal. Furthermore, the lower off-diagonal term  $(\tilde{X}_2 \tilde{G}_p \tilde{X}_1^T)$  tended to vanish compared with the upper off-diagonal term  $(\tilde{X}_1 \tilde{G}_p \tilde{X}_2^T)$ , which remained significant in comparison with the diagonal blocks. Thus the entire matrix  $\tilde{G}_T$  was of a dominantly upper-triangular form (the  $\tilde{L}$  matrix

being purely diagonal as given by (6.4)) and was therefore invertible. This allows the possibility of decomposing the entire plant to four single-loop systems by multiplying by a precompensating matrix equal to the inverse of the transformed plant. Therefore, for use in figure 6.5,

$$\tilde{P} = \tilde{G}_T^{-1} \dots \dots \dots (6.15)$$

These matrix characteristics noted by Fotakis and Grimble however, would appear to be characteristics due to the use of the Chebyshev polynomials, as they have not been reproducible by the present Author using the Gram polynomials. Similarly useful characteristics are however apparent. The transformed plant matrix produced by using the Gram polynomials to give  $\tilde{L}, \tilde{X}$  and  $\tilde{X}^T$  in equation (6.13) always tends to the multi-diagonal form:-

$$\tilde{G}_T = \begin{bmatrix} a & 0 & b & 0 \\ 0 & c & 0 & d \\ e & 0 & f & 0 \\ 0 & g & 0 & h \end{bmatrix}$$

for all  $\tilde{G}_p$  matrices investigated. The version of  $\tilde{G}_T$  corresponding to the case of eight (theoretical) covered rotors is given in Appendix A5.6. The determinant of the  $\tilde{G}_T$  matrix is given by

$$|\tilde{G}_T| = acfh - agfd - hecb + bdeg$$

and the terms (agfd), (hecb), (bdeg) are all small compared with the diagonal product (acfh). The matrix is therefore

again always considered to be full rank, and the pre-compensator given by

$$\tilde{P} = \tilde{G}_T^{-1}$$

as before.

Fotakis and Grimble have investigated the use of such a precompensator (17),(18) bearing in mind the uncertainties and inaccuracies in the computation of  $\tilde{G}_p$ , and showed that it is acceptable.

Having reduced the problem to four single loop systems, we return to equation (6.12) and having effectively removed any matrix interaction we are left with a system including the precompensator as

$$\hat{y}_m(s) = \frac{z(s)}{p(s)} \tilde{I}_4 u_c(s)$$

The dynamic terms, as mentioned before, are identical in each loop and are given (from the block diagram) as

$$\frac{z(s)}{p(s)} = g_m(s)g_s(s)g_a(s)$$

Using the various values given previously (for a medium strip speed of  $3\text{ms}^{-1}$  and 1.2m wide strip) we thus obtain from equations (4.2),(4.3),(4.4) and (4.1)

$$\frac{z(s)}{p(s)} = \frac{0.16 e^{-0.37s}}{(1.+ 0.74s)(1+0.12s)(s^2+0.8s+0.16)} \dots (6.16)$$

For which a Bode plot is given in figure 6.6, and Nyquist plot in figure 6.7. These indicate a system having a gain margin of 14.8 dB, and a phase margin of  $180^\circ$ .

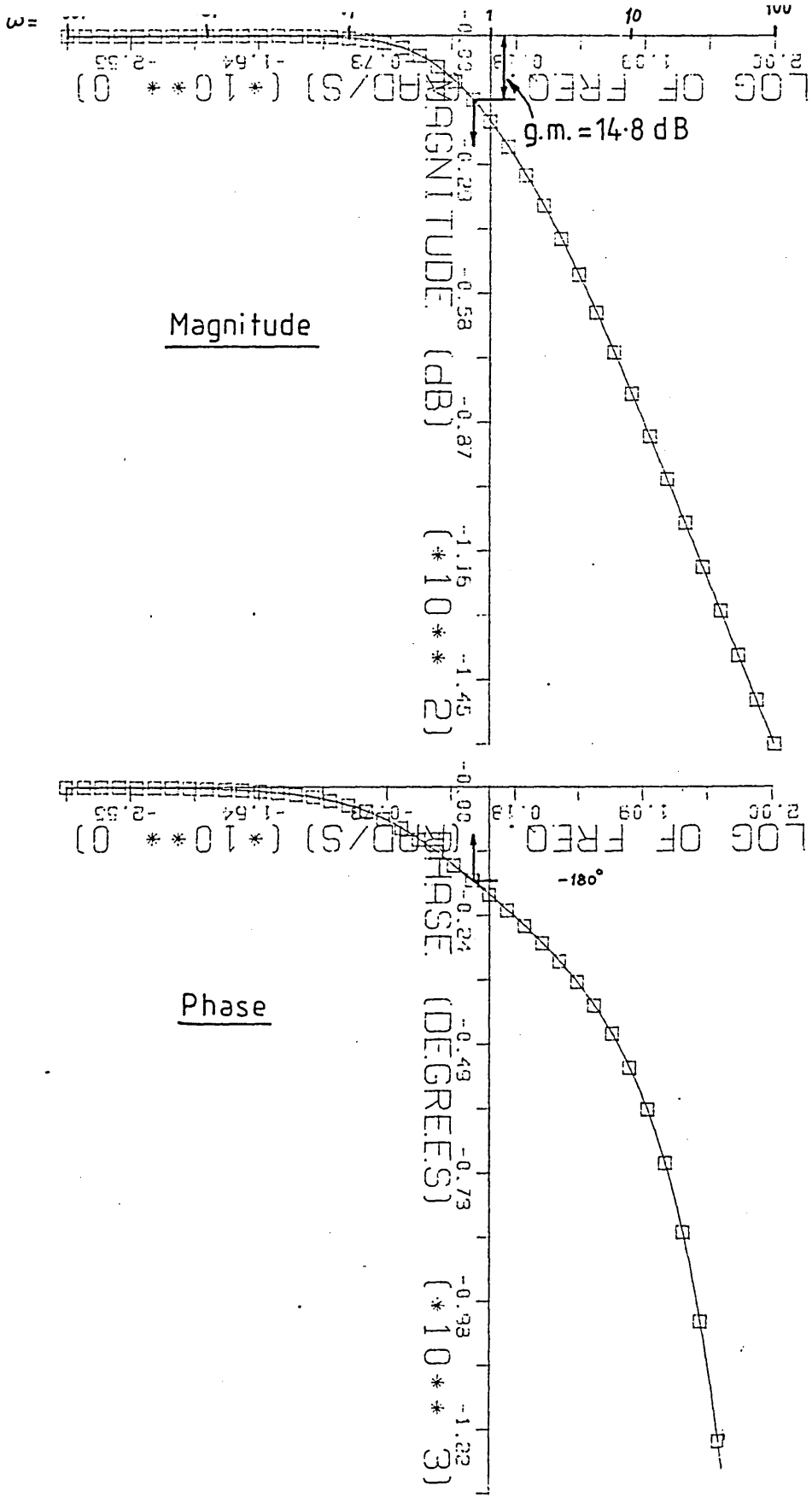


Fig. 6-6 Bode Plot - Uncompensated System

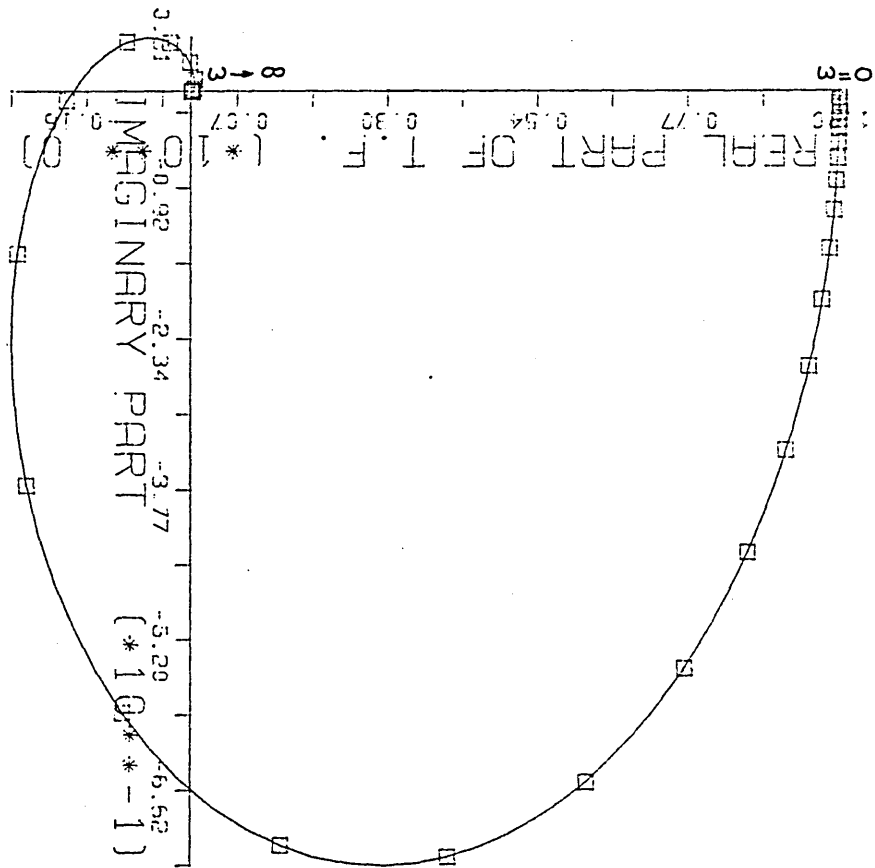


Fig.6-7 Nyquist Plot - Uncompensated System

An integral controller will ensure that this system has zero steady-state error, and can also be designed to give a gain margin having the usual value of say about 12 dB. We may write the controller transfer function as  $\frac{K_I}{s}$  where  $K_I$  is the integral gain.

Using the conventional classical design techniques on the Bode plot, we obtain  $K_I = 0.1$  for the dynamic compensator, giving the overall open loop transfer function as

$$\frac{z(s)}{p(s)} = \frac{0.016 e^{-0.37s}}{s(1+0.74s)(1+0.12s)(s^2+0.8s+0.16)} \dots (6.17)$$

for which the Bode plots are given in figure 6.8, and the Nyquist plot in figure 6.9. The gain and phase margins are then 12.4 dB and  $56.3^\circ$  respectively.

Using the same controller at low ( $1\text{ms}^{-1}$ ) and high (say  $8\text{ms}^{-1}$ ) strip speeds, we obtain (for the same strip width) the following:-

	Gain Margin (dB)	Phase Margin (Degrees)
Low speed :	6.4	35.2
High Speed:	15.2	60.6

It can be seen that at low speeds, the system response will be more oscillatory than one would like. This leads to the possibility that a different controller may be required at very low speeds. Furthermore, at high speeds, although undoubtedly stable, the controller is fairly slow. Nevertheless, this is not a severe problem, as changes in the controlled variable (strip shape) are generally fairly slow phenomena. Alternatively

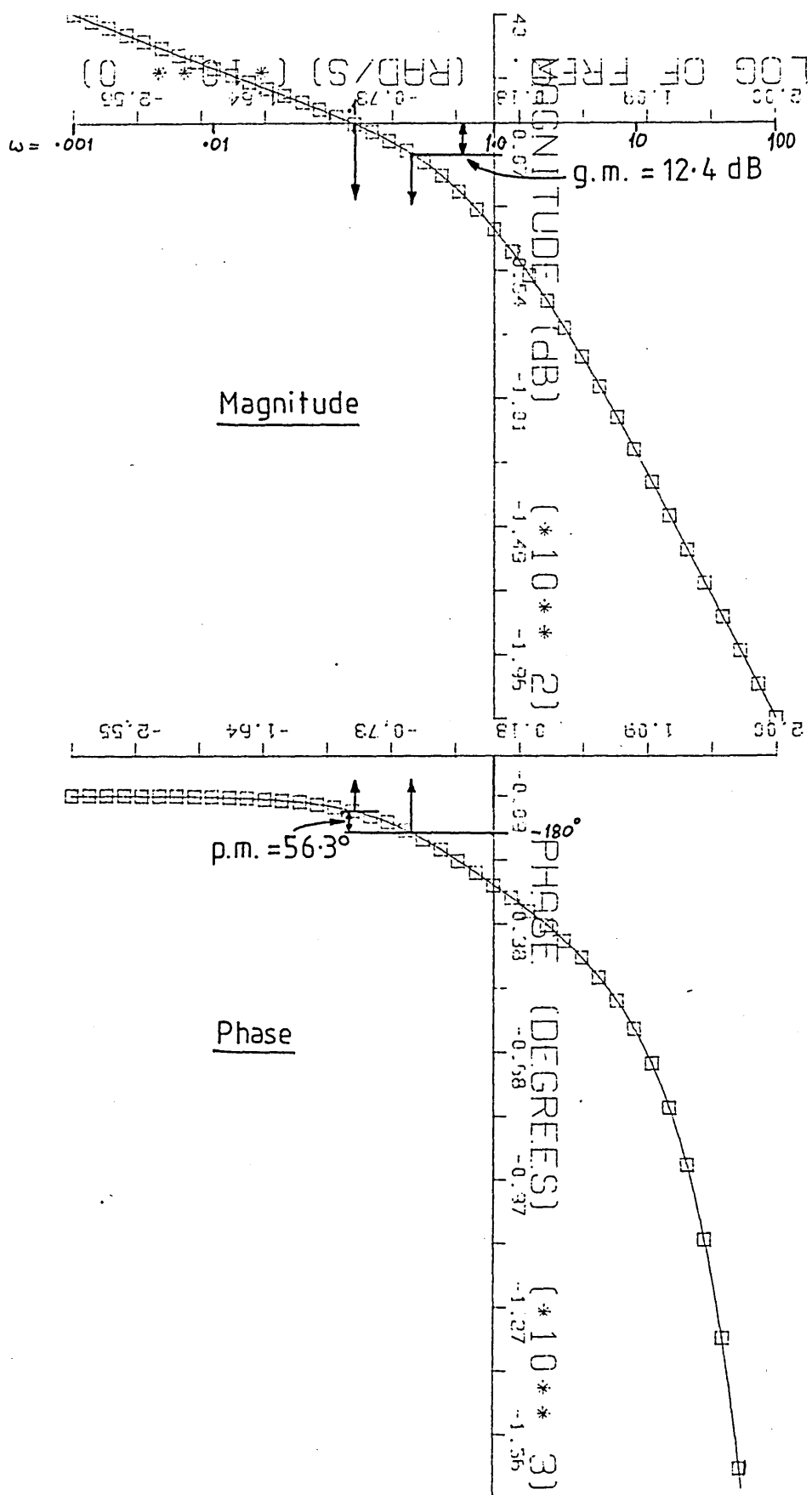


Fig.6-8 Bode Plot - Compensated System (Medium Speed, 3 m/s)

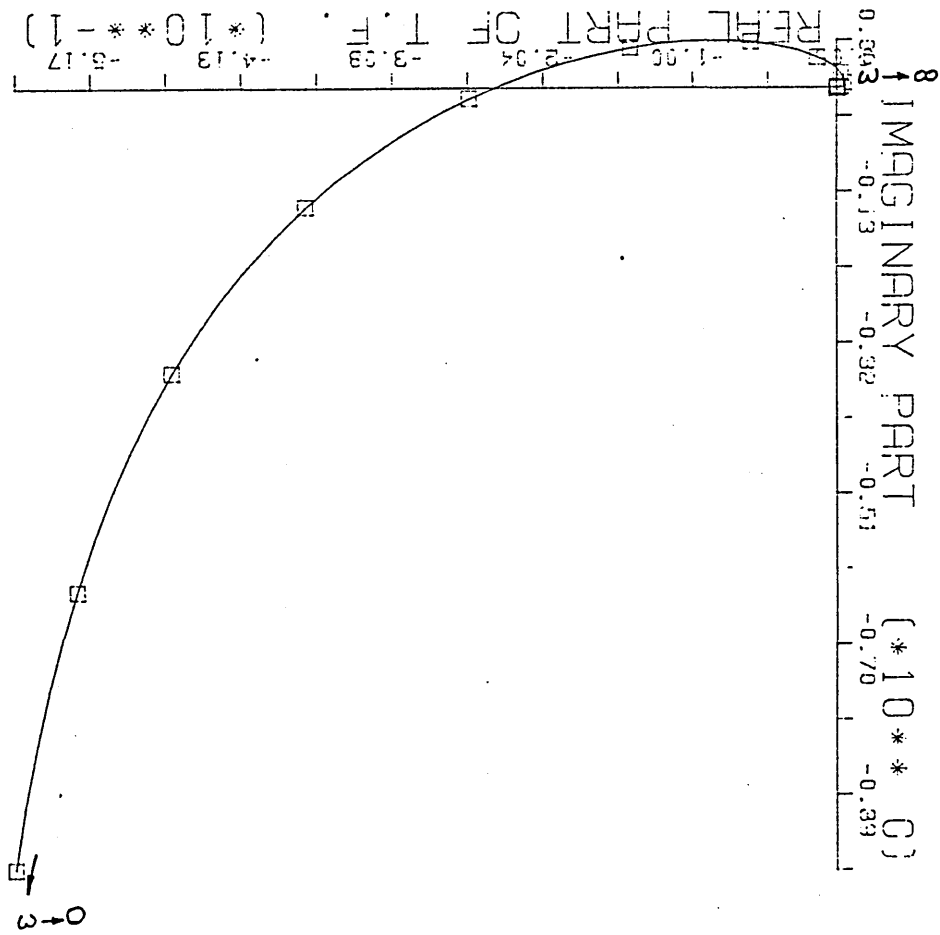


Fig. 6-9 Nyquist Plot - Compensated System (Medium Speed)

the integral gain could be reduced so as to give a greater margin of stability at low speeds, at the expense of response time at other speeds. This may well prove acceptable, due both to the reason just mentioned and to the fact that the limits of As-U-Roll relative motion will probably be reached fairly quickly whatever the response time (within reason) - see chapter 7.

CHAPTER 7  
DYNAMIC SIMULATION STUDIES

7.1 Introduction

A complete multivariable dynamic computer simulation of the plant, as described in the previous chapters, was written in order to compare the relative performance of various controllers, test the effects of different controller parameters and investigate the system's robustness in the face of uncertain gain matrices and mis-matched matrices and operating conditions.

The model is written in FORTRAN (specifically FORTRAN 77) and implemented on the PDP11/70 computer at B.S.C. Sheffield Laboratories under the RSTS/E operating system.

Appendix 6 gives the mathematical techniques used for the simulation routines. The package was written by the author, since no dynamic simulation package was otherwise available. From the appendix it will be seen that the routines in the package (with the exception of that for the transport delay) are all single-input-single-output routines. This is of no consequence in the present context, as all the system dynamical blocks are non-interactive, and so the full state-space treatment would reduce to purely diagonal systems in any case.

## 7.2 Description of the Simulation

The system as simulated is shown in figure 7.1, and comprises the mill gain matrix produced by the static model (Chapter 3), the dynamical elements of the plant (as modelled in Chapter 4) and the control system (of chapter 6.) The system state vectors for 8 control actuators, 4 controlled parameters and N covered shapemeter rotors are identified as follows...

- $\underline{a}_0 \in R^8$  positions of the eight As-U-Roll actuators at the start of the simulation (mm from datum, positive downwards). Also allows injection of "noise" onto the As-U-Roll control signals.
- $\underline{a}_d \in R^8$  As-U-Roll actuator position setpoints (mm from datum, positive downwards).
- $\underline{a}_p \in R^8$  Actual As-U-Roll actuator measured positions (mm from datum, positive downwards)
- $\underline{y}_p \in R^N$ ,  $17 \leq N \leq 31$  Shape at roll gap caused by  $\tilde{G}_p$  operating upon  $\underline{a}_p$ . ( $Nmm^{-2}$ ). N depends upon strip width and the  $y_{p_i} \Big|_{i=1, N}$  are given at positions corresponding to the centres of covered shapemeter rotors.
- $\underline{y}_d \in R^N$ ,  $17 \leq N \leq 31$  Vector of shape disturbances at the roll gap, used to simulate incoming strip shape variation effects. (See also  $\underline{y}_w$  below)
- $\underline{y}_s \in R^N$ ,  $17 \leq N \leq 31$  Shape in strip at shapemeter ( $Nmm^{-2}$ ).
- $\underline{y}_m \in R^N$ ,  $17 \leq N \leq 31$  Shape measured by shapemeter (Shapemeter system output) ( $Nmm^{-2}$ ).
- $\underline{y}_o \in R^N$ ,  $17 \leq N \leq 31$  Shape offset vector ( $Nmm^{-2}$ ). Allows  $\underline{y}_m$  to be initialized to any desired value at the start of the simulation (when  $\underline{y}_m$  would

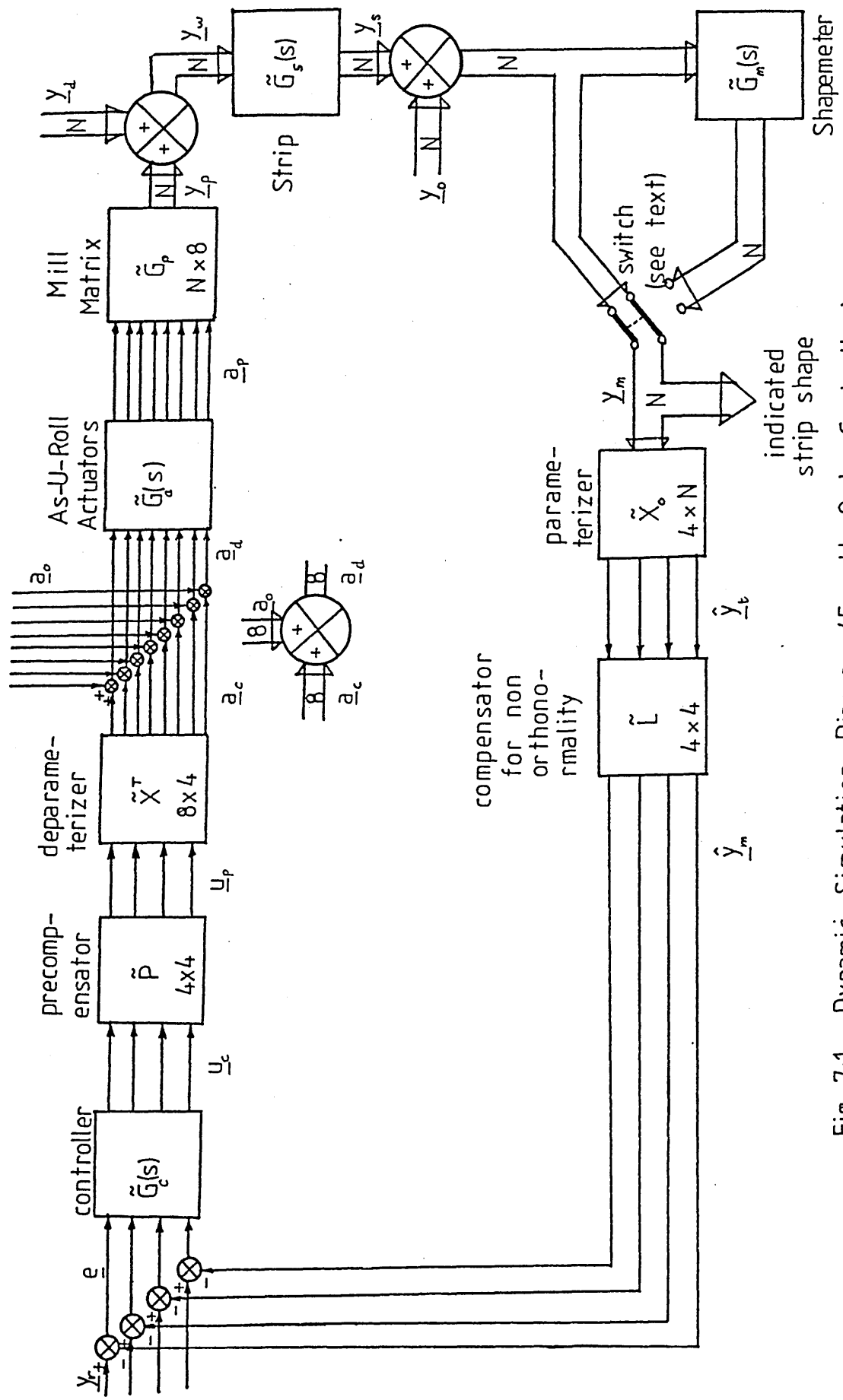


Fig. 7-1 Dynamic Simulation Diagram (Fourth Order Controller)

otherwise be unalterably fixed by the values given in  $\underline{a}_0$ ). Also allows injection of "measurement noise" onto the measured shape signals and simulation of out-of-action measuring zones.

- $\hat{\underline{y}}_t \in R^4$  Shape parameter values given when the matrix  $\tilde{\underline{X}}_0$  operates upon the measured shape signals.
- $\hat{\underline{y}}_m \in R^4$  Least squares estimate of the shape parameters corresponding to  $\underline{y}_m$ .
- $\underline{y}_r \in R^4$  Setpoint values for shape parameters.
- $\underline{e} \in R^4$  Shape parameter error.
- $\underline{u}_c \in R^4$  Controller outputs due to the error  $\underline{e}$ .
- $\underline{u}_p \in R^4$  Controller signals operated upon by the diagonalizing matrix  $\tilde{\underline{P}}$ .
- $\underline{a}_c \in R^8$  As-U-Roll actuator correction signals (to be added algebraically to  $\underline{a}_0$ ) given when  $\tilde{\underline{X}}^T$  operates upon  $\underline{u}_p$ . (mm, positive downwards).
- $\underline{y}_w \in R^N$ ,  $17 \leq N \leq 31$ , Version of  $\underline{y}_p$  perturbed by  $\underline{y}_d$   
 $(\underline{y}_w = \underline{y}_p + \underline{y}_d)$

The system matrices are identified as follows:

$\tilde{\underline{G}}_a(s)$  is the  $8 \times 8$  diagonal matrix of linearized As-U-Roll actuator transfer functions given by

$$\tilde{\underline{G}}_a(s) = \frac{0.16}{s^2 + 0.8s + 0.16} \cdot \tilde{\underline{I}}_8 \quad (\text{c.f. equation } 4.1)$$

where  $\tilde{\underline{I}}_8$  is the  $8 \times 8$  identity matrix.

$\tilde{\underline{G}}_p$  is the  $N \times 8$ ,  $17 \leq N \leq 31$ , matrix given by the static mill model relating strip shape to As-U-Roll positions.  
 $(N \text{mm}^{-3})$  (equation 3.124)

$\tilde{G}_s(s)$  is the  $N \times N$ ,  $17 \leq N \leq 31$ , diagonal matrix of strip transfer functions given by

$$G_s(s) = \frac{e^{[-(2.9-1.5w)s]}}{1 + \frac{w \cdot s}{3.3v}} \cdot \tilde{I}_N$$

(c.f. equation 4.3)

$\tilde{G}_m(s)$  is the  $N \times N$ ,  $17 \leq N \leq 31$ , diagonal matrix of shapemeter transfer functions, given by

$$G_m(s) = \frac{1}{1 + s \cdot T_m} \cdot \tilde{I}_N \quad (\text{c.f. equation 4.4})$$

However, this is shown switched "out of circuit" as it were, because since  $\tilde{G}_s(s)$  was identified by plant tests upon the measured shape signals  $\underline{y}_m$ , then  $\tilde{G}_m$  may be automatically included in  $\tilde{G}_s$  unless  $\tilde{G}_m$  is specifically extracted.

$\tilde{X}_o$  is the  $4 \times N$ ,  $17 \leq N \leq 31$  matrix which parameterizes the measured shape vector  $\underline{y}_m$  into first, second, third and fourth order orthogonal components.

$\tilde{L}$  is a  $4 \times 4$  diagonal matrix which compensates for the fact that  $\tilde{X}_o^T$  and  $\tilde{X}_o$  are not orthonormal, and is given by

$$\tilde{L} = (\tilde{X}_o \tilde{X}_o^T)^{-1}.$$

Hence  $\hat{\underline{y}}_m$  is obtained as the least squares estimate of the parameters.

$\tilde{G}_c(s)$  is a  $4 \times 4$  diagonal matrix of controllers given by for example

$$\begin{aligned} g_{c_{11}}(s) &= \frac{0.1}{s} & g_{c_{22}}(s) &= \frac{0.1}{s} \\ g_{c_{33}}(s) &= \frac{0.1}{s} & g_{c_{44}}(s) &= \frac{0.1}{s} \end{aligned}$$

(Provision is made for proportional terms to be introduced if required).

$\tilde{P}$  is the  $4 \times 4$  matrix which diagonalizes the system to allow use of non interactive controllers. It is given by

$$\tilde{P} = (\tilde{L}\tilde{X}_0 \tilde{G}_p \tilde{X}^T)^{-1}.$$

$\tilde{X}^T$  is the  $8 \times 4$  matrix which deparameterizes the controller outputs so as to give the As-U-Roll positions changes  $\underline{a}_c$ .

### 7.3 Calculation of Initial States

It is assumed that the system is at steady-state before the simulation begins. The method is to specify existing As-U-Roll positions and existing strip shape, and from these to calculate a consistent set of initial values of all the other states in figure 7.1. This includes an initial calculated value for the shape set-point  $\underline{y}_r$  vector, since this must be consistent with the existing shape given above if a steady state is assumed to exist. The matrices  $\tilde{X}_0$ ,  $\tilde{L}$  and  $\tilde{P}$  are obtained as per Chapter 6, based upon a knowledge of strip width. The  $\tilde{G}_s$  matrix is obtained as in the previous section, using knowledge of strip width and speed. All other matrices are fixed, so all the necessary information is now to hand.

Given the existing shape vector  $\underline{y}_m$ , we can immediately calculate  $\hat{\underline{y}}_t$  and  $\hat{\underline{y}}_m$  as

$$\hat{\underline{y}}_t = \tilde{X}_0 \underline{y}_m$$

$$\hat{\underline{y}}_m = \tilde{L} \hat{\underline{y}}_t$$

Now, for steady state

$$\underline{e} = 0$$

$$\therefore \underline{y}_r = -\underline{y}_m$$

Given also the existing As-U-Roll rack position vector  $\underline{a}_p$  and assuming steady state conditions, the transient response of the actuators  $\tilde{G}_a$  makes no contribution; therefore, since the gain of each diagonal element of  $\tilde{G}_a$  is unity, it must be the case that

$$\underline{a}_d = \underline{a}_p$$

Furthermore, at steady state, no change in actuator positions can be demanded, therefore

$$\begin{aligned} \underline{a}_c &= 0 \\ \text{and } \underline{a}_o &= \underline{a}_d \end{aligned}$$

Since  $\underline{a}_c$  is zero, we see that

$$\begin{aligned} \underline{u}_p &= 0 \\ \therefore \underline{u}_c &= 0 \end{aligned}$$

and since we have previously shown that the error vector  $\underline{e} = 0$ , then in order for  $\underline{u}_c$  to be zero it is clear that the outputs of the proportional and integral portions of all the controllers must be zero.

Finally,

$$\underline{y}_p = \tilde{G}_p \underline{a}_p \quad \text{and, since } \underline{y}_d = 0 \text{ initially, } \underline{y}_w = \underline{y}_p$$

and, since the strip transfer functions are of unity gain, and steady state obtains,

$$\underline{y}_s = \underline{y}_p$$

Therefore, in order to make this consistent with  $\underline{y}_m$ ,

$$\underline{y}_o = \underline{y}_m - \underline{y}_s$$

The initial condition of the simulation is therefore completely defined, and can be summarized as:-

Given  $\underline{a}_p$  and  $\underline{y}_m$ , \*

$$\left. \begin{aligned}
 \underline{e} &= \underline{u}_c = \underline{u}_p = 0 \\
 \underline{a}_c &= 0 \\
 \underline{y}_d &= 0 \\
 \underline{a}_o &= \underline{a}_d = \underline{a}_p \\
 \underline{y}_p &= \underline{y}_s = \underline{y}_w = \tilde{G}_{p-p} \underline{a}_p \\
 \underline{y}_o &= \underline{y}_m - \underline{y}_s \\
 \hat{\underline{y}}_t &= \tilde{X}_o \underline{y}_m \\
 \hat{\underline{y}}_m &= \tilde{L} \hat{\underline{y}}_t
 \end{aligned} \right\} \dots \dots \dots (7.1)$$

All controller outputs (P&I) = 0

\*Note that these vectors are specified to the program in terms of divisions on the operators displays for convenience. The program converts  $\underline{a}_p$  to mm of rack movement from the datum position, and  $\underline{y}_m$  to  $Nmm^{-2}$ .

#### 7.4 Post-Initialization Operation of the Simulation

After the system vectors have been assigned their initial values (equations (7.1)), the simulation may proceed in a number of ways, depending upon the reasons for which it is being run. These include:-

- a) In order to simulate the "bump" which would occur when the mill operator selects automatic control, (unless measures are taken to prevent it - see section 8.3), the vector  $\underline{y}_r$  may be replaced with a new set of target parameters. Thus, the setpoint shape for which the controller is to seek can replace the present (manually) rolled shape as a step function.
- b) The vector  $\underline{a}_0$  may be perturbed in any desired manner to investigate the ability of the controller to hold the initial shape in the face of "noisy" As-U-Roll control signals. It will also be possible for the mill operator to move the actuators whilst in the "auto" mode under certain conditions. These effects can also be simulated at  $\underline{a}_0$ .
- c) The vector  $\underline{y}_0$  may be perturbed in any desired manner to investigate the ability of the controller to hold the initial shape in the face of "noisy" and/or non-operational shapemeter segments.
- d) The effects of variations of shape in the incoming stock to the mill (including possible step changes in shape where incoming coils are welded together) can be investigated by appropriate perturbations of the vector  $\underline{y}_d$ .

Whichever of these modes is employed, the procedure by which the simulation progresses is identical, and may be summarized as follows.

Firstly, the integration step size is selected as 0.1 times the smallest of the system time constants.

(The user is given the option of selecting a different step size, should he so wish).

The number of integration steps over which the simulation is to run is entered.

The user can then select listing and/or plotting of any of the state vectors.

A step in input shape may be selected, to be applied after a specified interval.

The user must enter the interval between samples of the strip shape by the controller. This allows the effect of different controller sample times to be investigated. The inclusion of this effect is considered important, since a computer-based controller sampling at an ill-chosen rate can easily destabilize an otherwise stable scheme.

The method of limiting relative As-U-Roll actuator movements (as mentioned in section 4.2 and discussed in section 8.2) may be selected to allow the "unlimited" operation of the control scheme to be investigated, which is not allowed in practice. Thus the As-U-Roll actuators can be limited correctly (as in Chapter 8) or they can be completely unconstrained, or they can be limited to the working range of the racks but

without the relative motion constraints. The purpose of these choices is to allow simulations to reach steady-state, so that the meeting of design criteria can be checked. Otherwise, it is likely that the relative motion constraints would come into action (and restrain further control action) before the system had reached its natural steady state.

Several options are then offered to the user (by the program) pertaining to outputting of results.

Any state vector or vectors in figure 7.1 can be output to a terminal, to a disc-based data file, or both, in tabular or plotted (time response) form. The data sent to file can be subsequently offlined to a line printer for examination.

The simulation then runs in a manner fundamentally identical to the simple example given in section 7 of Appendix 6, with results being updated and output as previously specified by the user.

#### 7.5 Simulation Results

The vast range of tests which could be performed using this extremely flexible model will be appreciated from the foregoing sections. It will also be appreciated that the number of such tests which can be practically performed on a time-sharing installation of mediocre power (slowed mainly by its operating system in this case) is somewhat more limited! In fact it is considered a feat of programming that this model (occupying up to

100k byte of memory on another machine) was overlaid into the 28k byte available space on the PDP11/70 at all! Nevertheless, many useful runs were carried out, and some of the findings follow.

For the basis of comparisons in the results which follow, a "standard" set of input data to the model was used. The strip width was taken to be 1610mm so that all 31 shapemeter rotors were covered. The initial input strip shape was a typical early-pass shape measured from the plant, and is given in Table 7.1

Rotor No. (from front)	Shape (Nmm <sup>-2</sup> )	Shape (Operator's Display Units)
1	78	1.95
2	36	0.9
3	8	-0.2
4	-36	-0.9
5	-52	-1.3
6	-60	-1.5
7	-60	-1.5
8	-52	-1.3
9	-42	-1.05
10	-24	-0.6
11	0	0.0
12	28	0.7
13	54	1.35
14	72	1.8
15	76	1.9
16	80	2.0
17	72	1.8
18	64	1.6
19	48	1.2
20	28	0.7
21	6	0.15
22	-16	-0.4
23	-32	-0.8
24	-48	-1.2
25	-56	-1.4
26	-56	-1.4
27	-52	-1.3
28	-44	-1.1
29	-20	-0.5
30	24	0.6
31	80	2.0

TABLE 7.1 "STANDARD" INCOMING STRIP SHAPE

The As-U-Roll initial positions were always set to zero. An integral controller having a gain of 0.1 was used upon each parameter error. The parameterization and precompensating matrices are computed as per Chapter 6, using the 31\*8 mill gain matrix given in Appendix 5 (section A5.10). The target shape was calculated using equations (6.10) with N=31, and was then parameterized using the calculated parameterization matrix. This gives us the parameter values of Table 7.2

Order of Parameter	1	2	3	4
Initial Shape (Table 7.1)	-1.04	-26.13	-9.41	+570.28
Target Shape	0	-25.57	0	-84.60
Initial Parameter Error	1.04	0.56	9.41	654.88

TABLE 7.2 "STANDARD" PARAMETER VALUES (Units to give shape in Nmm<sup>-2</sup>)

For a strip speed of  $3\text{ms}^{-1}$  (a medium speed), the simulation was allowed to achieve steady-state from these initial conditions. In order to permit the target shape to be achieved, the As-U-Rolls were not limited in any manner whatsoever. The resultant time responses of the four parameters of measured shape are shown in figure 7.2 by the traces labelled 1 to 4 (the traces denoted by the "primed" indicators will be discussed later). It can be seen that the system is "slow" by the normal standards of rolling mill control schemes, but it must be remembered that strip shape is in general a slowly-varying parameter, there is a transport delay in the control loop (although this is only relatively small at a strip speed of  $3\text{ms}^{-1}$ ),

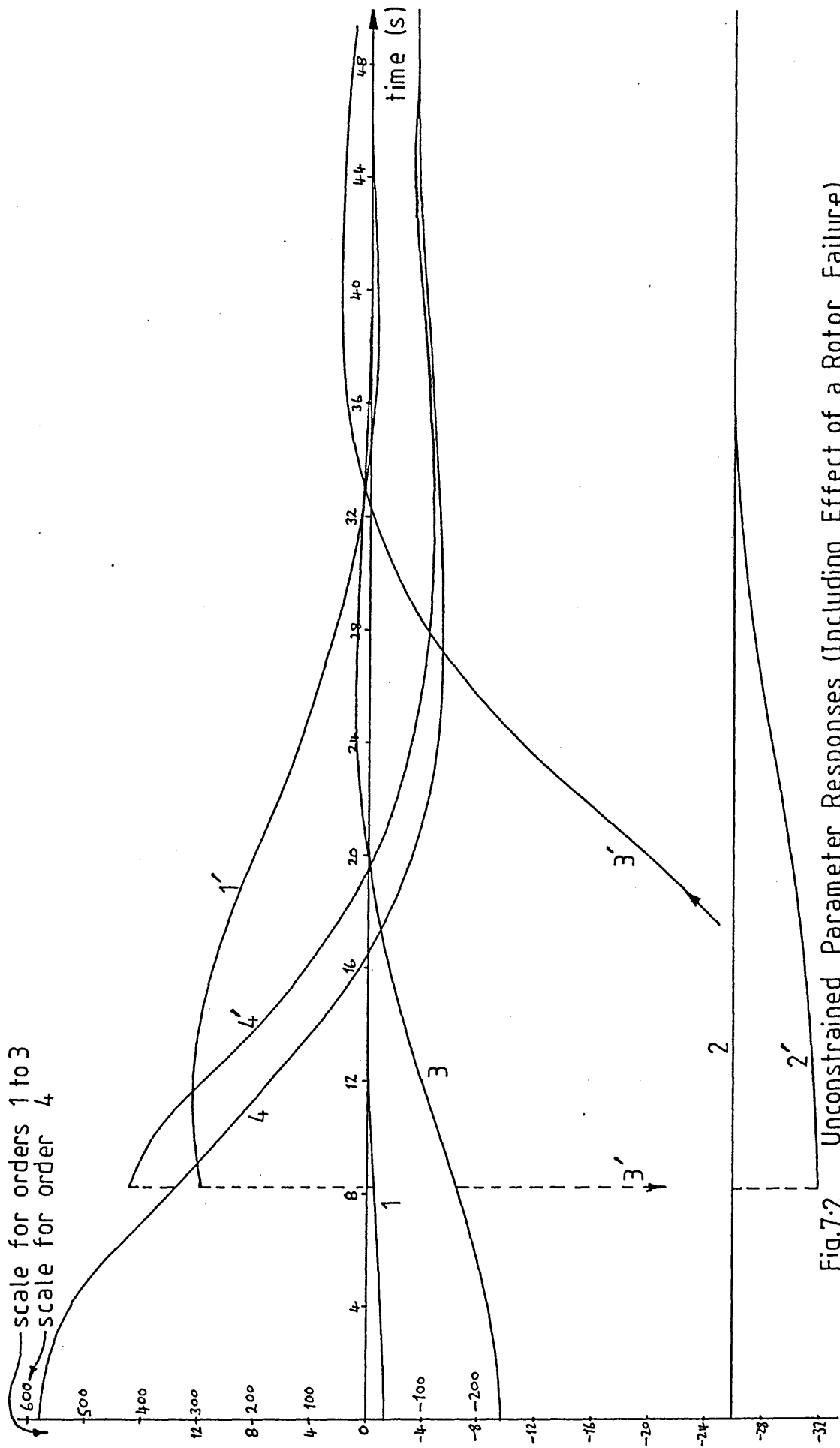
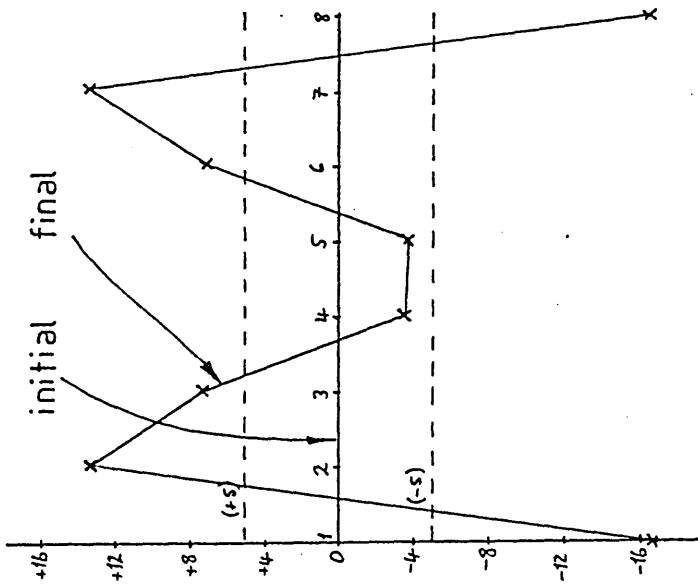


Fig.7.2 Unconstrained Parameter Responses (Including Effect of a Rotor Failure)

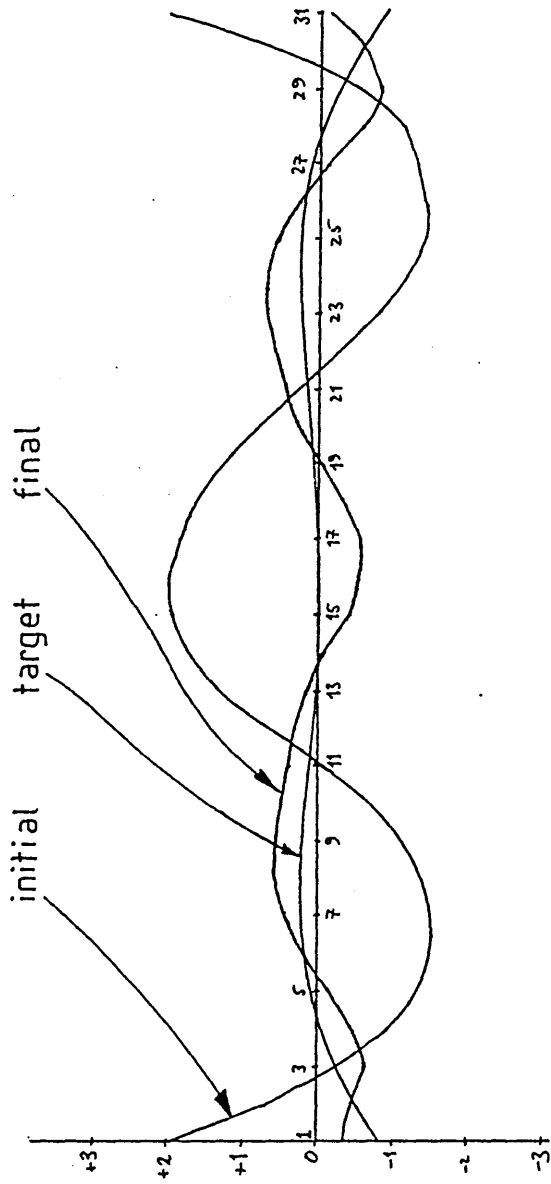
and the As-U-Roll actuators themselves are slow. It will also be noted that the fourth-order parameter response exhibits an overshoot of some 8% even at this speed of response (i.e. the overshoot taken from initial position). This suggests that attempts to increase the speed of response would be unwise, which has been borne out by other simulation runs using different controllers.

Although the target parameters were achieved by the control system, the final strip shape did not coincide with the target shape in the simulation. This is illustrated in figure 7.3 which shows the initial, target and final shapes corresponding with the parameter responses given in figure 7.2 and discussed above. The discrepancy is principally due to the errors in the gain matrix discussed in Chapter 3 (section 3.12), whereby As-U-Rolls 2 and 7 have disproportionately large effects at sections of strip below As-U-Rolls 1 and 8 respectively. This has led in this instance, to a pronounced "turning" in strip shape at the strip edges (see the figure) which would not occur in practice. The strip shape has thus become markedly sixth-order in appearance, and will not adequately be represented by the fourth-order parameter fitting. Therefore, although the parameters have been controlled to their target values, the strip shape thus represented is itself in error. Even so, it is a great improvement over the initial shape.

The major difficulty with figures 7.2 and 7.3 is that in order to achieve this performance, the As-U-Roll actuators (which were unconstrained) have had to adopt



As-U-Rolls



Shape

Fig.7.3 Unconstrained Performance Against Target  
 (Both Vertical Axes are Operator's Display Units)

totally impractical values. This is shown in figure 7.3, where the dotted lines on the As-U-Rolls graph represent the physical limits of absolute As-U-Roll motion ( $\pm 5$  divisions on the operator's scales), not to mention the relative motion constraints which also apply in practice! This simulation run was therefore repeated with the correct As-U-Roll limiting algorithm (described in section 8.2 of Chapter 8) included to constrain the As-U-Roll motion. The resulting final shape and As-U-Roll positions are shown in figure 7.4 together with the same initial and target shapes previously given in figure 7.3. The obvious feature of figure 7.4 is the negligible improvement in shape which was achieved before the As-U-Roll constraints prohibited any further action. This underlines dramatically the very limited gain of the As-U-Roll system alone as a means of shape control. However, in practice the As-U-Rolls would not be expected to cope alone with such a large shape error. The first intermediate roll tapers would be positioned over the strip in such a way as to greatly loosen the strip edges (initially by the mill operator, but eventually automatically when the first I.R.s are included in the control system). As the shape is displayed as a deviation from mean, this loosening of the edges will be reflected in the display not only at the edges, but as a relative tightening of the strip centre also. This calls for an increase in mill crown (or camber) to counteract it, and the As-U-Rolls are much more suited to making such a change than to trying to remove the W shape

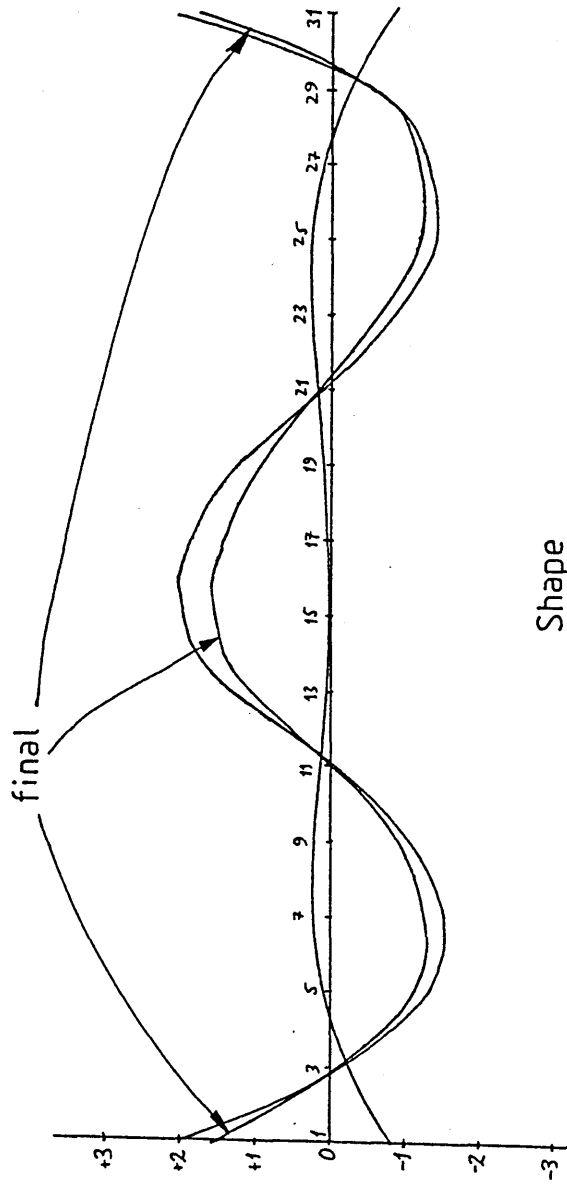
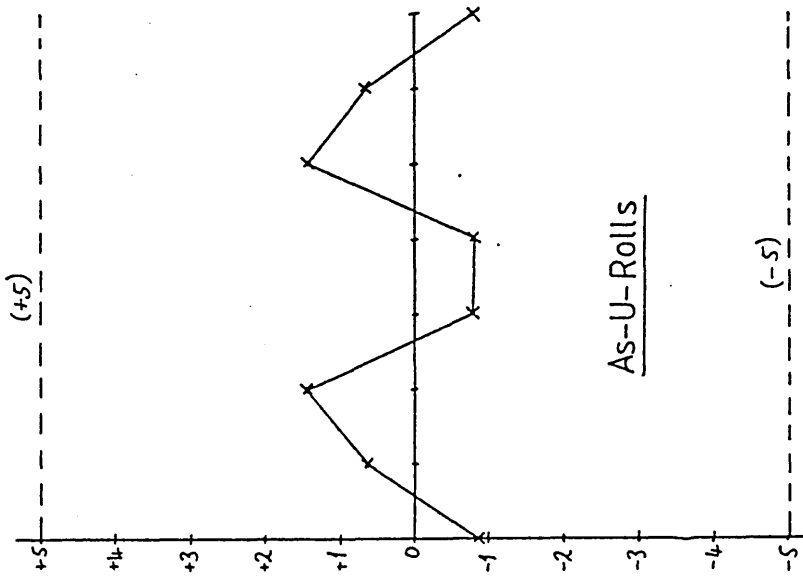


Fig.7.4 Constrained Performance (c.f. Previous Figure)

as shown in figure 7.4. Observations on the mill, of the operators at work, confirm that this is in fact a typical mode of operation. The weakness of the As-U-Rolls in correcting the defect of figure 7.4 unaided is therefore not serious. So far as these simulation studies are concerned, the As-U-Rolls were always allowed to run unconstrained (unless otherwise stated) so as to permit a realistic steady-state to be achieved and to allow a consistent basis for comparisons.

Having obtained an initial satisfactory response, the simulation was repeated under varying conditions. The first of these was to investigate the effects of non-operative shapemeter rotors. One rotor was selected randomly (rotor 6) and was caused to fail after 8 seconds of the simulation. The mode of failure chosen was a shape reading which is permanently off-scale in the negative direction ( $-225 \text{ Nmm}^{-2}$ ) as this has been observed in practice. The resulting time responses of the parameters are shown as traces 1', 2', 3' and 4' in figure 7.2. (Note that the step in the 3rd order parameter caused saturation of the plotting routine - hence the gap!). It can be seen that in spite of this failure of rotor 6, the target parameters are achieved after the failure, albeit in a more oscillatory manner. The strip shape represented by these final parameters is however not good. It takes the form of the final shape in figure 7.3, but with the first positive peak about three times as large (peaking at 1.6 operator's divisions).

A further run was performed in which both rotors 6 and 7 were caused to fail in this manner. The parameter "steps" at the instant of failure were much larger, as would be expected (except for the second-order parameter whose step was the same). Again the target values were achieved within a total time of 60 seconds from the failure, and again the shape represented by these parameters was most abnormal, the three major maxima being +3, -1.5 and +1.0 divisions. A run with rotors 11 and 26 failing gave a result only about 20% worse than the final shape of figure 7.3. The As-U-Rolls also moved to more extreme positions in all these cases in order to achieve the target shape.

One reason for the magnitude of these disturbing results (apart from the obvious one of the measured shape being not representable by the fourth order fitting due to the discontinuities at the failed rotors) is that the model continues to use the failed rotors in its calculations of mean stress. The plant equipment may or may not do this, depending upon precisely in which part of the shape-meter system the failure occurs. If, for example, the failure was only in the display drivers, then the mean stress would be correct, and the effect upon the shape display much less pronounced. These results suggest however, that, if sufficient time is eventually available in the control scheme software, it would be possible to cope with a single failed rotor by replacing the "failed" measured shape value (which can be detected by its magnitude) with the mean of the two neighbouring values.

As an example, at the instant before rotor six failed in the first of the three failure cases studied, the shape measured at rotors 5,6 and 7 was -1.023, -1.084 and -1.003 operator's divisions respectively. Taking the mean for the rotor 6 value immediately after failure would have given -1.023, -1.013 and -1.003 at rotors 5,6 and 7. The minimum of the waveform which previously occurred at rotor 6 (see "initial shape trace in figure 7.3) has been moved to rotor 5 by this operation, but the change is small, and the target parameters would be achieved with a much more acceptable final shape. In the case where rotors 11 and 26 were caused to fail, the values at rotors 10, 11 and 12 would be changed from (-0.342, 0.059, 0.545) to (-0.342, 0.102, 0.545); and the values at rotors 25, 26 and 27 from (-0.911, -0.986, -1.016) to (-0.911, -0.963, -1.016). Both these are insignificant errors, and would allow continuation of reasonable control as opposed to simply switching back to MANUAL mode.

Next, the effect of severe disturbances in input shape (which may occur at a weld for example) were examined by re-running the simulation of figures 7.2 and 7.3, and injecting a huge disturbance onto the incoming strip shape after some 13.5 seconds of the simulation (traces 1 to 4 in fig. 7.2 show that the original shape was well under control by this time). The disturbance added to the incoming shape took the form of the initial shape with all values in table 7.1 multiplied by 125% and the order of the rotors reversed.

The performance of the parameter values due to the disturbance are summarized in Table 7.3. (Tolerances are due to measurement from low-resolution plots):-

Parameter order	1	2	3	4
Error just prior to disturbance	-0.4 $\pm$ 0.2	0 $\pm$ 1	-2.8 $\pm$ 0.2	+120 $\pm$ 6
Maximum error immediately following disturbance	+1.2 $\pm$ 0.2	-32 $\pm$ 1	+10.4 $\pm$ 0.2	> +600 (saturated)
Time from disturbance to first crossing of target value (s)	no crossing	20.9	21.7	18.2
Overshoot (%)	none	7.5	9.2	$\approx$ 8.5
Time from disturbance to stable achievement of target values (s)	17.7	34.9	40.8	41.3

TABLE 7.3 Dynamic Response of Parameters to a Large Step Disturbance

The final shape was approximately 75% further away from target than that of figure 7.3, but this was due solely to the fact that the much larger As-U-Roll motions required (As-U-Rolls 1 and 8 at -34 divisions, for example!) exacerbated the effects of the inaccuracies in the mill gain matrix, causing an extremely marked edge turn-up effect.

All the runs described so far were carried out at the medium strip speed of 3ms<sup>-1</sup>. In order to examine the performance of a fixed controller over the range of practical strip speeds, the basic simulation of figures 7.2 and 7.3 was repeated, firstly at a strip speed of 1ms<sup>-1</sup> and then at 8ms<sup>-1</sup>. The final shape achieved in

each case was virtually identical to that of figure 7.3. The dynamic performances are summarised in table 7.4, from which it appears likely that the single controller will suffice. This of course is only strictly true for a strip width of 1610mm (31 covered shapemeter rotors). At the time of writing sensible simulation results are not available for narrower strips due to problems with the accuracy of the mill gain matrices. However, a qualitative judgement is possible based upon the fact that narrower widths only affect the dynamics directly in the transfer function of the strip between the mill and the shapemeter (the effects of speed were examined in Chapter 6). The controller employed in the simulations was actually designed for a 1200mm wide strip (equation (6.16)). The oscillatory nature of the 4<sup>th</sup> order parameter response in Table 7.4 for  $1\text{ms}^{-1}$  strip speed tends to confirm the predictions made in Chapter 6 following equation (6.17), but is not thought to justify a different controller. For narrower strips, the transport lag between the mill and shapemeter increases, and the time constant of the build-up of shape decreases (see equations (4.2) and (4.3) in Chapter 4). The controller was designed for a transport lag of 0.37s and a time constant of 0.12s. For extreme values of width and speed, the transport delay can vary between (approximately) 0.06s and 1.54s; whilst the corresponding time constant varies between (approximately) 0.03s and 0.48s. To limit changes to a single variable at a time, Table 7.5 shows

Order of Parameter	1		2		3		4	
	1	3 (Fig.7.2)	1	3 (Fig.7.2)	1	3 (Fig.7.2)	1	3 (Fig.7.2)
Line Speed ( $\text{ms}^{-1}$ )	1	8	1	8	1	8	1	8
Time to first crossing of target value (s)	NO CROSSING		NO CROSSING		19.6	20.4	19.32*	19.9
Overshoot(%)	0	0	0	0	12.5	8.3	14.5 <sup>†</sup>	7.3
Time to Stable								
Target achievement(s)	15.9	15.6	0	0	40.6	38.6	58.4	42.9

\* This was followed by a second crossing (to undershoot) after 44.2 s      † undershoot was 1.8%

TABLE 7.4 COMPARISON OF DYNAMIC PERFORMANCE FOR THREE DIFFERENT LINE SPEEDS

the ranges of transport lag and time constant which obtain as the width changes from 1.61m to 0.91m, for each of the three speeds considered above. The controller has already been tested (simulations above) for conditions of (transport lag = 0.485s, time constant = 0.483s) (transport lag = 0.16s, time constant = 0.16s) and (transport lag = 0.06s, time constant = 0.06s) by the runs described

Strip speed ( $\text{ms}^{-1}$ )	1		3		8	
Strip width (m)	1.61	0.91	1.61	0.91	1.61	0.91
Range of Transport Lag (s)	(0.48	1.54)	(0.16	0.51)	(0.06	0.19)
Range of Time Constant (s)	(0.48	0.27)	(0.16	0.09)	(0.06	0.03)

TABLE 7.5 Variation of Strip Transfer Function with Width & Speed

previously; and was tested (control design in Chapter 6) by Bode and Nyquist analysis over ranges of (transport lag = 1.1s, time constant = 0.36s) (transport lag = 0.37s, time constant = 0.12s) and (transport lag = 0.14s, time constant = 0.04s). The entire range of possibilities with the exception of the combination of extreme narrow width and slow speed has therefore been examined by one means or another, and has generated some confidence in the use of a single controller.

The final simulations to be discussed here test the effect of the controller sampling rate upon system performance. The original setup leading to figures 7.2 and 7.3 was again employed. The controller sampling rate for all simulations discussed previously was set at one

integration step of the simulation, which happened to be 37.3Hz. The sampling rate was varied, for these tests, between this value and 0.2Hz. Over the whole of this range, the target values were in fact achieved, and the final shapes did not significantly differ from the final shape of figure 7.3. However, at the very slow sampling end of the range (5s sampling period), the dynamic behaviour of the parameters was becoming greatly degraded, and approaching instability. For example, the response of the fourth order parameter overshoot by 24% and then took approximately 90 seconds to settle after a number of minor oscillations about the setpoint. Up to 1s controller sampling periods however, the dynamic behaviour of all four parameters was almost indistinguishable from traces 1 to 4 of figure 7.2. This is most encouraging for the final system as for various reasons (see Chapter 8) a microcomputer system will be used, and there is much "number-crunching" for such a system to perform. Low sampling rates may therefore be found necessary in order to provide sufficient calculation time.

## 7.6 Hybrid Simulation of As-U-Roll Control

It will be recalled that in Chapter 4, a control scheme was introduced for closed-loop position control of the non-linear "As-U-Roll" actuators. Since the performance of this loop is crucial to the performance of the final control scheme and the accuracy of the dynamic plant simulation, it was to be investigated in a manner as close to reality as possible.

The chosen method was to employ an analogue computer simulation of the As-U-Roll system, including the non-linear characteristics, and to then place around this simulation the controller which was to be used on the plant, programmed into the same computer which would be used on the plant. The only differences between the simulation and reality were therefore the accuracy of the representations of the hydraulic components and non-linear characteristics (the "integrator" type representation of the rack itself being well known from the plant trials - Chapter 5, section 5.4.1).

Figure 7.5 shows the analogue simulation diagram, using the normal conventions for such diagrams. Amplifier A2 performs the function of a first order lag, simulating the transfer function of the relay, valve and hydraulic motor shown in figure 4.2 (Chapter 4) using the "correct" plant values. Amplifier A3 represents the integrator action of the rack, and amplifiers B3, B1 and A4 create the backlash function, whose width is set by potentiometers B2 and B4 to represent 0.1mm (c.f. figure 4.2). The rack position is read by the microcomputer (see Chapter 8 and Appendix 7 for details) which performs the necessary control algorithm (the error calculation, gain and dead-space shown in figure 4.2 - equivalent to a variable width deadspace), and applies a "raise rack", "lower rack" or "off" signal back to the analogue simulation.

Various response tests were carried out using this simulation to tune the microcontroller for optimum performance. The responses finally obtained were extremely

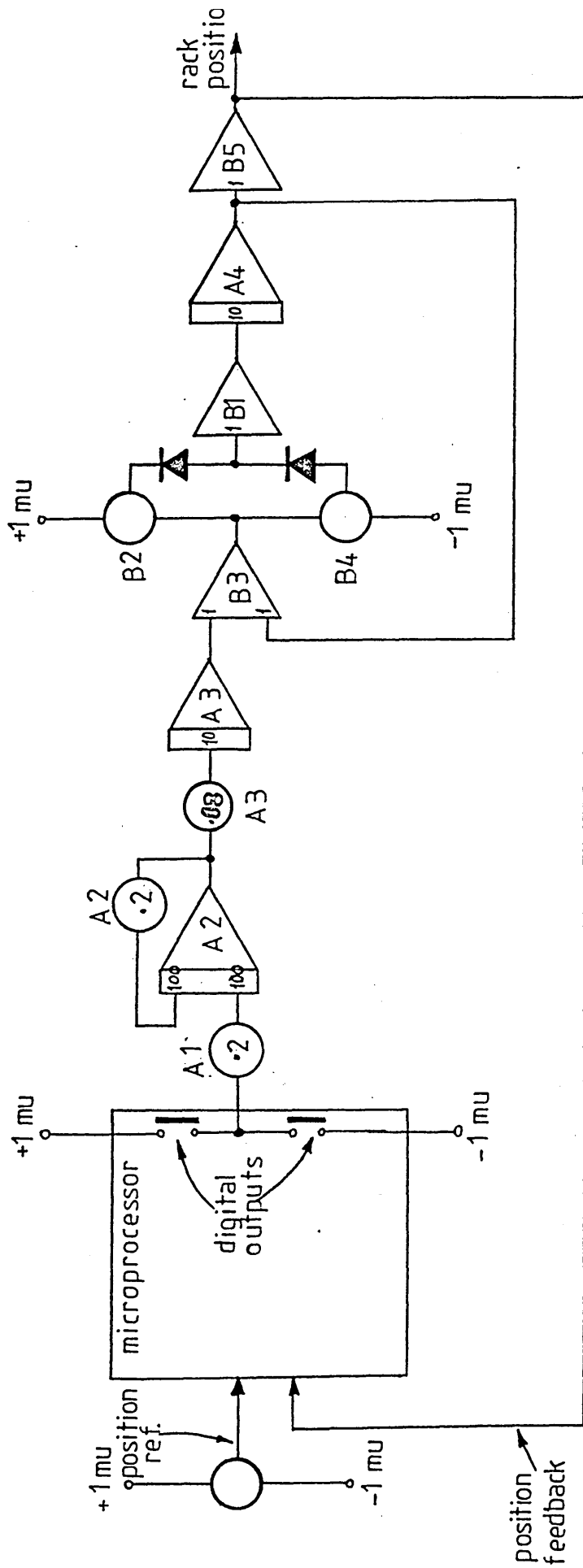


Fig.7.5 Hybrid Simulation of As-U-Roll Rack Control System

close to the response of fig.5.4 which was obtained during plant commissioning . In order to reduce wear on the mechanical components, it is necessary to minimize any hunting around the set point due to limit cycling. This can be achieved for any given set of conditions by tuning of the controller gain (or deadspace width - the effect is the same). However, it is also necessary for the controller to be able to respond to small changes in set point (of say one percent of full travel) for an accurate position control system. The controller parameters necessary for this are somewhat at variance with the requirement for minimum hunting.

Although (as is usually the case) suitable compromise values were achieved by using this simulation, consideration was therefore also given to an alternative controller. This may be described as a pulse width modulation (pwm) controller. In this controller, rather than simply asking the rack to "raise", "lower" or remain stationary, a "raise" or "lower" signal is applied for a given time whenever the controller output leaves the deadspace (of figure 4.2). The duration of this pulse is proportional to the magnitude of the error signal generated in the controller, and is calculated so as to remove the error when the rack has moved for the specified time (pulse width). Thus, for a rack integral characteristic of say  $8\text{mms}^{-1}$ , the pulse width is given (in seconds) by taking 0.125 of the magnitude of the error signal (in mm).

This pwm controller has several advantages over the simple deadspace controller, but is more difficult to program (and more expensive in terms of run time) since it involves the use of timed interrupts for each of sixteen digital outputs ("raise" and "lower" for eight actuators). The advantages include better dynamic performance (i.e. less hunting around the set point; although this is dependent upon accurate knowledge of the rack "ramp" rate) and, most significantly from the plant maintenance viewpoint, fewer on/off cycles of the hydraulic controls. The main reason preventing its use in practice is the fact that the As-U-Roll ramp rates vary enormously depending upon how many racks move simultaneously. For example, a rack moving alone may travel at say 10mm/s, but if all eight racks move together this may be reduced to about 6.5mm/s. The effect is due to flow limiting in the hydraulic supplies, which is necessary to keep the rack rate down to a manageable level for the mill operators under manual control. To attempt an algorithm which was only allowed to move one As-U-Roll at a time (thus fixing the ramp rate) was considered impractical.

SYSTEM IMPLEMENTATION ON THE MILL

8.1 Introduction

As this was always a practical project, with a working system as the end result, the thesis would be incomplete without this Chapter. At the time of writing, installation and commissioning work is still in progress, and is not expected to reach fruition for several months. However, certain aspects of the installation are complete, whilst others are specified in detail, and information about these can therefore be given.

The scope of the Chapter therefore covers the choice of computer hardware, its configuration, the operator and plant interfaces and so forth. Also of great importance are the safety factors such as the limiting of relative As-U-Roll rack travels as laid down by the mill manufacturer, and the behaviour of the control system under fault conditions.

8.2 Limiting of Relative Actuator Travel

The As-U-Roll actuator racks have a working range of some 100mm, which is displayed to the operator on arbitrarily scaled meters of -5 to +5 divisions. The mill manufacturer and plant personnel lay down limits of relative motion between the actuators, so as to safeguard the mechanical components of the plant. The limit criterion may be expressed as follows, "the position of any As-U-Roll actuator shall not deviate by more than 1.5 operator's scale division from the mean position of its two immediate neighbours, or from the position of its

only neighbour if it is an end As-U-Roll." The control system therefore must not impose upon the plant a vector of As-U-Roll position set-points which would violate these constraints.

After much consideration, it was concluded that the only point at which this limiting could be carried out is upon the vector of As-U-Roll setpoints,  $\underline{a}_d$  in figure 7.1, so that the controller would continue to operate at all times unaware that its outputs were being tampered with. This however, leads to the well known problem of integrator wind-up in the P+I controller elements  $\tilde{G}_c(s)$  (see (57) for example), which is considered in the next section.

In limiting the relative As-U-Roll movements, two fundamentally different approaches are possible. Either the As-U-Roll(s) which will violate the constraints may be restrained whilst all other As-U-Rolls are allowed to move to the updated setpoints unhindered, or all the As-U-Rolls can be moved to a scalar submultiple of the proposed vector of updated setpoints, which does not violate the constraints (i.e. the system gain is effectively reduced). Both these methods have their drawbacks, and they will now be discussed in turn.

If the As-U-Roll(s) which violate the constraints are to be restrained, whilst the others are allowed full motion, it is clearly necessary to develop some means of deciding which are the offending As-U-Rolls. This

inevitably involves placing a bias upon the system, whereby certain As-U-Rolls will be moved in preference to others. Since the strip edges are acknowledged to be the most critical areas, it is reasonable that the edge As-U-Rolls should be allowed maximum response whenever possible. An exceedingly sophisticated algorithm was developed which optimized the motion of the As-U-Rolls, so as to allow the absolute maximum number of actuators to move to their new setpoints without the constraints being violated and gave preference to motion of As-U-Rolls near the strip edges. However, the routine was so complex that although it functioned well in the simulation model, it would be impractical to use it on-line for reasons of storage and execution time (the routine involved twenty-four decision nodes, arranged in nineteen interconnected loops around which several iterations were typically necessary)! A second routine was therefore developed giving a sub-optimal solution, but in a much simpler algorithm, an outline flowchart for which is given in figure 8.1. The philosophy here is firstly to test as a whole the set of actuator setpoints demanded by the controller. If the constraints are not violated then all the actuators are allowed to move. If the constraints are breached, then the present set of actuator positions (which are considered to lie within the constraints otherwise they would not have been achieved - apart from plant faults) is taken, the present positions of the edge two As-U-Rolls in the mill are replaced with the demanded setpoints. The set of demands thus formed is then tested against the constraints. If

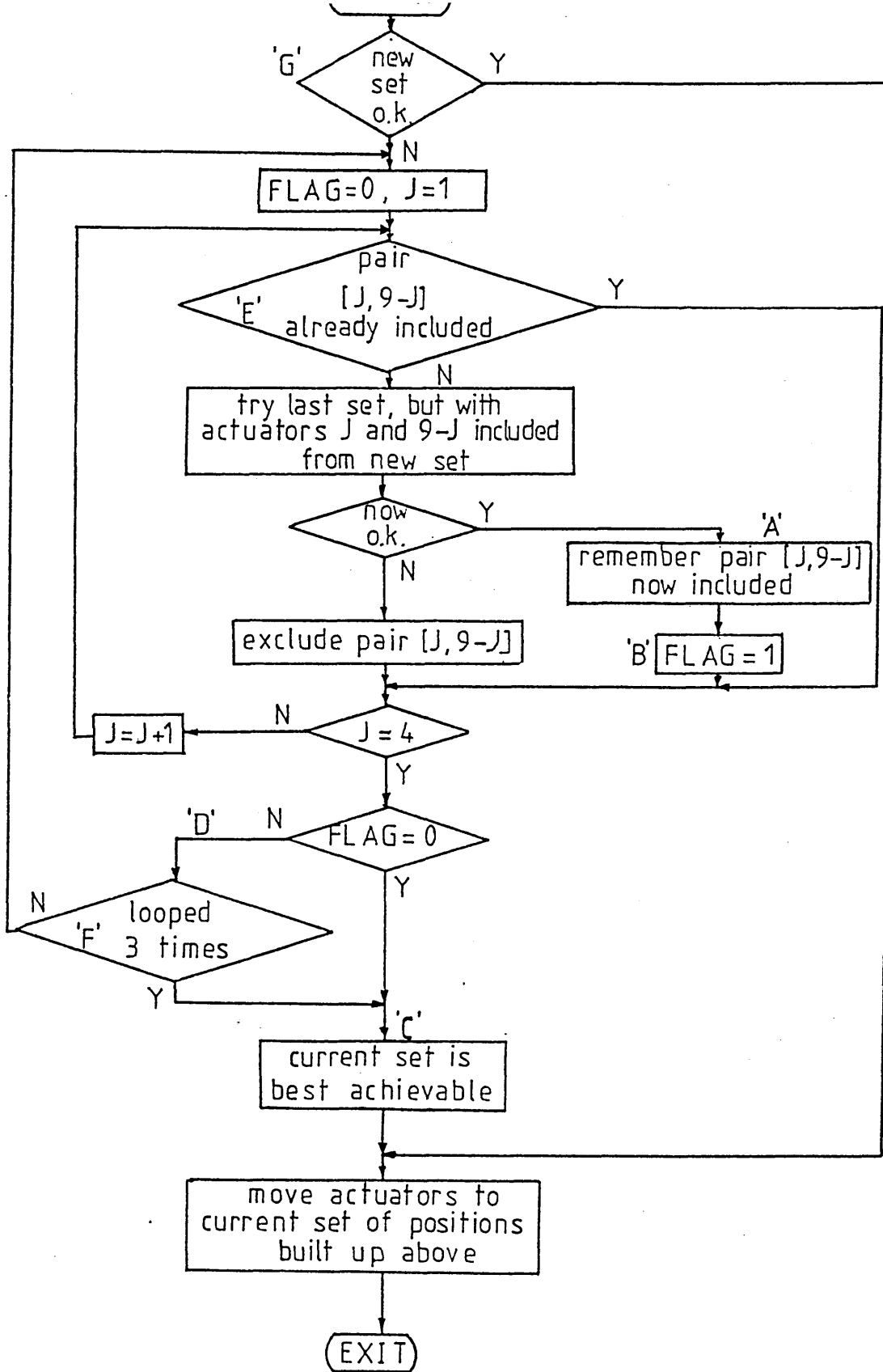


Fig.8.1 Limiting of Relative As-U-Roll Motion By Selection.

the result is acceptable, the next two As-U-Roll positions inwards from the edges of the mill are replaced with their demanded setpoints also, and the procedure repeated. If the constraints are violated on the other hand, then the outer two As-U-Roll positions in the "allowable" setpoint vector which is being built up, revert to their present positions before trying the next inboard pair. This procedure is repeated four times so that all eight of the proposed set points are tried in the admissible setpoint vector one pair at a time, and accepted or rejected as appropriate. Flags are set at "A" in fig.8.1 to indicate which pairs of demands have been admitted. If the flag at "B" has not been set at all during these four iterations none of the new setpoints are acceptable and the setpoint vector has not therefore been updated from its previous values before exiting at "C" (hence there will be no As-U-Roll movement). If however the flag at "B" has been set, then the admissible setpoint vector is now different from the existing As-U-Roll positions and it is worthwhile trying the whole procedure again as another pair of demands which were rejected at the first try, may now become admissible (loop "D" in fig.8.1). The flags set at "A" are now used at "E" to avoid including any new demands more than once. If the test at "F" is true, then the procedure has gone as far as it can, since it is already known that no more than three pairs can be included as a result of the test at "G". This procedure works well, but suffers from the disadvantages that the demanded As-U-Roll "profile" is distorted, and the

As-U-Rolls are limited in pairs whereas only a single As-U-Roll may need to be limited in practice, thus a degree of freedom is to some extent lost. Nevertheless, it is anticipated at the time of writing, that this method will be used in practice.

The alternative of reducing the effective system gain is achieved by the algorithm of figure 8.2. Here, the vector of demanded setpoints is progressively reduced by a percentage of its initially proposed values, until either the constraints are observed, or zero is reached in which case no action is possible and the existing set of positions is maintained. The flowchart of figure 8.2 allows ten iterations, removing 10% of the initial values at each. This method has the advantages of extreme simplicity and of maintaining the form of the required bending profile, but the severe disadvantage that all eight As-U-Rolls are restrained whenever a single demand causes violation of the constraints.

### 8.3 Integral Desaturation in the Controller and Bumpless Transfer

Since it is necessary to limit the relative As-U-Roll rack movements as discussed in the preceding section, it is almost inevitable that the control system as a whole will never achieve the shape demanded by the setpoint vector  $\underline{y}_r$  in fig.6.5. Thus some error  $\underline{e}$  will always exist, even when no further control action is allowed. Since the controller for each parameter contains an integral term (see fig.8.3(i)), the outputs from these

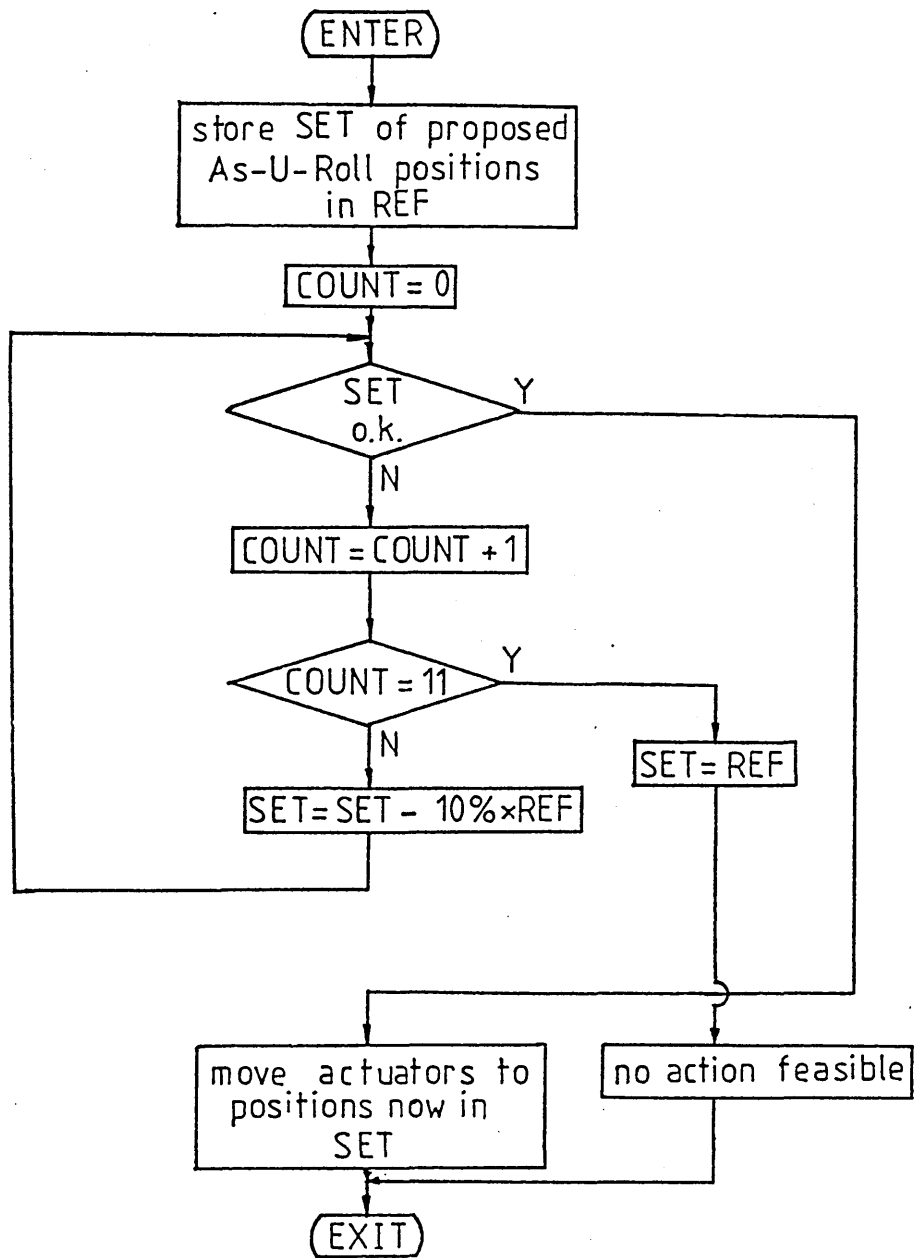
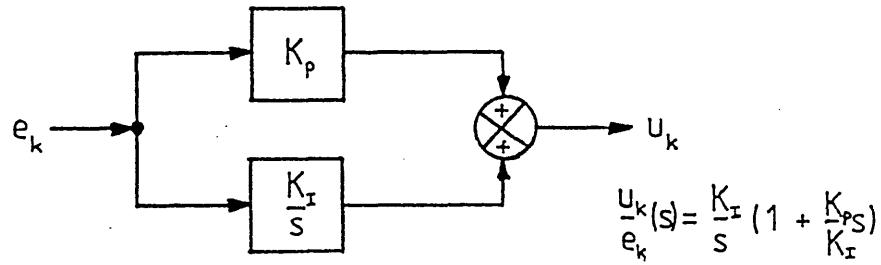
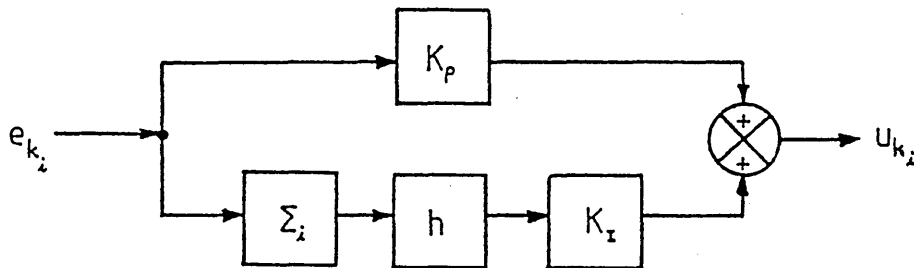


Fig. 8.2 Limiting of Relative As-U-Roll Motion by Gain Reduction



i) Transfer Functional Representation



Where:

h = Digital Controller Sample Interval  
 $\Sigma_i$  = Running Sum of Errors, Desaturated:  
 $= \Sigma_{i-1} + e_{k_i}$  if  $0 \leq u_{k_i} \leq u_{k \text{ max}}$   
 $= \Sigma_{i-1}$  otherwise

ii) Block Diagram of Computer Mechanization at  $i^{\text{th}}$  Step

Fig. 8-3 Digital Realization of P+I Controller for  $k^{\text{th}}$  Parameter

integrators will "wind-up" until the maximum of the computer's number range is reached, after which the count will wrap around, and thus totally unrepresentative values will occur. Furthermore, catastrophic failures may occur due to various overflows etc. in the computer.

This phenomenon of integral wind-up is well known in digital P+I controllers (57), and many methods have been used to overcome it, some being extremely sophisticated. However, it is felt that in the present case, once the As-U-Roll travel has been limited, and the integral of the error begins to build up, it will often be the case that no further control action will be feasible during the current pass of the coil (due to the slowly-varying shape function). Therefore, the simplest method of integral desaturation is employed, namely to clamp the output of the integral term at the level it has attained when the controller output reaches some specified maximum value. This value is different for each parameter and is chosen on the basis of measured strip shapes from the plant. Figure 8.3(ii) shows the digital equivalent of the controller of fig.8.3(i) with this clamping included. The integrators are, of course, reset for each new pass of a coil, and each time the "AUTO" mode is entered from manual. Which leads conveniently to the consideration of bumpless transfer.

Since the automatic system controls the As-U-Rolls by using the identical relays to the manual system, there is no problem when transferring from "AUTO" to "MANUAL"

modes - the operator simply takes over adjustment of the same ("ON/OFF") controls. However, when changing from "MANUAL" to "AUTO", steps must be taken to ensure that the control signals applied to the As-U-Rolls begin at the existing As-U-Roll positions so as to give a bumpless transfer. It is clear from fig.8.3 that if the integrator output ("running sum") is held at zero, then the controller output is due solely to the proportional controller gain acting upon the error signal. Thus, referring to figure 7.1, even when in "manual" mode there will be a non-zero vector at  $\underline{a}_c$  (given that some error exists). This must be held at a level which will cause no immediate As-U-Roll motions when transferring from "Manual" to "Auto" control. Therefore, in the "Manual" mode, every cycle through the control algorithm, the "running sum" of errors is held at zero, and the vector  $\underline{u}_c$  (fig.7.1) is updated as

$$\underline{u}_{c_k} = K_{p_k} e_k \quad \left| \quad \begin{array}{l} k=1,4 \quad (\text{for four controlled} \\ \text{parameters}). \end{array} \right.$$

we then calculate  $\underline{a}_c = \tilde{X}^T \tilde{P} \underline{u}_c$

and set  $\underline{a}_o = \underline{a}_p - \underline{a}_c$  where  $\underline{a}_p$  is the vector of measured As-U-Roll positions. Thus  $\underline{a}_d$  (which is given by  $\underline{a}_c + \underline{a}_o$ ) is always held equal to  $\underline{a}_p$  in the "manual" mode. Therefore when transfer from "manual" to "Auto" is effected, the automatic control scheme will begin by applying a vector

$\underline{a}_d$  of demanded setpoints to the As-U-Rolls, which is identical to the vector  $\underline{a}_p$  of As-U-Roll measured positions. Thus a true bumpless transfer is achieved.

#### 8.4 Computer Hardware

The choice of computer hardware was not straightforward. A mini computer system already exists on each of the mills in question, and it was originally envisaged when the mills were laid down that automatic shape control would be included, at some time in the future, in this machine. However, rather than attempt to interface with the presently operating software, with which neither the author nor his colleagues was familiar (and also for various other reasons) it was decided that the automatic shape control system would be better installed as a "stand-alone" system with its own hardware. Financial strictures within BSC also limited available capital and therefore a microcomputer system was really the only choice - but which?

Many microcomputer systems were considered, but most were considered immediately unsuitable due either to "non-industrialized" construction, insufficient input/output capacity, lack of a fast (compiled) high level language for ease of program development, cost etc. It was realized that a system which could be guaranteed fast enough to perform the complex calculations required, and having sufficient I/O capability would be fairly expensive (say of the order of at least £10,000 per system).

A decision was therefore made to employ on each mill, two single-board microcomputers, which together should be perfectly capable of implementing the scheme, but which were of extremely low cost and well-known to the author.

A brief specification of the computer is given in Appendix 7, and two such machines are wall-mounted side-by-side in rugged steel enclosures in each of the existing mill computer rooms.

The computers are sited remotely from the plant (several tens of metres) and new cabling was installed as required, by the plant personnel. The majority of the required signals, however, was already available at the existing computer interfaces in the computer rooms.

#### 8.5 Plant Interfaces

The purpose of this section is briefly to outline the interaction between the automatic control scheme and the mill operators. The operator's controls which are allowed for, and are being installed at the time of writing, are as follows.

MANUAL (Push-Button) Pressing of this button gives the mill operator sole control of strip shape. Relay interlocking is arranged so that even if the microcomputer system has completely failed, the MANUAL push button will still give control back to the operator. A relay in the LTAC board (known as the "AUTO ON" relay) is disabled, which disconnects all the microcomputer control signals from the As-U-Roll controls. Furthermore, the microcomputer (unless a

failure occurs) will never attempt to move an As-U-Roll in MANUAL mode in any case. Thus double "fail-safe" measures have been included to ensure that the mill operator can regain and maintain MANUAL control under any circumstances, and at any time.

Additionally, the microcomputer system itself (if in AUTO mode) returns control to the operator by switching to MANUAL whenever the strip speed falls outside the range 60m/min to 550m/min (when the shapemeter readings are unreliable). This will occur automatically at the end of every pass of course, and also perhaps at welds and faults. The operator himself must re-engage AUTO if he requires it - (the computer will never of itself assume that AUTO mode is required).

As a further safety measure, the microcomputer performs regular self-checking of a nature which will identify faults in many parts of the computer (although it obviously is far from exhaustive in a real-time system). Should this self-check fail, the computer will again revert to the MANUAL mode, giving control back to the mill operator.

MANUAL (Indicator Lamp). This indicator is illuminated whenever the system is in MANUAL mode. It is interlocked by relays so that it will illuminate under the correct conditions even if the microcomputer should fail.

CONTROL AVAILABLE (Indicator Lamp). This indicator tells

the mill operator that the microcomputer system will accept an AUTO push-button demand. It is only illuminated when the microcomputer system is healthy, the strip speed is between 60 and 550 m/min, and the control software has performed certain calculations required for each pass, and dependent upon strip width etc.

AUTO (Push-Button) If this button is pressed when the CONTROL AVAILABLE indicator is extinguished, it will have no effect.

If the CONTROL AVAILABLE lamp is illuminated, then pressing the AUTO button will cause the microcomputer system to attempt to assume AUTO control. This will not occur, however, if the mill operator has set the As-U-Roll actuators in a set of positions which violates the relative motion constraints. If, on the other hand, the As-U-Roll positions are acceptable to the microcomputer system, then AUTO mode will be entered. The "AUTO ON" relay will be energized (see above) and the microcomputer system will move the As-U-Roll actuators in a controlled manner so as to obtain and maintain a strip shape which is as near as possible to the target shape for the pass in question. The microcomputer system does not permit itself to violate the As-U-Roll relative motion constraints, and possible control action may necessarily therefore be limited on some occasions.

If the microcomputer should fail, or the strip speed falls outside the range 60 m/min to 550 m/min, control is passed back to the MANUAL mode immediately via the fail-safe hardware (see above).

If the mill operator at any time presses the MANUAL push button, he will immediately obtain MANUAL control.

Under certain circumstances, the mill operator will find himself able manually to adjust the As-U-Rolls whilst running in AUTO mode. However, this will upset the microcomputer system's error signals, and the microcomputer will immediately return the As-U-Roll to its previous position when the operator releases the switch.

AUTO (Indicator Lamp). This indicator is illuminated whenever the computer system is controlling the strip shape in either AUTO or HOLD PRESENT SHAPE modes.

HOLD PRESENT SHAPE (Push-Button). Pressing the HOLD PRESENT SHAPE push-button will enter the microcomputer system into a mode in which the shape at the moment the button is pressed becomes the target shape, and is therefore maintained until either the MANUAL button is pressed, the strip speed falls outside the range 60 m/min to 550 m/min, or the microcomputer system fails. Under any of these circumstances, control immediately reverts to MANUAL mode. If the CANCEL button is pressed, control reverts to AUTO mode.

The fact that the microcomputer system will not

permit itself to violate the As-U-Roll relative motion constraints still applies.

HOLDING PRESENT SHAPE (Indicator Lamp). This lamp is illuminated to tell the mill operator that a HOLD PRESENT SHAPE request is being obeyed.

CANCEL (Push-Button). If this pushbutton is pressed whilst the HOLDING PRESENT SHAPE indicator is extinguished, it will have no effect. Otherwise, control is returned from the HOLD PRESENT SHAPE mode to the auto mode, with the appropriate target shape for the pass in question.

TAKE LOG (Push-Button). It was mentioned in Chapter 5 that a microprocessor-based data-logger was used during plant trials. The control microcomputers do not have the capacity to perform this function at the same time as the control function, and a separate machine has not been installed purely for this purpose. Nevertheless, if at any time the plant personnel require hard-copy logging of strip shape for a limited period, this can be had at the expense of automatic shape control by replacing the set of PROM chips in one of the control computers. The TAKE LOG button then initiates the printing of a log.

When the auto control PROM set is mounted, the TAKE LOG button has no effect.

## 8.6 Shapemeter Edge Rotor Compensation

Some consideration was also given to the behaviour of shapemeter rotors which are only partially covered by the edges of the strip. Consider a strip 1000mm wide. For a shapemeter rotor width of  $L_R = 52\text{mm}$ , equation (3.120) in Chapter 3, section 3.10, gives the number of shapemeter rotor centres covered by the strip as  $J_H = 19$ . The equation following equation (3.120) then gives the value of  $L_{ps}$  in figure 3.38 (section 3.10) as

$$L_{ps} = \frac{L_s - L_R(J_H - 1)}{2} = 32 \text{ mm} \quad \dots \dots (8.1)$$

The fractional coverage of the rotors at the strip edges may be found as follows:

$$C_e = \frac{L_{\text{frac}}}{L_R} \text{ (p.u.)}$$

where  $L_R$  = length of shapemeter rotor (m)

$L_{\text{frac}}$  = length of covered portion of rotor under strip edge (m)

$$= L_{ps} + \frac{L_R}{2} \quad \text{for } L_{ps} \leq \frac{L_R}{2} \quad \text{(see fig.3.38 for clarification)}$$

$$= L_{ps} - \frac{L_R}{2} \quad \text{for } L_{ps} > \frac{L_R}{2}$$

Thus for the value given at (8.1),

$$C_e = 0.115 \text{ p.u. coverage of rotors at strip edges.}$$

Now, the shapemeter electronics systems on the mill under consideration make no allowance for such partially covered rotors (an omission which has been corrected on later generations of the ASEA equipment). Therefore,

these partially covered rotors will register a small radial force as the strip passes over them, which will be included in the signal analysis of the shapemeter system in precisely the same way as a fully covered rotor (see Chapter 2 section 2.4.2). Thus, the 19 fully covered rotors (rotors 7 to 25 inclusive) will give the operator his display of strip shape (as shown in figure 6.1 in Chapter 6 for example), but rotors 6 and 26 will also show some stress differential. Since the forces on these two edge zones are comparatively light, the strip is shown as being relatively loose, and the two edge rotors (6 and 26) can often be seen to be displayed at very low values of differential stress outboard of the extreme rotors shown in fig.6.1 (for 1000 mm strip) - see figure 8.4. This, of course, implies that a fourth-order parameter fit will fail, as the behaviour is apparently sixth-order and there are few data points. However, in reality the behaviour is predominantly fourth-order, and it is only the false readings of the shapemeter rotors at the strip edge which cause the lack of fit over the entire width.

Some means therefore had to be found to compensate for such partially-covered rotors. This could be done rigorously by going right back to the force measurements in the ASEA equipment and compensating for the fractional coverage before performing the shape calculations of section 2.4.2. This approach is impractical however, due to the cabling and calculation requirements which would

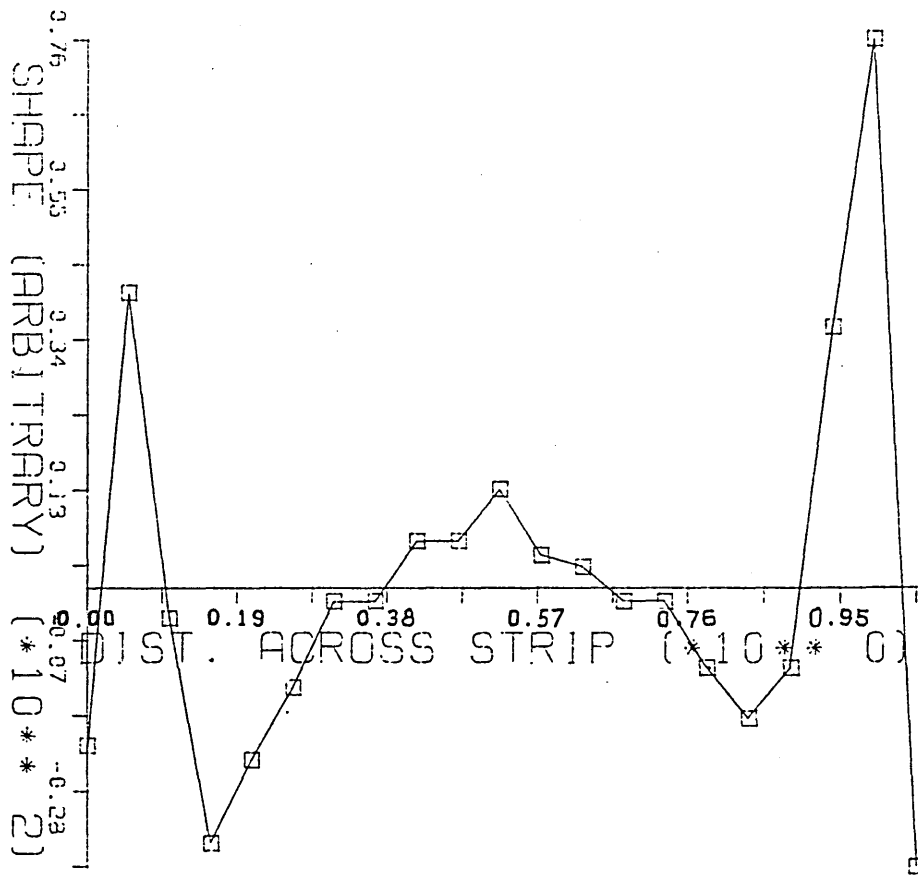


Fig. 8.4 Actual Plant Shape Display (Before Modifying to fig.6.1)

be involved in interfacing the force signals for each rotor (which are derived within the ASEA electronic systems) with the (remote) control microcomputers, and then performing the necessary compensation to the edge two signals before finally duplicating the calculations performed by the ASEA equipment to generate the strip measured shape vector for further processing.

Compensation cannot be carried out upon the measured shape signals at the control computers, as there is no way of evaluating the mean stress. Therefore the only practical solution is to disregard the readings of edge rotors which are less than say 50% covered. This is done by only considering the number of rotors given by  $J_H$  above. Therefore, for a shapemeter having 31 rotors, the only rotors which are considered are from rotors  $\frac{33-J_H}{2}$  to  $\frac{31+J_H}{2}$  inclusive, for strip assumed to be tracking centrally.

This however, leads to a problem in that the area under the shape display must be maintained at zero. Table 8.1 shows in the central column, the values plotted in figure 8.4. It can be seen from the "overall sum" entry that the area under the curve is zero (within rounding errors). Now consider the omission of rotors 6 and 26 (since we know that these rotors are only 11.5% covered for this strip width). The table entry now shows a large discrepancy ( $60.78\text{Nmm}^{-2}$ ).

Let the number of rotors covered by at least 50% =  $J_H$

Let the sum of shape readings of these covered rotors be given by

$$S = \sum_{x = \frac{31+J_H}{2}}^{\frac{33-J_H}{2}} \Delta\sigma_x \quad (\text{Nmm}^{-2})$$

where  $\Delta\sigma_x$  is the shape at the  $x^{\text{th}}$  rotor of 31 from the front of the mill ( $\text{Nmm}^{-2}$ ).

Shapemeter Rotor Number (x)	Actual Strip Shape measured on the plant (see fig.8.4) (Nmm <sup>-2</sup> ) ( $\Delta\sigma_x$ )	Adjusted strip Shape used for Control (see fig.6.1) (Nmm <sup>-2</sup> )
6	-21.95	-
7	40.85	37.65
8	- 4.31	- 7.51
9	-35.55	-38.75
10	-23.95	-27.15
11	-13.95	-17.15
12	- 1.95	- 5.15
13	- 1.95	- 5.15
14	6.45	3.25
15	6.45	3.25
16	13.65	10.45
17	4.45	1.25
18	2.85	- 0.35
19	- 1.96	- 5.16
20	- 1.95	- 5.15
21	-11.15	-14.35
22	-18.15	-21.35
23	-11.15	-14.35
24	36.05	32.85
25	76.05	72.85
26	-38.75	-
Positive Sum	186.80	161.55
Negative Sum	-186.72	-161.57
Overall Sum	0.08	- 0.02
Sum excluding Rotors 6 & 26	S =60.78	

TABLE 8.1 "Edge Compensation" for partially covered rotors

In order to remove this value of S from the sum, we simply correct the reading at each of the  $J_H$  rotors by algebraically adding a value  $\delta$ , where

$$\delta = - \frac{S}{J_H} \quad (\text{Nmm}^{-2})$$

For the values above,  $\delta = - \frac{60.78}{19} = -3.20 \text{ Nmm}^{-2}$ .

The right hand column of table 8.1 gives the values corrected by this amount, and it can be seen that the area under the curve is maintained at zero. These are the values which were plotted in figure 6.1, and upon which the control system will operate.

It is somewhat unfortunate that, for certain widths of strip, this loss of resolution must be tolerated at the strip edges. It is however fairly insignificant, and has caused no noteworthy problems during simulation studies at least.

#### 8.7 System Interaction with First Intermediate Roll Control

Although the first intermediate roll tapers (which can be slid laterally into and out of the mill cluster for shape control purposes) have been considered in the static and dynamic modelling work (Chapter 3-section 3.8, Appendix 4-section A4.3 and Chapter 4-section 4.3), nothing has so far been said about their control. The reason for this is that initially the automatic system will control the As-U-Roll actuators only, the first IRs being still manually controlled. Work is still proceeding into the means by which control of the first IRs may be included in the automatic scheme. Consideration must therefore be given to interaction between the manually controlled first IRs and automatically controlled As-U-Rolls.

The mill operator may be observed during rolling almost invariably to have a parabolic type of bending

profile set on the As-U-Roll actuators (typically in such a manner as to tend to tighten the strip at the edges and slacken it in the centre). From intuitive reasoning however, and also from the results of the dynamic simulation studies in Chapter 7, it would be expected that since the shape in the strip is typically of a W nature, the As-U-Roll profile required to correct it would be M-shaped.

This apparent discrepancy is due to the operator's use of the tapered first IRs. The operator mentally divides the strip into two edge zones and a centre zone. On the first pass of a coil, the first IR tapers and As-U-Rolls are set by experience to obtain the characteristic W shape profile. On subsequent passes, the operator (typically) gradually withdraws the tapered portions of the first IRs from the cluster so as to lengthen the strip edges and thus bring "down" the extremes of the W in an attempt to reach the target shape (see Chapter 6-section 6.3 for details of target shape). Since shape is displayed with respect to mean, this also raises the central peak of the W. The As-U-Roll actuators are then used to alter the mill camber so as to reduce this central peak. No As-U-Roll action is required to assist the first IRs at the edges, as the gain of the first IRs is large for shape control. This explains the parabolic type of As-U-Roll bending profile used by the mill operators - it is simply an adjustment of mill crown, with the fourth-order behaviour at the strip edges being taken care of by the (higher gain) first IRs.

From observations on the plant, the W shape is always likely to exist to some extent when the operator switches to AUTO. The control system will therefore tend to move the As-U-Roll actuators into the M profile discussed above. This is especially true as the algorithm which limits relative As-U-Roll motion (section 8.2) gives preference to movements which will tend to correct shape at the strip edges. Only time will tell whether this behaviour will be acceptable to the mill operators. There are alternative philosophies of operation which may be adopted should it prove necessary during commissioning. One of these is to give preference to As-U-Roll motions which tend to correct the shape at the strip centre. This appears very sensible at first sight, as the mill operator is still manually controlling the edges in any case (via the first IRs). However, in the interests of safety, since the automatic control scheme will attempt to control shape over the entire width using the As-U-Roll actuators, it is more desirable to allow maximum control at the most critical area - i.e. the strip edge.

A second option is to rely heavily upon the operator maintaining the strip edges correctly with the first IRs, and bias the automatic scheme (including alteration of the target parameters for example), towards control of the central area of the strip only. This could be achieved by limiting the set of As-U-Roll positions to roughly parabolic forms (as used by the mill operator) and generating an error vector corresponding only with some central region of the strip.

Clearly this is all conjecture at this stage. The modelling effort necessary to investigate these conditions is formidable, and would probably not be completed before the system is in operation in any event. Therefore, it was decided at the time of writing to adopt an empirical approach to these problems as and when they arise during commissioning. The main point is that no detrimental effects are expected due to continued manual operation of the first IRs - they will merely make the strip shape closer to the target, which can only assist the automatic system.

CHAPTER 9  
CONCLUDING REMARKS

In response to ever increasing customer demands for rolled strip quality, the introduction of automatic gauge control schemes onto rolling mills has been well understood for several years now (i.e. automatic control of strip thickness along the length of a coil). Such AGC systems are virtually mandatory on all new steel rolling mills, and it is proving essential in many areas also to retro-fit such schemes to existing mills in order to maintain competitiveness and market share.

Having solved the AGC problem, researchers in the metal rolling field turned their attention to the problem of automatic shape (or flatness) control, again stimulated by market pressures. The purpose of AFC systems is to allow the roll gap profile to be adjusted so as to conform with the cross sectional profile of the incoming material, thus obtaining a rolled product free of internal stresses; or to alter the roll gap profile in a manner calculated to remove existing internal stresses in the strip. Strip free from internal stresses is free from any tendency to warp or buckle, or to bow sideways when slit into narrower widths. Thus it is more saleable, and also easier to feed through any further processing lines after the rolling process.

Such AFC systems were first installed on four-high aluminium mills, and then on four-high steel mills (for

both strip and plate). Most new four-high steel mills are now built incorporating roll-bending jacks so as to allow for shape control systems to be installed, and many such automatic systems are now in use around the world.

Although AFC systems on four-high mills are now widely accepted, the problem of AFC on a Sendzimir cluster mill has not yet been fully solved. This is largely due to the multivariate nature of the control problem, since the Sendzimir mill has many more degrees of freedom for control than does the four-high mill. The four-high mill for example may only have roll-bending jacks for shape control (in addition to the inherent facility of differential adjustment of the mill screws). Thus limiting control action to linear and quasi-parabolic forms of roll bending. (It should be noted that differential cooling across the roll barrel is becoming more widespread in the steel industry however, having been more favoured in the aluminium sector to date). On the other hand, the type of Sendzimir mill discussed in this thesis (a large, twenty-roll, 1-2-3-4 stack type of mill) has eight separate shape control actuators distributed across the mill width and two further sets of actuators specifically designed for high gain shape control at the strip edges. Movement of any one of these ten actuators will cause a shape change of greater or lesser magnitude to be registered at every measuring zone (of the thirtyone segment shapemeter) which the strip covers. Furthermore, it is conceivable that shape errors of fourth order behaviour and more could be

controlled by an automatic system using these actuators. The content of this thesis is concerned with the development of an AFC scheme for such a mill.

The thesis describes the work carried out on a project of great practical value, and covers the entire course of the project from conception to implementation on the plant. This is justified firstly on the ground that it gives a complete overview of the work; and secondly on the basis that the entire project taken as a whole is original work, which has been done nowhere else in the world to the author's knowledge, although since the thesis covers such a wide range of subject-matter there is inevitably a fair amount of standard work distributed through it.

During the course of this project, the author was employed by British Steel Corporation, Research Services, and was effectively for most of the time the project engineer responsible for the work. The author carried out virtually all the theoretical work (except for the basic development of the control strategy) and computer modelling single-handedly, but was assisted (of course) in the plant trials and plant implementation phases of the work by his own engineers and by personnel employed by BSC Stainless on the Sendzimir mill site (see acknowledgement).

The first Chapter of the thesis forms an introduction to the shape control problem including some historical background into various methods of shape measurement and control. The Sendzimir mill installation

together with details of the various control actuators on the mill and the strip shape measuring system are described in detail in Chapter two, so as to provide a basis of understanding for the following Chapters. Chapter three describes the development of a mathematical model of the static behaviour of the mill stand, including very detailed modelling of the various control actuators. Some details of the computer mechanization of this model are also given. The work of Chapter three is entirely original, including a more rapid solution of Bland and Ford's roll force model than has been reported before. The model can be run for an infinite variety of plant conditions, and therefore only a few representative results are discussed in any detail. The result of running the model is a plant gain matrix relating movement of any As-U-Roll actuator to the resulting shape change at various points across the strip. Many runs of this model have shown that different matrices are produced for different mill conditions. For example, when rolling harder materials, the gains in the matrix are reduced. When rolling narrower materials, the gains also reduce and so on. Various portions of the static model requiring further work are mentioned in Chapter three, but in essence the matrices for wide strip are thought to be more reliable than those for narrower strip due to edge effects. The model is much faster in execution than that of Gunawardene (16) due to the non-iterative structure.

Chapter 4 describes the dynamic (transfer functional) analysis of the plant items including the As-U-Roll actuators for shape control (which contain non-linearities), the shape measuring equipment and the progress of shape changes between the mill and the shapemeter. By the end of Chapter Four therefore, a proposed model of the entire plant exists. This takes the form of transfer functional descriptions of all the dynamic plant elements, together with a static model providing a gain matrix for the mill stand itself, which is non-dynamic. A controller design is specified for the position control of the non-linear As-U-Roll actuators, and the resulting closed loop system is linearised for use in control scheme design (the actuators were originally open-loop on the plant, being controlled by "RAISE-OFF-LOWER" switches by the mill operator).

Chapter Five gives details of attempts to verify the various models and tune them to the plant. This proved to be an exceedingly time-consuming (and not wholly successful!) task, and involved the use of over £100000 worth of test equipment, much of which had to be custom designed by the author. Verification of some of the dynamic modelling was successful, notably the As-U-Roll actuator transfer functions and As-U-Roll controller simulations, but verification of the transfer function of the strip between the mill and shapemeter and verification of the static model, proved very difficult for a number of reasons. Included among these are unexplained (but significant) variations in recorded strip

shape which made it virtually impossible on many occasions to distinguish spurious from deliberately induced effects (the magnitude of induced test signals being limited by operational constraints, and the use of PRBS testing being unreliable due to the plant construction and design.) As a result of these tests confidence was generated in most of the transfer-functional modelling and the intuitive confidence in the gain matrices produced for wide strip was upheld (if not totally vindicated!). The most reliable mathematical description of the plant available had thus been generated for use in control system design and simulation.

The basic philosophy of the multivariable controller design was proposed by Grimble and Fotakis (17,18), but was not directly useable in the form presented by them. Chapter 6 describes the Author's work in modifying this basic philosophy into a practically realizable scheme. The major areas of the Author's contribution are in the parameterization of the measured shape signals, and the introduction of non-square plant matrices (the dimensions depending upon strip width). Work was also enacted pertaining to the selection of target (reference or set-point) shapes for the control scheme, and it was discovered that a width independent target was feasible, thus removing some selection programming. The control scheme involves the parameterization of the measured shape signals (using orthogonal polynomials) into four values (orders 1 to 4 of the polynomials). Errors in these parameters are then calculated and fed into controllers. Each controller takes the form of an integral

only controller of fairly low gain (provision for proportional terms being made in case it should prove necessary). The four loops are designed separately due to the fact that the transformed plant (including the parameterization, deparameterization and plant matrices) can be shown to be invertible and can be operated upon by a precompensator comprising its inverse.

Chapter seven describes a multivariable dynamic simulation of the entire plant and control scheme, to allow investigations of stability and performance under varying conditions. The simulation is an extremely flexible and powerful tool, and uses packages exclusively written by the Author (no simulation suites being available on the computer installation in question). The operation and facilities of the model are described, and the results of several aspects of simulation are discussed. These include the reaction of the system to changes in strip speed, shape disturbances in the incoming strip, failure of parts of the measurement system and changes in the sampling rate of the control computer, which is itself simulated. It was concluded that a suitable controller design had been selected for initial commissioning on the plant, and various other points were also highlighted - for example, a means of coping with single failed shapemeter rotors was proposed which would allow the system to continue working in AUTOMATIC mode with reasonable results, rather than simply passing control back to the operator. It was also found

that a relatively slow-sampling control computer system would be well tolerated (e.g. one sample per second), so as to allow as much calculation time per scan as possible. A hybrid computer simulation of the local As-U-Roll actuator position control loops is also described, by which the controller for these loops was successfully designed.

Chapter eight completes the picture by giving details of the system implementation on the plant, and some rather specialised considerations which arise for this particular scheme. An algorithm is developed for limiting the relative motion of the control actuators, as laid down by the mill manufacturers and plant engineers. Consideration is then given to the problems of integral desaturation and bumpless transfer in the controller. The computer hardware and operator interfaces are then described. Attention is also directed to the problem of compensating for shapemeter rotors which are only partially covered by the strip edges, and thus distort the shape measurements. In fact, the distortion was often found to be so great, that the fourth-order parameter fitting would completely fail without this compensation, as the appearance of the strip shape was predominantly sixth order. A suitable practical method of compensation was developed. Finally, since the initially installed system will only control the As-U-Roll actuators and not the first intermediate rolls, a short section is included to explain how the system will interact with the mill operator.

In conclusion, a system has been developed through a comprehensive programme of theoretical modelling and design, plant testing and extensive computer simulation, which shows great promise of providing an excellent aid to the production of better quality strip on a Sendzimir mill. Initially the system will control the As-U-Roll actuators only, but work is still progressing towards inclusion of the tapered first intermediate rolls into the automatic scheme (until this is done, performance will necessarily be limited by As-U-Roll mechanical constraints). At the time of writing, the control computers have been installed on the plant, all necessary cabling modifications have been carried out and tested, and the vast majority of software has been designed. Most of the software has been written and tested under laboratory conditions, and currently the software is being gradually installed on plant. Some aspects, such as the closed loop position control loops around the As-U-Roll actuators, have already been successfully commissioned. Several months will pass yet however, before the first trials of the entire system.

## REFERENCES

1. Bryant, G.F., (Ed.), "Automation of Tandem Mills,"  
The Iron and Steel Institute, 1973.
2. Sheppard J. and Roberts J.M., "Shape Control and  
Correction in Strip and Sheet," Int.Metall.Re.,  
1973, 18, Review 171.
3. Pearson, W.K.J., "Shape Measurement and Control,"  
J.Inst.Metals, 1964-1965, 93, p.169.
4. Sivilotti, O.G., Elfyn-Davies, W., Henze, M. and Dahle, O.,  
"ASEA-ALCAN AFC System for Cold Rolling Flat Strip,"  
Int.Metall.Rev., 1973, 18, p.83.
5. Henze, M. and Linde, L., "Stressometer Flatness Trans-  
ducer for Cold Strip Mills," ASEA Pamphlet AV86-104E,  
Sept. 1970, Ed.1.
6. Knox, T., "Operating Experience with the Loewy-Robertson  
'Vidimon' Shapemeter at Shotton Works," Shape Control  
Conference Proc., Metals Society, 1976, p.55.
7. Pawelski, O., Schuler, V., and Berger, B., "Development  
of a Shape Control System in Cold Rolling," Suppl.  
Trans.Iron and Steel Inst. of Japan, 1971, 11, p.692.
8. Haraguchi, S., Kajiwara, T. and Hata, K., "Shape of  
Strip Steel in Cold Rolling Process," Bull. of Japan  
Soc. of Mech. Eng., 1971, 14, p.104.
9. Wistreich, J.G., "Measurement and Control of Strip  
Shape in Cold Rolling," BISRA Report No. EG/-/20/70.  
(Magnetic Device)
10. Santo, T. and 5 others, "Automatic Shape Control,"  
Suppl. Trans. Iron and Steel Inst. Japan, 1971, 11,  
p.698 (Optical Device).
11. Mitsubishi Electric Corporation, "Shapemeter for Cold  
Rolling Flat Strip Mills," M.E. Corp. Pamphlet  
CA1495A SE7701, Jan.1977.  
(Magnetic/Capacitive Device)

12. Bravington, C.A., Barry, D.C. and McClure, C.H.,  
"Design and Development of a Shape Control System,"  
Shape Control Conference Proc., Metals Society,  
1976, p.82.
13. Stone, M.D. and Gray, R., "Theory and Practical  
Aspects in Crown Control," Iron and Steel  
Engineer, August 1965, p.73
14. Gunawardene, G.W.D.M., Grimble, M.J. and Thompson, A.,  
"Development of a Static Model for a Sendzimir Cold  
Rolling Mill," Metals Technology, 1980.
15. Carter, C.E. and Grimble, M.J., "Dynamic Simulation  
and Control of a Sendzimir Cluster Mill," Int.Conf.  
on Systems Engineering, Lanchester Polytechnic,  
Sept. 1980.
16. Gunawardene, G.W.D.M., "A Static Model of a Sendzimir  
Mill for Use in Shape Control," Thesis for Ph.D.,  
Sheffield City Polytechnic, 1982.
17. Fotakis, I.E., "Design of Optimal Control Systems  
and Industrial Applications," Ph.D. Thesis,  
Sheffield City Polytechnic, 1981.
18. Grimble, M.J. and Fotakis, I.E., "The Design of Strip  
Shape Control Systems for Sendzimir Mills," IEEE  
Conf. on Decision and Control, Albuquerque, New  
Mexico, 1980. To be published IEEE Trans. A-C, Oct.1982.
19. Urayama, S., Takatoku, Y., Niwa, Y. and Sawada, Y.,  
"Experience in Developing Shape Control for a  
Sendzimir Mill" Shape Control Conference Proc.  
Metals Society, 1976, p.101.
20. Bill, A.J. and Kilmister, G.T.F. in discussion on the  
above paper, ibid, p.121-122.
21. Anon., "Hitachi's New 6-hi Cold Strip Mill Improves  
Flatness, Increases Yield," 33 Magazine, March, 1976,  
p.53.

22. Orowan, E., "The Calculation of Roll Pressure in Hot and Cold Flat Rolling," Proc.I.Mech.E., Vol.150, 1943, p.140.
23. Bland, D.R. and Ford, H., "The calculation of Roll Force and Torque in Cold Strip Rolling with Tensions," Proc.I.Mech.E., Vol.159,1948,p.144.
24. Stone, M.D., "Rolling of Thin Strip," I.S.E., Feb.1953, p.61.
25. Roberts, W.L., "A Simplified Cold Rolling Model," I.S.E., Oct.1965, p.75.
26. Bryant, G.F., and Osborn, R., "Derivation and Assessment of Roll Force Models," in Reference 1, p.245.
27. Okamoto, T., Misaka, Y., and Takeuchi, H., "Advanced Tension and Gauge Control for a Tandem Cold Mill," Proc. IFAC Symposium on Automatic Control in Mining, Mineral and Metal Processing, Sydney, 1973.
28. Carlton, A.J., Edwards, W.J. and Thomas, P.J., "Formulae for Cold Rolling Analysis," Proc. AIME Symposium on Automation in the Iron and Steel Industry, Atlanta, 1977, p.223.
29. Hitchcock, J.H., ASME Special Research Committee Report on Roll Neck Bearings, 1935, Appendix 1.
30. Scheid, F., "Theory and Problems of Numerical Analysis," Schaum's Outline Series, McGraw Hill, 1968, p.311.
31. Conte, S.D. and de Boor, C., "Elementary Numerical Analysis," McGraw-Hill Kogakusha Ltd., 1972.
32. Hetenyi, M., "Beams on Elastic Foundation," Univ. of Michigan Press, 1946.
33. Timoshenko, S.P., "Strength of Materials," Ed.I.Vol.II, Van Nostrand, 1930, p.401.
34. Roark, R.J., and Young, W.C., "Formulas for Stress and Strain," Ed.V, McGraw-Hill, 1975.

35. Föppl, A., "Technische Mechanik," Ed.IV, Vol. V, 1907.
36. Love, A.H., "Treatise on the Mathematical Theory of Elasticity," Dover Publications, 1944, p.131.
37. Edwards, W.J. and Spooner, P.D., "Analysis of Strip Shape," in Reference 1, p.176.
38. Sabatini, B. and Yeomans, K.A., "An Algebra of Strip Shape and its Application to Mill Scheduling," JISI, Vol.206,p.1207,Dec.1968.
39. Shohet, K.N. and Townsend, N.A., "Roll Bending Methods, of Crown Control in Four-High Plate Mills," J.I.S.I., Nov.1968,p.1088.
40. Graupe, D., "Identification of Systems," Van Nostrand Reinhold, 1972, p.41.
41. Hovanessian, S.A. and Pipes, L.A., "Digital Computer Methods in Engineering," Mc-Graw Hill, 1969.
42. ibid p.235
43. Ref.31, p.346
44. Draper, N. and Smith, H., "Applied Regression Analysis," Wiley Interscience, 1966, p.52.
45. Hamming , R.W., "Numerical Methods for Scientists and Engineers," McGraw Hill, 1973, p.470.
46. Dutton, K., Barrett, J.F. and Grimble, M.J., "The Shape Control Problem for a Sendzimir Cold Steel Rolling Mill," proc.symposium on Application of Multivariable Systems Theory, Plymouth, Oct.1982,p.217.
47. Kunz, K.S., "Numerical Analysis," McGraw Hill, 1957, p.236.
48. Carnahan, B., Luther, H.A. and Wilkes, J.O., "Applied Numerical Methods," Wiley, 1964, p.575.
49. Ref.17, Appendix 13.

50. Ref.30, p. 132.
51. Lanczos, C., "Linear Differential Operators,"  
Van Nostrand, 1961, p.124.
52. MacFarlane, A.G.J., and Kouvaritakis, B., "A  
Design Technique for Linear Multivariable Feedback  
Systems," Int.J.of Control, Vol.25,No.6,1977,p.837.
53. Rosenbrock, H.H., "Computer Aided Control System  
Design," Academic Press, 1974.
54. Ref.17, p.110.
55. Grimble, M.J., "An Optimal Output Feedback Solution to  
the Strip Shape Multivariable Control Problem,"  
Sheffield City Polytechnic Report EEE/55/1980.
56. Ref.17,p.94, equation (4.29).
57. Bennett, S. and Linkens, D.A. (Eds.), "Computer Control  
of Industrial Processes," IEE Control Engineering  
Series 21, Peter Penegrinus Ltd., 1982.
58. J.B. Microsystems Ltd., Sales Brochure, "Merlin Low  
Cost Industrial Controller," J.B. Microsystems Ltd.,  
Ashby-de-la-Zouch, England.

## Appendix 1

### Hetenyi's Theory of beams on Elastic Foundations

#### (Reference 32) - Basic Derivation

##### Al.1. Differential Equation of the Elastic Line

Figure Al.1 depicts an originally straight beam AB, entirely supported by a foundation which is assumed to obey Hooke's law, and acted upon by various vertical loadings (i.e. a concentrated force F at point a, and a distributed loading q between points b and c). These loadings produce a distributed reaction in the foundation of  $q_R$  ( $\text{Nm}^{-1}$ ) which is proportional to the deflection (y) of the beam at any section, hence,

$$q_R = k \cdot y \quad (\text{Nm}^{-1}) \quad (\text{Al.1})$$

A foundation modulus is defined, being equal to that force which when distributed over unit area of the foundation will cause unit deflection. It is written as  $k_0$  ( $\text{Nm}^{-3}$ ). Therefore, if the beam AB has uniform cross-sectional-area, and a width b (m) in contact with the foundation, unit deflection will cause a reaction of  $bk_0$  ( $\text{Nm}^{-2}$ ) in the foundation, i.e.

$$q_R = bk_0 y \quad (\text{Nm}^{-1})$$

However, for brevity, the foundation modulus is "re-defined" as  $k = bk_0$  giving (Al.1) above.

The well known equation for a bending beam is

$$EI \cdot \frac{d^2 y_x}{dx^2} = -M \quad (\text{Nm})$$

where E = Young's Modulus ( $\text{Nm}^{-2}$ )

I = Second moment of area ( $\text{m}^4$ )

$y_x$  = deflection (m) at section x

x = distance along beam (m)

M = bending moment (Nm)

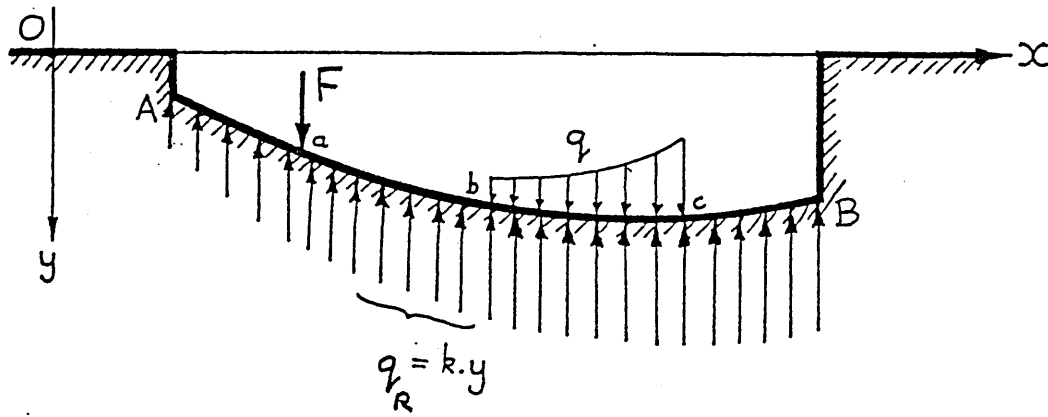


Fig. A.1.1 Effect of Loading a Beam on an Elastic Foundation

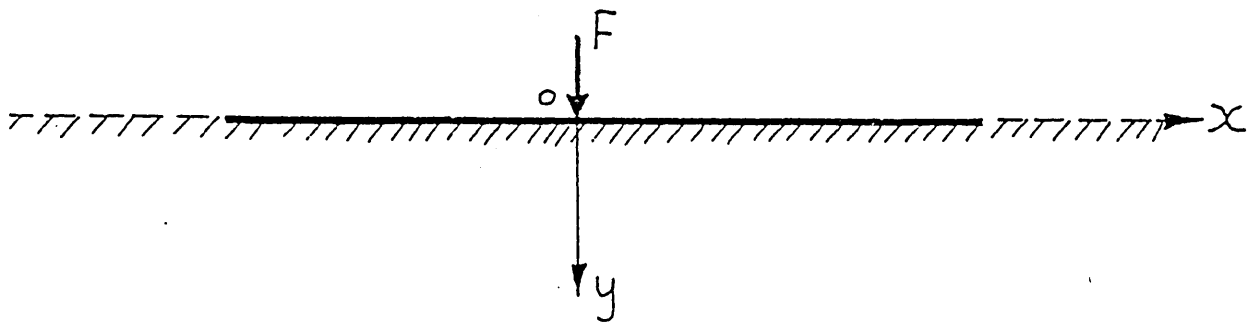


Fig. A.1.2 B.O.E.F. With a Single Concentrated Force

Double differentiation yields

$$EI \cdot \frac{d^4 y_x}{dx^4} = - \frac{d^2 M}{dx^2} \quad (\text{Nm}^{-1}) \quad (\text{A1.2})$$

By considering an infinitely small element of the beam of length  $dx$ , at a point where the beam is under a UDL of  $q$  ( $\text{Nm}^{-1}$ ), it can be shown that

$$\frac{d^2 M}{dx^2} = ky_x - q \quad (\text{Nm}^{-1})$$

therefore, from (A1.2)

$$EI \frac{d^4 y_x}{dx^4} = - ky_x + q \quad (\text{Nm}^{-1})$$

Therefore, along unloaded portions of the beam ( $q=0$ ) we can state the differential equation of the deflection curve as

$$EI \cdot \frac{d^4 y_x}{dx^4} = - ky_x \quad (\text{Nm}^{-1}) \quad (\text{A1.3})$$

By substituting  $y_x = e^{nx}$  we obtain the characteristic equation

$n^4 = - \frac{k}{EI}$ , which leads to the general solution of (A1.3) as given below.

$$y_x = e^{\lambda x} (C_1 \cos \lambda x + C_2 \sin \lambda x) + e^{-\lambda x} (C_3 \cos \lambda x + C_4 \sin \lambda x) \quad (\text{A1.4})$$

where  $\lambda = \sqrt[4]{\frac{k}{4EI}}$  ( $\text{m}^{-1}$ )

and  $C_1$  to  $C_4$  are constants.

This therefore represents the deflection of a straight bar resting on an elastic foundation and subject to transverse bending forces, but with no  $q$  loading. An additional term is necessary when  $q$  is present.

#### Al.2. Beams of Infinite Length

From equation Al.4, we can now derive equations for deflection ( $y_x$ ), deflection angle ( $\theta_x = \frac{dy_x}{dx}$ ),

$$\text{moment} \left[ M_x = \frac{d^2 y_x}{dx^2} \right]$$

$$\text{and shear} \left[ Q_x = \frac{d^3 y_x}{dx^3} \right] \text{ along the infinite beam for}$$

various types of loading. Positive quantities are as defined in section 3.1, chapter 3.

At a point infinitely far from the point at which loading is applied, deflection must be zero. I.e., as  $x \rightarrow \infty$ ,  $y_x \rightarrow 0$ . This can only be true if the terms in  $e^{\lambda x}$  vanish in equation Al.4. Therefore,  $C_1 = C_2 = 0$  and so the deflection curve for the RH half of the beam takes the form

$$y_x = e^{-\lambda x} (C_3 \cdot \cos \lambda x + C_4 \cdot \sin \lambda x) \quad (m) \quad (\text{Al.5})$$

##### Al.2.1 Results for a concentrated force acting on the beam

Consider figure Al.2. Due to the symmetrical nature of the deflection which will be caused by such a loading, we can say that

$$\frac{dy_0}{dx} = 0$$

Therefore, from equation A1.5,  $C_3 = C_4 = C$ , say,  
 so that  $y_x = Ce^{-\lambda x}(\cos\lambda x + \sin\lambda x)$  (m) (A1.6)

Also, the sum of reactions from the foundation must  
 balance the force  $F$ , i.e.

$$2 \int_0^{\infty} ky_x \cdot dx = F \quad (N)$$

leading to  $C = \frac{F\lambda}{2k}$  (m)

Therefore, from (A1.6) above

$$y_x = \frac{F\lambda}{2k} \cdot e^{-\lambda x} \cdot (\cos\lambda x + \sin\lambda x) \quad (m)$$

however, if we let  $A_{\lambda x} = e^{-\lambda x} (\cos\lambda x + \sin\lambda x)$   
 $B_{\lambda x} = e^{-\lambda x} \sin\lambda x$   
 $C_{\lambda x} = e^{-\lambda x} (\cos\lambda x - \sin\lambda x)$   
 $D_{\lambda x} = e^{-\lambda x} \cos\lambda x$

we obtain

$$y_x = \frac{F\lambda}{2k} A_{\lambda x} \quad (m) \quad (A1.7)$$

By taking successive derivatives of (A1.7) we similarly  
 obtain equations for  $\theta_x$ ,  $M_x$  and  $Q_x$  as shown in fig.A1.3,

where

$$\theta_x = -\frac{F\lambda^2}{k} \cdot B_{\lambda x} \quad (\text{rad}) \quad (A1.8)$$

$$M_x = \frac{F}{4\lambda} \cdot C_x \quad (\text{Nm}) \quad (A1.9)$$

$$Q_x = \frac{-F}{2} \cdot D_x \quad (N) \quad (A1.10)$$

Note that  $\theta_x$  and  $Q_x$  change sign to the left of the  
 point of application of the force.

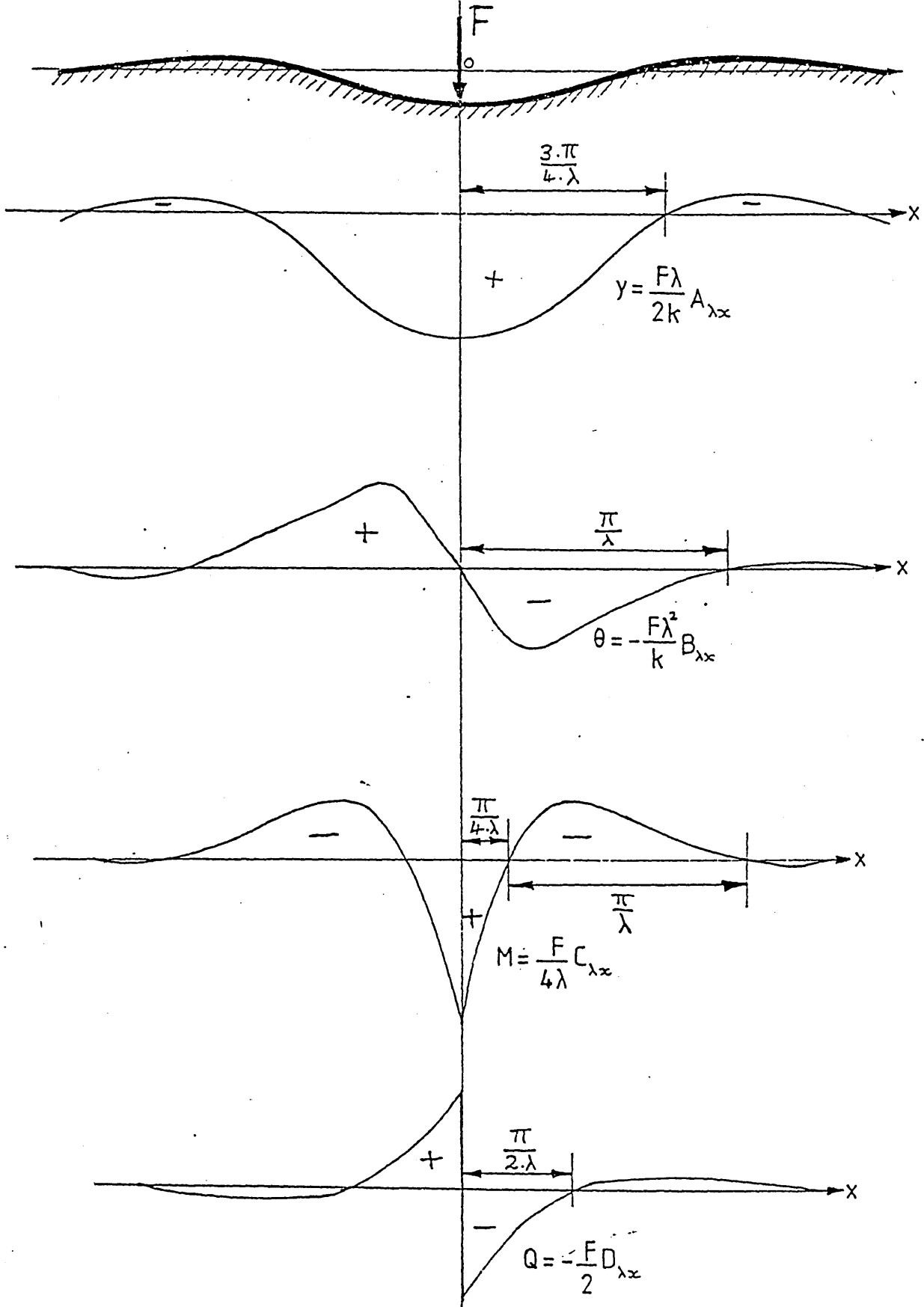


Fig. A.1.3 Variation Along Beam of  $y, \theta, M$  &  $Q$   
Due to a Single Conc. Force

### Al.2.2 Results for a concentrated moment acting on the beam

Consider fig. Al.4. The loading shown at (a) can be considered as the limiting case of that shown at (b), assuming that as  $d \rightarrow 0$ ,  $Fd \rightarrow M_0$ . Examination of equations Al.7 to Al.10 shows that all involve proportionality to  $F$ , therefore super-position and reciprocity principles apply. We can therefore use equations (Al.7) to derive the deflection result for fig, Al.4 (equation (Al.11) below), and then successively differentiate this to obtain the other results (see fig. Al.5):-

$$y_x = M_0 \cdot \frac{\lambda^2}{k} \cdot B_{\lambda x} \quad (\text{m}) \quad (\text{Al.11})$$

$$\theta_x = M_0 \cdot \frac{\lambda^3}{k} \cdot C_{\lambda x} \quad (\text{rad}) \quad (\text{Al.12})$$

$$M_x = \frac{M_0}{2} \cdot D_{\lambda x} \quad (\text{Nm}) \quad (\text{Al.13})$$

$$Q_x = -M_0 \cdot \frac{\lambda}{2} \cdot A_{\lambda x} \quad (\text{N}) \quad (\text{Al.14})$$

Note that  $y_x$  and  $M_x$  change sign to the left of the point of application of  $M_0$ .

### Al.2.3 Results for a UDL acting on the beam

Fig.Al.6 depicts a UDL of  $q(\text{Nm}^{-1})$  acting over a portion AB of the infinite beam. We wish to find the effects of the loading at a third point C, which is at a distance  $a$  (m) from A and  $b$  (m) from B. We regard the loading as an infinite number of infinitely small concentrated forces, each of magnitude  $q \cdot \delta x$ , and sum their results at point C.

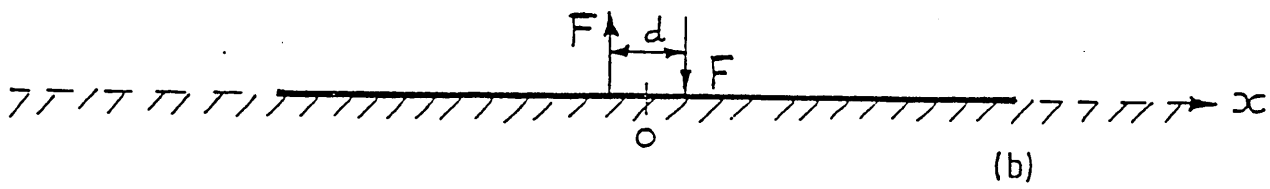
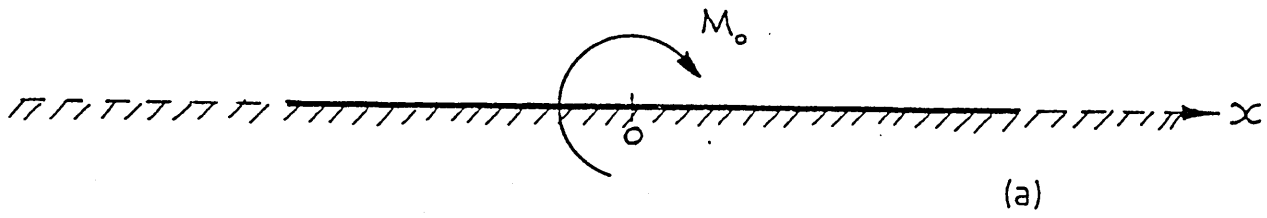


Fig. A1.4 B.O.E.F. With a Single Conc. Moment

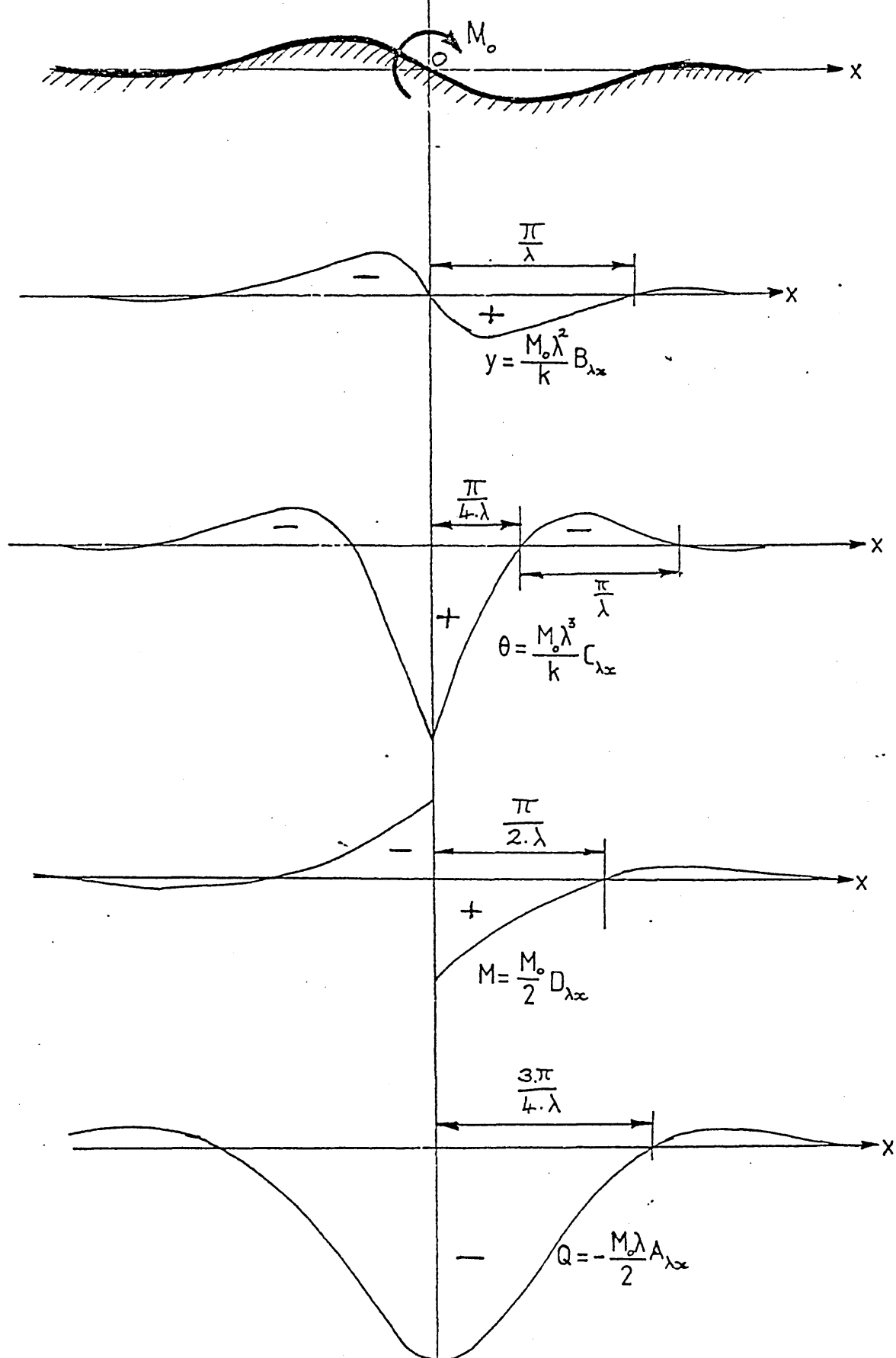


Fig. A.15 Variation Along Beam of  $y, \theta, M$  &  $Q$   
Due to a Single Conc. Moment

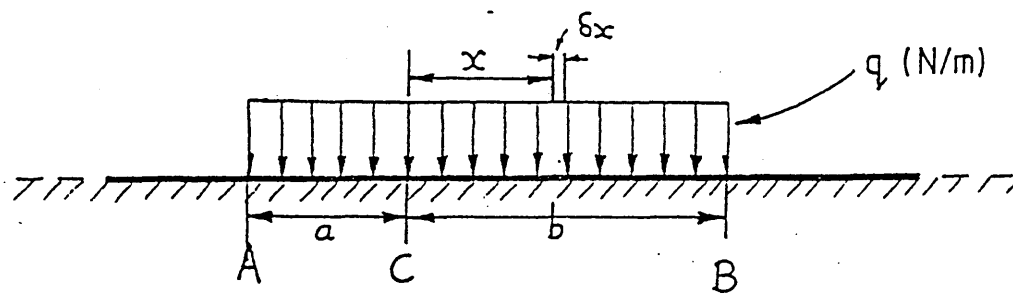


Fig. A.1-6 B.O.E.F. With Uniformly Distributed Load

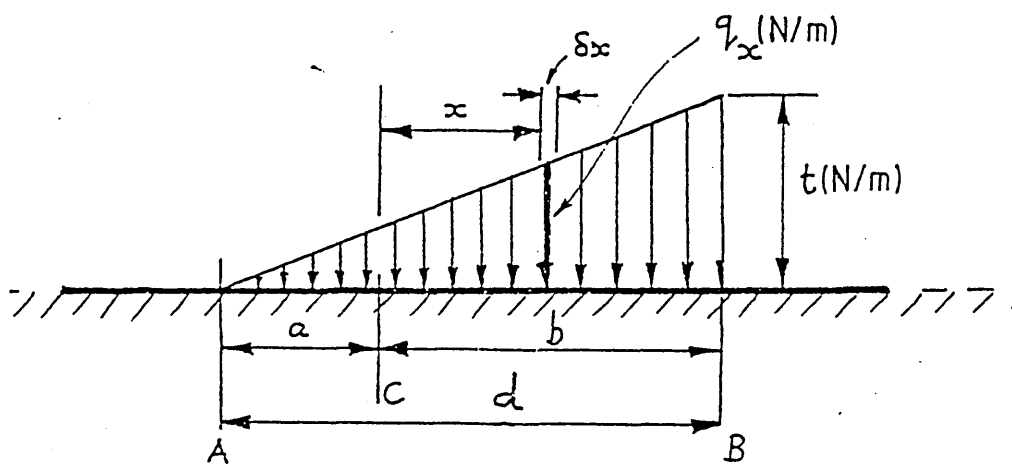


Fig.A.1-7 B.O.E.F. With Triangular Distributed Load

Using equation A1.7,

$$\delta_{y_x} = \frac{q \cdot \delta x \cdot \lambda \cdot A}{2k \lambda_x}$$

where  $x$  = distance from point C.

Integration over the a-b limits of the loaded portion of the beam yields equations A1.15, A1.19 and A1.23 below. Equations for  $\theta_c$ ,  $M_c$  and  $Q_c$  are obtained by performing similar operations on equations A1.8 to A1.10 respectively. Three cases arise (note that  $x, a$  and  $b$  are always taken positive):-

A1.2.3.1 When point C is under the loading

$$y_c = \frac{q}{2k} (2-D_{\lambda_a} - D_{\lambda_b}) \quad (\text{m}) \quad (\text{A1.15})$$

$$\theta_c = \frac{q\lambda}{2k} (A_{\lambda_a} - A_{\lambda_b}) \quad (\text{rad.}) \quad (\text{A1.16})$$

$$M_c = \frac{q}{4\lambda^2} (B_{\lambda_a} + B_{\lambda_b}) \quad (\text{Nm}) \quad (\text{A1.17})$$

$$Q_c = \frac{q}{4\lambda} (C_{\lambda_a} - C_{\lambda_b}) \quad (\text{N}) \quad (\text{A1.18})$$

A1.2.3.2 When C is to the left of the loading

$$y_c = \frac{q}{2k} (D_{\lambda_a} - D_{\lambda_b}) \quad (\text{m}) \quad (\text{A1.19})$$

$$\theta_c = \frac{q\lambda}{2k} (A_{\lambda_a} - A_{\lambda_b}) \quad (\text{rad}) \quad (\text{A1.20})$$

$$M_c = -\frac{q}{4\lambda^2} (B_{\lambda_a} - B_{\lambda_b}) \quad (\text{Nm}) \quad (\text{A1.21})$$

$$Q_c = \frac{q}{4\lambda} (C_{\lambda_a} - C_{\lambda_b}) \quad (\text{N}) \quad (\text{A1.22})$$

A1.2.3.3 When C is to the right of the loading

$$y_c = -\frac{q}{2k} (D_{\lambda a} - D_{\lambda b}) \quad (\text{m}) \quad (\text{A1.23})$$

$$\theta_c = \frac{q\lambda}{2k} (A_{\lambda a} - A_{\lambda b}) \quad (\text{rad}) \quad (\text{A1.24})$$

$$M_c = \frac{q}{4\lambda^2} (B_{\lambda a} - B_{\lambda b}) \quad (\text{Nm}) \quad (\text{A1.25})$$

$$Q_c = \frac{q}{4\lambda} (C_{\lambda a} - C_{\lambda b}) \quad (\text{N}) \quad (\text{A1.26})$$

A1.2.4 Results for a triangular loading acting on the beam

Consider fig.A1.7. We wish to find the deflection at point C as in the case of the UDL. Again three cases arise, and x, a and b are always positive.

A1.2.4.1 When point C is under the loading

Measuring x from point C,

in the region AC

$$q_x = \frac{t}{d} (a-x) \quad (\text{Nm}^{-1})$$

and in the region CB

$$q_x = \frac{t}{d} (a+x) \quad (\text{Nm}^{-1})$$

Equation A1.7 therefore gives the deflection at C as

$$y_c = \frac{t\lambda}{2kd} \left[ \int_0^a (a-x) A_{\lambda x} dx + \int_a^b (a+x) A_{\lambda x} dx \right]$$

which yields

$$y_c = \frac{t}{4\lambda kd} (C_{\lambda a} - C_{\lambda b} - 2\lambda d D_{\lambda b} + 4\lambda a) \quad (\text{m}) \quad (\text{A1.27})$$

similarly, from A1.8 to A1.10:-

$$\theta_c = \frac{-t}{2kd} (D_{\lambda a} + D_{\lambda b} + \lambda_d A_{\lambda b} - 2) \quad (\text{rad}) \quad (\text{A1.28})$$

$$M_c = \frac{-t}{8\lambda^3 d} (A_{\lambda a} - A_{\lambda b} - 2\lambda_d B_{\lambda b}) \quad (\text{Nm}) \quad (\text{A1.29})$$

$$Q_c = \frac{t}{4\lambda^2 d} (B_{\lambda a} + B_{\lambda b} - \lambda_d C_{\lambda b}) \quad (\text{N}) \quad (\text{A1.30})$$

Similarly for the other two cases:-

A1.2.4.2 When C is to the left of the loading

$$y_c = \frac{t}{4\lambda kd} (C_{\lambda a} - C_{\lambda b} - 2\lambda_d D_{\lambda b}) \quad (\text{m}) \quad (\text{A1.31})$$

$$\theta_c = \frac{t}{2kd} (D_{\lambda a} - D_{\lambda b} - \lambda_d A_{\lambda b}) \quad (\text{rad}) \quad (\text{A1.32})$$

$$M_c = -\frac{t}{8\lambda^3 d} (A_{\lambda a} - A_{\lambda b} - 2\lambda_d B_{\lambda b}) \quad (\text{Nm}) \quad (\text{A1.33})$$

$$Q_c = -\frac{t}{4\lambda^2 d} (B_{\lambda a} - B_{\lambda b} + \lambda_d C_{\lambda b}) \quad (\text{N}) \quad (\text{A1.34})$$

A1.2.4.3 When C is to the right of the loading

$$y_c = \frac{t}{4\lambda kd} (C_{\lambda a} - C_{\lambda b} + 2\lambda_d D_{\lambda b}) \quad (\text{m}) \quad (\text{A1.35})$$

$$\theta_c = \frac{-t}{2kd} (D_{\lambda a} - D_{\lambda b} + \lambda_d A_{\lambda b}) \quad (\text{rad}) \quad (\text{A1.36})$$

$$M_c = \frac{-t}{8\lambda^3 d} (A_{\lambda a} - A_{\lambda b} + 2\lambda_d B_{\lambda b}) \quad (\text{Nm}) \quad (\text{A1.37})$$

$$Q_c = \frac{t}{4\lambda^2 d} (B_{\lambda a} - B_{\lambda b} - \lambda_d C_{\lambda b}) \quad (\text{N}) \quad (\text{A1.38})$$

### Al.3. Beams of Finite Length

The present application to rolls in a rolling mill obviously is concerned with beams of finite length. It is assumed that the rolls can be regarded as beams having free ends (with the exception of the backing bearings), and so the theory for beams with free ends only is outlined here.

Consider an infinitely long beam on an elastic foundation subject to loadings as shown in fig. Al.8(a). Due to this loading, certain values of  $y$ ,  $\theta$ ,  $M$  and  $Q$  will exist at points A and B on the infinite beam. By superimposing pairs of concentrated forces and moments acting infinitely closely to the left of point A ( $F_{OA}$ ,  $M_{OA}$ ) and the right of point B ( $F_{OB}$ ,  $M_{OB}$ ) as shown in fig. Al.8(b) the elastic curve can be modified in such a way that the required end-conditions for the finite beam AB exist at A and B on the infinite beam (hence these forces and moments are collectively called the "end-conditioning-forces"). For a beam having free ends, (e.g. fig. Al.8(c)), the values of  $M$  and  $Q$  at points A and B must be zero. Therefore, the ECFs must make the values of  $M_A$ ,  $Q_A$ ,  $M_B$  and  $Q_B$  vanish on the infinite beam of fig. Al.8(a) to create the conditions of fig. Al.8(c) so that the infinite beam between points A and B will behave as if there were a finite beam of length  $L$  with free ends at A and B. Thus the combination of all four ECFs must produce  $-M_A$  and  $-Q_A$  at A, and  $-M_B$  and  $-Q_B$  at B. From equations Al.9, Al.10, Al.13 and Al.14, the required conditions are:-

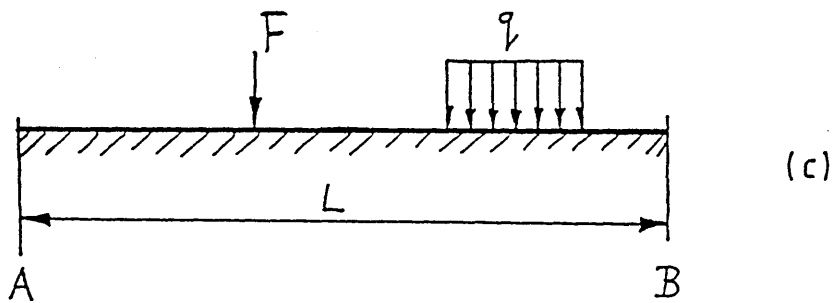
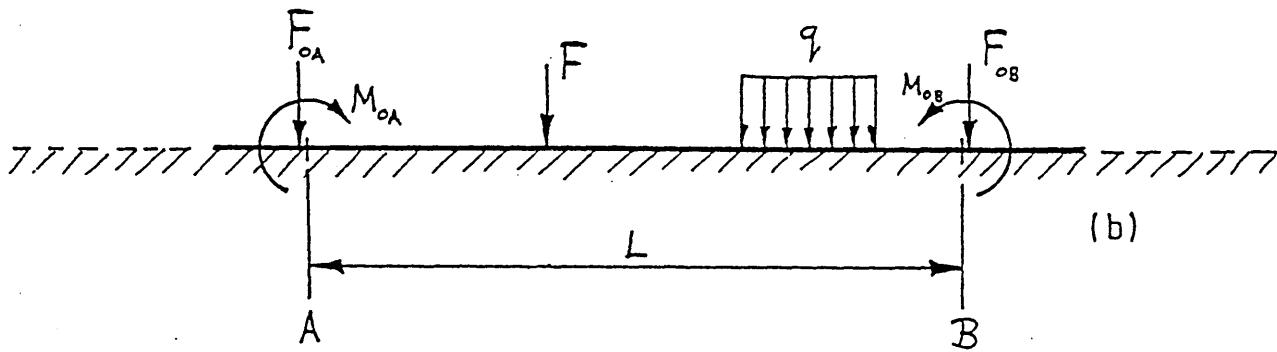
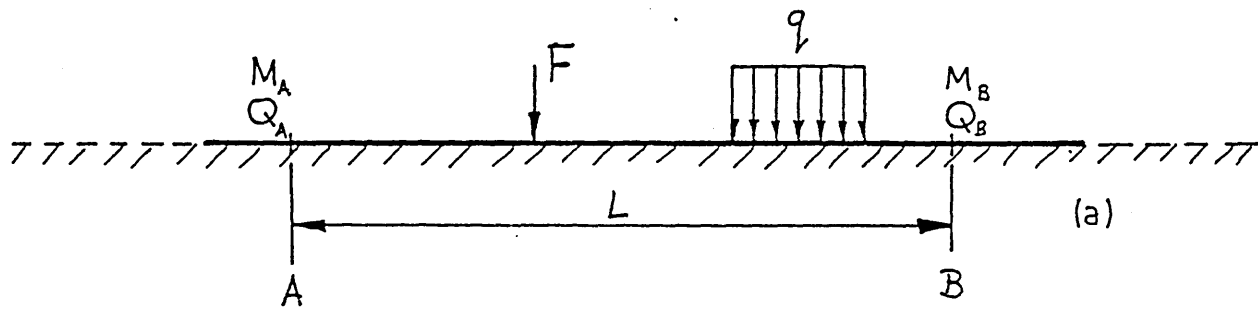


Fig. A.1-8 Principle of End Conditioning Forces

$$\begin{array}{r}
M_A + \frac{F_{OA}}{4\lambda} + \frac{F_{OB}}{4\lambda} C_{\lambda L} + \frac{M_{OA}}{2} + \frac{M_{OB}}{2} D_{\lambda L} = 0 \\
Q_A - \frac{F_{OA}}{2} + \frac{F_{OB}}{2} D_{\lambda L} - \frac{\lambda M_{OA}}{2} - \frac{\lambda M_{OB}}{2} A_{\lambda L} = 0 \\
M_B + \frac{F_{OA}}{4\lambda} C_{\lambda L} + \frac{F_{OB}}{4\lambda} + \frac{M_{OA}}{2} D_{\lambda L} + \frac{M_{OB}}{2} = 0 \\
Q_B - \frac{F_{OA}}{2} D_{\lambda L} + \frac{F_{OB}}{2} - \frac{\lambda M_{OA}}{2} A_{\lambda L} - \frac{\lambda M_{OB}}{2} = 0
\end{array} \quad (A1.39)$$

The simultaneous solution of these equations is greatly simplified by resolving the original loading into symmetrical and antisymmetrical components as shown for the example of a single concentrated force in fig. A1.9. It is clear from the figure that

$$\begin{array}{ll}
M_A = M'_A + M''_A \quad (\text{Nm}) & M_B = M'_A - M''_A \quad (\text{Nm}) \\
Q_A = Q'_A + Q''_A \quad (\text{N}) & Q_B = -Q'_A + Q''_A \quad (\text{N})
\end{array}$$

giving

$$\begin{array}{ll}
M'_A = 0.5(M_A + M_B) \quad (\text{Nm}) & M''_A = 0.5(M_A - M_B) \quad (\text{Nm}) \\
Q'_A = 0.5(Q_A - Q_B) \quad (\text{N}) & Q''_A = 0.5(Q_A + Q_B) \quad (\text{N})
\end{array} \quad (A1.40)$$

where  $M_A$ ,  $M_B$ ,  $Q_A$  and  $Q_B$  are found from the original loading using equations A1.9 and A1.10, A1.13 and A1.14, A1.21 and A1.22 etc. as appropriate. These moments and shears are now removed from A and B by applying ECFs as in fig. A1.10 which shows the assumed positive directions of the necessary ECFs.

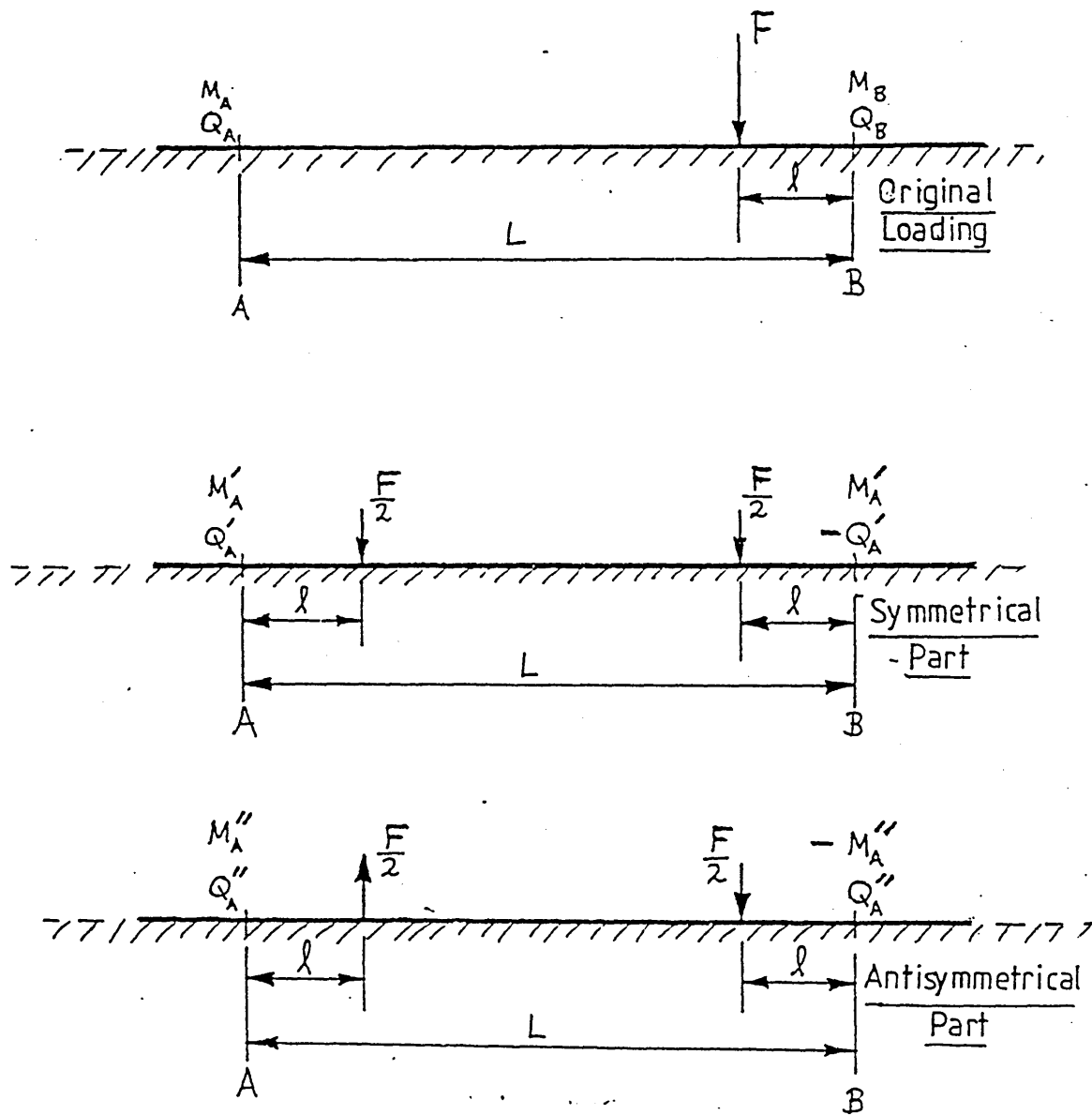


Fig. A.1-9 Division of Loading Into Two Components

The equations A1.39 now reduce to two pairs of easily soluble simultaneous equations, one set for  $F'_O$  and  $M'_O$ , and the other for  $F''_O$  and  $M''_O$ . The solutions are:-

$$\begin{aligned}
 F'_O &= 4 E_1 \cdot \left[ Q'_A \cdot (1+D\lambda L) + \lambda M'_A \cdot (1-A\lambda L) \right] & (N) & \left. \begin{array}{l} ) \\ ) \\ ) \end{array} \right\} \\
 M'_O &= \frac{-2E_1}{\lambda} \cdot \left[ Q'_A \cdot (1+C\lambda L) + 2\lambda M'_A \cdot (1-D\lambda L) \right] & (Nm) & \left. \begin{array}{l} ) \\ ) \\ ) \end{array} \right\} \\
 F''_O &= 4E_2 \cdot \left[ Q''_A \cdot (1-D\lambda L) + \lambda M''_A \cdot (1+A\lambda L) \right] & (N) & \left. \begin{array}{l} ) \\ ) \\ ) \end{array} \right\} \\
 M''_O &= \frac{-2E_2}{\lambda} \cdot \left[ Q''_A \cdot (1-C\lambda L) + 2\lambda M''_A \cdot (1+D\lambda L) \right] & (Nm) & \left. \begin{array}{l} ) \\ ) \\ ) \end{array} \right\}
 \end{aligned} \tag{A1.41}$$

$$\begin{aligned}
 \text{where } E_1 &= \frac{0.5 e^{\lambda L}}{\sinh \lambda L + \sin \lambda L} \\
 E_2 &= \frac{0.5 e^{\lambda L}}{\sinh \lambda L - \sin \lambda L}
 \end{aligned}$$

Then it is clear from fig. A1.10 that

$$\begin{aligned}
 F_{OA} &= F'_O + F''_O \quad (N) & F_{OB} &= F'_O - F''_O \quad (N) & \left. \begin{array}{l} ) \\ ) \\ ) \end{array} \right\} \\
 M_{OA} &= M'_O + M''_O \quad (Nm) & M_{OB} &= M'_O - M''_O \quad (Nm) & \left. \begin{array}{l} ) \\ ) \\ ) \end{array} \right\}
 \end{aligned} \tag{A1.42}$$

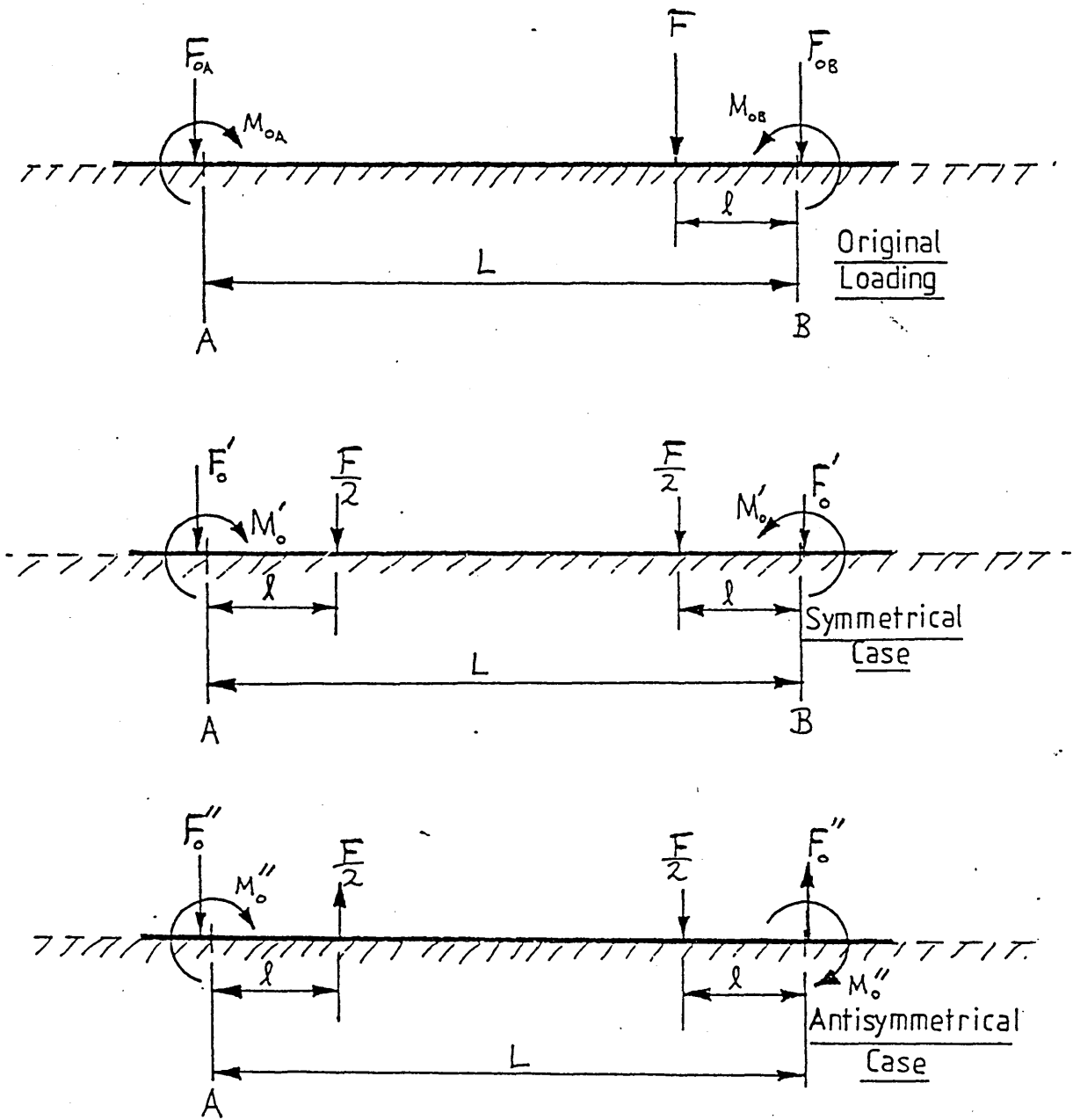


Fig. A.1-10 End Conditioning Forces for fig.A.1-9

#### A1.4 Summary of Procedure

- A1.4.1 Evaluate  $M_A$ ,  $M_B$ ,  $Q_A$  and  $Q_B$  on the infinite beam for all components of the loading under investigation, using the appropriate equations of section A1.2.
- A1.4.2 Use these values in equations A1.40.
- A1.4.3 Use the resulting values of  $M_A'$ ,  $M_A''$ ,  $Q_A'$  and  $Q_A''$  to evaluate  $F_0'$ ,  $F_0''$ ,  $M_0'$  and  $M_0''$  using equations A1.41.
- A1.4.4 Use equations A1.42 to evaluate the ECFs (which will make the portion AB of the infinite beam behave like a beam of length L with free ends at A and B and subject to the loading under investigation).
- A1.4.5 Use equations A1.7 to A1.10 and A1.11 to A1.14 to find the value of the desired quantities ( $y$ ,  $\theta$ , M or Q) due to all four ECFs (at the required section of the beam).
- A1.4.6 Use the appropriate section A1.2 equations to find the value of the desired quantities ( $y$ ,  $\theta$ , M or Q) due to all the applied loadings (at the required section of the beam).
- A1.4.7 Sum the values found at A1.4.5 (i.e. one value of the required quantity per ECF) and A1.4.6 (i.e. one value of the required quantity per applied loading) above to yield the total  $y$ ,  $\theta$ , M or Q at the required section of the beam.

Appendix 2

Calculation of Foundation Modulus (References 33-35)

Consider two cylindrical rolls loaded by a distributed loading  $q(\text{Nm}^{-1})$  as shown in fig. A.2. Due to local deformation of the roll material along the line of contact, a narrow contact rectangle of width  $b$  will be formed, and the roll axes will move together by a distance  $d$ .

The width of the contact rectangle is given in Hertz's contact stress theory (Ref.33) as:-

$$b = \sqrt{\frac{16(1-\nu^2) q D_1 D_2}{\pi E (D_1 + D_2)}} \quad (\text{m}) \quad (\text{A.2.1})$$

where  $\nu$  = Poisson's Ratio

$E$  = Young's Modulus ( $\text{Nm}^{-2}$ )

$D_1, D_2$  = Roll diameters (m)

Also from Ref.34-35  $d = \frac{2q(1-\nu^2)}{\pi E} \left[ \frac{2}{3} + \ln \frac{2D_1}{b} + \ln \frac{2D_2}{b} \right] (\text{m})$  (A.2.2)

The foundation modulus is given by

$$k = \frac{q}{d} \quad (\text{Nm}^{-2})$$

which gives, upon substitution of (A.2.1) and (A.2.2):-

$$k = \frac{f_1}{\ln(f_2) + \ln(D_1 + D_2) - \ln |q|} \quad (\text{Nm}^{-2}) \quad (\text{A.2.3})$$

where  $f_1 = \frac{\pi E}{2(1-\nu^2)} \quad (\text{Nm}^{-2})$

$$f_2 = \frac{\sqrt[3]{e^2 \pi E}}{4(1-\nu^2)} \quad (\text{Nm}^{-2})$$

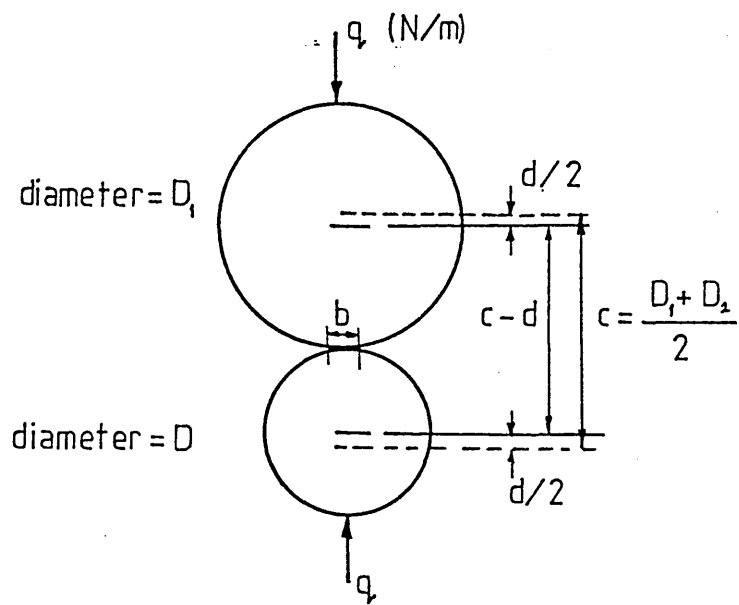


Fig.A·2 Roll Flattening Due to Loading

Note that the absolute magnitude of  $q$  has been used in (A.2.3). This is because in the main model,  $q$  will occasionally be negative and the log of a negative number is non-existent. The fact that  $q$  is negative has no significance in the context of Fig.A.2 but is explained in the main model.

### Appendix 3

#### Bending Theory for a Cantilever having an Elastically Supported Root (Original)

Consider a conventionally supported cantilever as shown in fig.A.3.1. At a section  $x_M$  from the unsupported LH end, the bending moment is given by

$$M = F_{WN} (x_M - x_{WF}) \quad (\text{Nm}) \quad \text{for } x_{WF} \leq x_M \leq L_U$$

$$\text{i.e. } M = F_{WN} (L_U - b - x_{WF}) \quad (\text{Nm}) \quad \text{for } 0 \leq b \leq (L_U - x_{WF})$$

The equation of the elastic line of the cantilever over this range is given by

$$\frac{d^2 y_{x_M}}{db^2} = \frac{M}{EI} = \frac{F_{WN}}{EI} (L_U - b - x_{WF}) \quad (\text{m}^{-1})$$

Integrating yields

$$\frac{dy_{x_M}}{db} = \theta_{x_M} = \frac{F_{WN}}{EI} (L_U b - \frac{b^2}{2} - bx_{WF}) + C_1 \quad (\text{rad}) \quad (\text{A.3.1})$$

and integrating again,

$$y_{x_M} = \frac{F_{WN}}{EI} (L_U \frac{b^2}{2} - \frac{b^3}{6} - \frac{b^2}{2} x_{WF}) + bc_1 + c_2 \quad (\text{m}) \quad (\text{A.3.2})$$

At this stage in the analysis it is usual to prove that  $c_1 = c_2 = 0$ . However, consider the LH unsupported end of the WR as a cantilever as shown in fig.A.3.2. The above results still apply, but since this cantilever's root is elastically supported rather than rigidly fixed, it is clear that values of deflection and angle will exist at the point of suspension. Let these "initial conditions" be given by

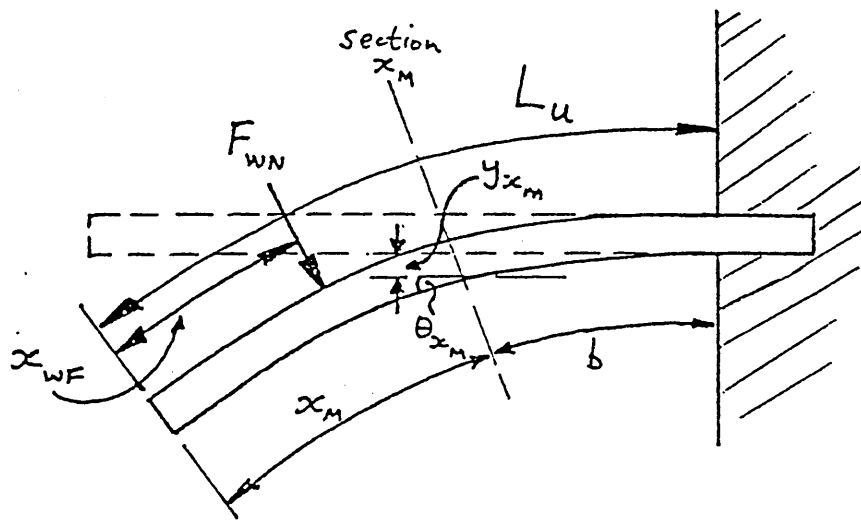


Fig. A.3-1 Basic Cantilever Bending

$$\left. \frac{dy_{x_M}}{db} \right|_{b=0} = -\theta_L \quad \text{and} \quad \left. y_{x_M} \right|_{b=0} = y_L$$

Note that  $\theta_L$  is negative according to the sign convention of section 3.1 in Chapter 3 (see figure A.3.2.), but for the present analysis a positive value is required, hence the sign change above.

Substituting these values into (A.3.1) and (A.3.2) we see that  $c_1 = -\theta_L$  and  $c_2 = y_L$ . Furthermore  $b = (L_U - x_M)$ , and substituting back into (A.3.1) and (A.3.2) gives:-

$$\theta_{x_M} = \frac{F_{WN}}{EI_W} \cdot \left[ (L_U - x_{WF}) (L_U - x_M) - \frac{(L_U - x_M)^2}{2} \right] - \theta_L \quad (\text{rad}) \quad (\text{A.3.3})$$

$$y_{x_M} = \frac{F_{WN}}{EI_W} \cdot \left[ \frac{(L_U - x_{WF})}{2} (L_U - x_M)^2 - \frac{(L_U - x_M)^3}{6} \right] - (L_U - x_M) \theta_L + y_L \quad (\text{m}) \quad (\text{A.3.4})$$

for  $x_{WF} < x_M < L_U$

Now, at the point of application of the force,

$x_M = x_{WF}$  therefore

$$\theta_{WF} = \frac{F_{WN}}{2EI_W} (L_U - x_{WF})^2 - \theta_L \quad (\text{Rad}) \quad (\text{A.3.5})$$

$$y_{WF} = \frac{F_{WN}}{3EI_W} (L_U - x_{WF})^3 - (L_U - x_{WF}) \theta_L + y_L \quad (\text{m}) \quad (\text{A.3.6})$$

The portion of the cantilever to the left of the force is considered to remain straight, so that

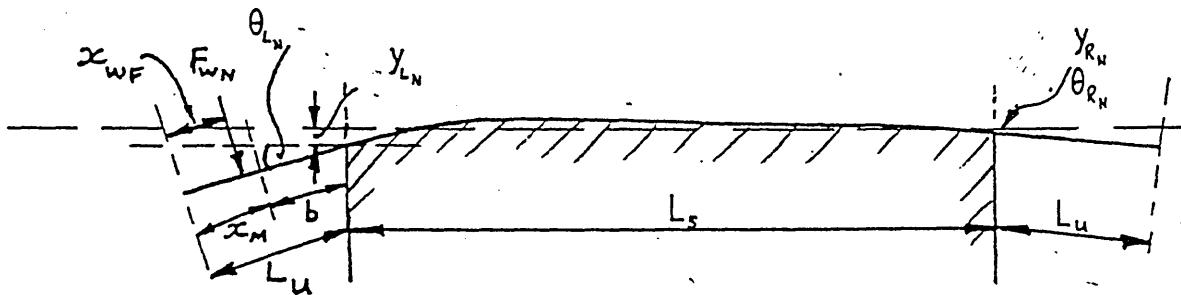


Fig. A.3.2 Representation of Workroll as a Beam

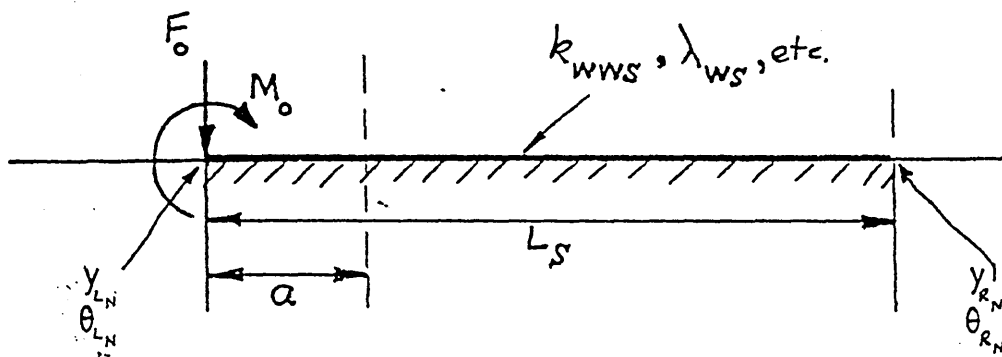


Fig. A.3.3 Central Supported Portion

$$y_{W_{x_M}} = y_{WF} + (x_{WF} - x_M) \sin \theta_{WF} \quad (m) \quad (A.3.7)$$

$$\text{for } 0 \leq x_M < x_{WF}$$

Substituting (A.3.5) and (A.3.6) into (A.3.7), and gathering the equations together, we have:-

$$y_{W_{x_M}} = \frac{F_{WN}}{3EI_W} \cdot (L_U - x_{WF})^3 - \theta_L \cdot (L_U - x_{WF}) + y_L + (x_{WF} - x_M) \sin \left[ \frac{F_{WN}}{2EI_W} \cdot (L_U - x_{WF})^2 - \theta_L \right] \quad (m) \quad (A.3.8a)$$

$$\text{for } 0 \leq x_M < x_{WF}$$

$$y_{W_{x_M}} = \frac{F_{WN}}{2EI_W} \cdot \left[ (L_U - x_{WF}) \cdot (L_U - x_M)^2 - \frac{(L_U - x_M)^3}{3} \right] - \theta_L \cdot (L_U - x_M) + y_L \quad (m) \text{ for } x_{WF} \leq x_M < L_U \quad (A.3.8b)$$

To solve these, we must evaluate  $y_L$  and  $\theta_L$ . The force  $F_{WN}$  of fig.A.3.2 will exert a force and moment on the LH end of the supported section of the WR as shown in fig.A.3.3, where

$$F_O = F_{WN} \quad (N)$$

$$M_O = -F_{WN}(L_U - x_{WF}) \quad (Nm)$$

The procedure of Appendix 1, section A1.4 is used to find expressions for deflection and angle at any point along the "beam" of fig. A.3.3 (i.e. the section of the WR over the strip) as follows:-

For the force  $F_O$ , equations A1.9 and A1.10 (using  $\lambda_{WS}$  as given following equation (3.95) in Chapter 3)

yield:-

$$M_{AF} = \frac{F_{WN}}{4\lambda_{WS}} \quad (\text{Nm})$$

$$M_{BF} = \frac{F_{WN}}{4\lambda_{WS}} \cdot C \lambda_{WS} L_S \quad (\text{Nm})$$

$$Q_{AF} = \frac{F_{WN}}{2} \quad (\text{N})$$

$$Q_{BF} = \frac{-F_{WN}}{2} \cdot D \lambda_{WS} L_S \quad (\text{N})$$

For the moment  $M_O$ , equations A1.13 and A1.14 yield

$$M_{AM} = \frac{-M_O}{2} \quad (\text{Nm})$$

$$M_{BM} = \frac{M_O}{2} \cdot D \lambda_{WS} L_S \quad (\text{Nm})$$

$$Q_{AM} = \frac{-M_O \lambda_{WS}}{2} \quad (\text{N})$$

$$Q_{BM} = \frac{-M_O \lambda_{WS}}{2} \cdot A \lambda_{WS} L_S \quad (\text{N})$$

Summing these effects,

$$M_{A_L} = M_{AF} + M_{AM} \quad (\text{Nm}) \quad M_{B_L} = M_{BF} + M_{BM} \quad (\text{Nm})$$

$$Q_{A_L} = Q_{AF} + Q_{AM} \quad (\text{N}) \quad Q_{B_L} = Q_{BF} + Q_{BM} \quad (\text{N})$$

Application of equations A1.40, A1.41 and A1.42 (using the values of  $k_{WWS} \cdot \lambda_{WS}$ ,  $E_{1WS}$  and  $E_{2WS}$  given by equation (3.95)ff in the main text then yields the ECFs ( $F_{OA_L}$ ,  $F_{OB_L}$ ,  $M_{OA_L}$  and  $M_{OB_L}$ ). Equations A1.7, A1.8, A1.11 and A1.12 are then used with these ECFs and the original

$F_O$  and  $M_O$  to give the deflection and angle at any given point on the supported section of the WR as:-

$$y_{w_a} = \frac{\lambda_{WS}}{2k_{WWS}} \cdot \left[ (F_{WN} + F_{OA_L}) \cdot A \lambda_{WS}^a + F_{OB_L} \cdot A \lambda_{WS} (L_S - a) \right] \\ + \frac{\lambda_{WS}^2}{k_{WWS}} \cdot \left[ (M_O + M_{OA_L}) \cdot B \lambda_{WS}^a + M_{OB_L} \cdot B \lambda_{WS} (L_S - a) \right] \quad (m) \quad (A.3.9)$$

for  $0 \leq a \leq L_S$

$$\theta_{w_a} = \frac{\lambda_{WS}^2}{k_{WWS}} \left[ -(F_{OA_L} + F_{WN}) \cdot B \lambda_{WS}^a + F_{OB_L} \cdot B \lambda_{WS} (L_S - a) \right] \\ + \frac{\lambda_{WS}^3}{k_{WWS}} \cdot \left[ (M_O + M_{OA_L}) \cdot C \lambda_{WS}^a - M_{OB_L} \cdot C \lambda_{WS} (L_S - a) \right] \quad (rad) \quad (A.3.10)$$

for  $0 \leq a \leq L_S$

where  $a$  is given by  $x_M - L_U$  and  $M=1, \dots, M_W$

Note the use of the minus sign associated with  $M_{OB_L}$  in the  $\theta_W$  equation. This is due to the sense in which  $M_{OB_L}$  acts (c.f. Figs.A1.10 and A1.5)

These equations can now be used to find  $y_{L_N}$ ,  $\theta_{L_N}$ ,  $y_{R_N}$  and  $\theta_{R_N}$  due to the  $N^{th}$  force  $F_{WN}$  by substituting  $a = 0$  and  $a = L_S$ . Note here that  $A \lambda_0 = C \lambda_0 = D \lambda_0 = 1$  and  $B \lambda_0 = 0$ . Therefore for the  $N^{th}$  force from the front of the mill ( $F_{WN}$ ),

$$y_{L_N} = \frac{\lambda_{WS}}{2k_{WWS}} \left[ F_{WN} + F_{OA_L} + F_{OB_L} \cdot A \lambda_{WS} L_S \right] + \frac{\lambda_{WS}^2}{k_{WWS}} \cdot M_{OB_L} \cdot B \lambda_{WS} L_S \quad (m)$$

(A.3.11)

$$y_{R_N} = \frac{\lambda_{WS}}{2k_{WWS}} \left[ (F_{WN} + F_{OA_L}) \cdot A \lambda_{WS} L_S + F_{OB_L} \right] + \frac{\lambda_{WS}^2}{k_{WWS}} \cdot (M_O + M_{OA_L}) \cdot B \lambda_{WS} L_S$$

(m)

(A.3.12)

$$\theta_{L_N} = \frac{\lambda_{WS}^2}{k_{WWS}} \cdot F_{OB_L} \cdot B \lambda_{WS} L_S + \frac{\lambda_{WS}^3}{k_{WWS}} \cdot \left[ M_O + M_{OA_L} - M_{OB_L} \cdot C \lambda_{WS} L_S \right] \quad (rad)$$

(A.3.13)

$$\theta_{R_N} = \frac{\lambda_{WS}^2}{k_{WWS}} \cdot (F_{WN} + F_{OA_L}) \cdot B \lambda_{WS} L_S + \frac{\lambda_{WS}^3}{k_{WWS}} \cdot \left[ (M_O + M_{OA_L}) \cdot C \lambda_{WS} L_S - M_{OB_L} \right]$$

(rad)                      (A.3.14)

The values of  $y_{L_N}$  and  $\theta_{L_N}$  can now be used in equation (A.3.8) to give the deflection at any section on the LH end or over the strip due to a force acting on the LH end of the WR. The values of  $y_{R_N}$  and  $\theta_{R_N}$  are used in the main text (section 3.9.2.1) to study the behaviour of the RH unsupported end.

## APPENDIX 4

### Effects of Non-Right-Cylindrical-Rolls on the Beam Theory

The analysis of Chapter 3 considered only parallel-ground rolls to avoid too much complication. However, any of the rolls in the mill cluster may be ground with a camber as shown in figure A.4.1. This camber is taken here to be ground off the roll diameter used in Chapter 3. Furthermore, the first intermediate rolls are also ground with tapered-off ends, which are slid into or out of the mill cluster for shape control purposes. This appendix sets forward a method whereby these effects may be incorporated in the model of Chapter 3.

#### A.4.1 Roll Camber Definition

Consider a general roll, N. The camber ( $c_N$ ) is assumed to be parabolic, so that if the upper surface only of the roll is considered, and Cartesian axes are drawn as in fig.A4.2 then the equation of the roll surface is given by

$$y_N = -\frac{c_N}{2} \cdot \left[ \frac{2x}{L_T} \right]^2 = \frac{-2 c_N x^2}{L_T^2} \quad (m)$$

If the y-axis is now shifted to the LH end of the roll, we see that

$$y_N = -\frac{2 c_N}{L^2} \cdot \left(x - \frac{L}{2}\right)^2 \quad (m)$$

The true value of the roll diameter at any point ( $x_M$ ) measured from the LH end of the roll is therefore

$$D_{N_{x_M}} = D_N - \frac{4 c_N}{L^2} \cdot \left(x_M - \frac{L}{2}\right)^2 \quad (m) \quad (A.4.1)$$

for  $M=1, \dots, M_N$

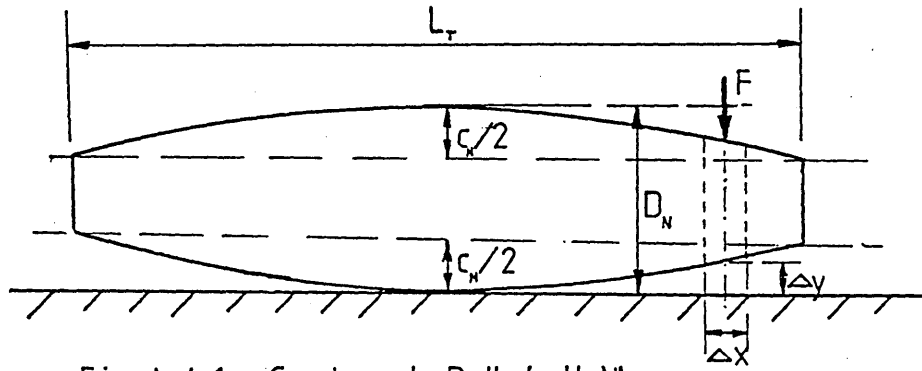


Fig. A.4.1 Cambered Roll (roll N)

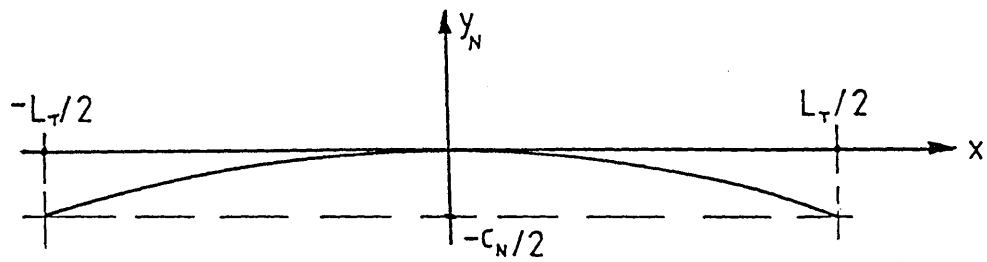


Fig. A.4.2 Upper Surface

#### A.4.2. Incorporation in the Theory

The b.o.e.f. theory of Appendix 1 considered a parallel roll resting upon a foundation. If the cambered roll is now considered as resting upon an elastic foundation as shown in fig.A.4.1, we may make the following observations.

For a force  $F$  applied as shown, a reduced amount of foundation deflection will occur below the point of application compared with the case for a parallel-ground roll of equivalent stiffness. In fact, one can conceive that for  $F$  very small, whereas some small deflection of the foundation would occur in the parallel case, none may occur in fig.A.4.1 if  $F$  is not large enough to close the gap  $\Delta y$ .

Therefore, whereas equation (A1.1) gives us the value of local distributed reaction as

$$q_R = k \cdot y \text{ (Nm}^{-1}\text{)}$$

the reaction in the case of figure A.4.1 will be

$$q_R = k(y - \Delta y) \text{ (Nm}^{-1}\text{)}$$

where  $y$  = deflection of lower surface of the roll (m).

Now, if the force  $F$  is taken to be equivalent to the loading acting over a length of the roll given by  $\Delta x$ , (which is how equivalent loadings were represented for the first intermediate rolls and workrolls in Chapter 3), then we may imagine the same effect to be produced locally by assuming a parallel roll in contact with the

foundation, and reducing F by an amount equal to

$$\Delta F = k \cdot \Delta y \cdot \Delta x \quad (N).$$

Now,  $\Delta y$ , is the gap between the foundation and the surface of the roll and is therefore easily found from the values given by equation (A.4.1) as

$$\Delta y_{x_M} = 0.5 (D_N - D_{N_{x_M}}) \quad \left. \begin{array}{l} (m) \quad \dots \dots \dots (A.4.2.) \\ M=1, \dots, M_N \end{array} \right\}$$

Furthermore, if the elastic foundation is itself formed by a cambered roll, the effect of the second camber must be similarly included. Thus, consider for example roll Y resting upon a foundation formed by roll Z, both of which are cambered. Equation (A.4.1) is used to evaluate both  $D_{Y_{x_M}}$  and  $D_{Z_{x_M}}$ , and then (A.4.2) gives

$$\Delta y_{x_M} = 0.5 (D_Y + D_Z - D_{Y_{x_M}} - D_{Z_{x_M}}) \quad \left. \begin{array}{l} \dots \dots \dots (A.4.3) \\ M=1, \dots, M_n \end{array} \right\}$$

Therefore, whenever the theory of beams on elastic foundations is used in the model, the above correction is included. Thus for example, equation (A1.7) becomes

$$y_{x_M} = \frac{\lambda \cdot (F - k \cdot \Delta y_{x_M} \cdot \Delta x)}{2k} \cdot A \lambda_{x_M}$$

where  $x_M$  is the section under consideration

$k, \lambda$  are the constants of the interface under consideration

$\Delta y_{x_M}$  is given by equation (A.4.3).

$\Delta x$  is given by for example  $L_T/J_{1F}$  in fig.3.28

Similarly equations (A1.8) to (A1.10) are modified by replacing F with  $(F - k \cdot \Delta y_{x_M} \cdot \Delta x)$ .

### A4.3 Tapered First Intermediate Rolls

Consider now the IIRs. These have a length  $L_T$  which may be cambered in the same way as the other rolls (fig.A4.1), but also an additional tapered-off length  $L_t$  is provided as shown in fig.A.4.3(i). The facility exists to slide these tapers into or out of the mill cluster, so that more or less of the tapered section is over the strip edge. This allows the reduction taken at the strip edges to be varied with respect to the reduction taken over the rest of the strip, so that shape control of the edges is facilitated. Fig.A4.3(ii) shows an upper IIR slid a distance  $L_{IT}$  into the mill cluster.

In fig.A4.3(i), with the x-axis drawn as in fig.A4.2 but with the y-axis shifted to the extreme LH end of the roll, the equation of the upper surface of the roll becomes

$$y_1 = -\frac{c_1}{2} - \frac{h}{2L_t} \cdot (L_t - x) \quad (\text{m}) \quad \text{for } 0 \leq x < L_t$$

$$\text{and } y_1 = \frac{-2c_1}{L_T^2} \cdot (x - L_t - \frac{L_t}{2})^2 \quad (\text{m}) \quad \text{for } L_t \leq x < (L_t + L_T)$$

In fig.A4.3(ii),  $x_M$  is measured from the front of the other (laterally fixed) mill rolls in order to obtain values at the same points across the mill as in the main model. These equations therefore give the magnitude of the deflection correction due to either surface of the shifted IIR as

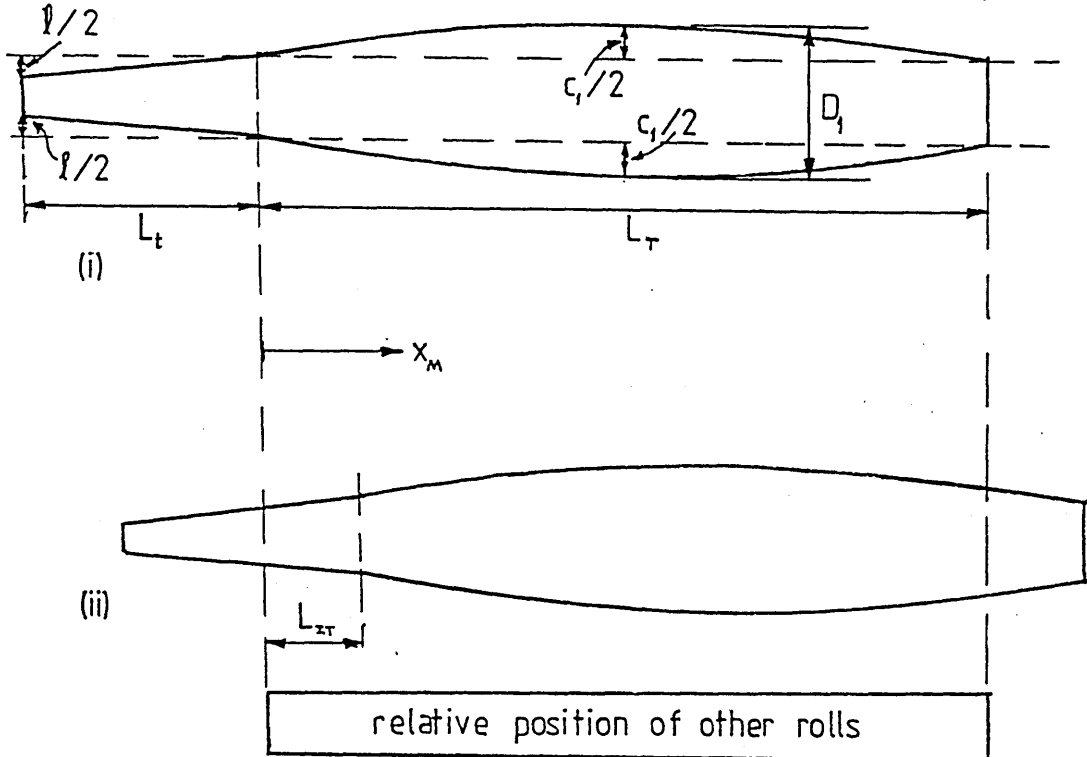


Fig. A.4.3 1IR Profile & Control Action

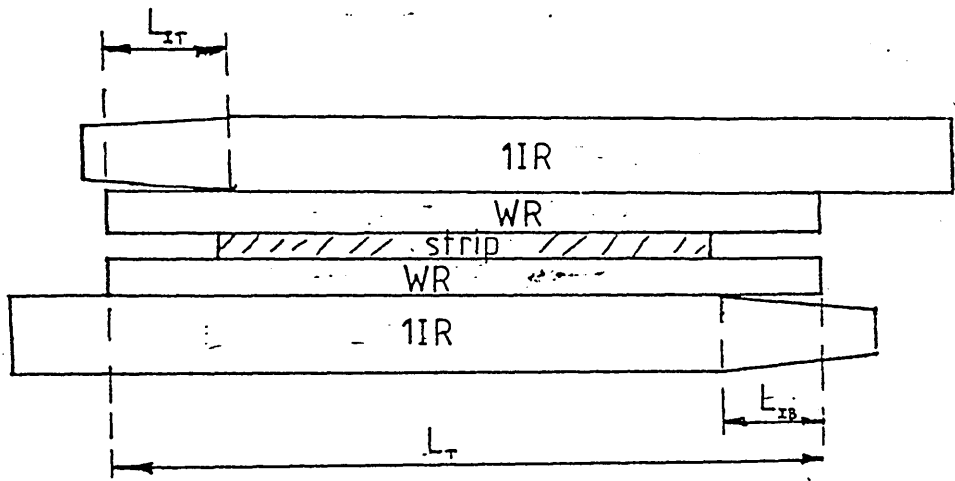


Fig. A.4.4 Upper & Lower 1IR Effects

$$\begin{aligned}
y_{1x_M} &= \frac{c_1}{2} + \frac{\lambda}{2L_t} (L_{IT} - x_M) & (m) & \\
&\text{for } 0 \leq x_M < L_{IT} & & \\
&& & (A4.4) \\
\text{and } y_{1x_M} &= \frac{2c_1}{L_T^2} \cdot (x_M - L_{IT} - \frac{L_r}{2})^2 & (m) & \\
&\text{for } L_{IT} \leq x_M \leq L_T & & \\
&& & \text{for } M=1, \dots, M_1
\end{aligned}$$

The upper IIRs are tapered off at the front of the mill, and the lower IIRs at the rear as shown in fig.A4.4. To obtain the magnitude of the deflection correction due to each surface of the lower IIR, equations (A4.4) are applied measuring  $x'_M$  from the RH end of the mill rather than the left, i.e.

$$\begin{aligned}
y'_{1x'_M} &= \frac{c_1}{2} + \frac{\lambda}{2L_t} (L_{IB} - x'_M) & (m) & \\
&\text{for } 0 \leq x'_M < L_{IB} & & \\
y'_{1x'_M} &= \frac{2c_1}{L_T^2} (x'_M - L_{IB} - \frac{L_r}{2})^2 & (m) & \\
&\text{for } L_{IB} \leq x'_M \leq L_T & & \\
&& & \text{for } M=1, \dots, M_1
\end{aligned}$$

The order of the set of values is then reversed so that  $x_M$  again runs from front to rear:-

$$y_{1x_M} = y'_{1x_{(M_1+1-M)}} \quad (m) \text{ for } M=1, \dots, M_1 \quad (A4.5)$$

Although the lower IIRs are not in the upper half of the cluster, their effect must be taken into account during the analysis of Chapter 3. The conditions around the roll bite during rolling are such that a profile change forced onto the lower WR only, will have the same effect on strip shape as the inverse profile change forced onto the upper WR only. Therefore, to a reasonable approximation, if the lower IIRs are conceptually moved into the upper half of the cluster, their effect upon strip shape should remain the same. An imaginary roll is therefore postulated whose surface profile includes all the effects due to the shifted upper and lower IIRs. Two obvious properties of such a roll can be stated. Firstly, when neither the upper nor lower IIR tapers are slid into the cluster at all, then the deflection correction due to its surface must be the same as that due to the camber only on either the top or bottom IIRs. Secondly, if both the upper and lower IIR tapers are slid into the mill to the maximum possible extent, then the deflection correction would be expected to be symmetrical about the vertical centre-line of the mill, and to be a maximum at each end of the roll. These conditions are met by assuming that the magnitude of the deflection correction due to all IIR effects (at one surface of the imaginary roll) is simply the arithmetic mean of the corrections for the upper and lower IIRs. Thus,

$$y_{I_{x_M}} = \frac{y_{T_{x_M}} + y_{B_{x_M}}}{2} \quad (m) \text{ for } M=1, \dots, M_1 \quad (\text{A4.6})$$

where  $y_{T_{x_M}}$  is given by equation (A4.4)

$y_{B_{x_M}}$  is given by equation (A4.5)

The value of roll diameter for this composite roll is then found as before (c.f. equation (A4.1)), viz..

$$D_{I_{x_M}} = D_1 + 2y_{I_{x_M}} \quad (m) \quad \left. \begin{array}{l} \dots \dots \dots (A4.7) \\ M=1, \dots, M_1 \end{array} \right|$$

When the first intermediate roll is involved in Chapter 3, the effects of this are included by using  $D_1$  and  $D_{I_{x_M}}$  (given by (A4.7) above) in equation (A4.3) instead of  $D_Y$  or  $D_Z$ .

APPENDIX 5

Examples of Matrices Generated

A5.1 Transpose of Parameterization Matrix (i.e.  $\tilde{X}_0^T$ ) for the Theoretical Case of 8 Covered Rotors

$$\tilde{X}_0^T = \begin{bmatrix} -1.000 & 0.571 & -0.245 & 0.080 \\ -0.714 & 0.082 & 0.175 & -0.148 \\ -0.429 & -0.245 & 0.245 & -0.034 \\ -0.143 & -0.408 & 0.105 & 0.103 \\ 0.143 & -0.408 & -0.105 & 0.103 \\ 0.429 & -0.245 & -0.245 & -0.034 \\ 0.714 & 0.082 & -0.175 & -0.148 \\ 1.000 & 0.571 & 0.245 & 0.080 \end{bmatrix}$$

(Note that the  $i^{\text{th}}$  column contains the coefficient of the  $i^{\text{th}}$  Gram polynomial)

A5.2  $(\tilde{X}_0 \tilde{X}_0^T)^{-1}$  Corresponding to the matrix of A5.1

$$(\tilde{X}_0 \tilde{X}_0^T)^{-1} = \begin{bmatrix} 0.292 & 0.000 & 0.000 & 0.000 \\ 0.000 & 0.893 & 0.000 & 0.000 \\ 0.000 & 0.000 & 3.095 & 0.000 \\ 0.000 & 0.000 & 0.000 & 12.440 \end{bmatrix} = \tilde{L}$$

These matrices were computer generated, and are rounded to the given accuracy. The greatest of the off-diagonal terms in this particular matrix is actually  $-0.44 \cdot 10^{-5}$ . When compared with the matrix given by evaluating  $(\tilde{X}^T \tilde{X})^{-1}$  for the equivalent matrix in ref.(49), the mistaken assumptions of Fotakis and Grimble concerning the Chebshev polynomials are evident (off-diagonal terms of significance being present).

A5.3  $\tilde{X}_0^T$  Matrix for 21 Covered Rotors

---

$$\tilde{X}_0^T = \begin{bmatrix} -1.000 & 0.633 & -0.342 & 0.166 \\ -0.900 & 0.443 & -0.137 & 0.000 \\ -0.800 & 0.273 & 0.014 & -0.087 \\ -0.700 & 0.123 & 0.118 & -0.117 \\ -0.600 & -0.007 & 0.179 & -0.105 \\ -0.500 & -0.117 & 0.204 & -0.070 \\ -0.400 & -0.207 & 0.199 & -0.022 \\ -0.300 & -0.277 & 0.170 & 0.026 \\ -0.200 & -0.327 & 0.124 & 0.066 \\ -0.100 & -0.357 & 0.065 & 0.093 \\ 0.000 & -0.367 & 0.000 & 0.102 \\ 0.100 & -0.357 & -0.065 & 0.093 \\ 0.200 & -0.327 & -0.124 & 0.066 \\ 0.300 & -0.277 & -0.170 & 0.026 \\ 0.400 & -0.207 & -0.199 & -0.022 \\ 0.500 & -0.117 & -0.204 & -0.070 \\ 0.600 & -0.007 & -0.179 & -0.105 \\ 0.700 & 0.123 & -0.118 & -0.117 \\ 0.800 & 0.273 & -0.014 & -0.087 \\ 0.900 & 0.443 & 0.137 & 0.000 \\ 1.000 & 0.633 & 0.342 & 0.166 \end{bmatrix}$$

Again, column  $i$  contains the coefficients of the  $i^{\text{th}}$  Gram polynomial (c.f. column 1 with equation (6.6) and  $x_{0ij}$  of equations (6.9)).

A5.4  $(\tilde{X}_0 \tilde{X}_0^T)^{-1}$  Corresponding to  $\tilde{X}_0^T$  of A5.3

---

$$(\tilde{X}_0 \tilde{X}_0^T)^{-1} = \begin{bmatrix} 0.130 & 0.000 & 0.000 & 0.000 \\ 0.000 & 0.446 & 0.000 & 0.000 \\ 0.000 & 0.000 & 1.605 & 0.000 \\ 0.000 & 0.000 & 0.000 & 5.949 \end{bmatrix} = \tilde{L}$$

Here, the greatest off-diagonal term is  $-0.18 \cdot 10^{-6}$ .

A5.5 A "Theoretical" 8x8  $\tilde{G}_p$  Matrix (Nmm<sup>-3</sup>)

(As used by Fotakis in ref. (17))

$$\tilde{G}_p = \begin{bmatrix} 3.79 & 3.46 & -0.75 & -1.44 & -1.38 & -1.18 & -1.56 & -0.96 \\ 1.30 & 2.30 & 1.03 & -0.41 & -0.62 & -1.43 & -1.60 & -0.87 \\ -0.44 & 0.86 & 1.88 & 0.67 & 0.23 & -1.04 & -1.33 & -0.80 \\ -1.02 & -0.75 & 1.29 & 1.61 & 1.35 & 0.10 & -1.34 & -0.96 \\ -0.96 & -1.34 & 0.10 & 1.35 & 1.61 & 1.29 & -0.75 & -1.02 \\ -0.80 & -1.33 & -1.04 & 0.23 & 0.67 & 1.88 & 0.86 & -0.44 \\ -0.87 & -1.60 & -1.43 & -0.62 & -0.41 & 1.03 & 2.30 & 1.30 \\ -0.96 & -1.56 & -1.18 & -1.38 & -1.44 & -0.75 & 3.46 & 3.79 \end{bmatrix}$$

A5.6 Transformed Plant Matrix for "Theoretical" 8x8 System

$$\tilde{G}_T = \tilde{L} \tilde{X}_o \tilde{G}_p \tilde{X}_o^T$$

where  $\tilde{L}$  is given in appendix A5.2

$\tilde{X}_o^T$  is given in appendix A5.1

$\tilde{G}_p$  is given in appendix A5.5

$$\tilde{G}_T = \begin{bmatrix} 8.37 & 0 & -0.52 & 0 \\ 0 & 6.19 & 0 & -0.62 \\ 0.80 & 0 & 3.04 & 0 \\ 0 & -2.34 & 0 & 1.08 \end{bmatrix} \quad \begin{array}{l} \text{(Greatest "0"} \\ \text{term =} \\ \text{-0.16*10}^{-5} \end{array}$$

A5.7 Precompensator for "Theoretical" 8x8 system

$$\tilde{P} = \tilde{G}_T^{-1}$$

$$\tilde{P} = \begin{bmatrix} 0.18 & 0 & 0.02 & 0 \\ 0 & 0.21 & 0 & 0.12 \\ -0.03 & 0 & 0.32 & 0 \\ 0 & 0.45 & 0 & 1.18 \end{bmatrix} \quad \begin{array}{l} \text{(Greatest "0"} \\ \text{term =} \\ \text{0.26*10}^{-6} \end{array}$$

A5.8 Calculated 8x8  $\tilde{G}_p$  matrix for 1.6lm strip (Nmm<sup>-3</sup>)

$$\tilde{G}_p = \begin{bmatrix} 1.60 & 2.14 & -0.06 & -0.94 & -1.05 & -1.00 & -0.92 & -0.45 \\ 0.68 & 1.43 & 1.13 & -0.06 & -0.90 & -1.02 & -0.93 & -0.45 \\ -0.05 & 0.54 & 1.44 & 0.98 & -0.19 & -0.91 & -0.93 & -0.45 \\ -0.43 & -0.43 & 0.73 & 1.36 & 0.80 & -0.29 & -0.90 & -0.46 \\ -0.46 & -0.90 & -0.29 & 0.80 & 1.36 & 0.73 & -0.43 & -0.43 \\ -0.45 & -0.93 & -0.91 & -0.19 & 0.98 & 1.44 & 0.54 & -0.05 \\ -0.45 & -0.93 & -1.02 & -0.90 & -0.06 & 1.13 & 1.43 & 0.68 \\ -0.45 & -0.92 & -1.00 & -1.05 & -0.94 & -0.06 & 2.14 & 1.60 \end{bmatrix}$$

A5.9 Comparable Matrix after Gunawardene (16) (Nmm<sup>-3</sup>)

$$\tilde{G}_p = \begin{bmatrix} 2.74 & 2.95 & -0.12 & -1.22 & -1.17 & -0.97 & -0.92 & -0.99 \\ 0.73 & 1.80 & 1.39 & 0.00 & -1.04 & -1.27 & -1.18 & -1.21 \\ -0.47 & 0.32 & 1.70 & 1.24 & -0.23 & -1.11 & -1.26 & -1.27 \\ -0.73 & -0.70 & 0.76 & 1.67 & 1.03 & -0.34 & -1.19 & -1.22 \\ -0.64 & -1.10 & -0.42 & 0.87 & 1.69 & 0.90 & -0.70 & -0.77 \\ -0.57 & -1.18 & -1.08 & -0.33 & 1.06 & 1.71 & 0.48 & 0.43 \\ -0.54 & -1.12 & -1.22 & -1.04 & -0.19 & 1.22 & 1.91 & 1.99 \\ -0.52 & -0.98 & -1.02 & -1.19 & -1.16 & -0.14 & 2.86 & 3.04 \end{bmatrix}$$

A5.10  $31 \times 8 \tilde{G}_p$  Matrix for 1.61m strip ( $Nmm^{-3}$ )

$$\tilde{G}_p = \begin{bmatrix} 2.49 & 3.12 & -0.63 & -1.12 & -1.04 & -1.00 & -0.94 & -0.46 \\ 1.80 & 2.35 & -0.23 & -1.00 & -1.05 & -1.00 & -0.95 & -0.46 \\ 1.36 & 1.91 & 0.15 & -0.85 & -1.05 & -1.00 & -0.95 & -0.47 \\ 1.11 & 1.72 & 0.50 & -0.65 & -1.04 & -1.00 & -0.95 & -0.47 \\ 0.91 & 1.59 & 0.81 & -0.41 & -1.00 & -1.00 & -0.95 & -0.47 \\ 0.73 & 1.46 & 1.06 & -0.15 & -0.93 & -1.00 & -0.95 & -0.47 \\ 0.54 & 1.30 & 1.28 & 0.14 & -0.81 & -1.00 & -0.95 & -0.47 \\ 0.34 & 1.08 & 1.40 & 0.42 & -0.65 & -1.00 & -0.95 & -0.47 \\ 0.14 & 0.84 & 1.46 & 0.69 & -0.50 & -0.98 & -0.95 & -0.47 \\ -0.04 & 0.57 & 1.45 & 0.93 & -0.23 & -0.92 & -0.96 & -0.47 \\ -0.19 & 0.29 & 1.35 & 1.12 & 0.01 & -0.83 & -0.96 & -0.47 \\ -0.31 & 0.03 & 1.22 & 1.28 & 0.28 & -0.69 & -0.96 & -0.47 \\ -0.40 & -0.22 & 1.00 & 1.35 & 0.54 & -0.51 & -0.96 & -0.47 \\ -0.45 & -0.44 & 0.76 & 1.37 & 0.79 & -0.30 & -0.93 & -0.48 \\ -0.48 & -0.62 & 0.49 & 1.32 & 1.02 & -0.05 & -0.86 & -0.48 \\ -0.48 & -0.76 & 0.21 & 1.18 & 1.18 & 0.21 & -0.76 & -0.48 \\ -0.48 & -0.86 & -0.05 & 1.02 & 1.32 & 0.49 & -0.62 & -0.48 \\ -0.48 & -0.93 & -0.30 & 0.79 & 1.36 & 0.76 & -0.44 & -0.45 \\ -0.47 & -0.96 & -0.51 & 0.54 & 1.35 & 1.00 & -0.22 & -0.40 \\ -0.47 & -0.96 & -0.69 & 0.28 & 1.28 & 1.22 & 0.03 & -0.31 \\ -0.47 & -0.96 & -0.83 & 0.01 & 1.12 & 1.35 & 0.29 & -0.19 \\ -0.47 & -0.96 & -0.92 & -0.23 & 0.93 & 1.45 & 0.57 & -0.04 \\ -0.47 & -0.95 & -0.98 & -0.50 & 0.69 & 1.46 & 0.84 & 0.14 \\ -0.47 & -0.95 & -1.00 & -0.65 & 0.42 & 1.40 & 1.08 & 0.34 \\ -0.47 & -0.95 & -1.00 & -0.81 & 0.14 & 1.28 & 1.30 & 0.54 \\ -0.47 & -0.95 & -1.00 & -0.93 & -0.15 & 1.06 & 1.45 & 0.73 \\ -0.47 & -0.95 & -1.00 & -1.00 & -0.41 & 0.81 & 1.59 & 0.91 \\ -0.47 & -0.95 & -1.00 & -1.04 & -0.65 & 0.50 & 1.71 & 1.11 \\ -0.47 & -0.95 & -1.00 & -1.05 & -0.85 & 0.15 & 1.91 & 1.36 \\ -0.46 & -0.95 & -1.00 & -1.05 & -1.00 & -0.23 & 2.35 & 1.80 \\ -0.46 & -0.94 & -1.00 & -1.04 & -1.12 & -0.63 & 3.12 & 2.49 \end{bmatrix}$$

A5.11 25x8  $\tilde{G}_p$  Matrix for 1.3m Strip (Nmm<sup>-3</sup>)

$$\tilde{G}_p = \begin{bmatrix} 9.52 & 13.82 & 2.32 & -0.82 & -1.33 & -1.21 & -1.09 & -0.51 \\ 2.62 & 3.98 & 1.14 & -0.61 & -1.26 & -1.22 & -1.12 & -0.54 \\ -0.29 & -0.03 & 0.71 & -0.38 & -1.17 & -1.22 & -1.13 & -0.55 \\ -1.02 & -0.96 & 0.75 & -0.10 & -1.05 & -1.22 & -1.13 & -0.55 \\ -0.88 & -0.71 & 0.92 & 0.17 & -0.89 & -1.22 & -1.13 & -0.55 \\ -0.55 & -0.22 & 1.09 & 0.44 & -0.70 & -1.19 & -1.13 & -0.54 \\ -0.34 & 0.59 & 1.17 & 0.68 & -0.48 & -1.14 & -1.13 & -0.54 \\ -0.28 & 0.08 & 1.13 & 0.87 & -0.24 & -1.04 & -1.14 & -0.54 \\ -0.32 & -0.07 & 1.01 & 1.03 & 0.03 & -0.90 & -1.14 & -0.54 \\ -0.41 & -0.31 & 0.79 & 1.10 & 0.29 & -0.72 & -1.13 & -0.55 \\ -0.48 & -0.55 & 0.55 & 1.11 & 0.54 & -0.51 & -1.10 & -0.55 \\ -0.52 & -0.76 & 0.28 & 1.07 & 0.77 & -0.26 & -1.04 & -0.55 \\ -0.55 & -0.93 & 0.00 & 0.93 & 0.93 & 0.00 & -0.93 & -0.55 \\ -0.55 & -1.04 & -0.26 & 0.77 & 1.07 & 0.28 & -0.76 & -0.52 \\ -0.55 & -1.10 & -0.51 & 0.54 & 1.11 & 0.55 & -0.55 & -0.48 \\ -0.55 & -1.13 & -0.72 & 0.29 & 1.10 & 0.79 & -0.31 & -0.41 \\ -0.54 & -1.14 & -0.90 & 0.03 & 1.03 & 1.01 & -0.07 & -0.32 \\ -0.54 & -1.14 & -1.04 & -0.23 & 0.87 & 1.12 & 0.08 & -0.28 \\ -0.54 & -1.13 & -1.14 & -0.48 & 0.68 & 1.17 & 0.59 & -0.34 \\ -0.54 & -1.13 & -1.19 & -0.70 & 0.44 & 1.09 & -0.23 & -0.55 \\ -0.55 & -1.13 & -1.22 & -0.89 & 0.17 & 0.92 & -0.71 & -0.88 \\ -0.55 & -1.13 & -1.22 & -1.05 & -0.10 & 0.75 & -0.96 & -1.02 \\ -0.55 & -1.13 & -1.22 & -1.17 & -0.38 & 0.71 & -0.02 & -0.29 \\ -0.53 & -1.12 & -1.22 & -1.26 & -0.61 & 1.14 & 3.98 & 2.62 \\ -0.51 & -1.09 & -1.21 & -1.33 & -0.82 & 2.32 & 13.82 & 9.52 \end{bmatrix}$$

A5.12 19x8  $\tilde{G}_p$  Matrix for 0.99m Strip (Nmm<sup>-3</sup>)

$$\tilde{G}_p = \begin{bmatrix} 18.38 & 29.18 & 8.81 & 1.07 & -1.39 & -1.51 & -1.36 & -0.56 \\ 2.22 & 3.90 & 2.37 & 0.21 & -1.23 & -1.49 & -1.41 & -0.63 \\ -3.37 & -4.42 & -0.15 & -0.04 & -1.05 & -1.46 & -1.43 & -0.65 \\ -4.11 & -5.58 & -0.61 & 0.07 & -0.83 & -1.41 & -1.44 & -0.66 \\ -3.09 & -4.18 & -0.30 & 0.30 & -0.59 & -1.31 & -1.44 & -0.65 \\ -1.86 & -2.48 & 0.10 & 0.55 & -0.33 & -1.17 & -1.43 & -0.65 \\ -1.01 & -1.35 & 0.28 & 0.69 & -0.07 & -0.99 & -1.40 & -0.63 \\ -0.59 & -0.87 & 0.25 & 0.74 & 0.18 & -0.76 & -1.32 & -0.60 \\ -0.47 & -0.83 & 0.06 & 0.71 & 0.41 & -0.49 & -1.17 & -0.55 \\ -0.49 & -0.99 & -0.21 & 0.58 & 0.58 & -0.21 & -0.99 & -0.49 \\ -0.55 & -1.17 & -0.49 & 0.41 & 0.71 & 0.06 & -0.83 & -0.47 \\ -0.60 & -1.32 & -0.76 & 0.18 & 0.74 & 0.25 & -0.87 & -0.59 \\ -0.63 & -1.40 & -0.99 & -0.07 & 0.69 & 0.28 & -1.35 & -1.01 \\ -0.65 & -1.43 & -1.17 & -0.33 & 0.55 & 0.10 & -2.48 & -1.86 \\ -0.65 & -1.44 & -1.31 & -0.59 & 0.30 & -0.30 & -4.18 & -3.09 \\ -0.66 & -1.44 & -1.41 & -0.83 & 0.07 & -0.61 & -5.57 & -4.11 \\ -0.65 & -1.43 & -1.46 & -1.05 & -0.04 & -0.14 & -4.42 & -3.37 \\ -0.63 & -1.41 & -1.49 & -1.23 & 0.21 & 2.37 & 3.90 & 2.22 \\ -0.58 & -1.36 & -1.51 & -1.39 & 1.07 & 8.81 & 29.18 & 18.38 \end{bmatrix}$$

## APPENDIX 6

### Details of The Author's Dynamic Simulation Package

Digital simulation of dynamical systems relies, as does analogue simulation, upon solution of the system differential equations. Many computer installations linked with academic institutions are furnished with software packages which will simulate dynamical systems expressed in state-space form. Such a package was not available to the author, and therefore a simple package previously written by the author for single-variable transfer function simulation was modified and extended. Details are now given of the various subroutines in the package, which take the form of one routine per block diagram element. Thus there is an "integrator" routine, a "first order lag" routine etc., and these are linked together by a main program to form block diagram simulations of arbitrary complexity.

#### A6.1 Fundamental Method of Solution of Differential Equations

References on numerical analysis (see for example (30), (31) and (41)) provide any number of methods of greater or lesser accuracy and complexity for the solution of ordinary differential equations. Perhaps the most widely used of these are the class of Runge Kutta methods. However, these need typically three or four intermediate function evaluations per step of the integration procedure (for the more accurate versions of the method) which is often inconvenient for the types of simulation

for which the present package is required. The simpler methods, such as Euler's method, have the disadvantage that a smaller integration step size is needed for acceptable results, and are also somewhat less accurate. In the current application, the step size requirements of Euler's method are almost acceptable, and this therefore is the basis of the package. In order to obtain sufficient accuracy and allow an increase in step size, a "predictor-corrector" method based upon Euler's method is used. This is strictly the "Fox-Euler" method (42), (43). Consider the differential equation

$$\begin{aligned} \frac{dy}{dt} &= y' = f(t,y) & (A6.1) \\ y(a) &= y_0 \end{aligned}$$

Over an interval (a,b) choose a step length

$$h = \frac{(b-a)}{N} \quad (\text{second})$$

whence  $t_0 = a$ ,  $t_n = a+nh$ ,  $t_N = b$

$$y(t_n) = y(a+nh)$$

Euler's method (which equates to Taylor's method of order 1) then states that

$$y_{n+1} = y_n + h \cdot f(t_n, y_n)$$

$$\text{i.e.} \quad y_{n+1} = y_n + h \cdot y'_n \quad (A6.2)$$

It can be shown that the local error of this method is given by

$$E = \frac{h^2}{2} y''(\xi) \quad t_n < \xi < t_n + h$$

A more accurate solution can be obtained by integrating the original equation A6.1 from  $t_n$  to  $t_{n+1}$

$$\text{giving } y_{n+1} = y_n + \int_{t_n}^{t_{n+1}} f(t, y(t)) dt \quad (\text{A6.3})$$

Approximating A6.3 by the trapezoidal formula for numerical integration gives

$$y_{n+1} = y_n + \frac{h}{2} (f(t_n, y_n) + f(t_{n+1}, y_{n+1})) \quad (\text{A6.4})$$

which is clearly an implicit formula for  $y_{n+1}$ .

The local error is now much better than Euler's method, and is given by

$$E = -\frac{h^3}{12} y'''(\xi) \quad t_n < \xi < t_n + h$$

In order to solve the implicit equation above (A6.4) an "inner iteration" is used (to distinguish it from the "outer iteration" on  $n$ ) as follows:-

- 1) Use Euler's method (A6.2) to obtain a first approximation

$$y_{n+1}^{(0)} = y_n + h \cdot y_n'$$

- 2) Evaluate  $f(t_{n+1}, y_{n+1}^{(0)})$  and use in (A6.4) to obtain the approximation

$$y_{n+1}^{(1)} = y_n + \frac{h}{2} (y_n' + f(t_{n+1}, y_{n+1}^{(0)}))$$

3) Continue to apply step (2) using the updated estimates as an iteration on k:-

$$y_{n+1}^{(k)} = y_n + \frac{h}{2} (y_n' + f(t_{n+1}, y_{n+1}^{(k-1)})) \quad k=1,2,3,\dots \text{until finished}$$

(A6.5)

until two successive iterates agree to the required accuracy, i.e. until

$$\frac{\left| y_{n+1}^{(k)} - y_{n+1}^{(k-1)} \right|}{\left| y_{n+1}^{(k)} \right|} < \epsilon \quad \text{where } \epsilon \text{ is the pre-scribed accuracy.}$$

(In the present context, the independent variable is always time, thus  $y' = \frac{dy}{dt}$ ,  $y'' = \frac{d^2y}{dt^2}$  etc.)

#### A6.2 Simulation of an Integrator

Consider the trivial block diagram of figure A6.1(a), which may be redrawn as fig.A6.1(b). This represents a general integrator in transfer functional form, and by inspection the variable at the unity-gain integrator input in (b) must be  $y'$ . Hence, it can be seen that

$$y' = k_I \cdot x$$

Substitution in (A6.2) yields

$$y_{n+1} = y_n + h \cdot k_I \cdot x_n \quad \text{(A6.6)}$$

(There is no need to apply the "corrector" part of the process here, as Euler's method alone is accurate for a pure integrator).

Hence, a subroutine is provided which is used as follows:-

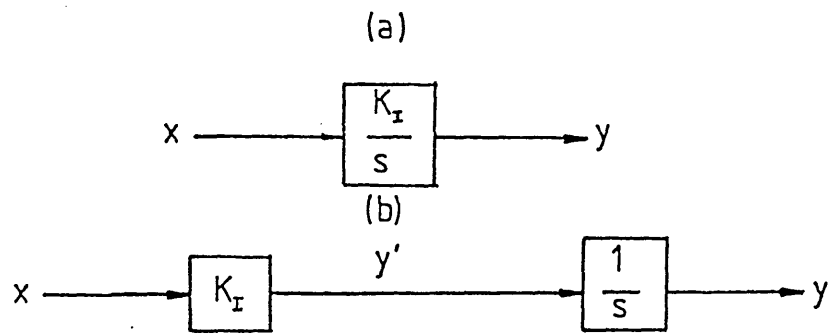


Fig.A.6.1 Integrator Block

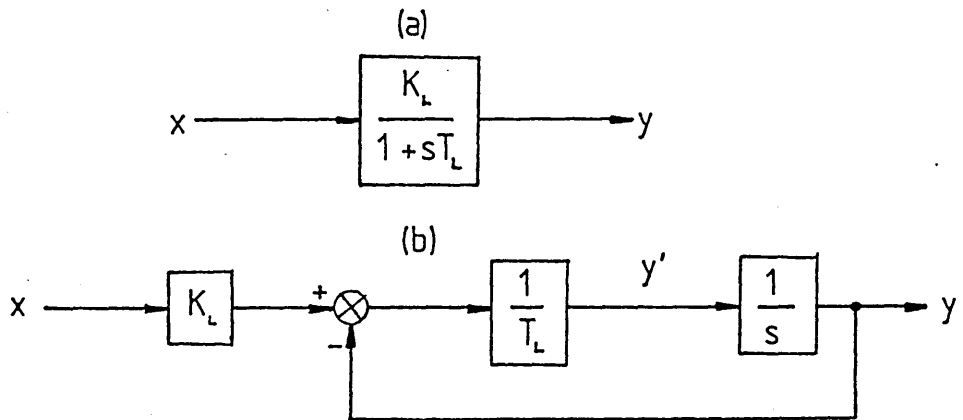
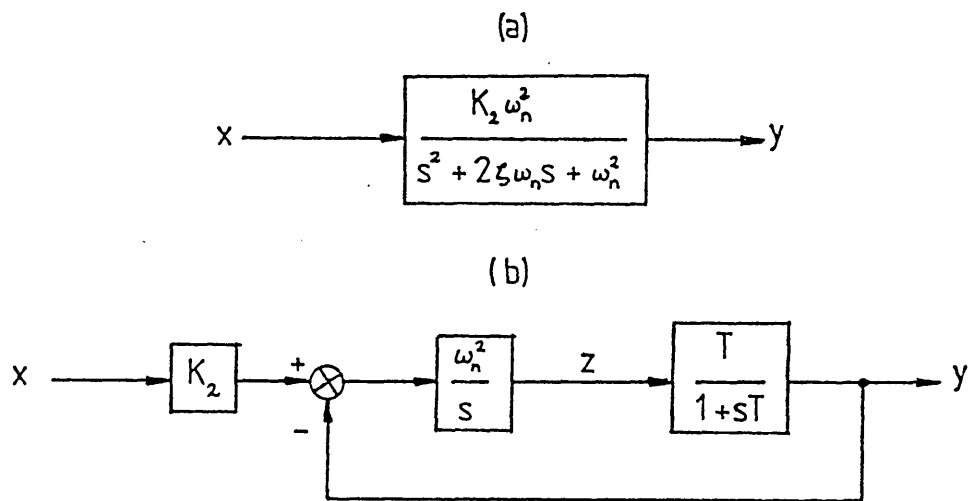


Fig.A.6.2 First Order Lag Block.



where  $T = \frac{1}{2\zeta\omega_n}$  and  $z_o = \frac{y_o}{T}$

Fig.A.6.3 Second Order System Block

CALL INTEG(K,X,Y,H,YNXT)

where K = (real) integral gain

X = existing input at present time

Y = existing output at present time

H = integration step length (s)

YNXT = value of output which will exist one time step  
(H) later.

### A6.3 Simulation of a First Order Lag

Figure A6.2(a) shows a block diagram of a first order lag in transfer functional form, and fig.A6.2(b) shows an equivalent representation. From fig.A6.2(b), we see that

$$y' = \frac{1}{T_L} \cdot (K_L x - y)$$

Substitution into (A6.2) gives

$$(o) \quad y_{n+1} = y_n + \frac{h}{T_L} \cdot (K_L \cdot x_n - y_n) \quad (A6.7)$$

This value is then used as the starting point for an "inner iteration" around the corrector equation (A6.5). It is usually found that for a correct choice of h (i.e. say  $T_L/5$ ) only two "inner iterations" will be needed. Therefore the subroutine allows only five iterations before printing a warning message and the value of  $y_{n+1}$  as the result. The routine is used by issuing the statement

```
CALL LAG(K,T,X,XNXT,Y,H,YNXT)
```

where K = (real) gain

T = Time constant(s)

X = existing input at present time

XNXT = input which will be known to exist one  
time step (H) later

Y = existing output at present time

H = integration step length (s)

YNXT = value of output which will exist one  
time step (H) later

#### A6.4 Simulation of a Second Order System

The generalized second order system is shown in figure A6.3(a), and in rearranged form in A6.3(b). Here the intermediate variable z is introduced to simplify matters. It is clear that fig.A6.3(b) makes use only of transfer functional blocks already dealt with in sections A6.2 and A6.3. Therefore the procedure here is simply to issue the calls (written in pseudo code for brevity).

```
CALL INTEG( $\omega_n^2$ , (K2x - y), z, H, ZNXT)
```

(where ZNXT = integrator output one time step (H) later), followed by

```
CALL LAG ( $\frac{1}{2\zeta\omega_n}$ ,  $\frac{1}{2\zeta\omega_n}$ , z, ZNXT, y, H, YNXT)
```

The call to the second order simulation subroutine which does this is written

```
CALL SECORD (K, ZTA, WN, X, Y, Z, H, YNXT, ZNXT)
```

where  $K$  = system gain

$ZTA$  = damping ratio ( $\xi$ )

$WN$  = natural frequency ( $\omega_n$ ) ( $\text{rad s}^{-1}$ )

$X, Y$  as before

$Z$  = existing value of intermediate value at present time\*

$H$  = Integration step length (s)

$YNXT$  as before

$ZNXT$  = value of intermediate variable which will exist one time step ( $H$ ) later.

\*On the first call, this can be given as  $Z_0 = Y_0/T$

#### A6.5 Simulation of a Lead-Lag (Phase Advance) Network

The transfer functional representation of a phase advance compensator is given in figure A6.4(a). From the rearranged version (fig. A6.4(b)) it can be seen that only a first-order lag block is required. Here, however, a call to the LAG routine cannot be used, as the new value of output will affect the input. Therefore, the following procedure is used:-

Euler's method is used as in the LAG routine (equation A6.7) to obtain a first estimate for the next value of  $z$  as

$$z_{n+1}^{(o)} = z_n + \frac{h}{T} (y_n - z_n)$$

Then, from fig A6.4(b)

$$y_{n+1}^{(o)} = \frac{1-\alpha}{\alpha} \left[ \frac{K_p \alpha x_{n+1}}{1-\alpha} - z_{n+1}^{(o)} \right]$$

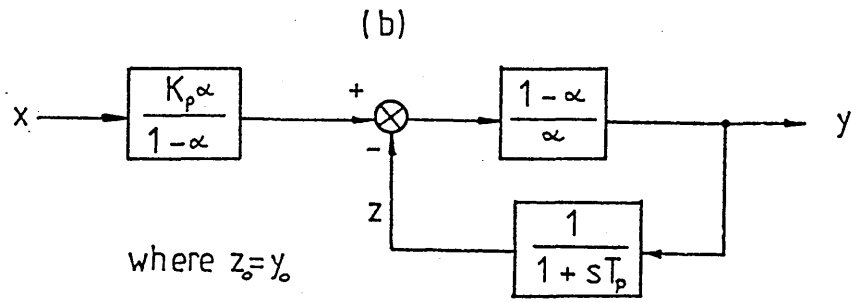
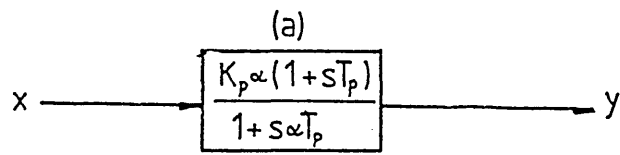


Fig. A.6.4 Lead-Lag Network Block

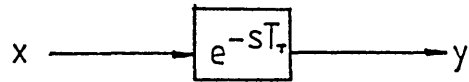


Fig. A.6.5 Transport Delay Block

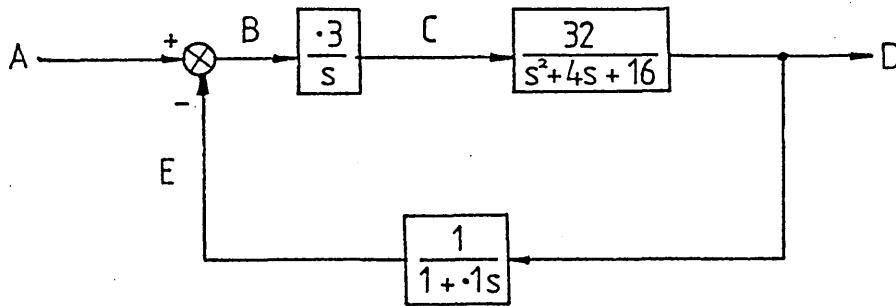


Fig. A.6.6 Example System

The "corrector" formula (A6.5) is then applied iteratively as follows, until  $z$  is obtained with sufficient accuracy, when the values  $y_{n+1}^{(k)}$  and  $z_{n+1}^{(k)}$  are given as the outputs.

$$z_{n+1}^{(k)} = z_n + \frac{h}{2T} \cdot \left[ (y_n - z_n) + (y_{n+1}^{(k-1)} - z_{n+1}^{(k-1)}) \right]$$

$$y_{n+1}^{(k)} = \frac{1-\alpha}{\alpha} \cdot \left[ \frac{k_p \alpha x_{n+1}}{1-\alpha} - z_{n+1}^{(k)} \right] \quad \begin{array}{l} k=1,2,\dots \\ \text{until} \\ \text{finished} \end{array}$$

The call to the routine takes the form

CALL LEDLAG(K,A,T,X,XNXT,Y,Z,H,YNXT,ZNXT)

where K = gain (real)

A = lead-lag factor ( $\alpha$ )

T = time constant (s)

Other variables as before.

N.B. on first step, Z may be given as  $Z_0 = Y_0$

#### A6.6 Simulation of a Transport Lag

Discussion of this routine is a little out of place here, as no differential equations are involved.

However, it is included for completeness. The routine simulates the transport lag of figure A6.5 and is used by the call:

CALL DELAY (N,X,Y,YNXT,RI)

with the named common block:

COMMON / DELAY / I, J

where N = number of parameters stored at each step  
(regard N = 1 for the moment)

I = number of simulation integration steps (H)  
comprising the transport lag, i.e.

$$I = T/H$$

J = number of current delay table entries in  
use (automatically updated by the routine  
after being entered as zero on the first  
step).

X = input to the delay element at the present  
time - this is placed into a rotating  
shift register created on a disc file.

Y = output from the delay element at the present  
time (read from the rotating shift register  
I places after X).

YNXT = output from the delay element one step (H)  
later (needed for use in the routines  
described above). (Read from the rotating  
register I-1 places after X)

RI = value existing initially at output of delay  
element (=  $y_0$ ). The rotating register is  
initially filled with this value which will  
therefore be output until I steps have  
been executed.

#### A6.7 Use of Simulation Package Routines

In order to use these routines, a main program must be written which controls the calling of the routines, sets up the initial state of the system, and handles the output. To illustrate the principles involved, consider the simple fictitious system given in figure A6.6. Let us take as an example a ramp input of  $A = 0.1t$  units, with an initial value  $A_0 = 5$  and  $D_0 = 5$ .

Firstly, it is necessary to calculate all system states at the initial values of  $A_0$  and  $D_0$  (it is assumed that steady state exists before the ramp is applied).

Assuming steady-state conditions, we can say that the time-varying (transient) responses of the first and second order blocks make no initial contribution. The second order block has a natural frequency of  $4 \text{ rad s}^{-1}$ , and gain of 2, therefore  $C_0 = D_0/2 = 2.5$ . It is not possible to work "backwards" to obtain  $B_0$  via the integrator, since an integrator can have (in theory) any output at steady state. Therefore we work in the other direction viz.  $E_0 = D_0/1 = 5$ ,  $B_0 = A_0 - E_0 = 0$ . Now, we choose the step length  $H$  to be 0.1 times the smallest time constant in the system for accuracy. The first order time constant is 0.1s, the second order "time constant" =  $(2\zeta\omega_n)^{-1} = \frac{1}{2*0.5*4} = 0.25\text{s}$  therefore we choose  $H = 10 \text{ ms}$ . Further, we must initialize the variable  $Z$  inside the second order block (see fig.A6.3). This is given as

$$Z_0 = \frac{D_0}{(2\zeta\omega_n)^{-1}} = \frac{D_0}{0.25} = 20$$

We can now state the problem as

$$A=5 \quad B=0 \quad C=2.5 \quad Z=20 \quad D=5 \quad E=5 \quad H=0.01$$

It is now necessary to call the appropriate simulation routines in such a way as to update the system states AS A CONSISTENT SET. Let us assume we wish to simulate 5 seconds of real time. Then  $N=5/H=500$  steps. The necessary pseudo code (FORTRAN) to perform the simulation would then be:-

```

T = 0
DO 100 I = 1,500
T = T+H
C*** RAMP INPUT ON NEXT LINE...
ANEXT = 5 + T/10
C*** CALCULATE CORRESPONDING SYSTEM STATES...
BNEXT = A-E
CALL INTEG(.3,B,C,H,CNEXT)
CALL SECORD (2,.5,4,C,D,Z,H,DNEXT,ZNEXT)
CALL LAG(1,.1,D,DNEXT,E,H,ENEXT)
OUTPUT OR PLOT SYSTEM STATES A TO E(FOR T=T-H)
C*** UPDATE PARAMETERS...
A = ANEXT, B = BNEXT, C= CNEXT, D = DNEXT, Z=ZNEXT,E=ENEXT
100 CONTINUE

```

It can thus be seen how easily these routines permit system simulation. Note that in general, when a routine requires knowledge of the input variable at the next time step (e.g. the LAG routine), it has always just been calculated by the routine for the previous block in the system (e.g. DNEXT calculated by SECORD in the example above).

APPENDIX 7

Outline Specification of Single Board Microcomputers Used

(For more detail, see Ref.(58), which is the manufacturer's literature).

Manufacturer: J.B. Microsystems Ltd., Ashly-de-la-Zouch.

Type: MERLIN MRL V3/1

Processor: Intel 8085

System Clock: 3 MHz

Communication: Three RS232-c Serial Link Interfaces  
One RS422 Data Link

Memory:  $\frac{1}{2}$ k RAM, plus six bytewise memory sockets which are all link-selectable for RAM or EPROM memory chips.

Maths Facility: High Speed Maths functions are available using the AMD9511 mathematics processor chip on-board.

Digital Inputs: Sixteen, opto-isolated (15V to 40V) ) Also 6-bit  
Digital ) TTL memory-  
Outputs: Sixteen, opto-isolated (60V, 0.5A) ) mapped I/O  
port.  
)

Analogue Inputs: Thirty, 12-bit, single-ended. (Expanded to sixty-one on one of the machines in the present scheme by adding external multiplexers, addressed by some of the digital outputs).

Analogue Outputs: Eight, 8-bit )  
Two, 12-bit ) (Voltage outputs)

Programming: (This application is of course unique, other users may use other methods and other languages). Parts of the software which do not require especially fast execution are written in the high-level FORTRAN language on a disc-based development

system (of DAI manufacture); and compiled into machine code and blown into EPROMS using this development system. These EPROMS can then be plugged into the sockets on the MERLIN board, and the programme can be run using the hardware reset and ROM-based monitor on the MERLIN board (the monitor programme is an optional purchase).

Parts of the programme requiring rapid execution are programmed directly in 8085 machine code which can be incorporated "in-line" with the FORTRAN source.

FORTRAN was chosen for the following reasons:

- i) Extremely familiar to the author.
- ii) It was definitely necessary (for reasons of execution speed) to use a compiled language rather than an interpreted language (such as BASIC).
- iii) A FORTRAN compiler was readily available for DAI development system used.

Other features:

Many other features could be mentioned, but are not relevant here.